Biosensing-inspired Nanostructures:

Author: Luke A. D'Imperio

Boston College Electronic Thesis or Dissertation, 2019

BIOSENSING-INSPIRED NANOSTRUCTURES

Luke A. D’Imperio

A dissertation submitted to the Faculty of the department of Physics
in partial fulfillment of the requirements for the degree of
Doctor of Philosophy

Boston College
Morrissey College of Arts and Sciences
Graduate School

August 2019

BIOSENSING-INSPIRED NANOSTRUCTURES

Luke A. D'Imperio
Advisor: Prof. Michael J. Naughton

Abstract: Nanoscale biosensing devices improve and enable detection mechanisms by taking advantage of properties inherent to nanoscale structures. This thesis primarily describes the development, characterization and application of two such nanoscale structures. Namely, these two biosensing devices discussed herein are (1) an extended-core coaxial nanogap electrode array, the 'ECC' and (2) a plasmonic resonance optical filter array, the 'plasmonic halo'. For the former project, I discuss the materials and processing considerations that were involved in the making of the ECC device, including the nanoscale fabrication, experimental apparatuses, and the chemical and biological materials involved. I summarize the ECC sensitivity that was superior to those of conventional detection methods and proof-of-concept bio-functionalization of the sensing device. For the latter project, I discuss the path of designing a biosensing device based on the plasmonic properties observed in the plasmonic halo, including the plasmonic structures, materials, fabrication, experimental equipment, and the biological materials and protocols.

ACKNOWLEDGEMENT

I thank the different funding sources through teaching assistantships and research assistantships and associated grants that have enabled my time at Boston College.

I have great appreciation for everyone at BC for being part of this valuable time in my life. I feel fulfilled in both my growth as a scientist and as a person. It's been my utmost privilege to be a part of a community with a long list great minds and wonderful people.

At the top of that list, Professor Naughton has been a perpetual source of wisdom, encouragement, and good times that make me feel very lucky to have him as an advisor. Your spirit of excitement and tenacious pursuit of understanding will shape my career as a scientist for the better. Thank you for your patience, support, and kindness.

To our amazing recent post-doc/now-professor Juan Merlo, I cannot thank you enough for your unparalleled wisdom, kindness and humor on all things scientific and philosophical. I am truly grateful for the help you have given to me on most days of my time here at BC, even to the last day as a member of my thesis committee. I thank my other thesis committee members, Prof. Ken Burch and Prof. Kris Kempa for their time and guidance in this last part of my graduate experience and in many other ways in the past several years. I thank all of the BC physics professors, particular those whom I have had the honor to take courses with and TA for. I thank Dr. Tim Connolly for his active role in several of my projects, and for his dedicated work ethic and patience. I thank the Professors of other departments whom I have had the distinct pleasure of collaborating with, including Prof. Tom Chiles, Prof. John Christianson, and Prof. Jinhee Park. I thank all of the supporting staff, whose hard work has enabled me to dedicate my time and mind on my research, including Jane Carter, Nancy Chevry, Síle Ni Scanlain, Scott Bortolotto, John O'Grady, Walter Carberry, Chris Cardoso, Kiel Smith, and Fabia Denaro. I thank all of the technical staff that have been an invaluable resource during my graduate experience, including Paul Dee, Rich Pijar, John Williams, Brett Judson and Svet Simidjiysky. Particularly, I want to thank Steve Shepard, whose training has most

significantly fostered the growth of my technical skillset. I thank Dr. Michael Burns for sharing his extensive knowledge on many technical and worldly matters.

I thank all of my fellow graduate students for making BC a truly enjoyable place to work. I give special thanks to my first-year trench-mates, Yitzi Calm, Alex Shvonski, Kun Jiang, Rebecca Dally, Nawaraj Dahal, Hong Pan, and Shenghan Jiang. I thank the two intelligent and kind biology graduate student collaborators that I worked with, Amy Valera and Michelle Archibald. I thank all of the dedicated undergraduate researchers who I have worked with throughout my years at BC, who I have been very happy to teach and learn from. I thank my fellow racquetballers Chris Darcy, Paul Scarnici, Lance Tucker, Mark Cooper, David Botwinik, Antoine Smith, and Brad Bates for the great exercise and friendship to keep my mind and spirit fueled for the lab.

I have great appreciation for all of the past and present members of the Naughton Lab, some mentioned above, and all of whom have constantly contributed to my personal growth and my, sometimes arduous, transformation into a scientist. To my fellow graduate lab mates Yitzi Calm, Aaron Rose, Nate Nesbitt, Chaobin Yang, Mark Schiller, Victoria Gabriele, Jeff Naughton, Binod Rizal and Fan Ye, I thank you for the multitude of ways you have improved my research and life; with hope that our futures remain connected. I extend extra cheers to Yitzi Calm for fighting out the last weeks with me.

Thank you to all of my friends, many of you already mentioned above, for improving my life in the ways that you have. I particularly thank Alex and Allie Shvonski for introducing me to a nice girl. I express my most avuncular appreciation to my fellow friends of the Corrib for making my life in Boston truly magical.

To my mom, dad, brothers and all of my family, I simply cannot thank you enough for all that you have done for me throughout my life that has led to this point. You have provided me the opportunity to live happily and achieve great things.

To the greatest joy of my life, Emily, thank you and I love you. Thank you for your dedication and commitment to me. Thank you for sharing with me your amazing family and friends. Thank you for joining me on this great journey that we are about to go on.

TABLE OF CONTENTS

LIST OF FIGURES

ACRONYMS

AFM – Atomic force microscope
ALD – Atomic layer deposition
EBL – Electron beam lithography
EC – Electrochemical
ECC – Extended core coax
CAD – Computer-aided design
CCD – Charge-coupled device
DI – Deionized
ELISA – Enzyme-linked immunosorbent assay
FIB – Focused ion beam
FWHM – Full width at half maximum
ITO- Indium tin oxide
LSPR – Localized surface plasmon resonance
IgG – Immunoglobin G
IL – Illuminated light
ISFET – Ion-sensitive field-effect transistor
LAM - Lipoarabinomannan
LED – Light emitting diode
MEMS – Microelectromechanical systems
NA – Numerical aperture
NEMS – Nanoelectromechanical systems
NDF – Neutral density filter
NP - Nanoparticle
NPGS – Nano pattern generation system
PBS - Phosphate-buffered saline
PDMS- Polydimethylsiloxane
PMMA- Poly(methyl methacrylate)
POC – Point of care
PVD – Physical vapor deposition
Qdot – Quantum dot
RIU – Refractive index unit
SA – Streptavidin
SAM – Self-assembled monolayer
SEM – Scanning electron microscope/micrograph
SPP – Surface plasmon polariton
SPR – Surface plasmon resonance
STS – Scanning tip spectroscopy
TIF - Total internal reflection
TL – Transmitted light
TBS - Tris-buffered saline

1. Introduction

1.1 Importance of Biosensing

A biosensor is a device that converts the physical and/or chemical interaction of a biological or bio-related substance into an analytical signal. In doing so, the characterization or quantification of these substances has been used to help us expand our understanding of nature and improve the quality of life.

Biosensors impact several aspects of our lives. We interact with many of them directly, such as glucose monitors for diabetics, pregnancy tests, and wearable heart rate monitors. Others play significant roles behind the scenes, such as food quality and beverage fermentation monitors, airborne allergen monitors, and those ubiquitous to drug research and development.

Diagnostic and health monitoring are some of the most common uses of biosensors. They are used from before birth in prenatal genetic testing until after death in pathology tests during autopsy. As a result of their regular application, especially in United States and Europe, the global diagnostics market value has been estimated at $40 – 45 billion USD (World Health Organization, 2016). Diagnostics may also be the most commendable application of biosensors, as accurate diagnosis is crucial to the control of infectious diseases, which disproportionately affect the populations of resource limited areas.

1.2 Nanoscale Sensing Devices

Developments in on-chip, portable electrochemical biosensing tools, which are suited to point-of-care (POC) use, are limited in part by a lack of appropriate surface architectures. Signal transduction and overall sensor performance is dictated by electrode design, and as a consequence, simplistic structures, such as planar gold, may not be sufficient to maintain high sensitivity on a miniaturized platform (Grieshaber et al., 2008; Lowe, 1984; Kasemo, 1998). As such, the field of biosensing has greatly benefited from the utilization of nanomaterials and nanofabrication techniques in order to overcome these limitations (Chen et al., 2010; Roy and Gao, 2009; Brazaca et al., 2017; Wongkaew et al., 2018; Zhang et al., 2017; Zhu et al., 2015; Rizal et al., 2013). Figure 1 below illustrates some common elements that are involved in biosensing devices.

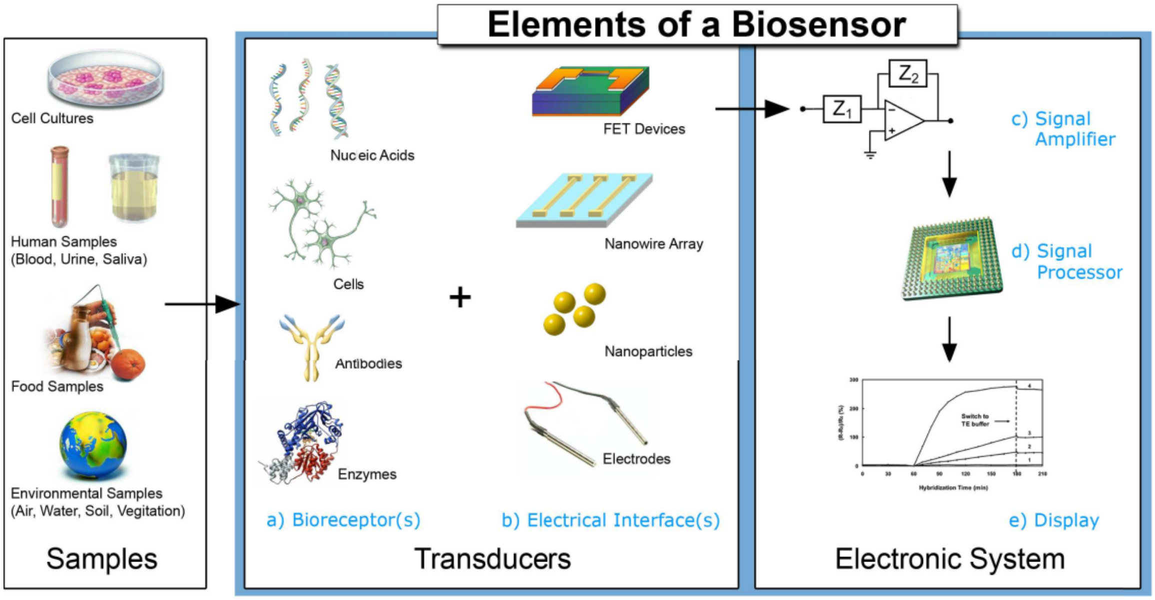

Figure 1. Elements and selected components of a typical biosensors. Shown are common tested materials (samples), designed nanoscale structures (transducer), and recording and processing equipment (electronic system) involved in nanostructure biosensors. Adapted from Grieshaber et al., 2008.

Among the applications, biosensors based on nanoscale materials or structures have demonstrated high levels of success in the detection of molecular and biological species related to human disease. This can be understood in part by consideration of typical spatial dimensions of targets of biosensing devices, *e.g.* viruses, proteins, and other virulence factors, on the order of single-to-tens of nanometers (Erickson, 2009; Purohit et al., 2005).

While all biosensing devices depend on material properties in one way or another, some biosensing devices are based entirely on the physical phenomena intrinsic to the constituent materials, *e.g.* ISFET-based devices (Lee et al., 2009; Bergveld, 2002), graphene-based devices (Peña-Bahamonde et al., 2018; Justino et al., 2017; Tehrani et al., 2014), and topological insulators-based devices (Kottaram Amrithanath et al., 2019; Mohammadniaei et al., 2018), as shown in Figure 2. It is important to note that these devices have physical phenomena that are dependent on nanoscale features. There is a large and growing interest in many of the materials incorporated into these devices for other research and applications, often preceding their appearance in biosensing devices. For this reason, the availability and understanding of the fabrication tools and techniques used to produce these materials is also increasing, thereby facilitating their ubiquitous research and development.

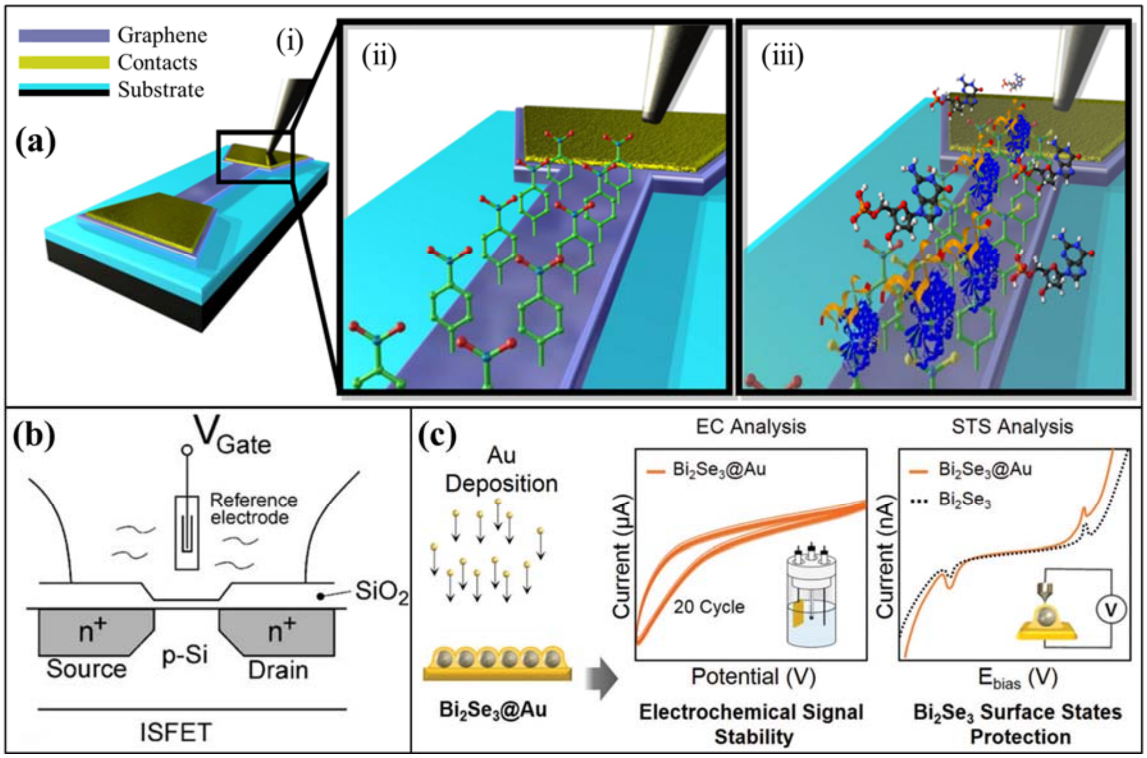

Figure 2. Materials-based biosensing devices. (a) Graphene-based biosensor (Tehrani et al., 2014), (b) ion-sensitive field-effective transistor biosensor (Bergveld, 2002), and (c) topological insulator-based biosensor (Mohammadniaei et al., 2018).

Another class of nanoscale sensing device can be described as those that are based on mechanical motion for features at the nanoscale. The most common example being those based off microelectromechanical systems (MEMS) and nanoelectromechanical systems (NEMS) (Takahashi et al., 2013; Sangeetha et al., 2013; Arlett et al., 2011; Yeri et al., 2011; Yu et al., 2015). Other systems rely on sensing through physical changes caused by target biomolecules, *e.g.* changes to the resonant frequency in piezoelectric devices (Pohanka, 2016; Tombelli, 2012; Cooper et al., 2007), through volumetric-expansion of conducting materials in the presence different chemicals (Maldonado et al., 2008). Figure 3 below depicts some of these examples, where detection of biological species corresponds to active changes in mechanical properties, most commonly micro- and nanoscale lengths. These changes are then coupled to signal transducers through electrical or optical recording mechanisms, for sensitive real-time measurement of antigen presence or characteristics.

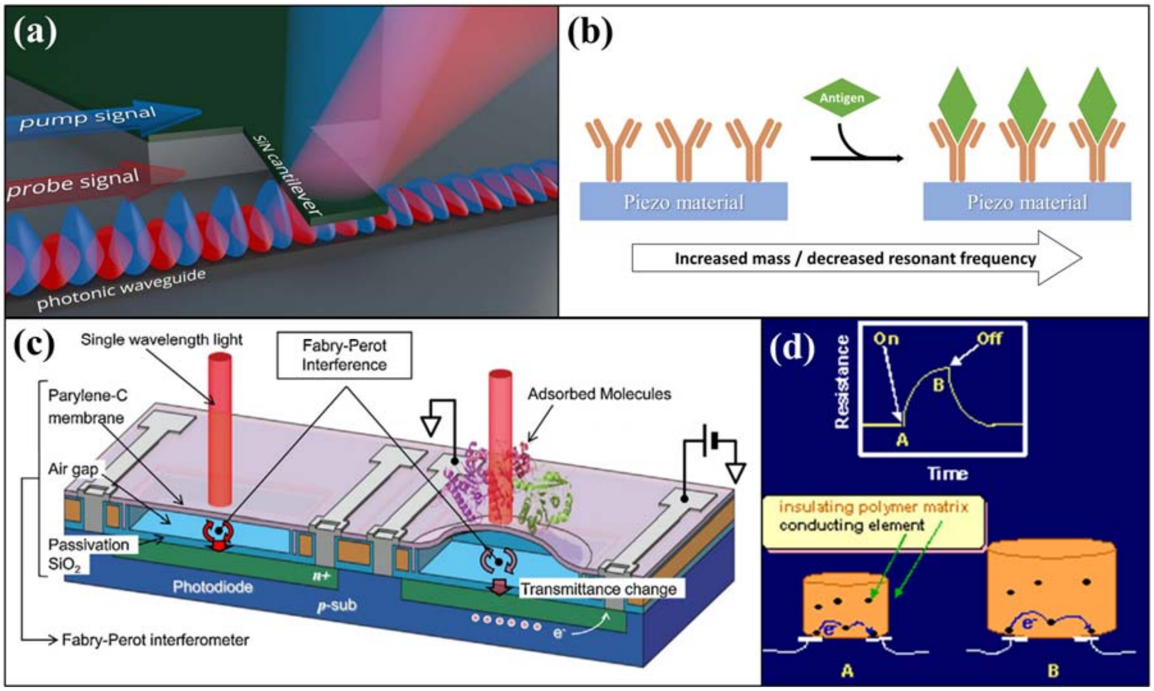

Figure 3. Biosensors based on mechanical actuation. (a) NEMS-based biosensor (Yu et al., 2015), (b) piezoelectric-based biosensor (Pohanka, 2016), (c) actuated Fabry-Perot cavity biosensor (Takahashi et al., 2013), and (d) polymer swelling based biosensor (Lewis et al., 1996).

Another class of nanoscale sensing device are those based on static structural characteristics and spatial properties (Figure 4). These nanoscale sensing devices improve and enable detection mechanisms by taking advantage of properties inherent to nanoscale structures, such as high surface-to-volume ratio (Arroyo-Currás et al., 2017; Liu et al., 2014), single molecule-sized pores (Feng et al., 2015), high aspect-ratio nanowire (Hsu et al., 2014), and small path-lengths in nanogap electrode arrays (Shim et al., 2013; Li et al., 2010).

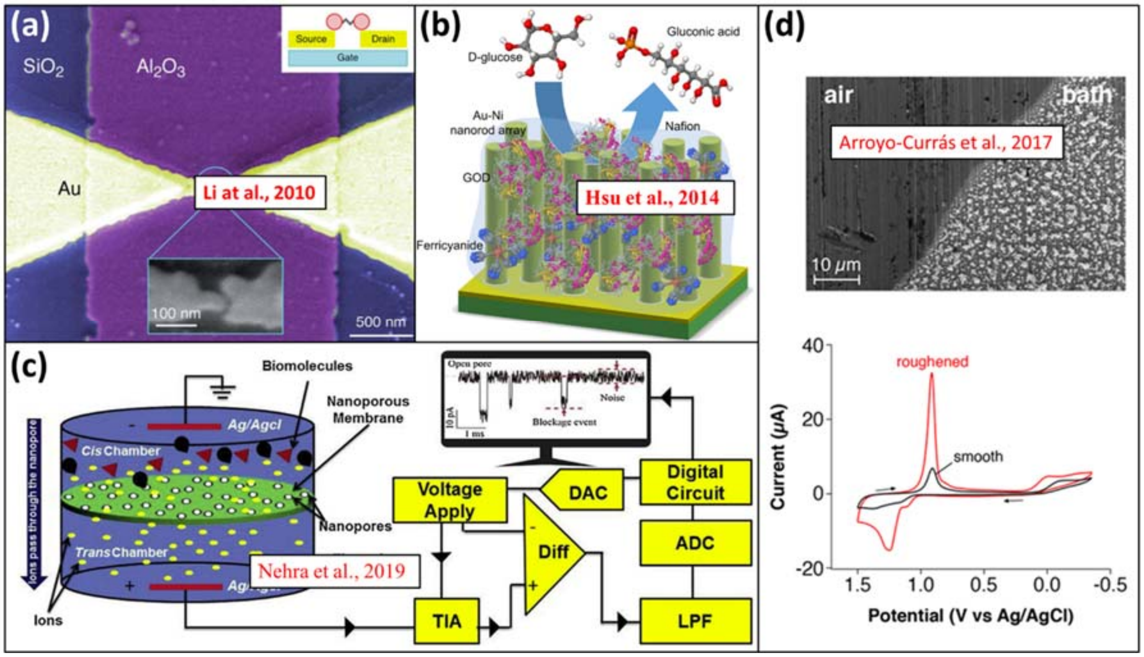

Figure 4. Biosensors based on nanoscale structural features. (a) nanogap-based biosensor (Li at al., 2010), (b) high aspect-ratio nanorod biosensor (Hsu et al., 2014), (c) nanopore-based biosensor (Nehra et al., 2019), and (d) high surface area biosensor (Arroyo-Currás et al., 2017).

These and other nanoscale properties facilitate the existence and enhancements of phenomena key to biosensing, such as redox cycling (Wolfrum et al., 2016), localized electric fields (MacKay et al., 2015), and Faradaic-to-capacitive signal ratio (Morgan and Weber, 1984; Otero et al., 2016). Since these phenomena depend on the nanoscale features, small, judicious changes to these parameters can potentially result in significant improvements in device capability (Rizal et al., 2013; Arroyo-Currás et al., 2017).

1.3 Plasmonic Sensing Devices

Plasmonic-based sensing devices have responses that are dominated by the material properties nearby the surfaces to which biological species can be selectively captured, thereby enabling their capacity for applications in sensitive biological detection. Synchronized design of plasmonic structures with corresponding biological assays has promoted the growing and impactful field of plasmonic-based biosensing devices.

This detection phenomenon is the combined consequence of aspects of the biological processes used to capture targeted biomolecular species as well as the inherent properties of surface plasmon polaritons. A surface plasmon polariton (SPP) is a quasiparticle hybridization of a photon with a surface plasmon resonance (SPR), which itself is a quasiparticle collective oscillation of electron density at the interface of a metal and dielectric, as first proposed by Pines and Bohm in 1952 (Pines et al., 1952). The solutions to Maxwell's equations at this interface are fields with exponentially decaying transverse-magnetic polarization. Put another way, the fields are greatest near the surface. Satisfying the electromagnetic boundary conditions reveals that the plasmon dispersion relationship is dependent upon both materials, specifically their relative dielectric permittivities. A principle mechanism of many biosensing devices involves the functionalization of the device for selective capturing of target antigens. Since the surface is intrinsically the location where biological functionalization occurs, the change to material properties during surface functionalization and subsequent antigen capture is most prominent in the same near-field region that the electric fields of the SPP are greatest. This fact is what enables plasmonic-based sensing devices to have high detection sensitivities of very low concentrations of biomolecular species, ultimately motivating research and development for their promising ability to have impactful applications in sensitive biosensing devices. There exist several different configurations of SPR-based sensors that exploit the different ways of coupling light to an interface where surface plasmons are formed, as shown in Figure 5 below. Other ways of exciting surface plasmons exist (Gong et al., 2014; Baragiola et al., 1999), though they are uncommon and inapplicable to biosensing.

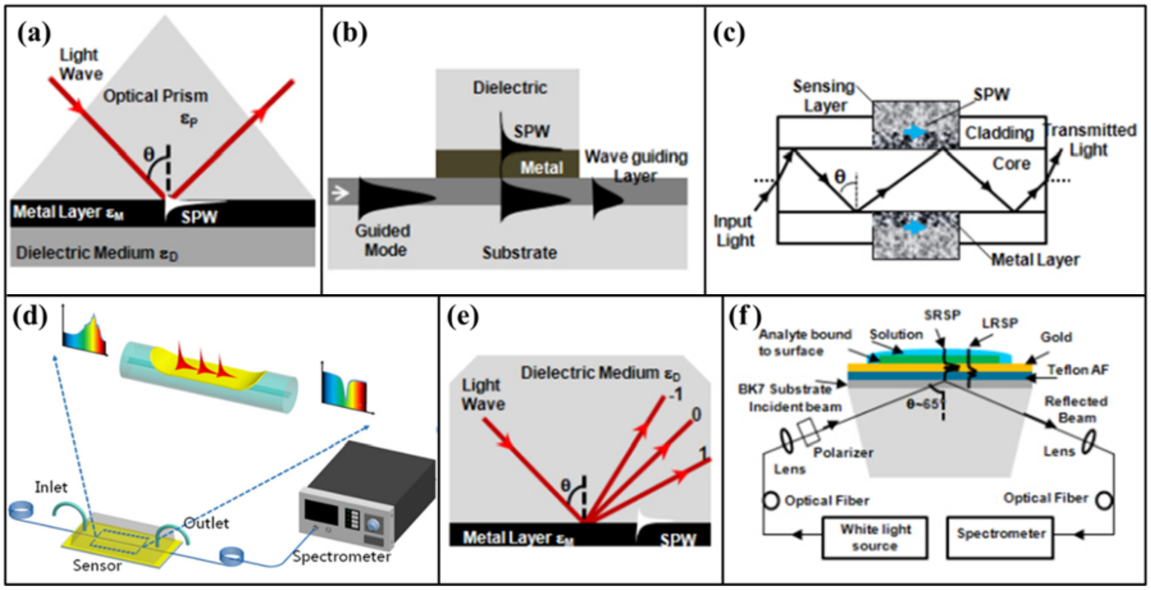

Figure 5. Different types of SPR-based sensing mechanisms. (a) Prism coupled TOI, (b) waveguide coupled, (c) microstructure optical fiber, (d) side-polished optical fiber, (e) grating-coupled, and (f) self-referencing SPR. Adapted from Homola, 2003; Klantsataya et al., 2014; Dong et al., 2019; Hastings et al., 2007.

In order to couple energy into the surface plasmon, energy must scatter from the light, as is discussed in section 3.1.1. This loss of energy corresponds to a decrease in intensity of the incident light for different wavelengths. Most commonly, measuring this change in intensity as a function of the device parameters and applied materials is the detection mechanism of plasmonic-based biosensors, though other detection mechanisms have been demonstrated, *e.g.* electronically (Peale et al., 2016).

Successful experimental demonstration of any device or phenomenon requires the appropriate equipment to be used in detection, discussed in section 3.2. The appropriate equipment is determined in part by the optical regime characteristic of the material incorporated in the plasmonic-based devices. One of the key material properties that influences this regime, and corresponding equipment, selection is the density of free charge carriers, as is shown in Figure 6.

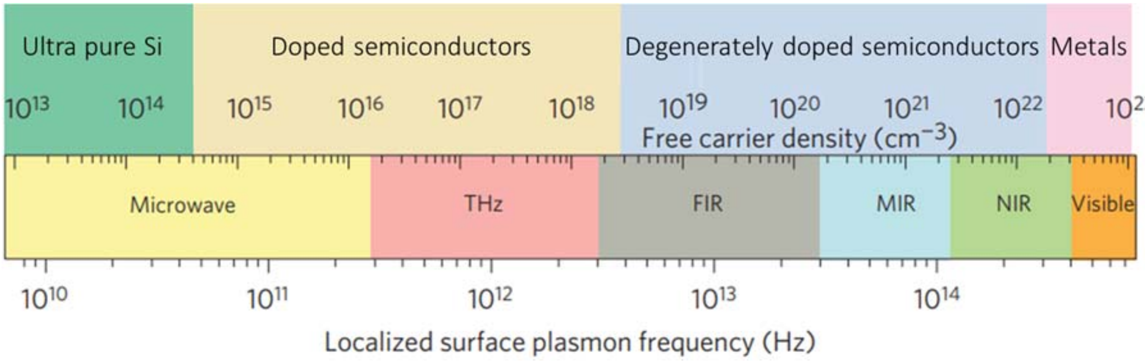

Figure 6. Optical regime and free carrier density. Adapted from Luther et al., 2011.

There is certainly a large range of tools, techniques and materials employed in the development of plasmonic-based biosensing devices (McPeak et al., 2015; Li et al., 2015; Mauriz et al., 2016). This enables plasmonic-based biosensors to have a broad impact in a variety of important applications, *e.g.* exceedingly high sensitivities capable of detecting single biomolecules (Zijlstra et al., 2012), precise quantitative measurement of individual DNA properties (Riedel et al., 2016), the detection of hepatitis B, malaria, tuberculosis and other of the world's most impactful infectious diseases (Chen et al., 2015; Sivaraj et al., 2016; Wood et al., 2019) , and multiple detection methods of cancer biomarkers (Ferhan et al., 2018), some of which are shown in Figure 7 below. The growing field of plasmonic-based biosensor has and can continue to benefit from the introduction of new structures and techniques, hopefully including those from this work.

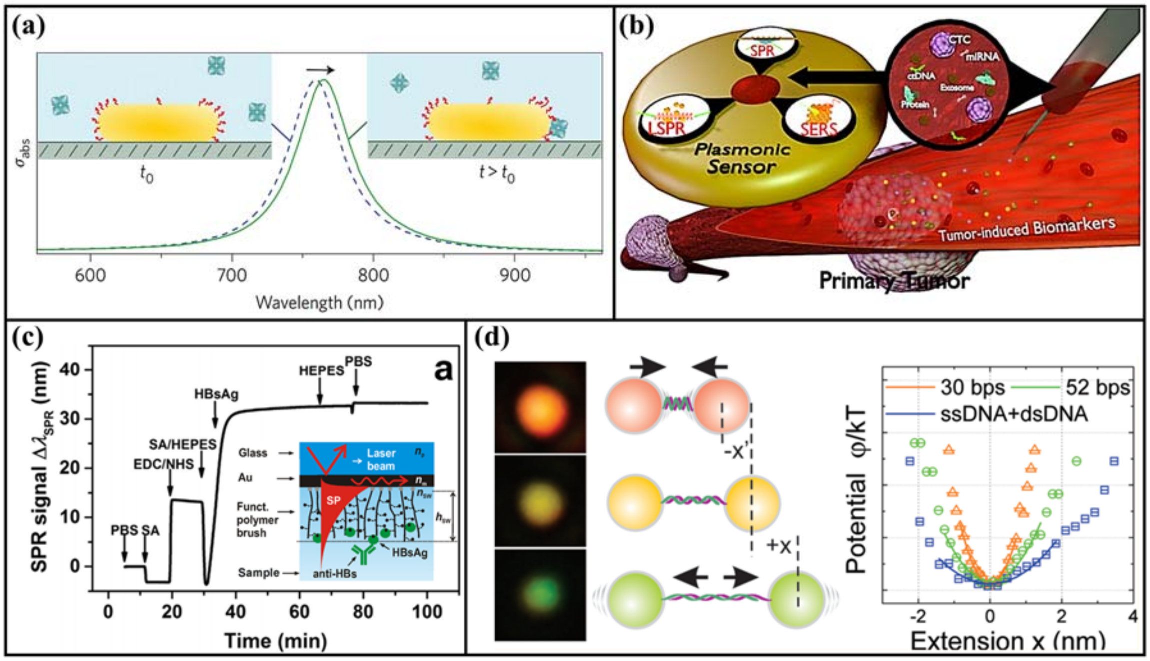

Figure 7. Some detected biomolecules. Detection includes that of (a) single biomolecules, (b) cancer biomarkers, (c) disease biomarkers, and (d) DNA. References in text above.

1.4 Organization of this thesis

In Chapter 2, I will discuss the development and experimentation of a biomolecular sensing device based on an array of nanocoaxial electrodes. I will introduce the tools and fabrication procedure used in creating the structures as well as the materials and testing involved in device measurements. In Chapter 3, I will discuss the process engineering of concentric ring nanostructures towards the development of a plasmonic-based biosensing device. Within each chapter, I will include a review of relevant literature pertaining to nanogap electrode and plasmonic-based sensing devices, respectively. Each chapter will conclude with a section on suggested future works.

2. Extended Core Coaxial Sensor

2.1 Nanogap Electrochemical Sensing

2.1.1 Introduction

Biosensors that incorporate nanomaterials and nanofabrication techniques enable molecular detection of chemical and biological macromolecules with a high degree of specificity and ultrasensitivity. In this chapter, we discuss a novel fabrication process that yields a nanostructure capable of detecting biological macromolecules (D'Imperio, Valera et al., 2019). The extended core nanocoax (ECC) structure builds on a previously reported nanocoaxial-based sensor. The fabrication of the device incorporates an extended inner pillar, with controllable extension above the annulus and into the surrounding solution. This new design eliminates structural constraints inherent in the original nanocoax architecture. We also provide results demonstrating improvement in biosensing capability. Specifically, we show the capability of the new architecture to detect the B subunit of the *Vibrio cholerae* toxin at improved sensitivity (100 pg/ml) in comparison to optical enzyme-linked immunosorbant assay (1 ng/ml) and previously reported coaxial nanostructures (2 ng/ml).

2.1.2 Previous Works.

A nanogap-based architecture, the nanocoax, was previously reported and shown to be able to transmit visible light (Rybczynski et al., 2007; Merlo et al., 2014), convert light to electricity (Naughton et al., 2010), and detect volatile organic compounds (Zhao et al., 2012). The nanocoax has also been used as an optrode for neurophysiology (Naughton et al., 2016). Its architecture consists of vertically oriented, concentric metal-insulator-metal layers, previously with inner and outer electrodes having the same height, as shown in the cross-sectional, false-color SEM in Figure 8 below. The high sensitivity demonstrated in chemical (Zhao et al., 2012) and electrochemical (Rizal et al., 2013) detection indicated that the nanocoax might also hold promise for biomolecular sensing.

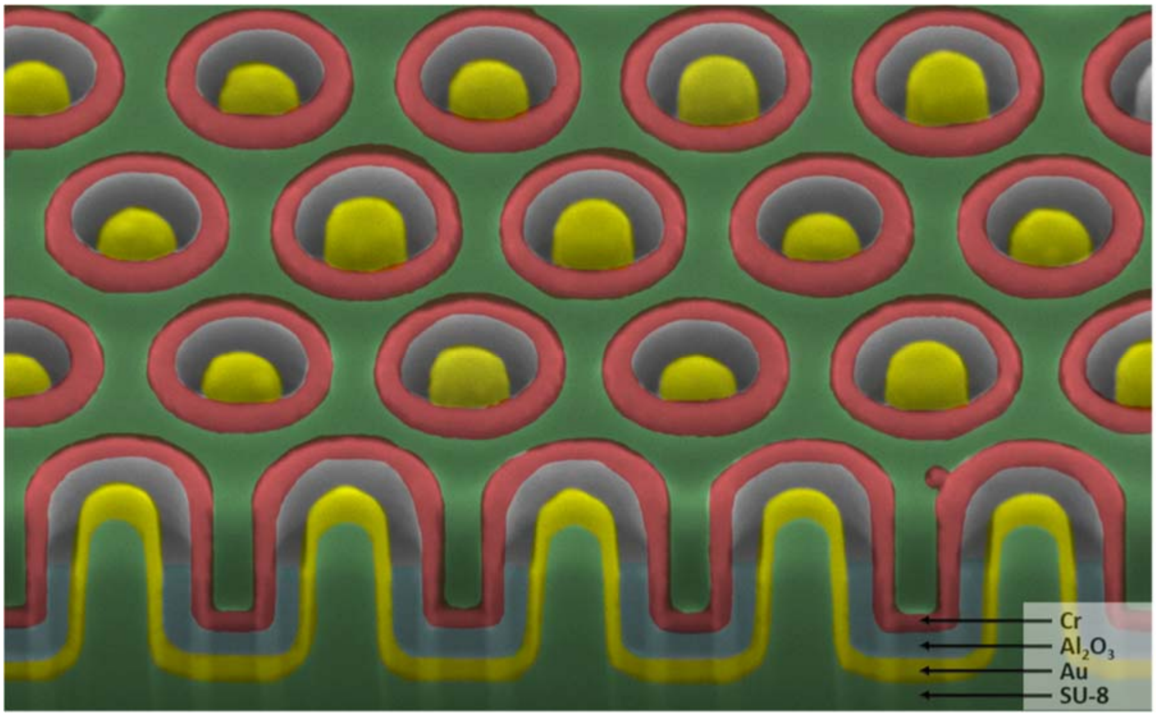

Figure 8. Cross-sectional, false-color SEM of the nanocoax. The general structure of the nanocoax and material boundaries of the MIM are shown. Adapted from Rizal et al. 2013.

Herein, we show how our novel fabrication, wherein the inner metal is extended above the annulus, affords a high density of biofunctionalization, greater sensitivity, and applicability for on-chip biosensing not possible in earlier iterations of the nanocoax structure (Archibald et al., 2015).

2.1.3 Equipment

Below are images of the core equipment used for this research.

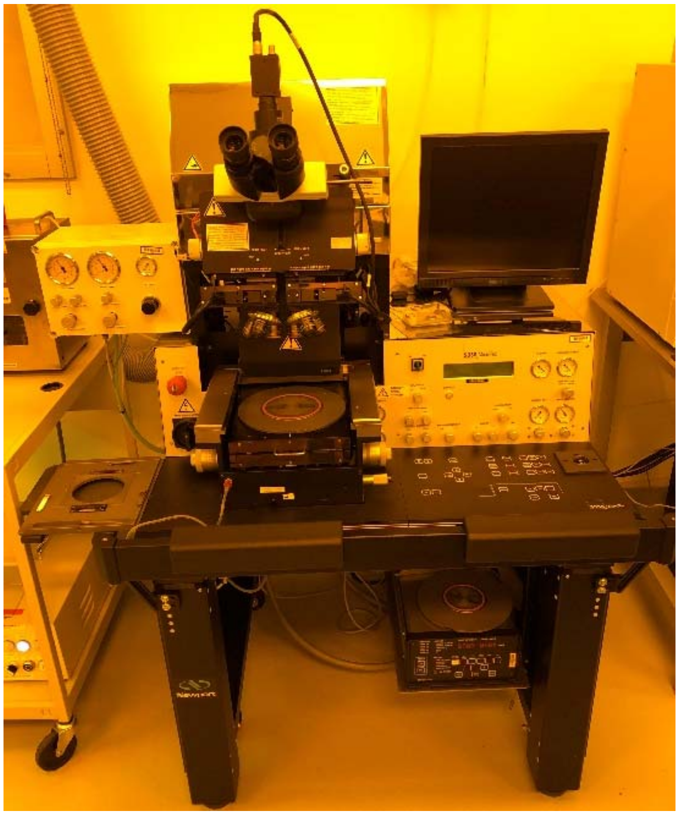

Figure 9. Karl SUSS MA6 Mask Aligner

Figure 10. AJA International Sputter Deposition system

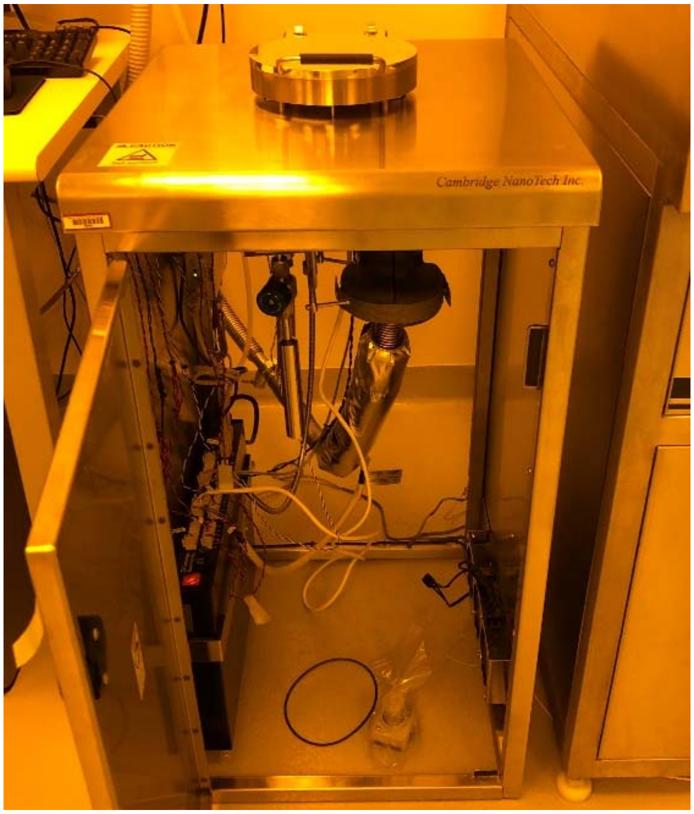

Figure 11. Cambridge NanoTech Atomic Layer Deposition System

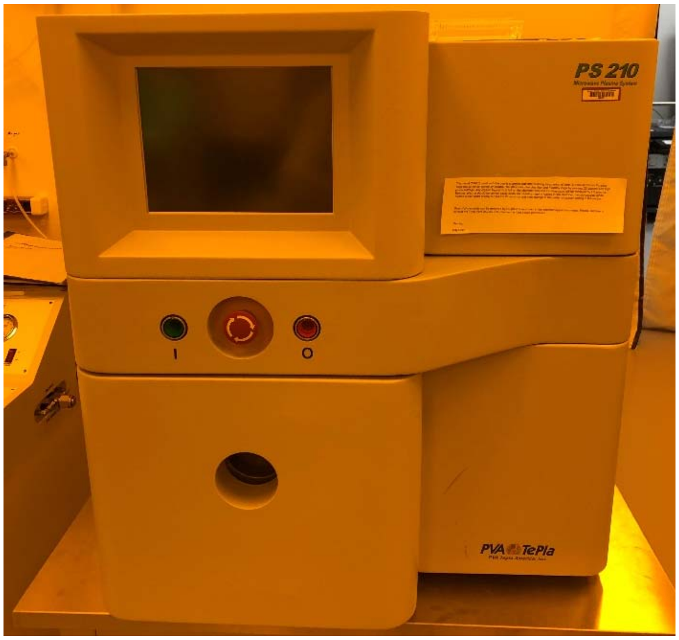

Figure 12. PVA TePla PS210 Plasma Barrel Etcher

Figure 13. JOEL JSM-7001F Scanning Electron Microscope

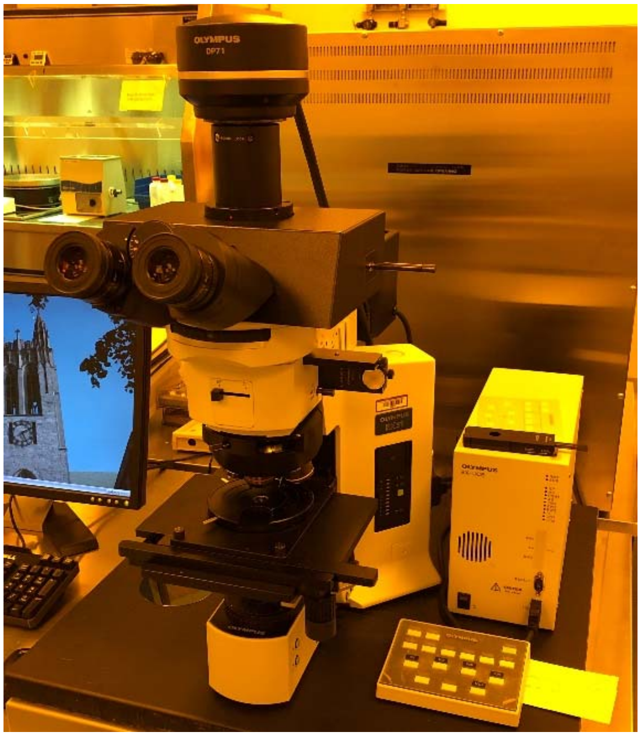
Figure 14. Olympus BX61 Optical Microscope

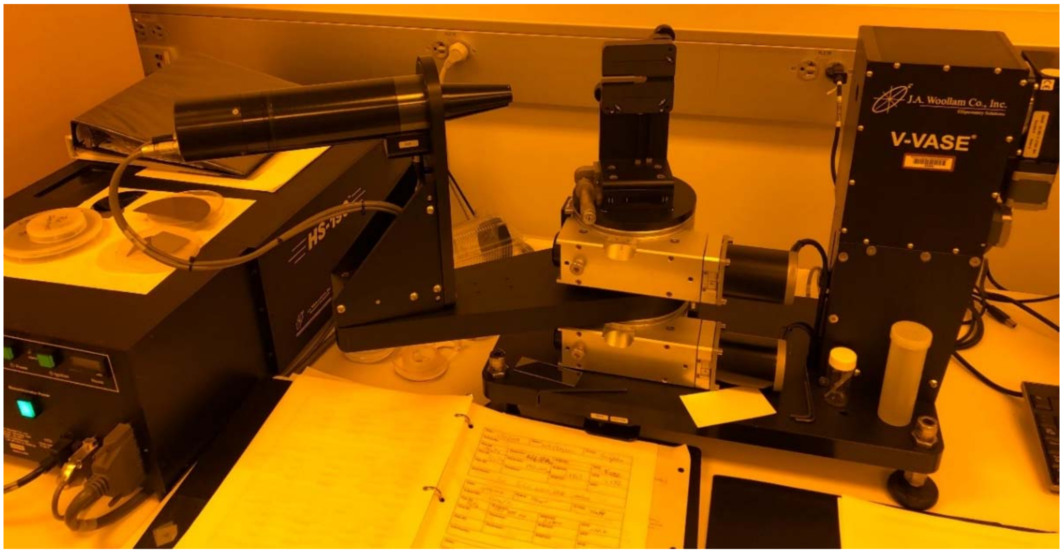
Figure 15. J.A. Woollam V-VASE Ellipsometer

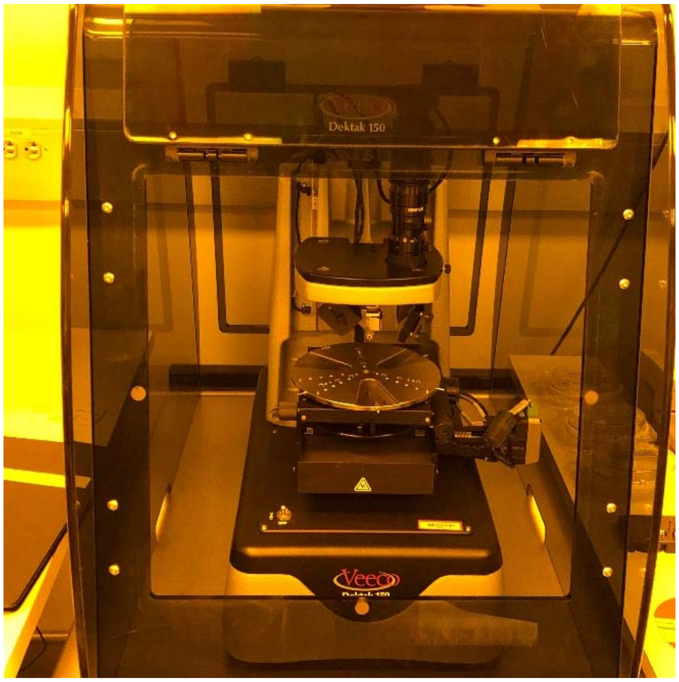

Figure 16. Veeco Dektak 150 Profilometer

Figure 17. Laurell Technologies WS-650-23B Spin Coater

Figure 18. Cleanroom user with personal protective equipment (PPE). Standard PPE for acid work includes cleanroom gown, acid gloves, arm sleeves, chemical goggles, and face shield.

Figure 19. Keithley 6512 Programmable Electrometer for GΩ resistance measurements

Figure 20. Gamry Instruments Potentiostat/Galvanostat Interface. Shown with reusable well apparatus and sample electronics interface for testing electrochemical experimentation.

Figure 21. Clausing Kondia Bridgeport Milling Machine in the SIMS Machine Shop

2.1.4 Chemicals and Reagents

Cholera toxin beta subunit antigen (CTX), ferrocenecarboxylic acid (FCA), ethanol, ethylenediaminetetraacetic acid (EDTA), and glycerol were purchased from Sigma-Aldrich (St. Louis, MO). Anti-cholera toxin subunit B polyclonal and monoclonal antibodies and alkaline phosphatase- (ALP) conjugated antibody were obtained from Abnova (Taipei, Taiwan). p-aminophenylphosphate (pAPP) was purchased from Gold Biotechnology, Inc. (St. Louis, MO). The BluePhos phosphatase substrate system was purchased from KPL (Gaithersburg, MD). Bovine serum albumin (BSA), Tween-20, phosphate buffered saline (PBS), and Tris base were obtained from Fisher Scientific (Pittsburgh, PA). Protein G was purchased from Protein Mods (Madison, WI). The Innovacoat gold nanoparticle 40 nm conjugation kit was obtained from Novus Biologicals (Littleton, CO).

Shipley 1813 photoresist, MF-319 developer, Microposit 1165, LOR-3B resist, and SU-8 were purchased from MicroChem Corp. (Westborough, MA). Transetch-N and Cr 1020 etchants were purchased from the Transene Company, Inc. (Danvers, MA). Epon resin 828 and Epikure 3140 curing agent were obtained from Miller-Stephenson Chemical Co. Inc. (Danbury, CT). Hydrogen peroxide (27%) and ammonium hydroxide (28%) were procured from Alfa Aesar (Ward Hill, MA).

2.1.5 Techniques

Optical ELISA: Optical ELISAs were performed identically to the off-chip ELISA, with the exception that for the last step, the BluePhos phosphatase system replaced pAPP as the reaction substrate. Absorbance was measured spectroscopically at λ=600 nm on a SpectraMax M5 (Molecular Devices, Sunnyvale, CA).

On-chip ELISA: ECC sensing arrays were biofunctionalized using a thiolated protein G diluted to 1 mg/ml in TBS. Substrates prepared as described in section 2.2.1 were incubated with protein G for 2 h at room temperature with rocking, after which the chips were rinsed thoroughly 3x in tris buffered saline (TBS). They were then incubated for 48 h at 4°C with a primary anti-cholera toxin polyclonal antibody diluted to 1 mg/ml in 10 mM HEPES. After incubation, they were rinsed 3x in TBS with tween-20 (TBST), and blocked for 1 h at room temperature using 5% bovine serum albumin (BSA) and 5% glycerol in TBST to prevent nonspecific binding to the well. A range of concentrations of CTX (100 pg/ml – 10 µg/ml) was prepared in 2% BSA/TBST, and incubated on the chip surfaces for 1 h at room temperature. The chips were again rinsed 3x with TBST. A secondary anti-cholera toxin antibody was diluted to 50 ng/ml in 2% BSA/TBST and was added to the chip surfaces for 1 h at room temperature, after which the chips were washed 3x with TBST.

Anti-mouse IgG conjugated to ALP was added at a concentration of 2.7 µg/ml for 1 h at room temperature. The chip was washed 6x with TBST and then 1 mM pAPP was added to the chip surface and incubated for 30 min in the dark at room temperature. The reaction was terminated with 20 µL of 50 mM EDTA in TBS. The 4-aminophenol (4-AP) generated in the reaction was oxidized directly on the sensing array *via* DPV in a potential range of -300 mV to 200 mV (to encompass the oxidation potential of 4-AP at -100 mV), with a potential step of 2 mV, a pulse amplitude of 50 mV, a pulse width of 50 ms, a sample period of 100 ms, and an equilibrium time of 10 s. Titrations of cholera toxin were analyzed by overlapping DVP signals. Nonspecific peaks were subtracted from all data points. Raw DPV signals were also subtracted to zero at -200 mV to ensure that observed peak currents were accurate.

Off-chip ELISA: Off-chip electrochemical ELISA assessments were carried out similarly to on-chip, with the following modifications. A 96-well microtiter plate was used in place of the gold chip surface for tethering of the primary capture antibody. In order to facilitate binding to the plastic microtiter plate, the primary antibody was diluted in 0.1 M $NaHCO_3$ for 2 h. The plate was then blocked overnight in 5% BSA in TBST. All subsequent reagent applications (cholera toxin, secondary antibody, tertiary antibody, and enzyme substrate) and wash steps were performed in the microtiter plate as previously described. The final redox product, 4-AP, was applied to the surface of the ECC for electrochemical measurement. DPV settings were as previously described for 4-AP redox.

2.2 Device Process Engineering

2.2.1 Operating Procedure

By far the largest use of my time for this project was in making new ECC samples. Hence, it is important to include an unabbreviated operating procedure. For completeness and succinctness, a summarized version will be included in the subsequent subsection *2.2.3 Fabrication*. There were many parameters to explore that required new chipsets. There were also many problems encountered with new processing steps and tools involved with the fabrication. Once viable chips were produced, the testing of the devices with biological materials was often a one-way trip and chips could not be easily cleaned for faithful resuse in subsequent testing. These and other factors resulted in the need for several chipset productions, with the total chip number produced at 113. Some of the values in the operating procedure below were subject to parameterization in order to see the influence on device performance, as is described in later sections. The values included below were those most recently used to produce viable samples.

Extended Core Coax Fabrication Procedure

Training on all equipment included is necessary before independent use is granted.

Wear all appropriate PPE when required.

If using silicon pillar sample skip to the section **Cleaning Si Pillar Samples.**

If producing pillar array in SU8 by nano-imprint lithography then follow the next section.

Nano-Imprint Lithography for Making SU8 Pillar Array

1. Ensure that the blinds are closed and open the nitrogen gas line to the mask aligner.
2. On the SUSS MA6 mask aligner, do the following waiting 3s between each:
   a. Press “On” on the SUSS power source
   b. Press “CP”
   c. Press “Start”
   d. Wait for lamp to warm up
   e. Press ‘Ch2’ if it’s indicator light is not already lit up
3. Obtain and clean substrate with procedure in **Cleaning Si Pillar Samples** below.
4. Turn on the Laurell spinner by pressing in the button on the back of the housing.
5. Open the vacuum line slightly to the Laurell spinner so you can hear gas flowing.
6. Set 2 hot plates to 65°C and 95°C, respectively.
7. On the mask aligner, carefully disconnect the vacuum hose from the mask holder and remove the mask holder, set aside.

8. Ensure that the screws of the NIL presser will clear the UV lamp guard. If they extend high enough to not clear UV lamp guard as it moves out, remove the circular wafer holder platform and set aside. Once removed, set a glass platform to support the presser on the black metal arms which used to house the wafer holder platform.
9. Change the parameters for the mask aligner to the following
   a. Process: “Lithografy”
   b. Exposure: “Flood”
   c. Time: 90 s
10. Place the appropriate chuck onto the spinner for the size substrate being used, making sure that the O-ring is secured.
11. Use the interface to select program “N” (6 s at 500 rpm followed by 35 s at 3000 rpm). If these parameters are changed, they can be adjusted by pressing the “F1” button.
12. Ensure that the substrate is centered on the spinner chuck and then press the “Vacuum” button on the spinner interface to secure the substrate to the chuck.
13. Obtain a bottle of SU8 2002 and transfer a sufficient amount (determined by the size of your samples) into a secondary container with a spout for easy pouring.
14. Slowly pour the SU8 onto the substrate so that a layer completely covers the entirety of the substrate. Be sure that the SU8 adheres to the corners and top edges of the substrate and does not detach. If any of the SU8 overflows the edges of the substrate, carefully wipe to remove the excess.
15. Close the lid of the Laurell spinner and press the “Run” button to begin spinning.

16. Once the program runs to completion, press the “Vacuum” button to free the substrate from the chuck and carefully move the substrate to the 65°C hot plate for 3 min.

*When placing the substrates on the hot plate, beware of discolorations or debris on the hot plate itself and try to avoid these, as they can lead to uneven heating.

17. After the 3 min, move the substrate to the 95°C hot plate for another 3 min.
18. Transfer the substrate to the base of the NIL presser with the SU8 side facing up.
19. Carefully align and place the PDMS mold onto the sample so that the pattern of the mold is facing down into the SU8 side of the sample.
20. Align a piece of glass onto the top of the mold for even pressure distribution.
21. Align the sample on the base of the NIL presser such that the pattern region of the PDMS mold will be exposed through the window in the top of the NIL presser.
22. Finger tighten the screws of the presser evenly. Alternate tightening each screw a small amount one at a time in order to prevent breaking of the glass or substrate.
23. Once the NIL presser has been tightened by hand, use tweezers for further tightening.

*Watch for air bubbles between the pressure distributing glass and the mold as the presence of these indicate that the presser is not clamped down hard enough and needs to be tightened further. Also, extreme or inconsistent tightening can break samples or glass.

24. Bake the entire sample in the presser on the hotplate at 95°C for 10 min.
25. As soon as 10 min have passed, move the presser to the mask aligner and expose it using the parameters as previously set.
26. After exposure, move the presser back to the 95°C hot plate for another 10 min.
27. After the time has elapsed, move the presser to the 65°C hot plate and immediately turn off the hotplate allowing it to slowly cool down for 30 min.

28. Remove the NIL presser from the hotplate and then remove the screws of the NIL presser and carefully peel the mold off of the substrate. Set hotplate back to 65°C.
29. Expose only the substrate in the mask aligner using the same parameters as before.
30. Place the substrate onto the 65°C hot plate and move the temperature up incrementally by 15°C intervals every 1 min.
31. Once the hot plate reaches 230°C, bake for 30 min.
32. After the 30 min has passed, incrementally decrease the temperature by 15°C every 1 min until it reaches 65°C once more. Hotplate may not cool this quickly.
33. Clean spinner and hotplates, disposing of chemicals, and powered down equipment.

Cleaning Si Pillar Samples in Piranha Etch

34. Set 16x30mm^2 samples in alumina rack and set rack into 250 mL beaker
    a. Set onto hotplate in chemical hood to and set hotplate to 150°C
    b. Carefully pour 100 ml of H_2SO_4 into beaker and heat for 10 min.
    c. Pour 33 ml of H_2O_2 (30%) into a graduated cylinder then VERY SLOWLY add the H_2O_2 into the heated H_2SO_4 (reaction with acid should be visible).
    d. After 20 min turn off heat and carefully remove sample rack from solution and immediately rinse THOROUGHLY with DI-H2O.
    e. Dry thoroughly with N_2 air and then remove samples from rack for processing.

Inner Electrode Photolithography and Sputter Deposition

35. Turn on Laurell pump in corridor.
36. Set up Mask aligner and developing chemicals.
    a. Obtain mask MEA_30100_2RN_BC and set up in mask aligner.
    b. Edit parameters to change exposure time to 8 s and mode to hard contact.

    c. Set out and label clean crystallization dishes with H_2O and developer MF319.

37. Place pillar samples in barrel etcher to clean and promote adhesion.
    a. Use oxygen etch.
    b. Pump down to 40mTorr.
    c. Change power setpoint to 550W
    d. Change oxygen MFC flow setpoint to 100sccm.
    e. Open MFC flow oxygen valve and let pressure stabilize, approx. 175mTorr.
    f. Press *Power* to start and stop power. Run for 1min.
    g. Turn off oxygen, return setpoints to zero, turnoff vacuum, vent slow then fast.
    h. Remove sample, pump down chamber and shut off barrel etcher.
38. Turn on Laurell spinner and set to program with the following parameters: 1) 500RPM for 5 s with Acl=4, 2) 1000RPM for 30 s with Acl=11.
39. Center substrate then press vacuum. Ensure vacuum level approx. 20.
40. Apply LOR3B liftoff resist to cover entire sample surface. Avoid air bubbles in LOR.
41. Once resist covers entire surface, close the spinner lid and run spin cycle.
42. When the spinning comes to a stop, carefully remove the sample from the spinner, and soft bake sample for 5 min at on a hotplate at 150°C.
43. Let sample cool for 1 min.
44. Set Laurell spinner to program with the following parameters: 500RPM for 8 s with Acl=4, 2000s for 45s with Acl=11, 3000RPM for 5s with Acl=16, 500RPM for 5s with Acl=5.
45. Center substrate then press vacuum. Ensure vacuum level approx. 20.
46. Apply S1813 photoresist to cover entire sample surface.

47. Once resist covers entire surface, close the spinner lid and run spin cycle.
48. Remove sample from spinner and softbake at 110°C for 2 min.
49. Align sample by eye with macro pads in photomasks and then with microscope.
    a. Press F1, then enter, then left
    b. Use dials to move sample forward, backward, left right, and adjust angle.
50. Expose sample for 8 s in hard contact mode.
51. Develop in MF319 for ~60 s followed immediately by rinsing in DI water.
52. Air dry with N_2 gun.
53. Observe sample in microscope to ensure appropriate amount of development.
54. Repeat step 37 to oxygen etch in barrel etcher.
55. Deposit 10nm of Ti followed by 100 nm of Au in AJA.
    a. Determine deposition rates of Ti and Au from recent measured depositions. From the deposition rates and desired thickness calculate a deposition time for each material and record in logbook. Approx. times are Ti:1 min and Au: 4 min
    b. Fix samples to AJA platen and include a witness sample with Kapton tape.
    c. Add platen to AJA insert arm, cover lid, **connect N_2 gas line**, and switch pump.
    d. After 15min open door to main chamber and slowly insert magnetic coupled arm.
    e. Use flashlight to observe the insertion and locking of the rotating axes key into the platen back.
    f. Lift the platen and remove the insertion arm.
    g. Lower platen and sample to appropriate height.
    h. Close main chamber gate to exchange chamber.
    i. Turn on rotation, then Ar flow at 18 sccm, then PRESSURE set to 20 mTorr.

j. Set Ti and Au voltage values to voltage values of predetermined rate for those guns, approx. 200 W for Ti and 250 W for Au, and the ramp times to 1min each. *If the Ti target is on an RF source then it will be necessary to turn the main chamber power to 10 W for the first 10 s of the Ti gun powering up, then to open and immediately close the Ti target so the chamber plasma to light the Ti target.*
k. Have both target reach their set power and then set the pressure to 3 mTorr.
l. Open the Ti target and after the predetermined amount of time (~1 min) open the Au target and immediately close the Ti target. Close the Au target after the predetermined amount of time (~4 min).
m. Set the ramp times of the Ti and Au to 1min and powers to 50s. After the ramp down turn off the targets.
n. Set pressure to 10 mTorr, 20 mTorr and then to OPEN. Turn off Ar and rotation.
o. Remove the platen in the opposite order of steps *e.-j.* and then shut off pump once the platen is in the exchange chamber and the main chamber door is closed.

56. Remove samples for platen and measure the thickness of witness on profilometer.
57. Set samples in the solution 1165 at 60°C to liftoff overnight (<24 h). Cover with watch glass to prevent complete evaporation of volatile 1165.
58. Rinse samples in new 1165, then H_2O, then acetone, then IPA, then H_2O, then N_2 dry.
59. Inspect deposited films by optical microscope.
60. Place the sample into an appropriate storage holder. Dispose of chemicals in the proper waste containers and ensuring that all electronic equipment is powered down.

Annulus by Atomic Layer Deposition

61. Vent the Cambridge ALD system and open the trimethalaluminum precursor valve.

62. Set samples and a Si witness sample into the ALD chamber on top of 4” Si wafer.
63. Close chamber lid and evacuate the chamber.
64. Select recipe of *0.1nm of* Al_2O_3 *with temperature* and chose number of loops to results in desired thickness, typically 100-150 nm, or 1000-1500 loops.
65. Start the program and monitor the pressure (after ~30 min heat-up time) to ensure that pulses of the precursor and water vapor are registering.
66. After the program is complete (~5 h), vent the chamber, remove the samples, evacuate the chamber and close the precursor valve.

Remove Al_2O_3 from Contact Pads by Wet Etch

67. Perform photolithography according to steps 46-53 to uncover the applied resist from on top of the macro contact pads.
68. Pour Transetch-N into a crystallization dish.
69. Set photolithographically patterned samples into the Transetch-N. Etch rate 20 nm/h
70. After the calculated amount of time (5-8 h) remove the samples and thoroughly rinse with DI-H_2O and dry with N_2 gas. *Save Transetch-N for* ***Pillar Decapitaion***.
71. Inspect by microscope to ensure complete removal of Al_2O_2 from contact pads.
72. Remove resist from samples with acetone, then IPA, then H_2O, then N_2 dry.

Outer Electrode Photolithography and Deposition

73. Perform photolithography according to steps 37-53 to define Cr metal electrodes. Make sure to align all 7 sensing regions using the microscope before exposing.
74. Repeat step 37 to oxygen etch in barrel etcher.
75. Sputter deposit 110 nm of Cr using the AJA using step 55 with the following changes:

   a. Use Cr target. *If on RF source then you will again light the main chamber first.*
   b. Approx. rates for 110 nm of Cr deposition are 225 W for 16 min. DC or RF target will affect the rate substantially. Use recently measured value to determine rate.
   c. Lift-off in 60°C 1165 should only take 15min. Rinse and clean with step 58.

Uncover Pillar Tops by Photolithography

76. Set Laurell spinner to program with the following parameters: 500 RPM for 8 s with Acl=1, 2000 RPM for 45 s with Acl=1, 500 RPM for 5 s with Acl=3.
77. Set up SUSS MA6 mask aligner according to step 2. Set to 'Flood' and '1.3s'.
78. Center substrate then press vacuum. Ensure vacuum level approximately 20.
79. Apply photoresist S1805 to entire sample surface, close lid, and then start the spin.
80. Remove the sample and softbake at 110°C for 3 min. Let cool for 1 min.
81. Expose sample in *Flood Exposure* mode for 1.3 s.
82. Post-exposure bake the sample at 120°C for 1min. Let cool for 1 min.
83. Develop in MF319 for 25 s.
84. Immediately rinse in DI-H_2O and then dry with N_2.
85. Use JOEL JSM-7001F SEM with 15 kV and probe current 2 to image pillar tops to ensure appropriate uncovering. Resist will remain permanently in regions imaged.

Pillar Decapitation

86. Label and pour glass containers of Chromium Etchant 1020, H_2O and Transetch-N.
87. Submerge and swish sample in Chromium Etchant 1020 for 105 s.
88. Rinse immediately in H_2O and dry with N_2 gas.
89. Use SEM to image one sample after each etch step to ensure removal from pillar tops.
90. Insert samples into Transetch-N for predetermine amount of time used in step 70.

91. Rinse samples in H_2O and dry with N_2 gas. Image with SEM.

92. Repeat step 87-91 to lower the outer Cr and Al_2O_3 further, creating the extended core.

93. Thoroughly rinse and clean the resist from each sample with acetone, then IPA, then H_2O, then by drying with N_2 gas.

94. Securely store the samples in carrying cases for transportation and testing.

The final chip with 7 separate sensing regions is shown in Figure 22 below.

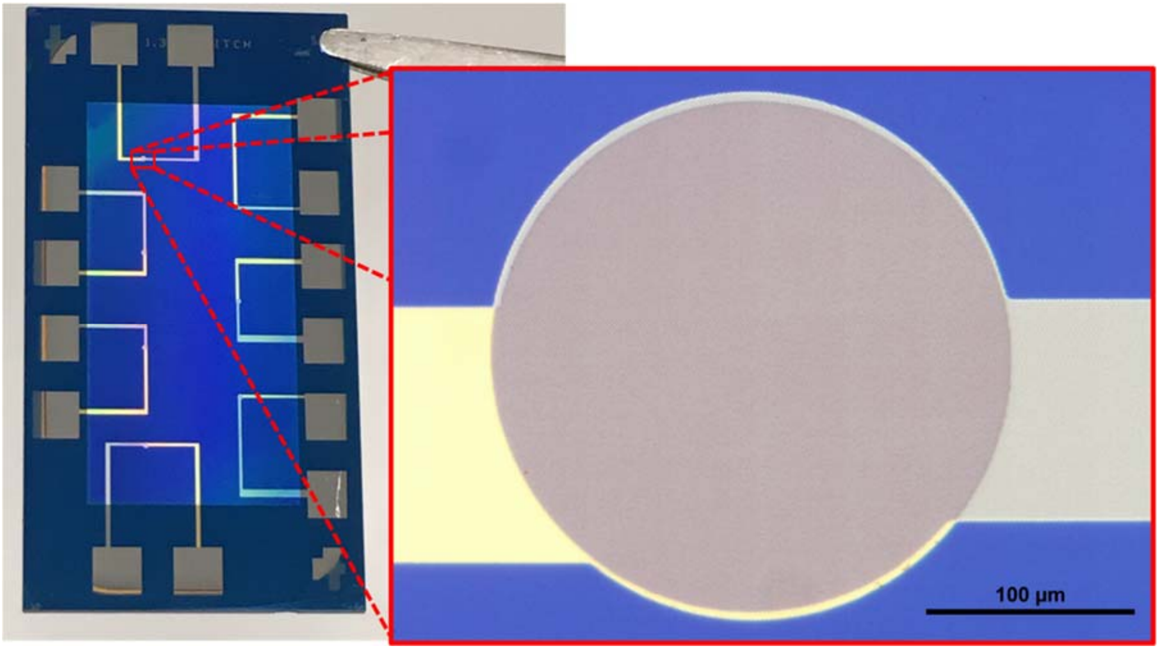

Figure 22. Picture of a 16 mm x 30 mm final sample with 7 sensing regions. Inset image is a x100 magnification of an individual sensing region, showing the leads for the inner (Au) and outer (Cr) electrodes converging to the circular nanocoax array.

2.2.2 Characterization.

ECC arrays were first tested for electrical integrity using a 6512 Electrometer (Keithley Instruments, Cleveland, OH). Resistance between the working and counter electrodes was measured, and any array with a resistance less than 10^6 Ω was considered electrically shorted and not used for further characterization. A scanning electron microscope (SEM, JOEL 7001F, Peabody, MA) was used to collect structure images, while another SEM (JEOL JCM 6000, Peabody, MA) was used for energy-dispersive x-ray (EDX) analysis to confirm that the nanostructure was composed of Si, Au, Al_2O_3 and Cr. Initial sensing capabilities of ECCs were assessed by differential pulse voltammetry (DPV) using a potentiostat (Gamry Instruments Interface 1000, Warminster, PA). The gold core functioned as the working electrode (WE), while the chrome shield was the counter electrode (CE). An external Pt wire served as the reference electrode (RE). The current vs. applied potential of the redox species FCA was measured, where the oxidation of 1 mM FCA in PBS (pH 7.4) is used as a benchmark assay for electrochemical performance. FCA is a commonly-used redox species in electrochemical sensing, which has been highly characterized (Stepnika, 2008). A potential range from 0 mV to 500 mV was used in order to encompass the FCA redox potential at 300 mV. The potential step was 2 mV, the pulse amplitude was 50 mV, the pulse width was 50 ms, the pulse period was 100 ms, and the equilibrium time was 10 s.

2.2.3 Fabrication

Since fabrication requires multiple steps of photolithography it was necessary to first produce Cr photomasks. Former iterations of photomasks were purchased through outside companies, most commonly Advance Reproductions Corporation. I designed the needed photomasks using the software L-Edit, as shown in the overlay images of the 2 metallic layers in Figure 23 below.

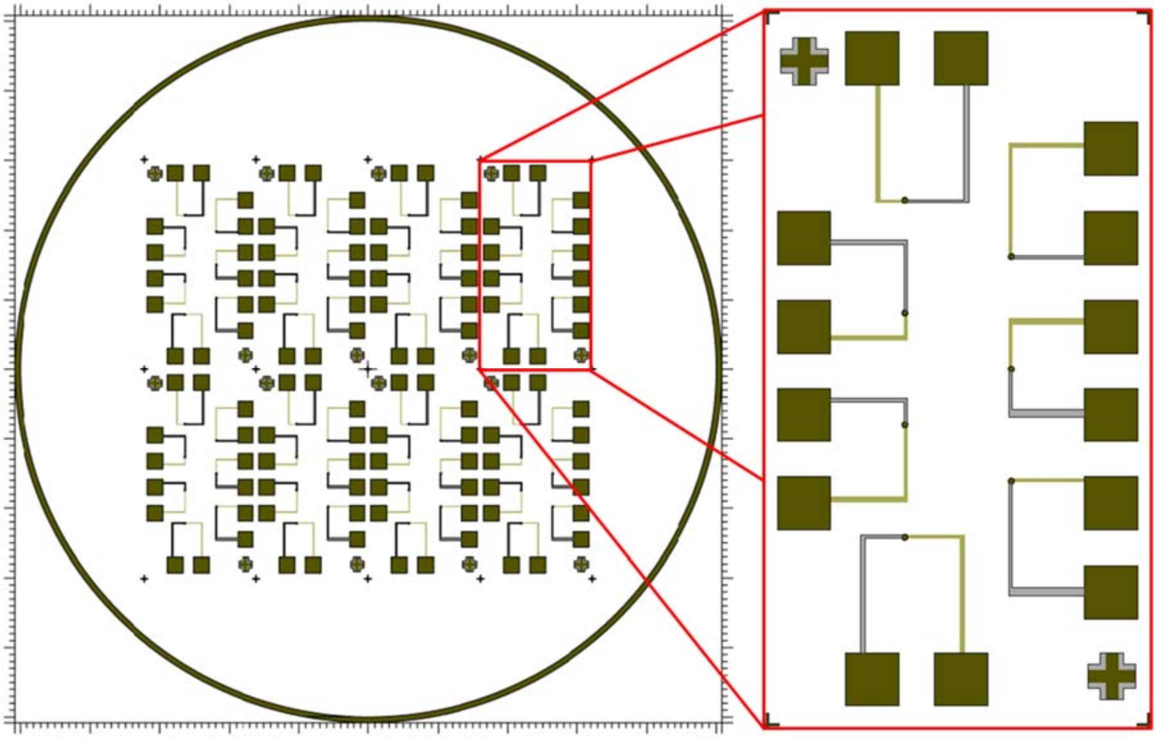

Figure 23. Print out of L-Edit layout file. Shown is a 2×4 array of chips designed for a 5” photomask, to be used in photolithography on a 4” wafer. Zoomed image is of a 16 mm x 30 mm chip with 7 separate sensing regions with both inner and outer metal layers and alignment fiducials at opposing corners.

A schematic of the fabrication process is shown in Figure 24. The nanostructures were fabricated on a hexagonal array of conical Si pillars with base diameter 400 nm, top diameter 200 nm, and pitch 1.3 µm (Figure 24a).

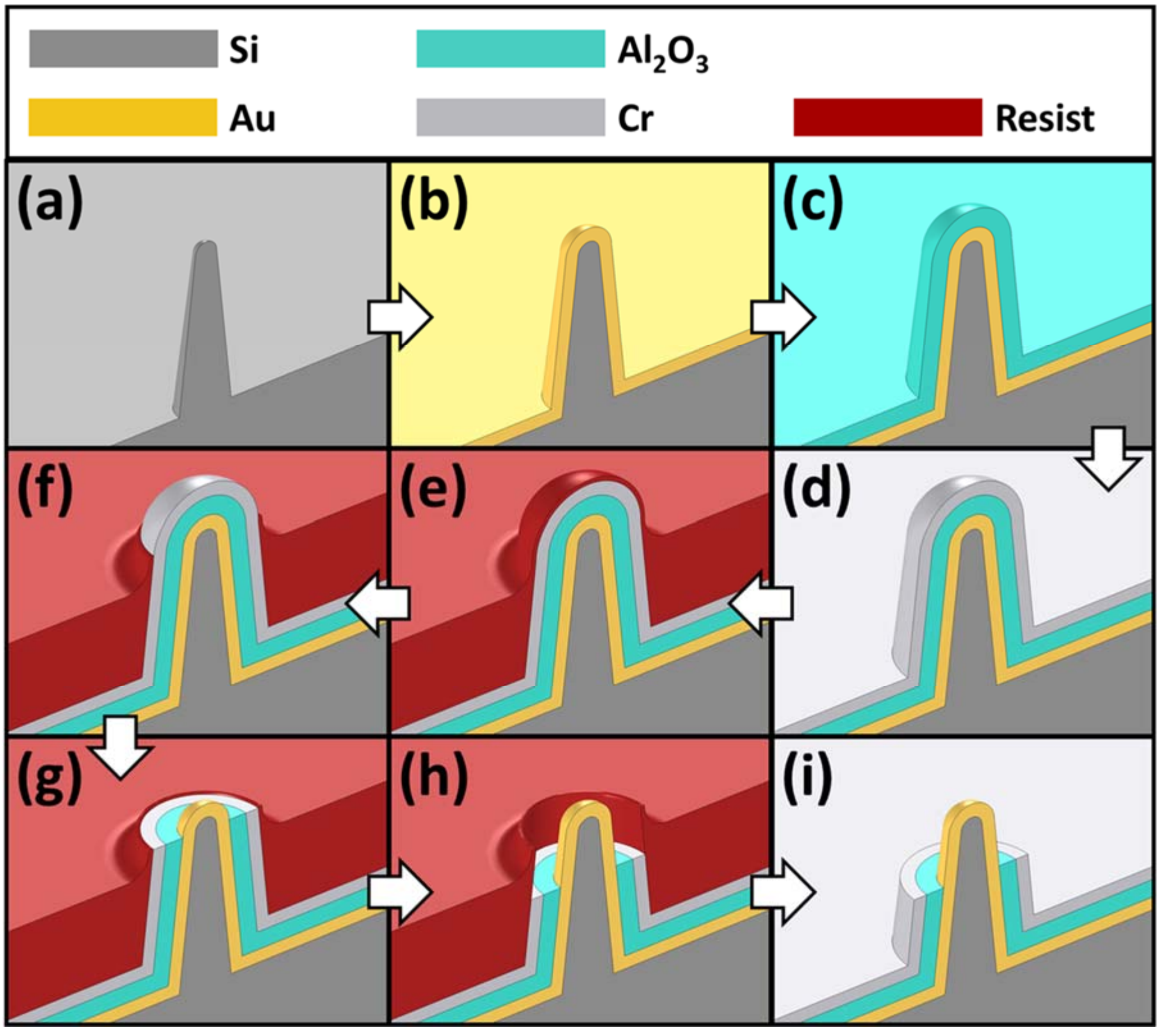

Figure 24. Cross-sectional tilted schematic of ECC process steps. This yields coaxial nanopillar arrays with extended inner cores. (a) Si pillar array. (b) Sputtered Au preceded by 10 nm Ti adhesion layer. (c) ALD-deposited Al_2O_3. (d) Sputtered Cr. (e) Spin coated photoresist. (f) Developed resist after a short UV exposure uncovering topmost region of pillars. (g) Wet chemical etched Cr and Al_2O_3. (h) Further wet etched Cr and Al_2O_3. (i) Resist dissolved and rinsed away.

Onto these pillars was sputter-deposited a photolithographically-patterned, 10 nm-thick Ti adhesion layer followed by a 100 nm-thick Au layer. This TiAu layer forms macroscopic contact pads (not shown) and what will become the cores of the coaxes, the latter also functioning as electrochemical working electrodes (Figure 24b). Next, annuli of the coaxial structures were formed by depositing a 150 nm thick insulating layer of Al_2O_3 by atomic layer deposition (ALD) (Figure 24c). The Al_2O_3 was removed by wet etching with phosphoric acid (Transetch-N) from the regions above the macroscopic gold contacts in order to enable electrical contact, though the Al_2O_3 is unchanged in the pillar regions. Next, a photolithographically-patterned 110 nm-thick Cr layer was deposited by sputtering in order to form additional macroscopic contacts (not shown) and what will become the coax shields that will function as the electrochemical counter electrodes (Figure 24d). Positive tone photoresist S1805 was then applied by spin coating at 2,000 rpm for 45 s and soft-baked for 3 min at 110°C on a hotplate (Figure 24e). The thickness of the resist in the planar regions was approximately 150 nm less than the pillar heights, and the resist formed a very thin layer on top of the pillar tops. A short 1.3 s UV flood exposure of the resist provided a dose sufficient to expose only the region at the pillar tops. Upon development in MF-319, the pillar tops became uncovered (Figure 24f). Etching in nitric acid / ceric ammonium nitrate (chromium etchant 1020) removed the topmost Cr region. Subsequent etching in phosphoric acid (Transetch-N) removed the topmost Al_2O_3 region (Figure 24g). The Cr and Al_2O_3 etch processes were repeated to further expose the inner Au electrode (Figure 24h). This 2nd etch step results in the inner Au extending above the concentric Cr and Al_2O_3 layers, and the structure is thusly named the extended core coax (ECC). The samples were rinsed with acetone, isopropanol, and deionized H_2O before drying with N_2 gas after each photolithographic step, including producing the final structure (Figure 24i). In order to promote adhesion, each of the Au, Cr, and Al_2O_3 deposition steps was preceded by treatment in an O_2 plasma at 400 W, 270 mTorr, and 50 SCCM O_2 flowrate for 1 min (PVA Tepla PS-210). Each sample is fabricated on a 16 mm x 30 mm Si substrate with 7 spatially and electrically separate regions comprised of arrays of ECCs.

SEM images of the structure at different steps of the fabrication process are shown in Figure 25a-f. Figure 25g shows the final ECC structure at x5 lower magnification than in Figure 25f, while Figure 25h shows a x150 lower magnification view of the final structure, with a wide enough field of view to show the leads to the 250 μm-diameter sensing region.

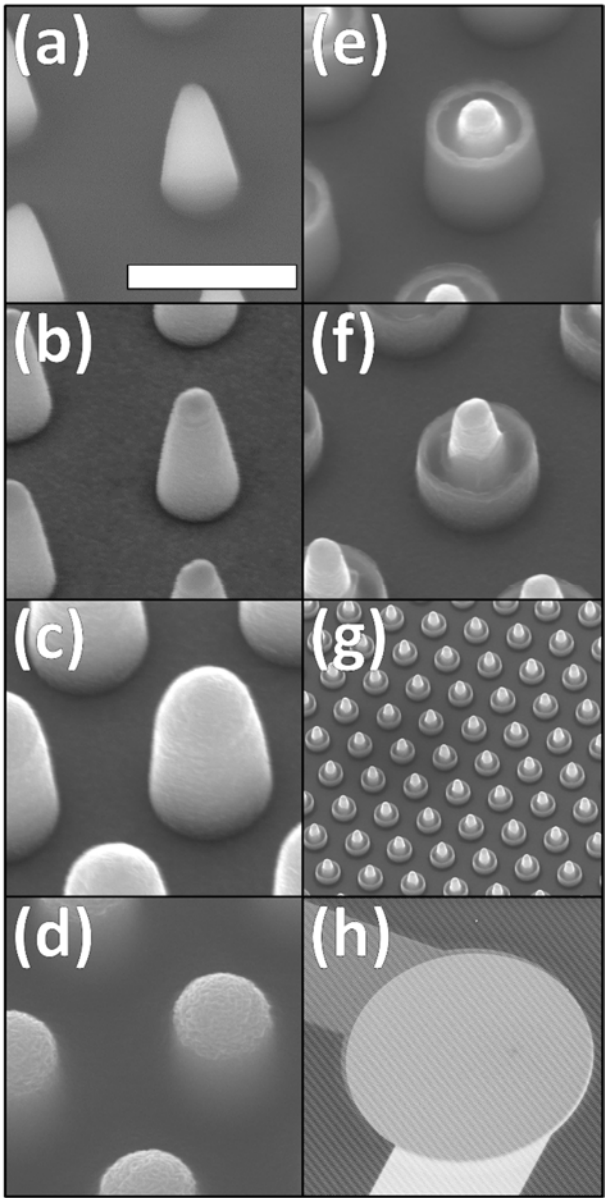

Figure 25. Tilted SEMs of ECC at different stages and magnifications. (a) Si pillar array. (b) Sputtered Au preceded by 10 nm Ti adhesion layer. (c) After ALD Al_2O_3 and sputtered Cr. (d) Spin coated, exposed and developed photoresist uncovering topmost region of pillars. (e) After wet chemical etched Cr and Al_2O_3 with resist removed. (f-h) After 2nd wet etched Cr and Al_2O_3 with resist removed at different magnifications. Scale bar in (a) is 1 µm for images (a-f), 5 µm for (g), and 150 µm (h). Tilt is 30°

Our work was motivated by an earlier generation nanocoax device that was capable of CTX detection *via* electrochemical ELISA using an off-chip strategy (Archibald et al., 2015). In that work, all steps of the ELISA were performed in a standard 96-well microtiter plate, with only the electrochemical detection carried out on the nanocoax array. The arrangement of the nanoscale gap between the working and counter electrodes precluded liquid exchange, preventing fully on-chip detection (*i.e.* the tethering of all sensing components to a chip surface).

To overcome this limitation, the gold core of the nanocoax reported herein is extended above the chrome shield, resulting in the ECC as described above. This retains the benefits of the coaxial architecture, with its nanoscale proximity of the WE and CE and also allows for facile reagent exchange. It also creates an unobstructed WE gold surface, which introduces the possibility for biofunctionalization.

In developing the ECC architecture, a set of fabrication parameters was identified to provide superior performance in response to FCA oxidation relative to that in a previously reported nanocoaxial sensor (Rizal et al., 2013). One focus was the size of the annulus gap, which is the dielectric layer between the WE and CE. In order to function as a nanogap electrode and allow for high sensitivity, as gauged by the current response during electrochemical oxidation, the WE and CE must be in nanoscale proximity. Previous non-ECC iterations fabricated with sub-100 nm annulus gaps experienced inconsistent liquid exchange in washing steps, and also experienced relatively lower manufacturing yield, possibly associated with electrical shorting caused by the size of the gap. Because of a necessity to be able to wash the chips between reagent incubation steps, as well as a desire for higher manufacturing yield, an annulus gap of 150 nm was used for all ECC chips. Al_2O_3 thicknesses above 150 nm were not used in order to maintain the nanogap electrode proximity. The 100 nm thickness of the Au and Cr layers was chosen to be thick enough for sufficient conductivity for these electrodes, while thin enough to maintain the aspect ratio in the pillar geometry.

We further explored a number of modifications at several steps in fabrication parameters in order to develop the final protocol shown in Figure 24 and Figure 25. For example, we explored fabricating devices on several different-shaped silicon arrays (Figure 26), and identified a core electrode shape that provided both a high level of reproducibility and a high manufacturing yield.

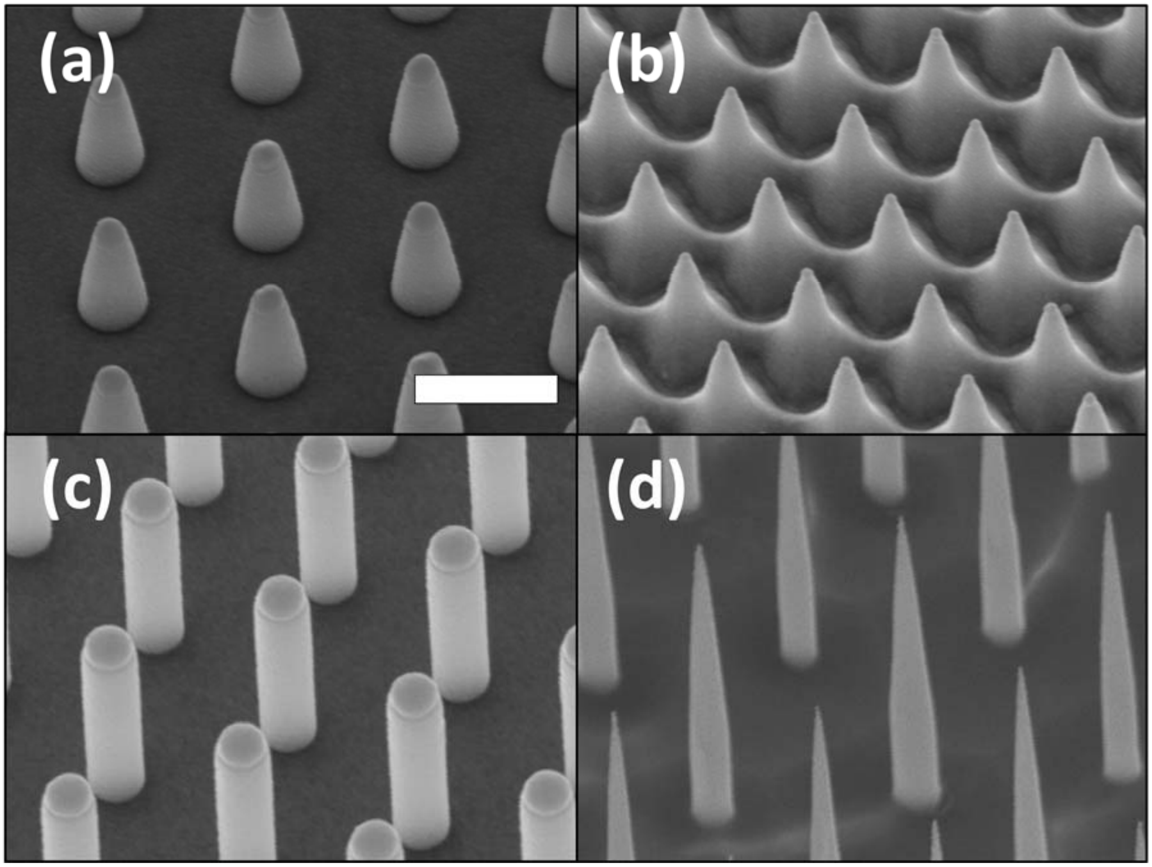

Figure 26. Different types of Si pillar arrays evaluated. FCA electrochemical results, in addition to the availability of chips, dictated the shape used for final testing. Slightly conical-shaped Si pillars (a) were chosen for further work. Sharp (b), cylindrical (c), and high-aspect ratio (d) pillars did not provide sufficient electrical and electrochemical consistency for further use. Scale bar inset is 1 µm for (a-c) and 2 µm for (d). SEM images taken at 30º tilt. Si substrates were imaged with a layer of Au deposited in order to reduce image distortion due to charge accumulation.

We next focused on modifications to the etching steps involved in forming the extended core (Figure 25e and f). The etch rates and selectivity of common materials, including those incorporated into these structures, are reported by the etchant's producing company and are well studied (Williams et al., 2003). The effects of all changes were gauged by

FCA redox performance and compared against the non-ECC devices and planar Au electrodes, in order to maximize sensitivity. Computer simulations performed in COMSOL Multiphysics were used to inform design changes. As an example, Figure 27a and 20b show the normalized electric field distribution corresponding to different shield heights for the nanocoax. The greater penetration of the Au WE into the high electric field region suggested that extended core configurations would facilitate higher current response and device sensitivity, which was corroborated by FCA (1 mM) redox data (Figure 27c). Based on these findings, we finalized our ECC architecture as a chip containing 7 individually addressed sensing arrays, each array comprised of ~30,000 nanocoaxes connected in parallel.

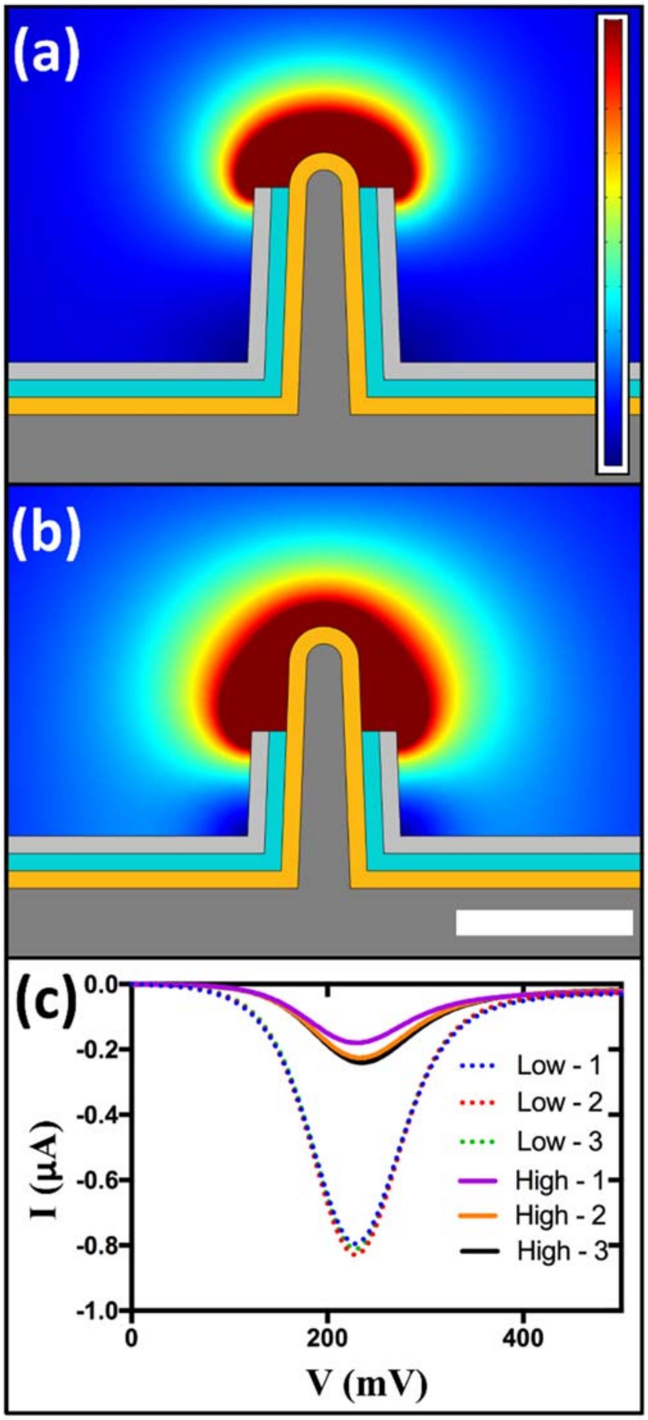

Figure 27. High shield and low shield comparison. Cross-sectional view of geometry with overlaid simulated electric field norm for 1 V applied to coaxial terminals for the (a) high shield configuration and (b) the low shield configuration (simulated in COMSOL). Inset linear color scale ranges from 0 V/m (blue) to 2×10^5 V/m (red) and inset white scale bar is 1 µm. (c) DPV current response of oxidizing 1 mM FCA comparing the two shield configurations (3 runs each) shows that the electric field distribution of the low shield results in a 4x relative increase in the current response, a metric of sensitivity.

2.2.4 FCA Testing.

As described above in the section Characterization 2.2.2, we used the current density of oxidizing FCA in differential pulse voltammetry as a metric for testing device performance and viability. Test and individual chip took about an hour and one was able to obtain multiple runs on one of all of the 7 separate sensing regions. In order to add the 1mM FCA above the sensing region desired to be tested a liquid well has to be made for regions that would be tested. At the onset of the project, these well were made by using an adhesion to bind a hand-positioned well to the region above the well desired to be tested. This was a tedious, serial and messy process that often lead to loss of throughput due to damaging devices and concerns over testing consistency due to non-uniformity of well positioning. To solve this problem, I created a re-useable well system and sample holder than facilitate quick, consistent and safe sample testing and was also used in later procedures, Figure 28.

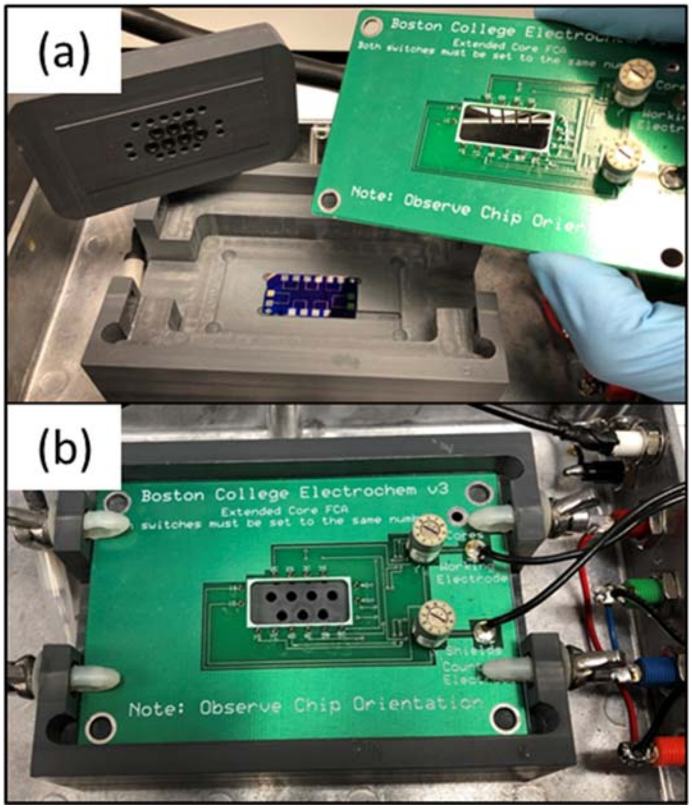

Figure 28. ECC sample in base of reusable well apparatus. (a) The electronics interface and bottom of reusable well inset with o-rings and (b) assembled well and electronics apparatus setup.

This well allows one to place the 16 mm x 30 mm sample into a precise recess that then allows the reusable 7 well inset to position in the same way when inserted into another corresponding recess. This inset also has holes for the electronics border to pass through and make contact with the sample contact pads. This all locks together with 4 flexible fasteners that apply a uniform pressure on the 7 o-rings that form the well seals. The electronics board, previously designed by Dr. Michael Burns, allows easy switching between the 7 separate sensing regions on a given chip.

The measured electrochemical current in response to 1 mM FCA oxidation of these arrays demonstrated a high level of experimental reproducibility *i.e.,* ~9% variation in peak current over 9 consecutive measurements (Figure 29b). This consistency was not achievable on previous nanocoaxes, which exhibited a drop in peak FCA oxidation current in each subsequent run until finally stabilizing at a significantly lower current (likely because of liquid exchange issues) (Figure 29a). Variation in peak current between independently fabricated ECCs is larger than that in repeated measurements on an individual sensing region (Figure 29c).

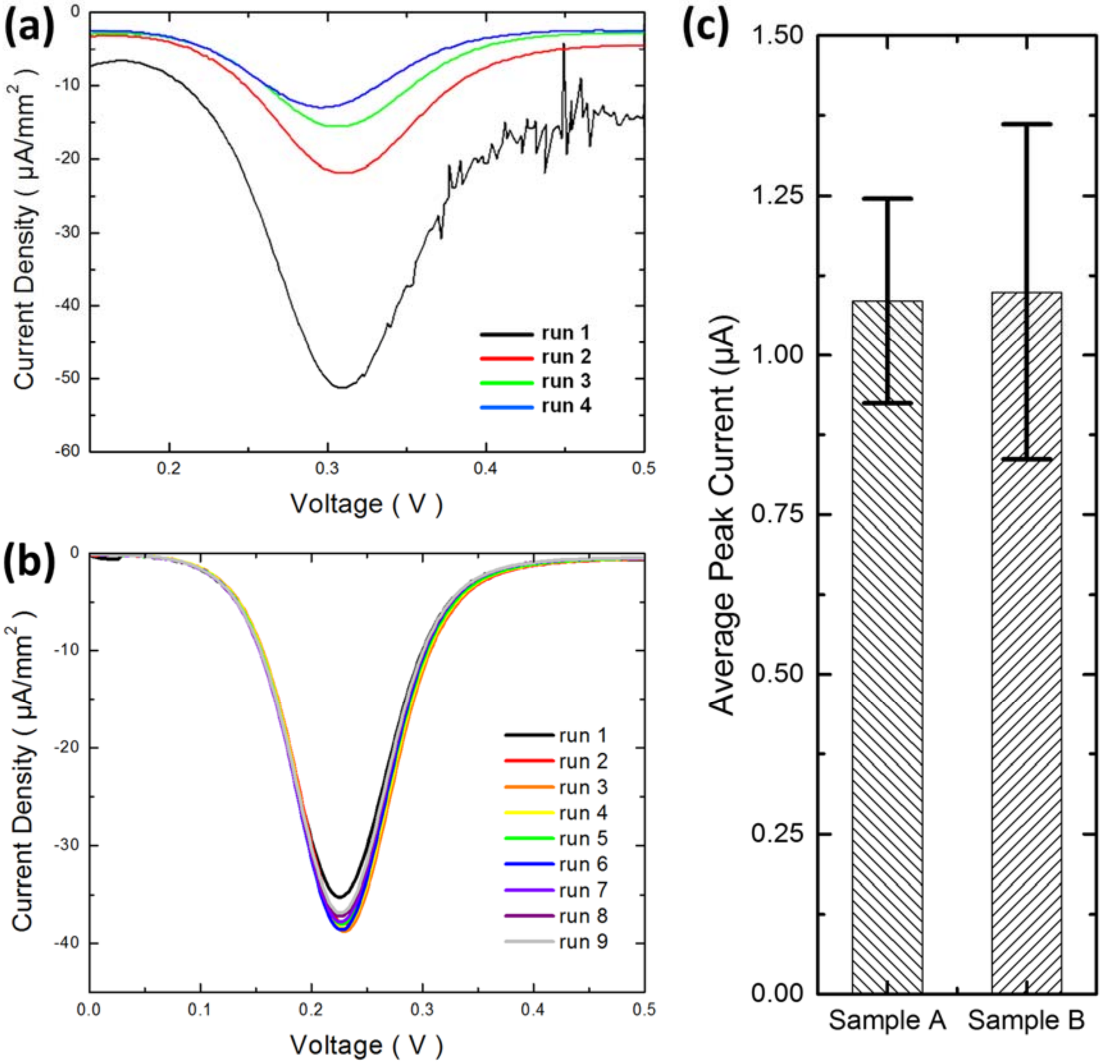

Figure 29. ECC current density comparison. Measured current density of (a) non-ECC and (b) ECC arrays for multiple repeated runs on the same region. The peak current density for non-ECC drops off quickly for subsequent runs, whereas for ECC, it shows high repeatability over 9 runs. Note the different axis ranges used. (c) Peak current and standard deviation from 6 separate sensing regions, each from independently fabricated ECC samples.

It should be noted that this variation does not affect an individual region's viability and that the important metric for detection is a region's response to 4-AP redox, which falls in the nA range. Thus, to overcome any potential issues resulting from the variability of individually fabricated chips, a baseline of 1 μA current in response to FCA oxidation was established to be the minimum acceptable performance. This corresponds to ~20 μA/mm^2 current density, which is also comparable to that used for the non-ECC (Archibald et al., 2015).

Figure 30a shows a comparison of the peak current density achieved on 3 sensing platforms: a simple planar electrode, the non-ECC, and the ECC nanocoax. It is apparent from the results that the ECC represents a significant improvement over its predecessor, as well as over simpler to fabricate architectures lacking a nanogap.

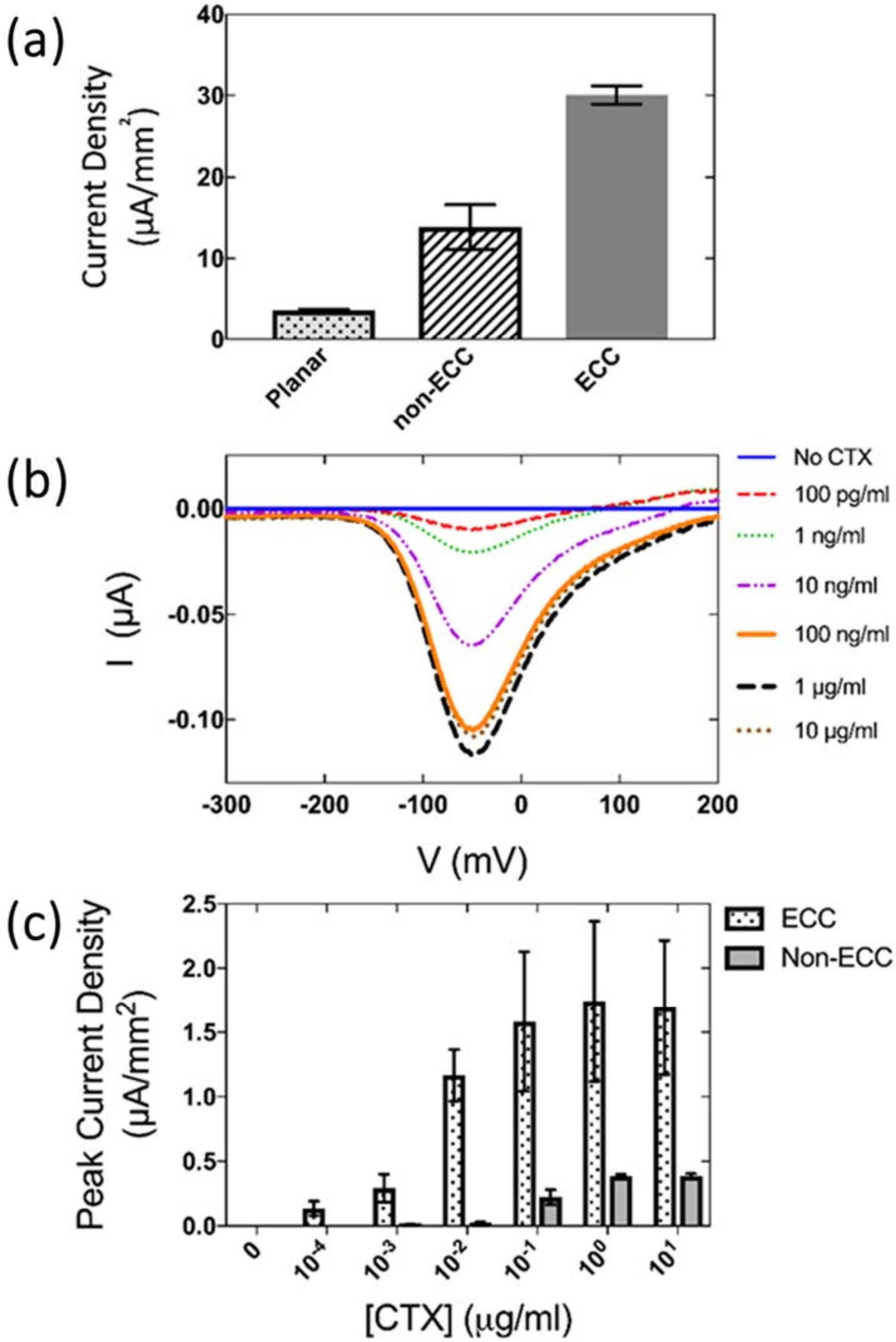

Figure 30. Electrochemical comparisons of the ECC vs. planar and non-ECC. (a) The average detected current density of the oxidation of 1 mM FCA for a representative ECC array, a non-ECC array and a planar gold electrode. (b) Current as a function of applied potential for electrochemical ELISAs performed off-chip for CTX concentrations ranging from 100 pg/ml to 10 μg/ml, analyzed on the ECC. All measurements were made on the same ECC array to minimize variability. (c) Peak ELISA current density as a function of CTX concentration, measured on an ECC chip and a non-ECC chip, showing both increased response and lower limit-of-detection for the ECC configuration. All error bars represent the standard deviation of 3 trials.

The increase in current density, which nanocoax architectures exhibit over planar electrodes, may be explained by the phenomenon of redox cycling. Redox cycling occurs between nanogap electrodes, where a species is oxidized at the WE, then reduced at the proximate CE, where it can then rapidly diffuse back to the proximate WE to be oxidized again (Wolfrum et al., 2016; White and McKelvey, 2018). Improvement in signal can be obtained by decreasing the size of the annulus gap that, in turn, may allow for faster redox cycling (Rizal et al., 2013), though eliminating electrical shorting for sub-100 nm annuli needs to be addressed. A simple planar gold electrode with millimeter-to-centimeter scale distances between electrodes cannot match the sensitivity because this cycling does not occur, and thus sensitivity is dominated by the rate of reagent diffusion to the electrode surface.

2.3 Electrochemical Sensing

2.3.2 Off-Chip ELISA Results.

After fabrication optimization and confirmation of electrochemical function, ECCs were evaluated for their biosensing capabilities and compared to the non-ECC version. Non-ECCs had previously been used to detect CTX in an off-chip setup; in other words, all ELISA steps were performed in a 96 well microtiter plate and only the final redox product was applied to the chip surface for detection. As a baseline for comparison of the non-ECC and the ECC as biosensors, an off-chip electrochemical ELISA was performed. CTX was chosen as the biomarker of interest due to its clinical relevance and overall stability. The off-chip ELISA was performed identically on the ECC and non-ECC, and in turn was identical to a standard optical ELISA, with the exception of the readout. For the electrochemical ELISA, pAPP was added as the enzymatic substrate as opposed to Bluephos for the optical readout. The current response of the ECC off-chip ELISA (Figure 30b) was superior to that of the non-ECC (100 pg/ml *vs.* 2 ng/ml). The ECC demonstrated a linear sensitivity range between 0.1-100 ng/ml. An optical ELISA utilizing the same antibodies was capable of detecting as low as 1 ng/ml of CTX, meaning the ECC outperformed this clinical standard. However, the ECC holds the potential to be functionalized (as will be discussed in section 2.4.1), allowing for all detection steps to be performed on a miniaturized platform, making it a more portable and lower-cost alternative to an optical ELISA. This is because the nanocoax device achieves its sensitivity while requiring significantly less analyte (as little as 10^{-5} as much) compared to macroscopic optical ELISAs, lowering the cost per assay. When current density was taken into account, the ECC vastly outperformed the non-ECC, as the ECC sensing area was significantly smaller than that of the non-ECC (0.049 mm^2 *vs.* 1.8 mm^2) (Figure 30c).

2.4 Biomolecular Sensing

2.4.1 Functionalization and blocking

The final details of the functionalization protocol are described above in section 2.1.5 under *On-chip ELISA*. A summary of the protocol steps is shown in Figure 31 below with a list of corresponding steps.

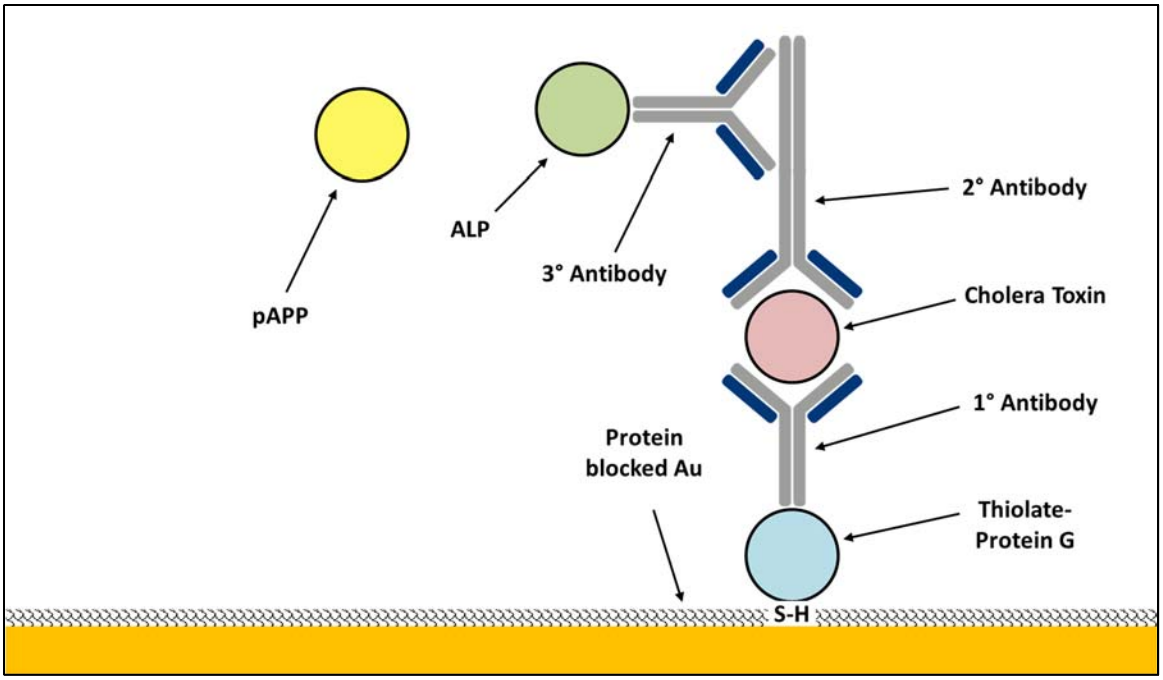

Figure 31. Schematic of on-chip functionalization and detection scheme.

Ideal process (wash between each step)

1. Bind thiolated Protein-G to Au
    - Thiol groups interact with gold to create a S-S bond, which is covalent and thus strong enough to withstand rigorous washing. Anything bound by a lesser strength interaction (like hydrogen boding or Van der Waals, will be washed away)
2. Bind constant region of the 1st antibody to Protein-G
    - Protein G is a protein found in bacteria, whose sole purpose in life is to bind to antibodies. Specifically, it will only bind to the constant region of Immunoglobulin type G antibodies.
3. Block remaining surfaces with protein to prevent non-specific binding.
    - For this, we use a random cocktail of protein that should not interact with our ELISA. This is done because Antibodies are notoriously “sticky”, and if they have

to opportunity to stick to the well, they will. The blocking agent we use is 5% Bovine Serum Albumin (BSA).

4. Bind CTX to variable region of 1st antibody
    - The first antibody has been raised to recognize CTX at its variable region. This will tether CTX at the gold surface. This step completes the "capture" part of the ELISA.
5. Bind variable region of 2nd antibody to CTX
    - The second antibody is also raised against CTX, but was produced in another animal (mouse, rather than rabbit). This is important for eliminating nonspecific antibody interactions. This is the first step of the "detection" part of the ELISA
6. Bind 3rd antibody variable region to 2nd antibody constant region. 3rd antibody is already conjugated to ALP enzyme
    - 3rd antibody has been raised against the 2nd antibody, and should only recognize it. There should be no nonspecific interactions with any other component.
7. Introduce 1mM solution of pAPP
    - pAPP stands for para-aminophenyl phosphate
8. ALP enzyme catalyzes the formation of 4AP from pAPP
    - ALP stands for alkaline phosphatase. In biology, if you see the ending "ase", that tells you you're dealing with an enzyme. In this case, the ALP is catalyzing a reaction with the phosphate from pAPP. To produce 4-aminophenol. Hence the name "phosphatASE". It has broken down the phosphate group
9. Apply voltage in electrochemical experiment to oxidize 4-AP thus release electrons at Au terminal.

2.4.2 On-Chip ELISA Results

Protein G was utilized to facilitate antibody tethering to the ECC surface. This is a bacterially-derived protein with a high affinity and specificity for the Fc region of IgGs (Björck and Kronvall, 1984; Sjöbring et al., 1991). For the purposes herein, it was modified with a thiol group, in order to also facilitate binding with a gold surface (Pensa et al., 2012). We first obtained visual (SEM) proof-of-concept of tethering by conjugating a 40 nm gold nanoparticle to our tertiary ELISA antibody (Figure 32). By comparing these images to control group without preceding antibodies in the assay, we can confirm the specific binding of the tertiary antibody and the specific location of binding, which is adjacent to the targeted Au inner electrode of the ECC.

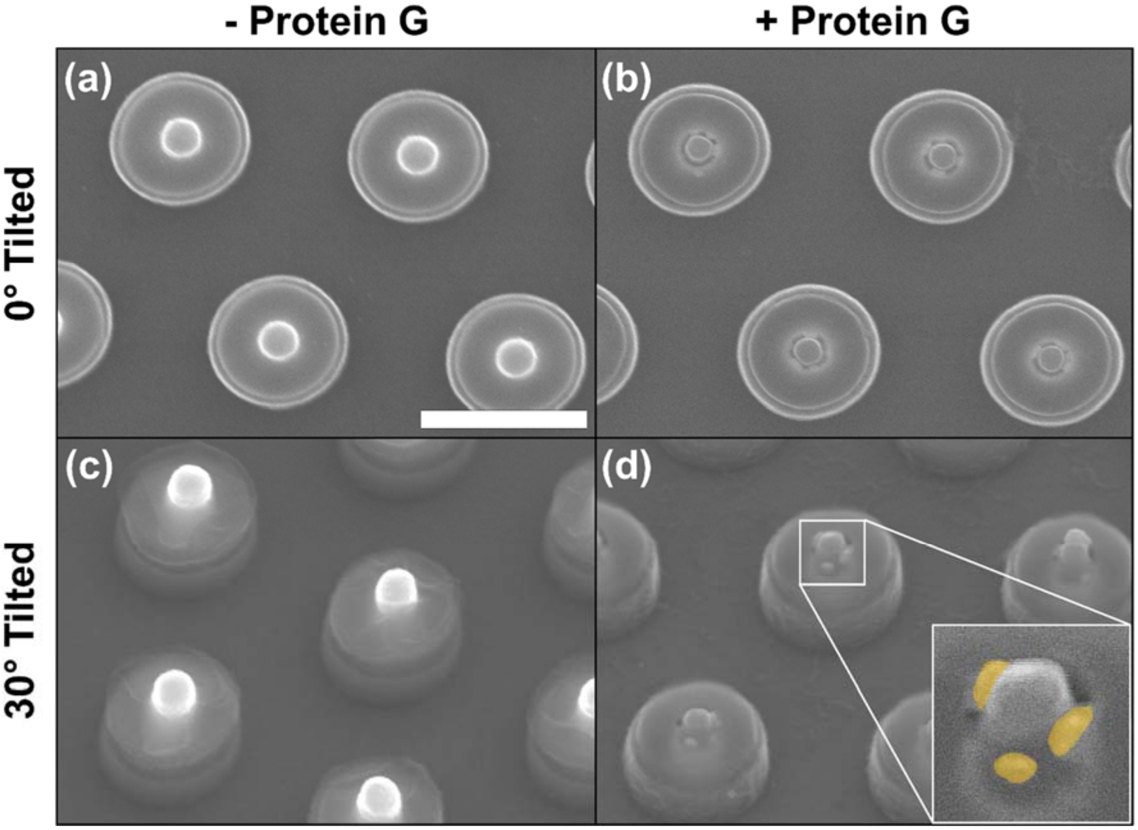

Figure 32. SEM images of the extended core nanocoax. SEMs of two separate arrays on the same ECC chip, (a) one incubated without protein G (- Protein G), and (b) one with protein G (+ Protein G), both prior to AuNP-conjugated antibody application. Corresponding 30° tilted views are shown in (c) and (d), respectively. AuNPs of ~40 nm diameter are visible around the extended cores of the test array (+ Protein G), but not the control array (-Protein G). Inset of (d) is 3x zoom with false color of AuNPs. Note that a particular iteration of ECC was utilized in this study, expected to be representative of the behavior of all ECC chips. Inset scale bar is 1µm in length.

This confirmation of biofunctionalization of the gold core of the ECC with an IgG is the key functional modification to previous generations of ECCs, necessary for meeting objects of POC applications. We next sought to complete a full on-chip ELISA on the ECC. Our results demonstrate on-chip detection of CTX by an ECC functionalized with protein G (Figure 33).

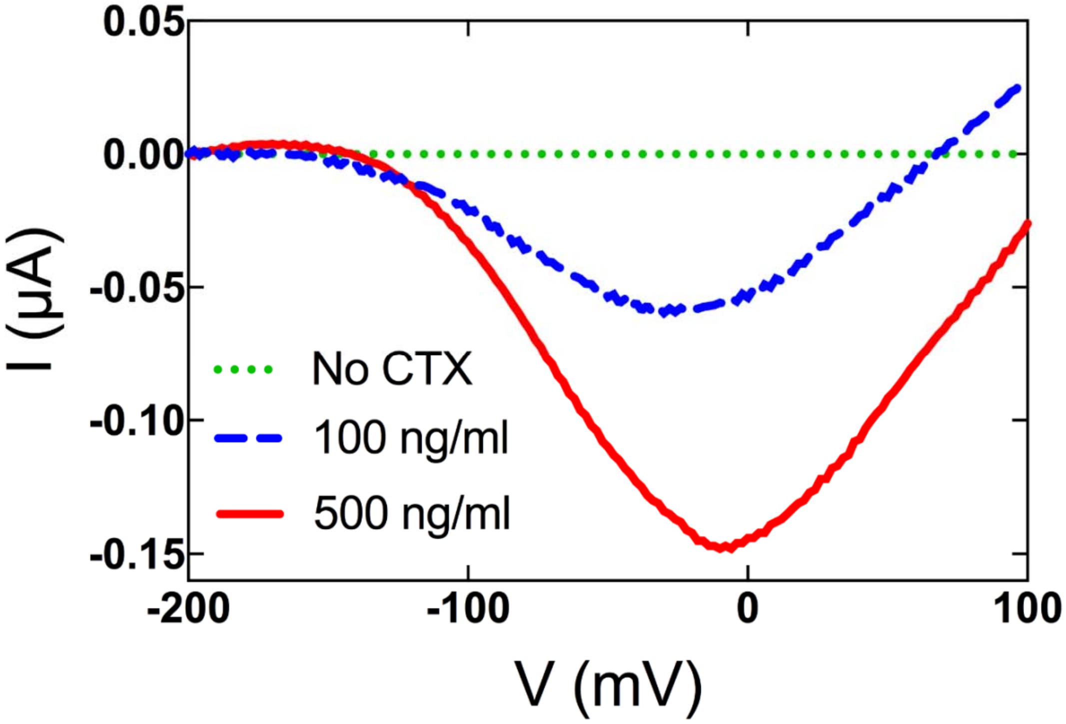

Figure 33. Current response as a function of applied voltage. Shown for ECCs in on-chip detection of CTX, using protein G to tether antibodies to the sensor surface. Shown are one trial for each condition of 500 ng/ml (red, solid) and 100 ng/ml (blue, dash) concentrations alongside a control sample with no CTX (green). Each trial was performed on a separate array on the same ECC chip. Data were subtracted to a baseline at -200 mV to better show peak current. Deviations from -100 mV for the 4-AP oxidation peak are likely due to the use of a pseudo-reference electrode.

2.5 Discussion and Future Works

2.5.1 Comparison to Previous Structures.

As both nanocoaxial architectures contain nanogap electrodes, the increase in current density that the ECC exhibits over the non-ECC may be explained by the ease of liquid exchange. In order to interact with the WE it will be necessary for liquid reagents to diffuse into the annulus gap of the non-extended core nanocoax. In actuality, high surface tension and morphology-induced hydrophobicity caused by the size of the gap hindered this, and additionally made it difficult to wash the chip surface for further reagent application. By contrast, the ECC WE extends into the solution and so it may be easier for FCA and 4-AP molecules to move from the bulk solution to the electrode surface to be oxidized.

As it stands, however, the current device is competitive with nanogap devices reported in literature (Figure 34). Once full on-chip capabilities are confirmed, the ECC will represent a promising alternative to simpler, planar nanogap-style electrodes because of the increase in functionalizable surface area resulting from the number of coaxes in each array, and their 3D architecture. We also believe that the protein G biofunctionalization assay represents a much simpler method of antibody tethering than those frequently used in the literature, such as silane or cystamine functionalization.

Citation	**Biomarker**	**Lowest concentration detected (ng/ml)**	**Recognition scheme**	**Transduction**
Our chip	*Cholera toxin subunit B*	*0.1 (off chip)* *100 (on chip)*	*Thiolated protein G antibody tethering*	*DPV*
(Singh et al., 2010)	C reactive protein	0.1	Cysteamine SAM	EIS
(Hsueh and Lin, 2016)	Cardiac-troponin T	0.1	Silane functionalization	CV
(Ilyas et al., 2012)	Epidermal growth factor receptor	50	Immobilized aptamer	Impedance
(Whited et al., 2012)	HE4 Biomarker	1.5 (standalone) 0.1 (mixed)	Cysteamine SAM	EIS
(Kim et al., 2009)	Prostate specific antigen	.0001	Protein G antibody tethering	Electrical
(Carlo et al., 2003)	Laminin	10	Silane functionalization	Capacitive

Figure 34. Comparison of nanogap-based literature. Shown are different protein detection platforms.

Another important feature of the ECC is its amenability to repeated use. The non-ECC chips exhibited signal degradation over the course of several uses. Conversely, ECC chips maintained signal integrity with less than 10% change in response over 9 runs, suggesting that the ECCs are relatively stable structures. Taken together, these data confirm that the ECC represents a significant improvement over the non-ECC architecture. However, while we have demonstrated the ECC's capability of consistent repeated use for measurements that are solely chemical detection, *e.g.*, in FCA and 4-AP tests, it is important to note that each ECC sensing region is currently used for a single on-chip detection assay. The regeneration of biosensing devices has shown promise for enabling repeated use, thereby potentially reducing diagnostic costs, although only a third of reported electrochemical biosensor studies meet previously-reported criteria (Goode et al., 2015). To forgo this problem, we made 7 separate submillimeter size sensing regions on an individual sample, thereby achieving the same end-of-line benefit as sample regeneration. Furthermore, the number of sensing regions could be increased beyond 7, as each region is less than 0.1% of the active sample area.

2.5.2 Future Works

In order for the benefits of such a biosensing device to be relevant to diagnostic applications, it must be affordable in order to meet the demands of the resource-limited areas where diseases like cholera are most prevalent. Several aspects of the ECC facilitate this criterion. The photolithographic processes involved in patterning each layer are amenable to large wafer-scale throughput. The chemical wet etching processes are high-throughput, while the chemicals are inexpensive and can be reused for extended periods, given the nanoscopic amount of material etched. Multiple sensing regions on a given chip, as previously discussed, can further reduce a sample's cost per test. Si pillar arrays used herein can be easily and inexpensively replicated in polymer (*e.g.* SU8) by nanoimprint lithography (NIL). As an electrochemical sensor, detection using an ECC is performed with equipment that is less expensive than that used in standard optical ELISA. As such, further reduction of electrochemical equipment cost is possible by incorporation of inexpensive microcontroller units such as Arduino.

We have demonstrated that an extended core nanocoax is capable of sensitive and repeatable detection of a target antigen in an off-chip setup with a detection limit of 100 pg/ml, with preliminary data suggesting it possesses utility as an on-chip electrochemical biosensor. We have demonstrated that the ECC architecture is a viable and promising alternative to the non-ECC nanocoax architecture. Future directions may include examining more coax core pillar shapes to further improve device sensitivity. We have demonstrated that the ECC fabrication is comprised of processes and chemicals that are suitable for high-throughput, and future works will target these advantages in order to further decrease the cost per sample. Future works will also include the fabrication of a more sophisticated chip housing that incorporates microfluidics and a portable analysis system in order to enable the ECC's use for POC detection of infectious disease biomarkers, offering the potential to meet the diagnostic needs of resource-limited areas.

3. Plasmonic Halo Sensor

3.1 Plasmonics

3.1.1 Introduction

In order to understand how plasmonic devices can be suitable for biosensing applications, it is important to first emphasize key attributes of surface plasmons. Derivations for the simplest case of a planar interface of a metal and dielectric can be found in many other texts and one such is succinctly given in Chapter 2 of the book *Plasmonics: Fundamentals and Applications* by Maier. Here I will list four main points:

i) The confined surface plasmon waves can exist only at interfaces between a conductor and an insulator.

ii) Surface plasmon polaritons only exist for TM polarization. That is, only TM polarized light (with E-field in the plane of incidence) can scatter energy in to surface plasmons.

iii) The dispersion relation is dependent on the materials that make up the interface.

iv) The solutions are propagating waves along the metal-dielectric interface that decay exponentially away from the surface, *i.e.* they are highest at the surface.

It is common to plot the plasmon dispersion relation listed in iii), highlighting the branches of the surface plasmon mode and bulk plasmon mode as shown in Figure 35.

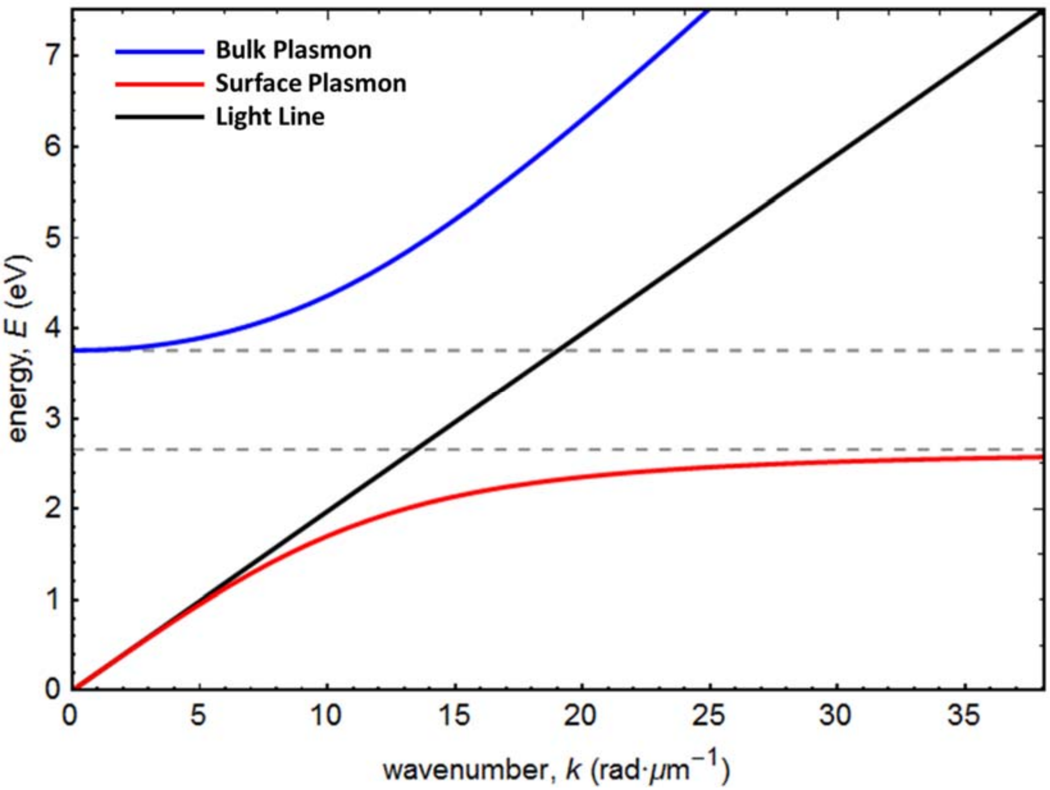

Figure 35. Plasmon dispersion relation for Ag. Shown for a lossless planar interface of Ag and air, showing the surface and bulk plasmon modes and the light line as a function of wavenumber.

What this dispersion relation means is that for a given energy, corresponding to a certain frequency of incident light, the surface plasmon will have a certain wavenumber. In order to couple the light into the plasmon, the **wavenumber needs to be matched** for that frequency. One way of doing this is discussed in section 3.2.1 where the angle of incident light is changed thereby changing the in-plane projected component of the wavenumber of the incident light. Since the dispersion relation is dependent on the materials, one can measure how the 'wavenumber needs to be matched' for the different materials and then use those differences to say something about the material properties, such as the permittivity of the dielectric material. Most related to biosensing detection mechanisms, the difference in wavenumbers is used as an indication of presence or amount of a targeted material. Regarding point iv), how much the matched wavenumber will change for different of materials will be most significantly influenced by material changes in the regions where electric fields are the highest, *i.e.* closest to the surface. This exponential field decay and distribution of field for a surface plasmon are shown in Figure 36.

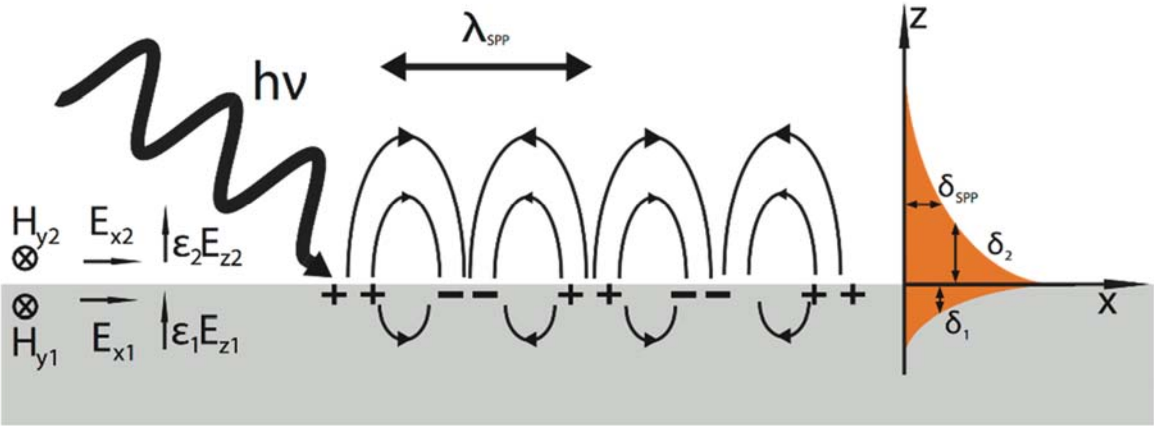

Figure 36. Schematic of SPP at interface. Incident light coupling to a surface plasmon at a metal-dielectric interface. Continuity conditions of magnetic field and electric field at the boundary from within each material are listed. Adapted from image by Anil Thilsted.

Commonly used biofunctionalization protocols are such that they capture targeted materials at those surfaces that most significantly influence the change in plasmon wavenumber. This efficiency in how a small amount of material can be localized to the region where it has the greatest impact on the detection mechanism is one of the main reasons plasmonic-based biosensing devices have demonstrated such promising use.

The field of research and development of plasmonic-based biosensing devices has received great attention and growth due in part to the promising inherent features discussed above (Mejía-Salazar et al., 2018; Hill et al., 2015; Chung et al., 2011; Anker et al., 2008). This recent growth is also largely due to the continued advancement and availability of the micro- and nanoscale tools, techniques and education that many devices incorporate. Figure 37 below shows this recent growing interest as an increasing number of publications under the search result 'Plasmonic Biosensor' as well as it's increasing fraction of all publications (Dimensions et al).

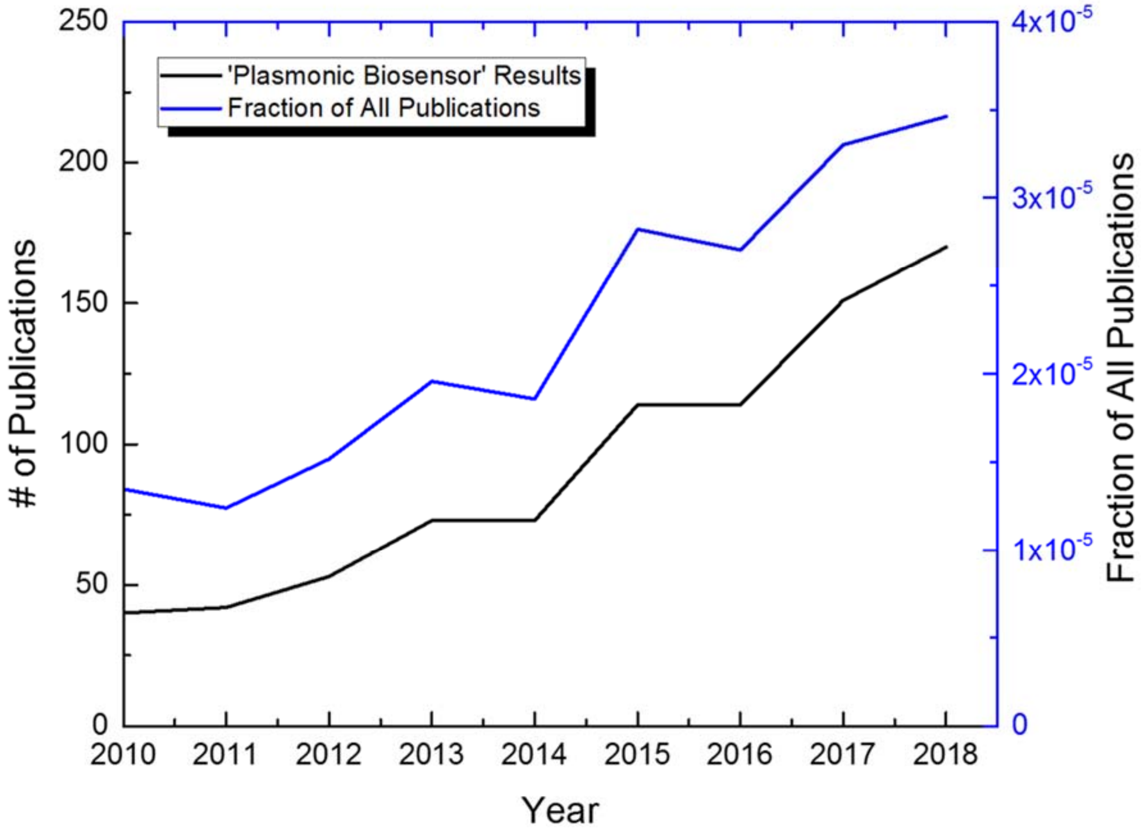

Figure 37. Plot of the number of publications vs. year. Results shown are for the query 'Plasmonic Biosensor'. The second y-axis shows the fraction of all indexed publications.

Despite the growing body of research, there remain unmet needs for sensitive detection of diseases and biomarkers suited to these devices. Eventually, design solutions need to address limitations of current devices and tools that extend beyond their technical capabilities, including their size, cost and ease of use. In this chapter I will describe our progress towards and challenges in the development of a biosensing device based on a plasmonic structure previously reported by our group.

3.1.2 Previous Works

In 2012, the plasmonic-halo was introduced (Ye et al., 2012). This work reported a resonant plasmonic structure that supported optical surface drumhead modes and demonstrated modulation of optical transmission, see Figure 38 copied below from that work.

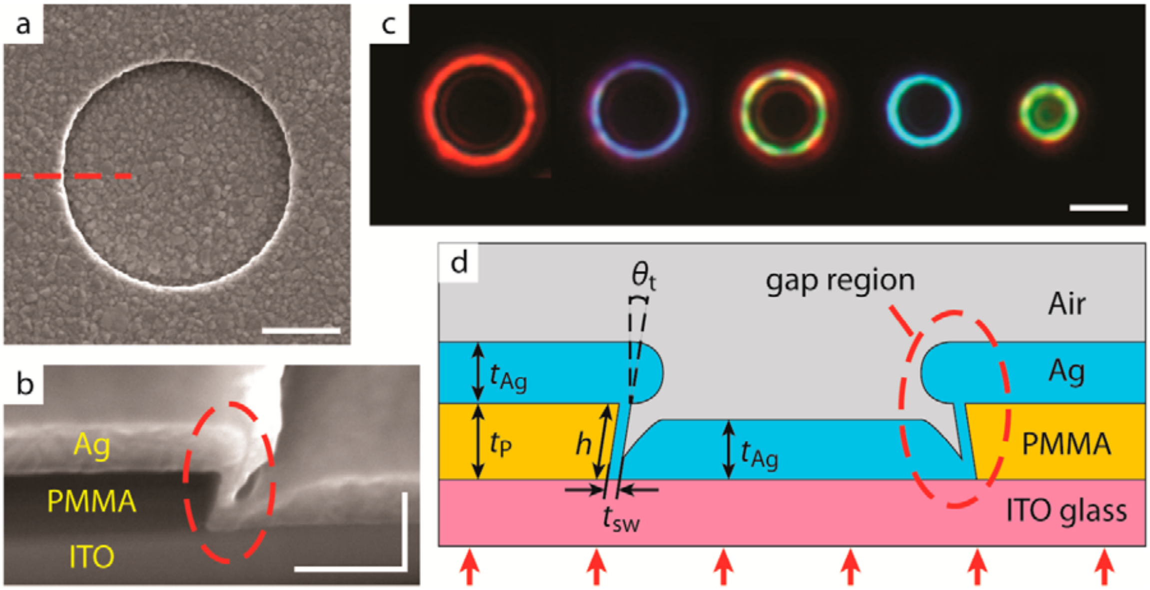

Figure 38. Structural and optical properties of the step-gap plasmonic circular cavity. (a) Top-view SEM image of a circular cavity. (b) 45 degree tilted cross-section SEM image of circular cavity taken in region indicated by dashed line in part a, highlighting the "step gap" region. (c) Optical images of transmission through circular cavity structures with different radii and electron-beam writing dosages, showing color tunability. (d) Cross-section view of the schematic design of the circular cavity, with red arrows indicating illumination direction. Scale bars: (a) 1 µm, (b) horizontal and vertical 500 nm, (c) 4 µm. Caption as in text (Ye et al., 2012).

This modulation of the transmitted light was tailorable through the parameters as listed in Figure 38d. Consequently, appropriate adjustment of different parameters, most notably the radius of the circular recession, would result in readily observable variation to the color of the far-field light, as can be seen in Figure 38c. These cavity modes were interpreted as separable solutions to the wave equation, where the radial component of the solutions are Bessel functions of the first kind. These cavity modes were first imaged using Near-field Scanning Optical Microscopy to show the distribution of enhanced electric fields in the cavity that are characteristic of the SPP. In a later work, the far-field appearance of the modes was studied for light transmitted in forward and reverse orientation with optical resolution limits considered (Ye et al., 2014). As the last line of the first plasmonic halo paper, Ye et al. proposed that these plasmonic structures could be applied in biosensing applications:

Such plasmonic devices can also be envisioned as useful in biosensing, wherein far field transmission is perturbed by interaction of the SPP with biomolecules (proteins, antibodies, etc.) immobilized on the drumhead surface.

It was later observed by Dr. Juan Merlo (research scientist of the Naughton Lab) that a potential significant increase in plasmon-mediated transmitted light was possible by structure the circular cavity such that they include multiple concentric trenches as shown in Figure 39.

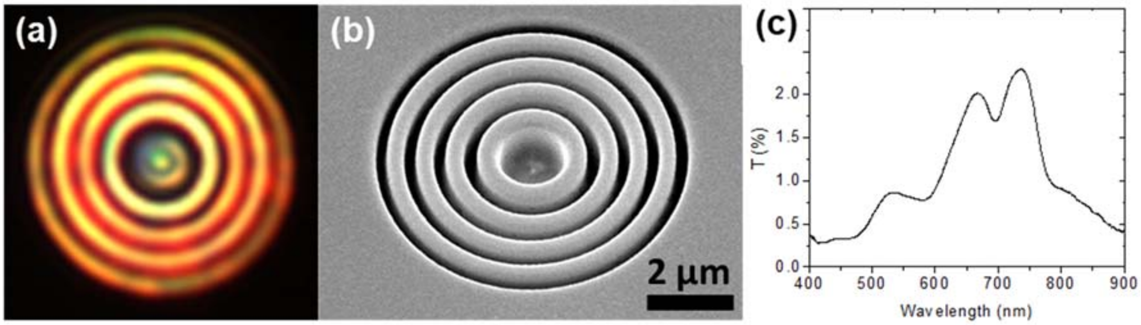

Figure 39. Concentric ring Fresnel structure. Imaged are those investigated (Dr. Juan Merlo) as an extension of the plasmonic halo. (a) Transmitted light with back-side incident white light, (b) 30° tilted SEM image of the EBL written structure and (c) present transmittance spectra.

This Fresnel lens structure showed promising characteristics compared to the halo structure, particularly a substantially higher transmittance while maintaining apparent plasmon-mediate filtering of the transmitted light spectrum. As previously discussed, the probable cause of this difference is the fact that the electric field of a surface plasmon exponentially decreases away from the surface and the Fresnel structure has relatively smaller gaps. Additionally, the gaps of the Fresnel structure make up a larger fraction of the projected surface area being illuminated.

3.2 Equipment and Experimental Setup

3.2.1 BioNavis SPR System

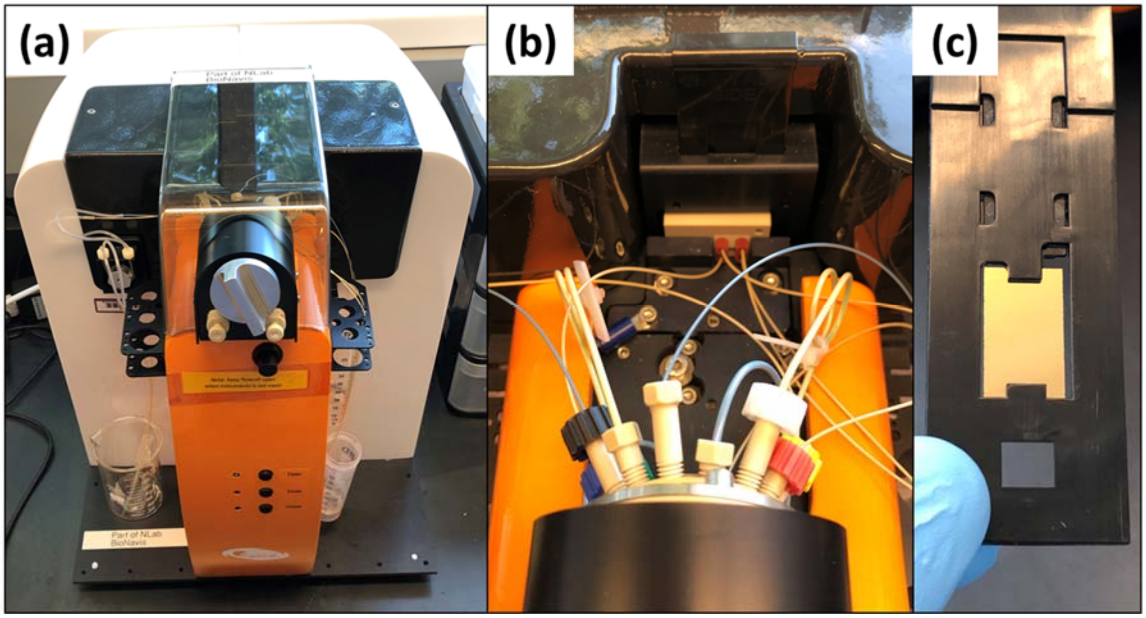

Figure 40. BioNavis SPR system. (a) Image of Navi 200 SPR system, (b) close up view of the 12-port injection valve and flow cell and (c) the sample slide holder with Au-coated glass sample.

As a part of this research we used a commercial SPR system, a BioNavis Navi200 (Figure 40). This tool was important for two main reasons: 1) the development of biological assays and functionalization protocols and 2) the investigation and testing of plasmonic materials for device consideration. First, I will discuss the plasmonic phenomena on which this system works and then I will describe operating procedure for the system.

The BioNavis Navi200 SPR system uses a plasmonic-based detection process based on the Kretschmann configuration (Figure 41), one of the most common ways of measuring characteristics plasmonic-based materials and devices (Ives et al., 2016).

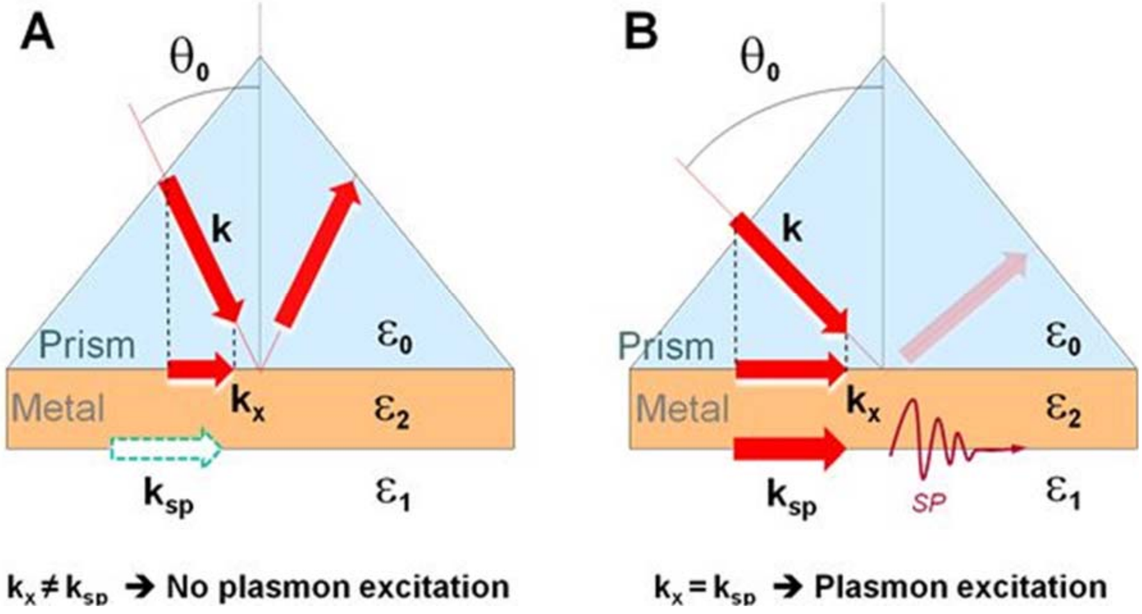

Figure 41. Schematic of Kretschmann configuration. Monochromatic TM-polarized incident light through a prism and substrate onto a thin metal layer in for (a) off resonance and (b) on resonance incident angles. The intensity of total internally reflected light is measured as a function of incident angle. Figure from BioNavis, Ltd.

In this configuration the sample is illuminated from the backside with monochromatic TM polarized light and the intensity of light by total internal reflection (TOI) is measured as the incident angle is swept over a range. When the angle is such that the in-plane component of the wave-vector, k_x, matches the wavenumber of the surface plasmon then the photon can sufficiently scatter energy into the surface plasmon, hybridizing to form the surface plasmon polariton. As the energy scatters into the SPP there is less energy to be reflected, and there is a subsequent attenuation in the intensity of reflected light. Figure 42 below shows a plot of the relative intensity as a function of incident angle.

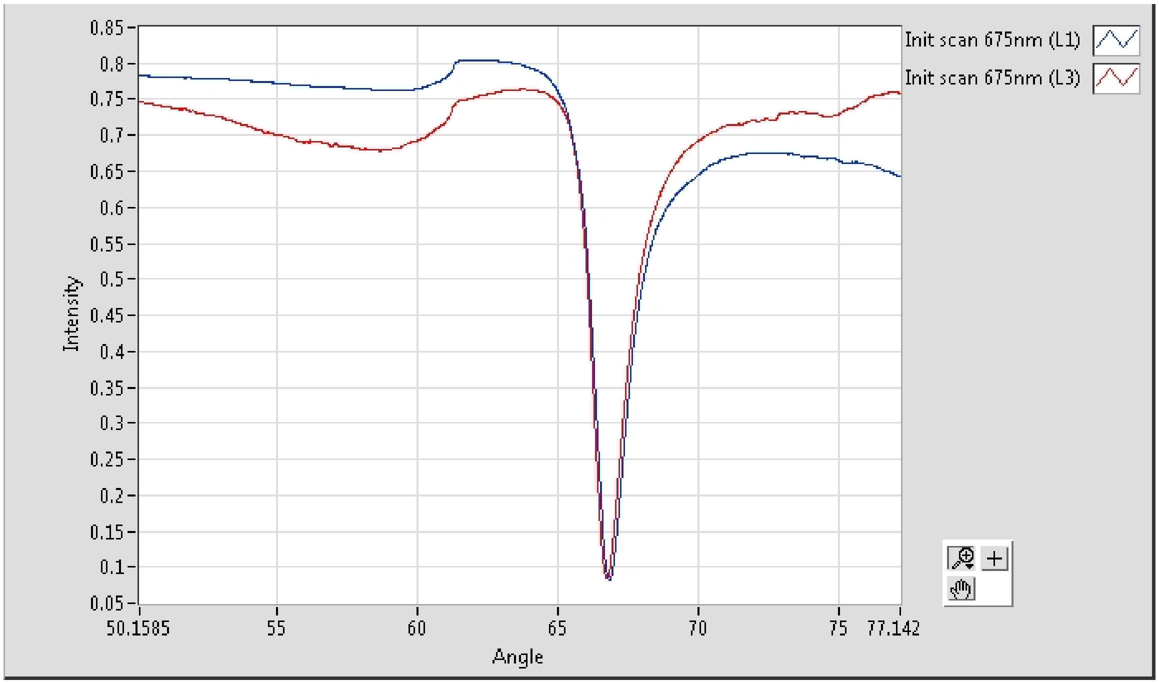

Figure 42. Intensity *vs.* angle for BioNavis SPR. Example data for DI-H_2O as dielectric. The similarities in the system and sample successfully show nearly the same angle of minimum reflectance and correspond plasmon wave-vector.

The thickness of the metal is large enough to contribute a sufficient amount of electrons to the SPP though small enough such that the penetration depth of the surface plasmon encompasses the entire film thickness, ideally around 50nm for Au films. Therefore, the interface between metal labeled ε_2 and the dielectric labeled ε_1 from Figure 41 will also influence the wavenumber of the surface plasmon. Specifically, larger ε_1 will require larger wavenumber and therefore a larger angle from the normal to the plane of incidence. By injecting a solution into the region of ε_1 with a higher index or by capturing a material to that interface the minimum will shift to the right in Figure 42 above. One can plot the change in the angle of the minimum intensity as a function of time in a plot referred to as a sensogram (Figure 43).

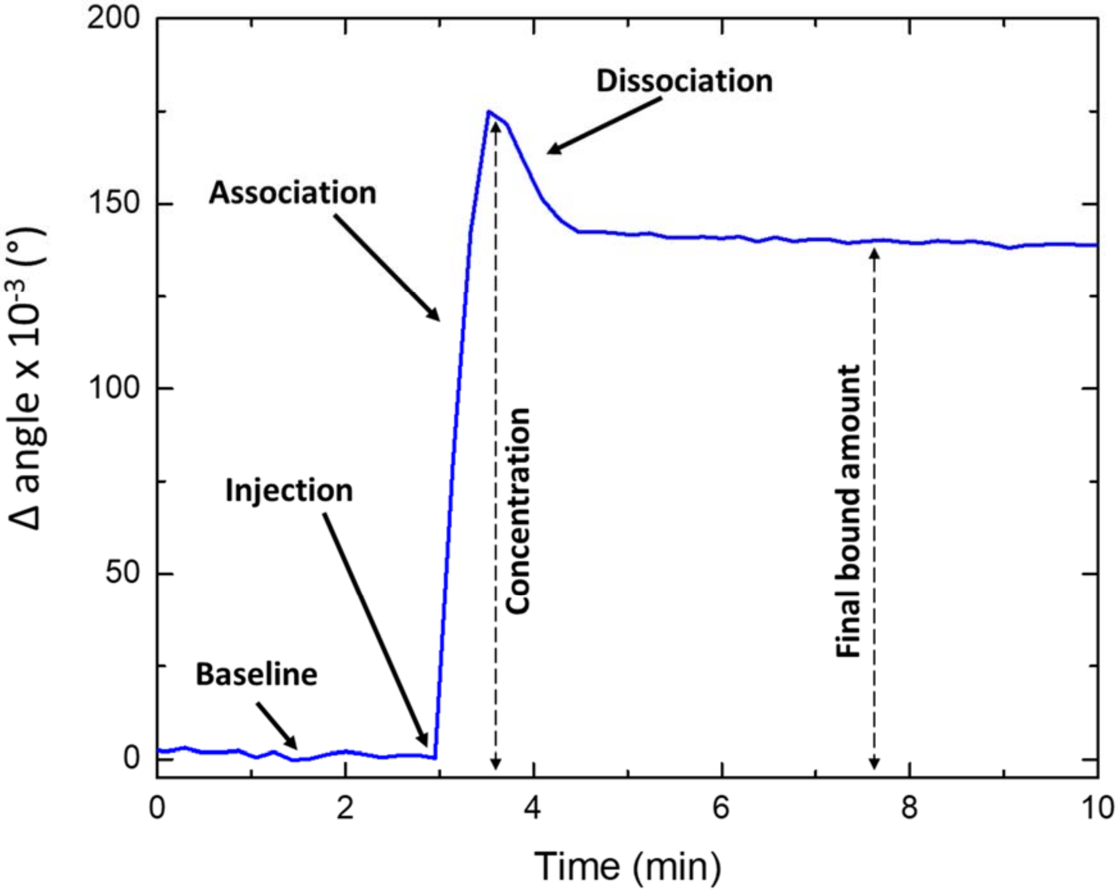

Figure 43. Sensogram from experiment on Navi200 SPR system. Plot for SA-Thiol functionalized surface capturing biotin-IgG titration. Captured material was injected at t=3min and resulted in a positive shift in the angle of minimum intensity due to increasing the local dielectric permittivity at the Au surface.

The features of the sensogram plot can give several aspects of information, such as the binding species, antigen concentration or presence, binding kinetics, binding strength and properties of the metal, which is most commonly gold due to its chemical stability.

Due to the expense and turn-around of purchasing samples from BioNavis ($40/chip and 1 week), I fabricated Au on glass chips for use with the Navi200 system. To do so, I started by cleaning a 4” soda-lime glass wafer with nominal thicknes 550 µm by sonication in acetone, then in IPA followed by rinsing with H_2O rinsing and drying with N_2 gas. Next the wafer was barrel etched with oxygen for 1min at 550 W and 270mTorr pressure. Next the wafer was inserted in the AJA sputter depsotion system for deposition. Most of the samples made for the Navi200 system were nominally 47nm of Au preceded by nominally 3nm of an adhesion layer of Ti or Cr. As will be discussed in section 3.4.2, different materials were explored and their Navi200 metallic chips were produced in the same way. After deposition a layer of S1813 photoresist was spin-coated on the metal surface of the wafer and soft baked to protect the metal during the following wafer dicing. The wafer was mounted to the UV-tape and dicing mount and then a Disco DAD322 dicing saw was used to dice the wafer providing 24 whole 20mm x 12mm rectangular samples. The samples were removed from the UV-tape and cleaned in agitated acetone for 5min, then IPA for 1min, then H_2O rinse and dried with N_2 gas. They are then stored for use in the Navi200, as is shown in Figure 44 below.

Figure 44. Au on glass. Samples made for use with the BioNavis Navi200 SPR system.

A sensogram is obtained by using the 12-port injection system on Navi200 (Figure 45) to inject a specified volume of solution into the region above the metal surface.

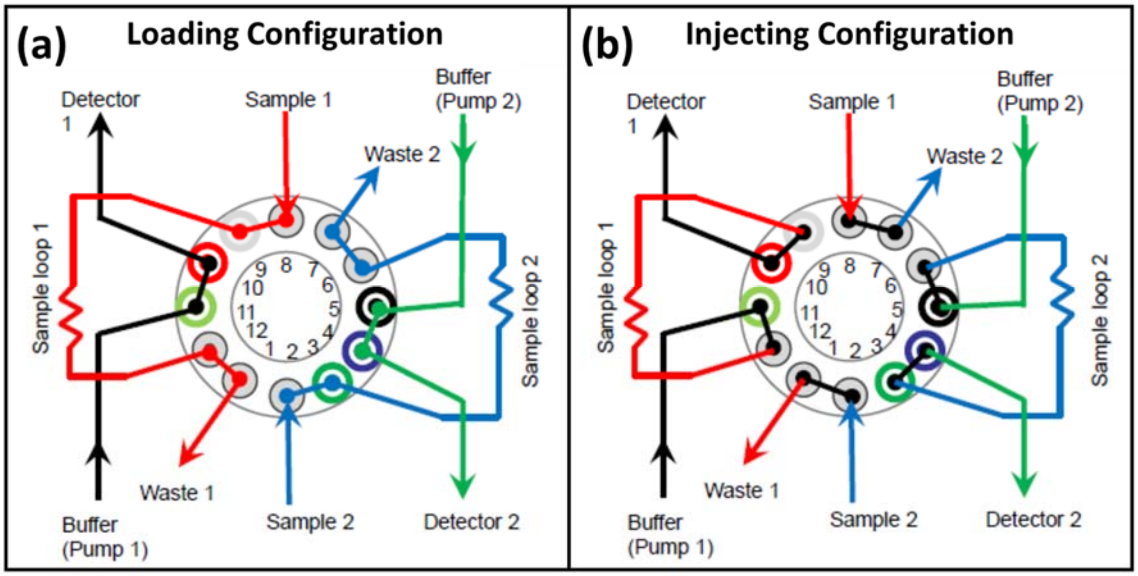

Figure 45. BioNavis Navi200 12-port injection system. (a) The loading configuration and (b) the injection configuration.

The key steps of the injection procedure are summarized below. For a detailed description of the measurement procedure and additional information, such as further background, software, and troubleshooting, see the SPR NAVI 200 USER MANUAL.

SPR Navi 200 Quick List

1) Load clean bare glass slide (12mm x 20mm x 0.55mm) into the slider holder.
2) Insert slide holder into instrument and close the flow cell. Misaligned chip or holder may cause the sample to crack or possible damage the index matched prism.
3) Turn dial on the face of the 12-port injection system to 'load'. Place both tubes that lead to the peristaltic pump into the buffer solution and set the flow value to desired rate in Navi200 software (typically higher just for this prepping step, ~100μL/min).
4) After a few minutes look to see if the waste tubing has liquid flowing out of it. If not then there may be a clog or possible a break in the system. Stop the flow and troubleshoot the problem. If there is flow, turn to the dial to 'inject' and wait a few minutes.
5) Repeat going back between 'load' and 'inject' once more.
6) Stop the flow and open the flow cell. Replace the bare glass slide with the metal coated glass slide with the metal side down.
7) Insert the slide holder into the system such that the metal side of the sample is facing the flow cell (forward). Close the flow cell.
8) Once the flow cell is closed, restart the flow and repeat flowing the buffer in both 'load' and 'inject' configurations to eliminate any possible bubbles in either of the paths. Finish with flowing in the inject configuration.
9) Use a syringe with a Hamilton blunt end G22 needle to inject the desired solution into the preferred injection port. Make sure bubbles have been flicked free from the solution within the syringe. Leave the syringe in the injection port until the experiment is over or until you return back to the load configuration from this

injection. *To avoid bubbles here, draw the solution into the syringe slowly such that a low pressure environment and boiling within the syringe does not occur*.

10) Set up the experimental details in software and begin recording. Observing the sensogram while the experiment is in progress is recommended.
11) After a few minutes of establishing a baseline quickly turn the injection dial from 'load' to 'inject'. The injection volume is 100µL. Given the flow rate, wait a few minutes after the injection volume has passed through the flow cell.
12) Save the data, stop the experiment and stop the flow.
13) Remove the metal sample and replace with bare glass sample for cleaning.
14) In the load configuration restart the flow and flow couple milliliters of the following solutions through both pump lines and also both injection ports: H_2O then IPA. Switch the injection dial back and forth a couple times in the process to catch any materials in between.
15) With IPA throughout the system, removal the tubing leading to the peristaltic pump and flow air for several minutes. Also, use the syringe to push air through both injection ports, switch the injection dial a couple times to push all excess IPA out.
16) Turn off the flow, open the flow cell, unload the glass slide, shutdown the software and the Navi200 and close the top to the system.

3.2.2 Leica Microscope and integrated equipment

Figure 46. Leica DM6000M optical microscope. Used to collect transmittance and reflectance spectra.

The Leica DM6000M microscope (Figure 46) was a key tool for the investigation of sample properties and running experiments towards achieving a plasmonic-based biosensor. As previously reported in the original halo work (Ye et al., 2012), the most common measurement configuration was to illuminate the sample from the bottom side and measure on the transmitted light (TL) axis. The transmitted light was collected by either a camera or spectrometer that both attached to the same port. A schematic summary of detection phenomena using modulation in transmitted light is shown in Figure 47 below.

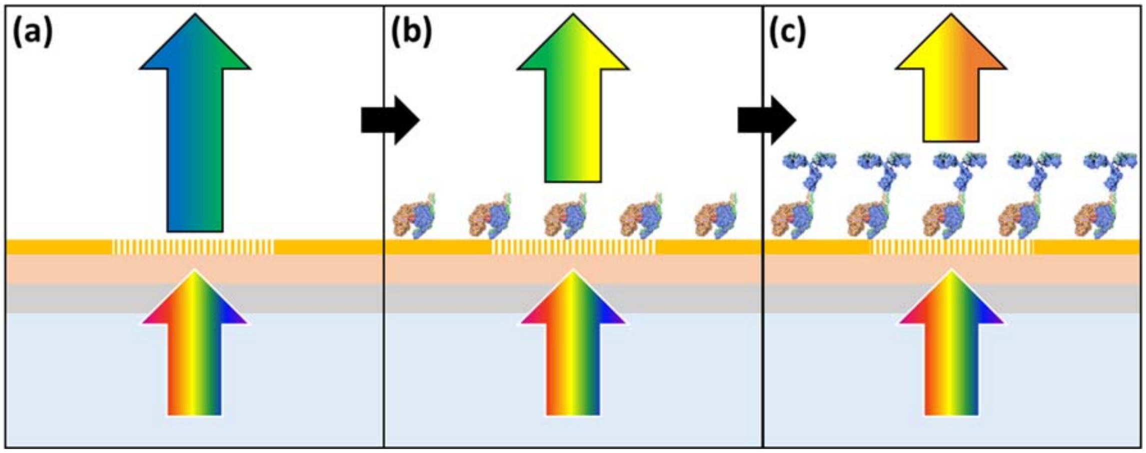

Figure 47. Schematic of transmitted light changes. Backside illuminated with white light for (a) the bare sample, (b) the sample after surface biofunctionalization with a capturing species, and (c) the sample after introduction and capture of targeted antigen. Each material can change the transmittance spectrum.

Biological and molecular species that are part of this capturing process will naturally have their own influence of transmitted light through typical absorption properties. The problem in detecting free antigens in a solution is two-fold; 1) the changes in transmitted intensities attributable to the targeted species are undetectably small, particularly for the sub-nM concentrations characteristic of many biological species associated with harmful diseases and 2) practical antigens or virulence factors that are distinguishing signs of targeted pathogens have similar absorption characteristics due to their similar molecular makeup, thereby diminishing the ability for selective detection. The importance of the incorporation of the plasmonic-based structure is their ability to solve both limitations by providing a surface that can enhance the effect of small concentrations of targeted antigens and that this enhancement occurs at the device surface that can be functionalized to capture specific antigens. The capturing of biological species to the plasmonic surface does not necessitate that the enhanced electric nearfield increases the antigen's absorption characteristic but rather that their presence simply modifies the physical properties at the material interface thereby causing a change in the in the dispersion properties at that interface.

In order to quantify and most effectively analyze changes in transmitted light we record the spectral intensity as a function of wavelength and calculate the transmitted spectra at the different steps in the functionalization and capturing process. Two of the spectrometers used in experiments are shown in Figure 48 below.

Figure 48. Spectrometers used for experiments. Ocean Optics Maya 2000PRO spectrometer (left) and an Ocean Optics USB2000 spectrometer (right). The spectrometers were used for recording different experiments' spectra.

One of the most important considerations for recording the transmitted light spectra is the ability to maintain a good signal-to-noise ratio. In doing so, one is capable of observing small changes in the transmitted light that are typical of capturing biologically relevant concentrations of targeted species. It was observed the USB2000 spectrometer had a relatively low sensitivity to the small transmission intensity characteristic of sample studied. This relatively low sign-to-noise raise made comparing features in the transmittance spectra difficult, especially in the 700nm -1000nm wavelength region.

In order to address this issue, we used the much more sensitive Maya 2000Pro. In order to do so (and the reason that the Maya spectrometer was not used in the first place), I needed to address the issue of the saturation of spectrometer for the recording of the source spectrum, which was considerably larger than the peak sample intensity due not being attenuate by largely opaque planar regions of the samples. This was achieved in two different ways: 1) by using separate integration times and fractions of light sent to the camera (half-camera/half-ocular) and then assuming the ratio of relative intensities was equal to the ratio of integration times, as is shown in Figure 58 of section 3.3.1. and 2) by using a neutral density filter to attenuate the source spectra so that it would not saturate the detector and then by dividing by the measured attenuation factor of the neutral density filter (NDF) when calculating the transmittance, see Figure 59 of 3.3.1. In order to integrate the NDF and other optical filters (to be discussed in section 3.6.2) into the Leica component holders needed to be made. In addition to these parts, I designed a XY-stage insert that would allow easy and repeatable positioning of the square substrates that sample were typically made of and, more importantly, would allow the collimating lens to come up to the bottom of the inserted sample such that the its 1mm focal distance could be coplanar with the sample surface and objective lens focal plane. These Leica components, made in the machine shop on the Clausing Kondia milling machine, are imaged in Figure 49 below.

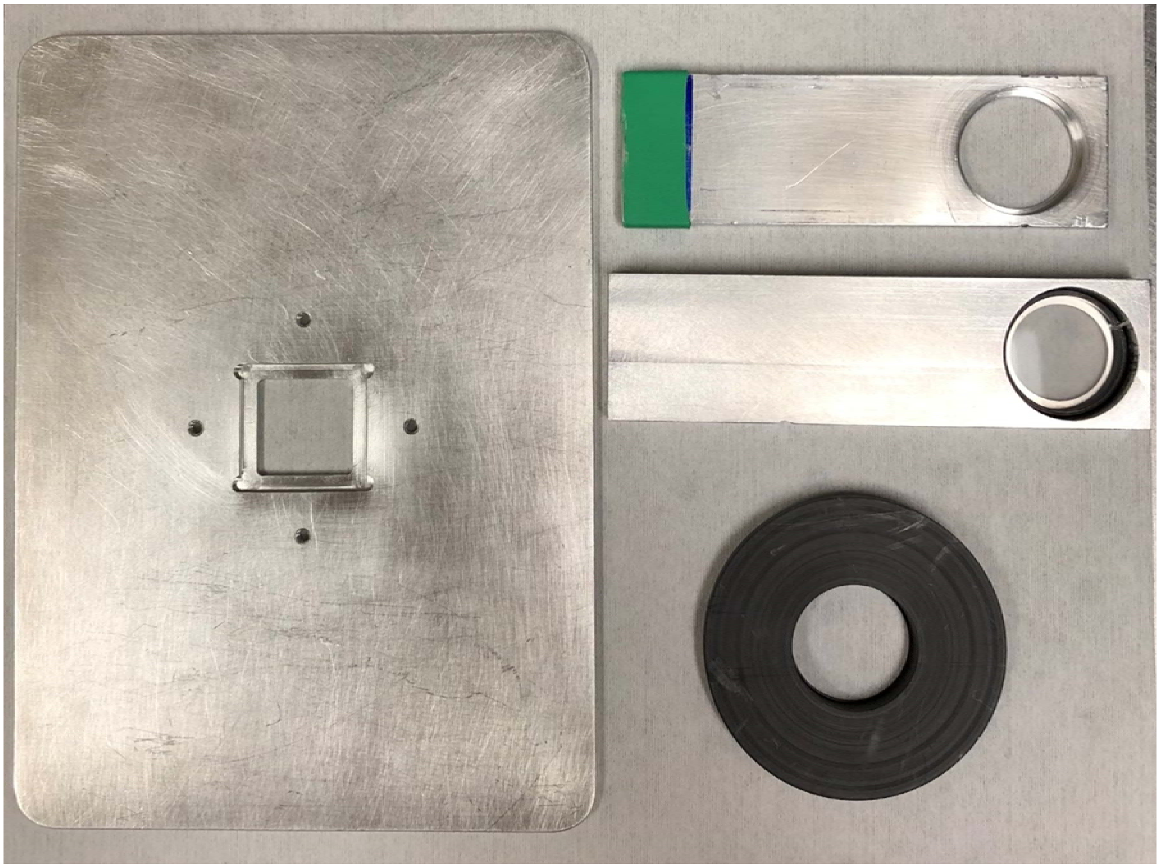

Figure 49. Leica accessories made in the machine shop. Left is a sample holder that inserts into XY-stage. The 3 pieces on the left are holders for different optical components used in experiments.

Below is a collimated LED light source that was used in experiments with quantum dots as will be discussed in section 3.6.2. This light source could be connected to the dovetail port on either the TL or IL axes.

Figure 50. Left is a Thorlabs M405LP1-C2 LED. Source with center-wavelength 405nm and FWHM 12nm attached to a COP2-A collimating lens with Leica dovetail port adapter. Right is the corresponding Thorlabs LED drive for this light source.

3.2.3 Cleanroom Equipment

Equipment used and already shown in chapter 2:

- Karl SUSS MA6 Mask Aligner (Figure 9)
- AJA International Sputter Deposition system (Figure 10)
- PVA TePla PS210 Plasma Barrel Etcher (Figure 12)
- JOEL JSM-7001F Scanning Electron Microscope (Figure 13)
- Veeco Dektak 150 Profilometer (Figure 16)
- Laurell Technologies WS-650-23B Spin Coater (Figure 17)

Figure 51. Disco DAD3220 Automatic Dicing Saw.

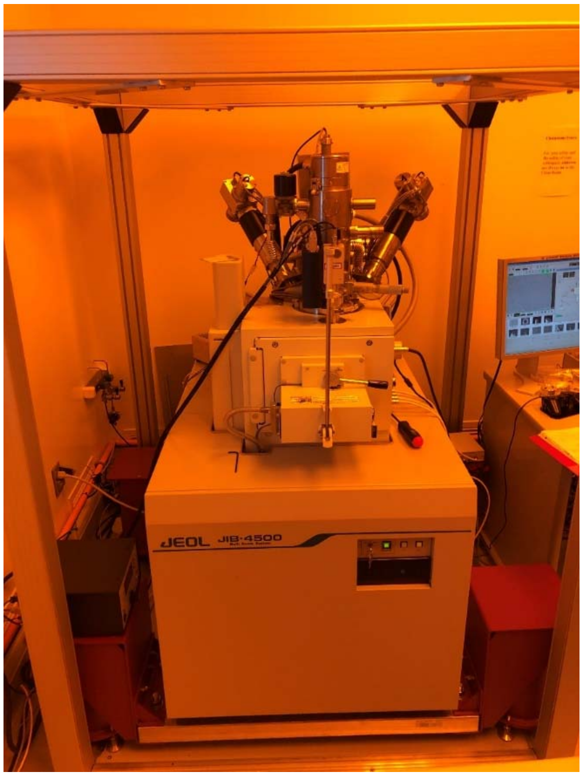

Figure 52. JEOL JIB-4500 scanning electron microscope and focused ion beam.

Figure 53. Heidelberg MLA150 maskless photolithography system.

Figure 54. Sharon E-beam Evaporator physical vapor deposition system.

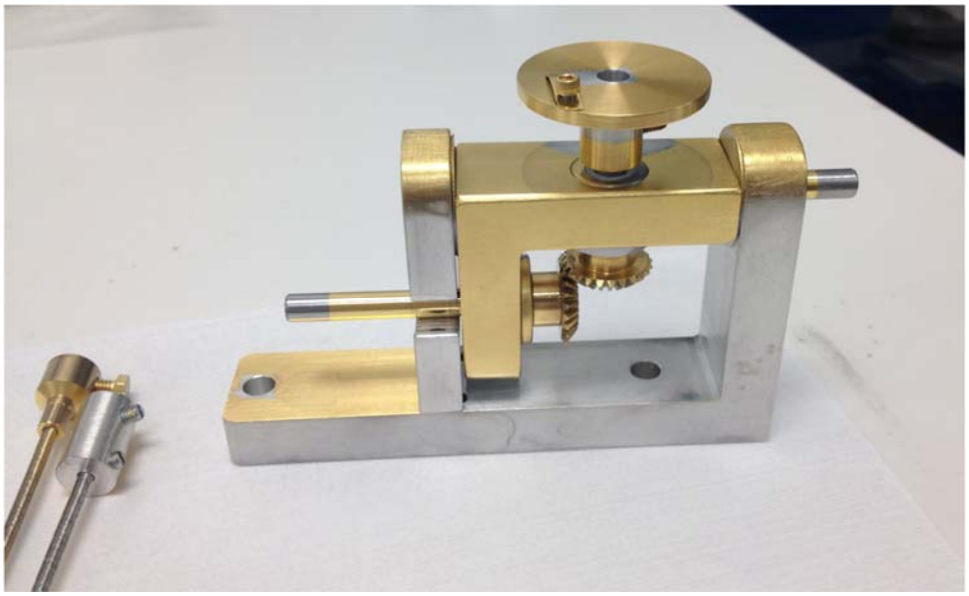

Figure 55. Angled rotation stage for Sharon system.

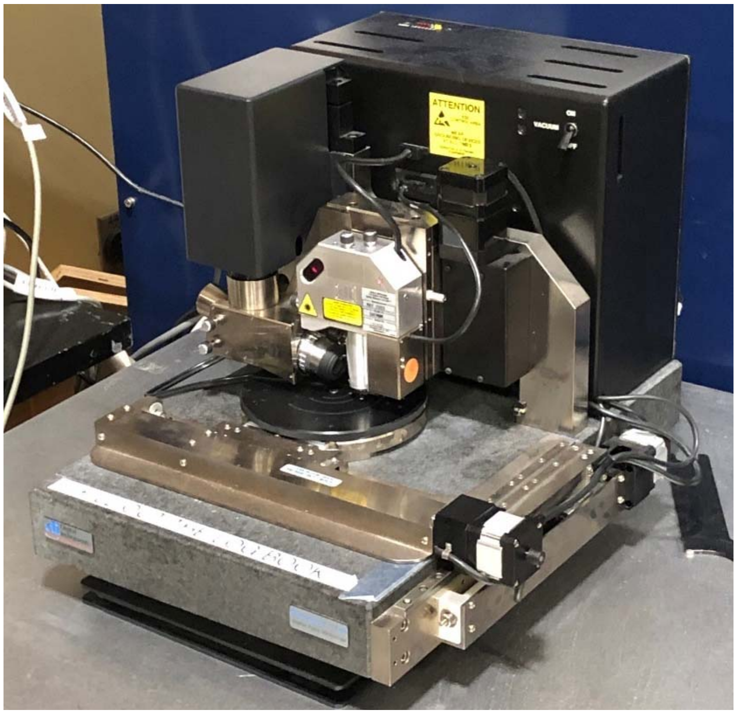

Figure 56. Veeco Dimension 3100 Atomic Force Microscope.

3.3 Software

3.3.1 Origin

The most common form of processing with spectral data was calculating transmittance spectra using Origin 2016. The raw data is recorded in the form of counts, where the counts for a given CCD-based spectrometer are linearly proportional to the number photons incident at that wavelength. Four spectra need to be collected to calculate the transmittance: 1) The counts of the sample region, 2) the dark counts for the sample region, 3) the counts of the source, and 4) the dark counts of the source, which can be the same as the dark counts for the sample if the integration times are the same. The Leica has the option to pass the light entirely to the oculars, entirely to the spectrometer, or half to each. If the source and sample are recorded with different fraction sent to the spectrometer then this factor needs to be included in the transmittance calculation. If the integration times are different for the collected counts, then this also needs to be included in the transmittance calculation as the ratio of the integration times. It is also important that the dark counts corresponding to the source and sample each be taken at the same integration times as their respective spectra, because the background counts are different for different integration times (Figure 57). When taking these recording conditions into account there will be multiple factors in the calculation of transmittance to correctly weight the different spectra. An example of a calculation of transmittance and the contributing factors is shown in Figure 58.

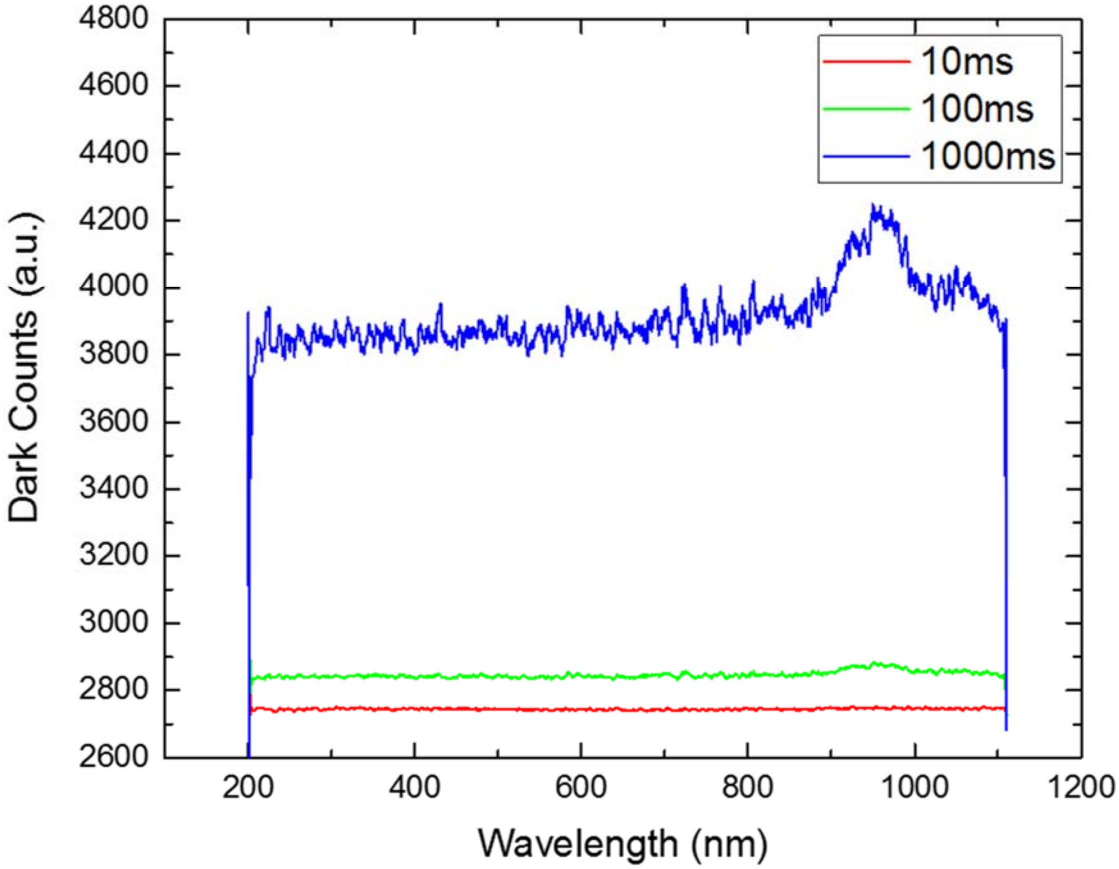

Figure 57. Plot of the dark counts. Spectra recorded by the Maya2000Pro spectrometer with no incident light for three different integration times, as controlled by spectra Suite.

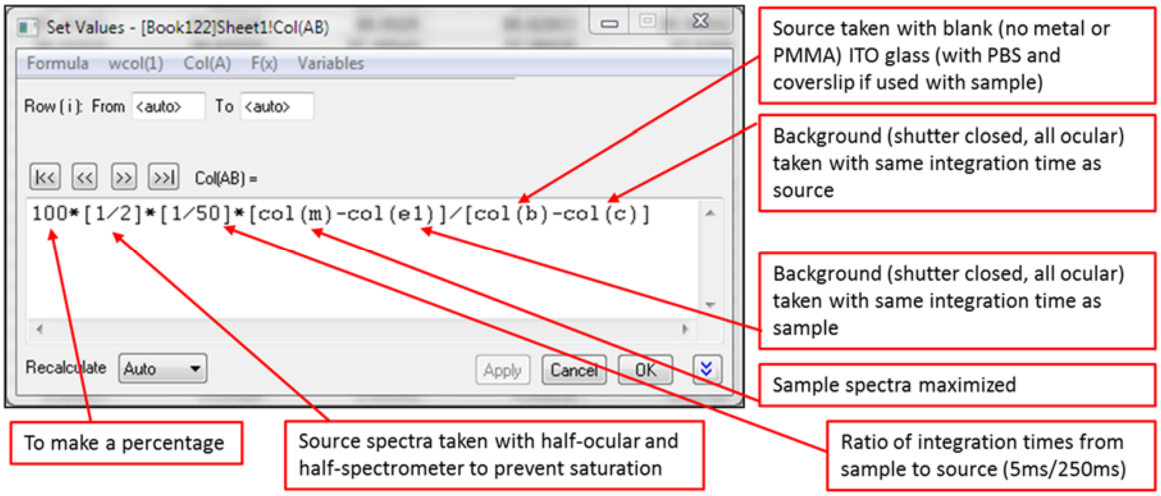

Row (i): From <auto> To <auto>

Col(AB) =

```
100*[1/2]*[1/50]*[col(m)-col(e1)]/[col(b)-col(c)]
```

Recalculate Auto

Source taken with blank (no metal or PMMA) ITO glass (with PBS and coverslip if used with sample)

Background (shutter closed, all ocular) taken with same integration time as source

Background (shutter closed, all ocular) taken with same integration time as sample

Sample spectra maximized

To make a percentage

Source spectra taken with half-ocular and half-spectrometer to prevent saturation

Ratio of integration times from sample to source (5ms/250ms)

Figure 58. Example transmittance calculation. Shown is a description of contributing terms for measurements taken at different integration times.

As mentioned previously, one can also use a NDF to reduce the much higher intensities of the source measurements compared to the sample counts. There main reason that this would be desired, is in order to record the sample and source counts with the same integration time. It was observed that, despite the equipment advertising otherwise, the ratio of the integration time was not linearly proportional to the integrated counts and had different non-linearities for different wavelengths.

In order to effectively convey the entire process of calculating the transmittance, I will first show the headers of the columns from the Origin file, I will describe what each column means, and then show the resulting plot data. Figure 59 below shows the headers and functions for columns A through N used to determine the transmittance of three separate sites for a given process. For completeness, optical images of these three regions when illuminated by white light and corresponding SEMs are shown in Figure 60 and final transmittance plots are shown in Figure 61.

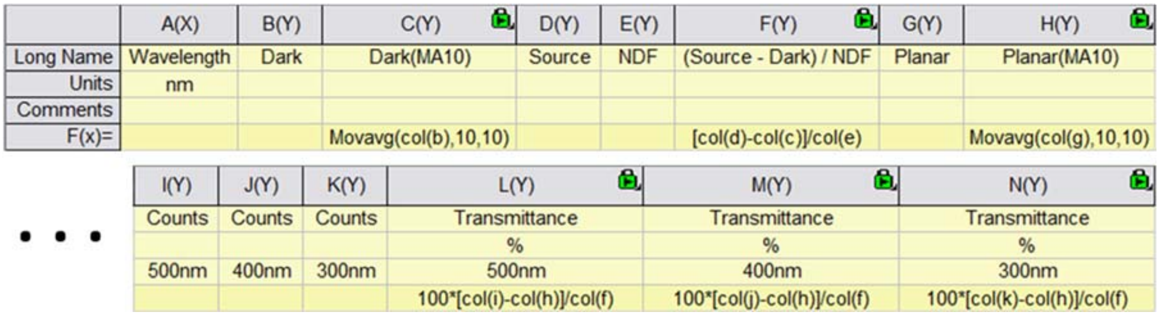

	A(X)	B(Y)	C(Y)	D(Y)	E(Y)	F(Y)	G(Y)	H(Y)
Long Name	Wavelength	Dark	Dark(MA10)	Source	NDF	(Source - Dark) / NDF	Planar	Planar(MA10)
Units	nm							
Comments								
F(x)=			Movavg(col(b),10,10)			[col(d)-col(c)]/col(e)		Movavg(col(g),10,10)

• • •

I(Y)	J(Y)	K(Y)	L(Y)	M(Y)	N(Y)
Counts	Counts	Counts	Transmittance	Transmittance	Transmittance
			%	%	%
500nm	400nm	300nm	500nm	400nm	300nm
			100*[col(i)-col(h)]/col(f)	100*[col(j)-col(h)]/col(f)	100*[col(k)-col(h)]/col(f)

Figure 59. Origin spectra processing. Image of column headers of workbook used to calculate a sample's transmittance.

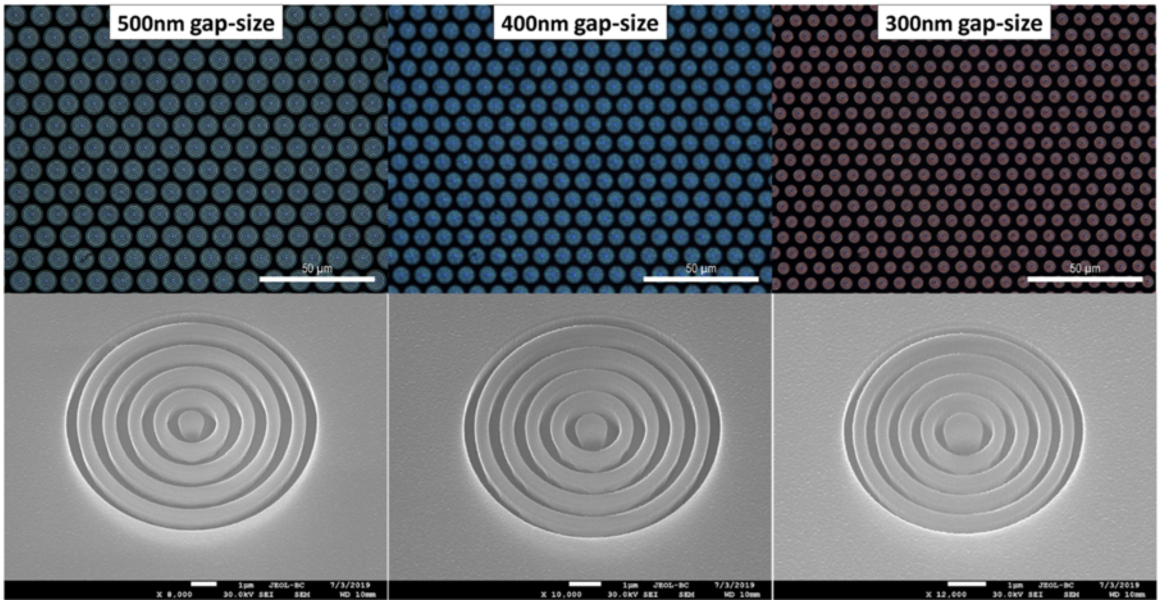

Figure 60. Transmitted light and SEMS. Images from light upon white light illumination and corresponding tilted scanning electron micrographs for the three regions calculated in the Origin file referenced above.

‘

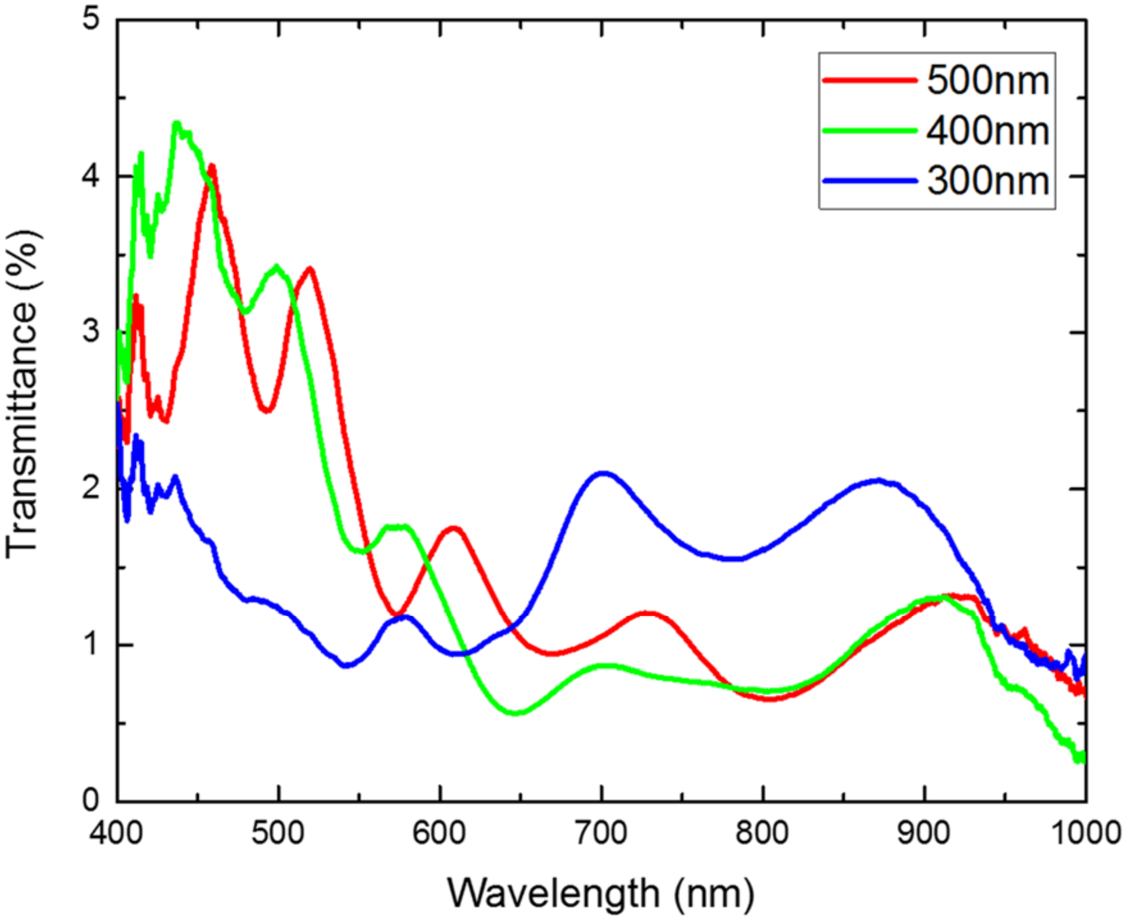

Figure 61. Example transmittance spectra. Spectra plotted for the three regions calculated in the Origin file referenced above.

Column A from Figure 59 contains the wavelength values of the spectra, ranging from 200.04 nm to 1111.08 nm at an interval of 0.47 nm to 0.42 nm (the gradually decreases). The near-optical wavelength range is characteristic of the Si-based CCD detector in the Maya 2000Pro. The transmittances are usually plotted for the wavelengths 400 nm to 1000 nm as the signal to noise ratio decreases substantially outside of this window.

Column B from Figure 59 contains the dark spectrum of both the sample and the source, since the same integration times were used. The dark spectrum was collected by turning closing the shutter of the light-source and recording at the conditions otherwise. During all spectra collection an opaque screen is set around the sample to block outside light. Additionally, the main white lights of the room where turned off and dim red-pass-filtered LED light where used as can be seen in Figure 62 below.

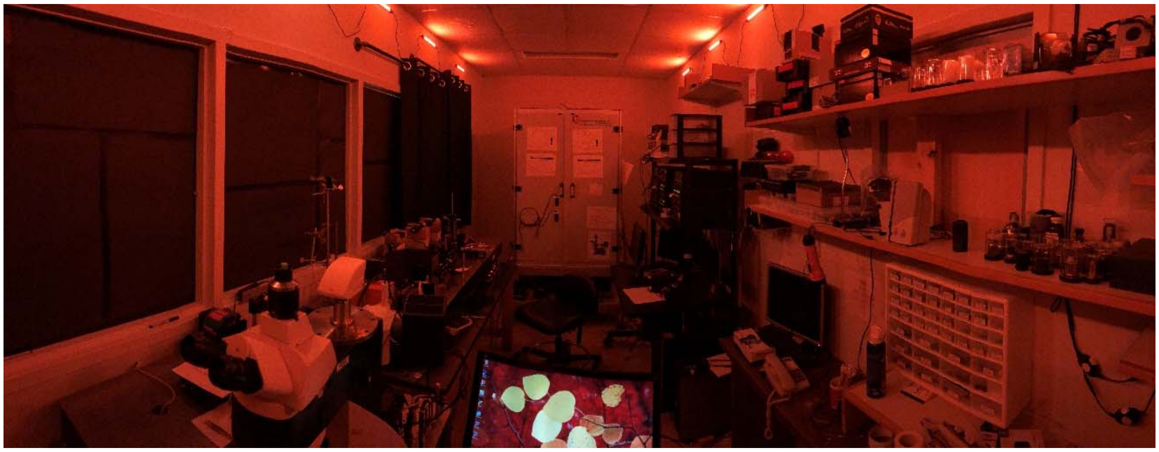

Figure 62. Leica microscope room. Image of room with dim red lighting where measurement occurred, used to reduce background noise contributions.

As shown in column C of Figure 59, the dark spectrum was then processed with a moving average function in order to reduce the effect of the higher frequency variations that were observed to vary in time. Figure 63 below shows the dark counts with the overlain moving average.

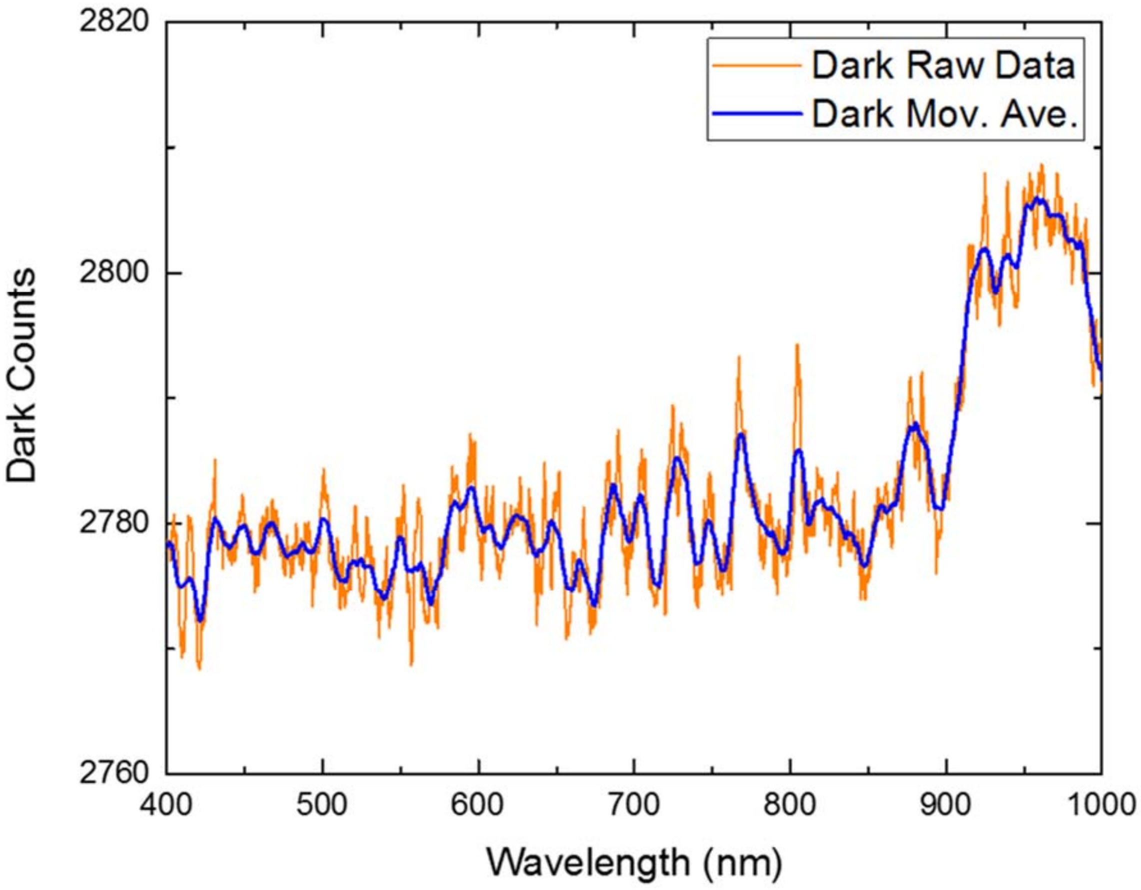

Figure 63. Moving average of dark counts. Recorded with (blue) and without (orange) average.

Column D of Figure 59 contains the source spectrum with the NDF. The x, y and z positions of the stage are recorded during measurement with the sample and the source is recorded at this same position substituting a blank ITO glass for the sample. The primary source used was an incandescent bulb set to maximum intensity after passing through a diffusing lens and it is referred to as white light in this text.

Column E of Figure 59 contains the NDF function that is its transmittance. In order to measure the transmittance of the neural density filter, transmittances were measure and calculated for a few different optical setups and then averaged. Next a moving average was applied to this average spectrum and constant values were chosen for values lower than 400 nm and higher than 1000 nm, further invalidating the high-noise data in this region from evaluation. An image of the final NDF factor is shown in red in Figure 64 below. While the NDF has somewhat neutral filtering for visible wavelengths, it is observably not neutral over the 400 nm – 1000 nm range, particularly in the near-infrared.

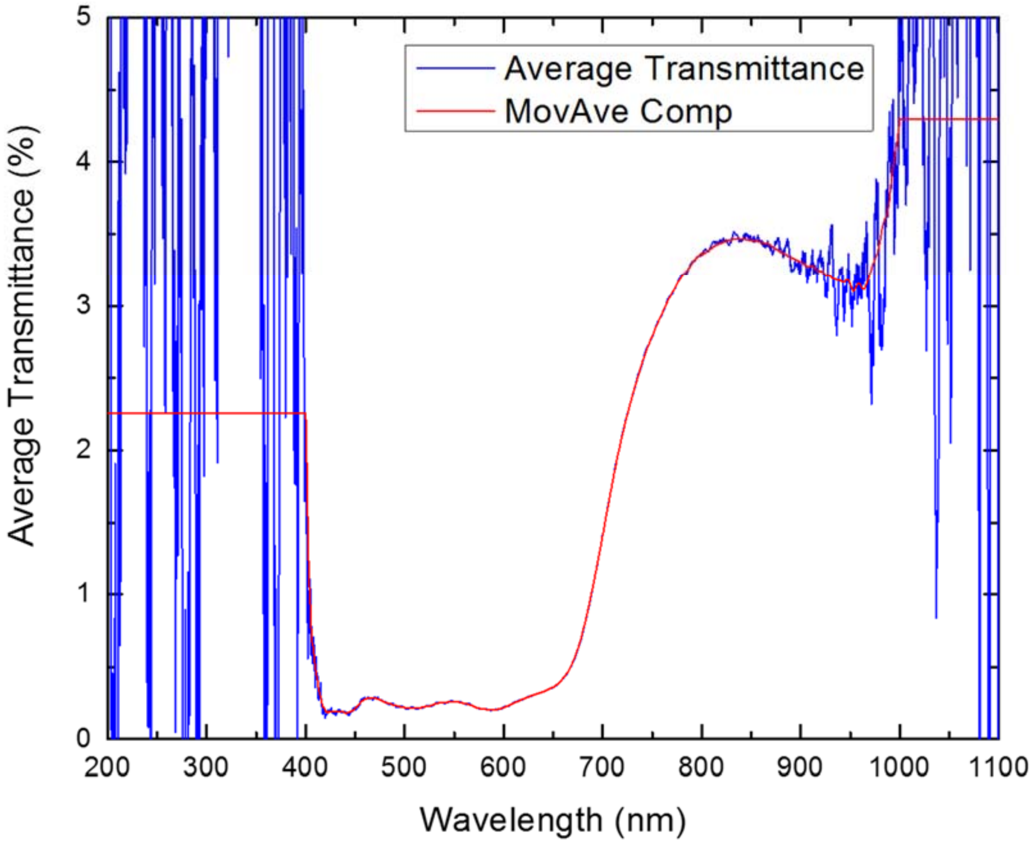

Figure 64. Transmittance spectrum of neutral density filter. (blue) averaged for different optical configurations. Moving average (red) of the transmittance and constant values specified for wavelengths below 400 nm and above 1000 nm due to high noise for these regions.

Column F from Figure 59 contains the calculation for the inversion of the NDF on the source. Since the NDF does not filter the dark spectrum (background of spectrometer), the dark spectrum first needs to be subtracted from the source spectrum before dividing by the NDF factor, obtaining the light source counts without the dark counts that would otherwise saturate the spectrometer.

If the metal in the planar regions of the sample is not opaque to the extent that transmittance can assumed to be zero, which is usually desired, then the transmitted light through this region can accounted for. To do so, the transmitted counts for a planar region are measured and processed with a moving average, as can be seen in Figure 59 columns G and H, respectively. When one calculates transmittance, this planar region spectrum is subtracted from the measured counts rather than the background.

Columns I, J and K of Figure 59 contain the transmitted counts for the three separate regions of interest, in this case they are arrays of structures with different sized geometries. Variations in these three spectra are the only sources of variations between their transmittances, which are calculated in columns L, M, and N, respectively. The equations for transmittance calculations are shown in the function row of each column, where each includes a factor of 100 in order to give a percentage transmittance.

3.3.2 COMSOL

Computer simulations were used to understand and motivate the changes to material and geometrical features. The power of using computer modeling for this purpose is that it allows us to explore a wide range of parameters, such as the radius discussed in the original halo works, whereas fabrication on a similar scale would impractical or impossible. The software used for simulations was COMSOL Multiphysics. COMSOL is a finite element solver software design for simulating problems in engineering, physics and chemistry. A detailed description of the niceties of COMSOL and the simulations explored would be extensive and beyond the scoop of this thesis, therefore this section will describe only a few of the simulations without describing the software itself.

When beginning a simulation model with a new system or software, it is wise to beginning with the simplest model and then add in additional complexity to reach the model. For simulating the case of light transmitting through the plasmonic structures, the simplest case is a planar interface of materials. Figure 65 below is an image of the *Electric Field Norm* plotted over the geometry of a planar sample, with inset zoom of the metal interface.

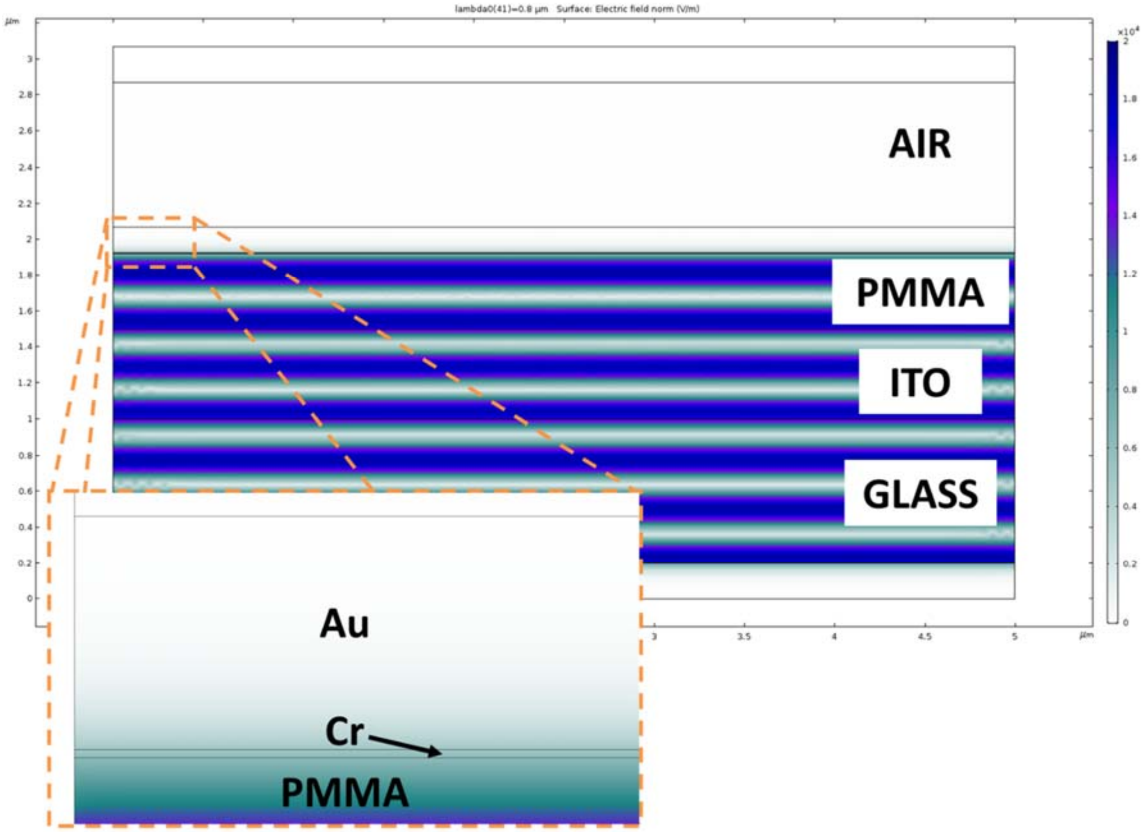

Figure 65. Electric Field Norm for planar interface. Simulation using the same materials used to make samples for experiments, with inset zoom of the metal interface. The color scale is from 0 V/m to 2×10^4 V/m. Window is 3 µm × 5 µm.

The sample simulated above was one previously made on ITO-coated glass, with a spin coated layer of PMMA, and a sputter-deposited layer of CrAu. The transmittance of the incandescent white light source for this sample was measured for 2 different time integration setting and plotted alongside the results simulated in COMSOL, as shown in Figure 66 below.

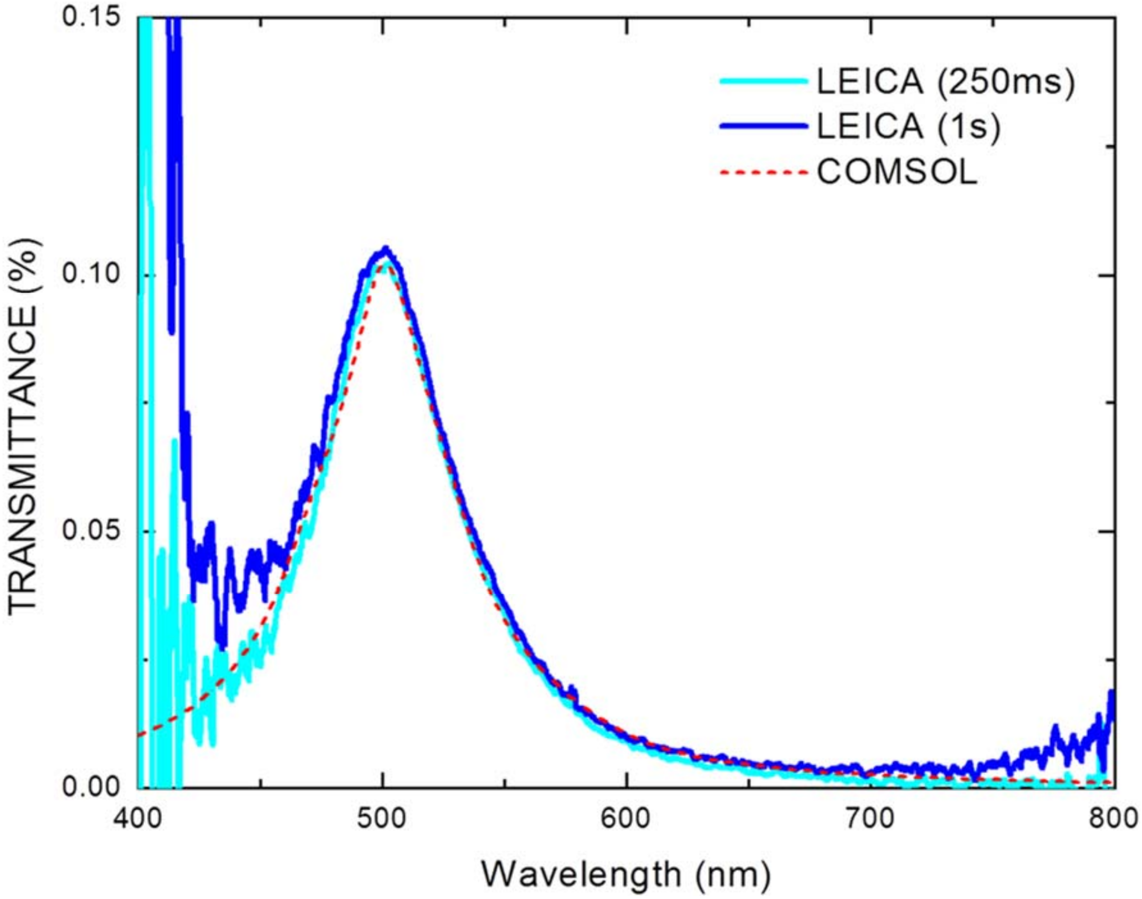

Figure 66. Plot of percent transmittance of a planar film. Measured spectra for CrAu on an ITO-coated glass substrate with spin-coated PMMA. Plotted are two experimentally measured spectra for the transmittance along with simulated transmittance for a COMSOL model.

When developing a model, it is important to investigate how small changes to the model features affect the resulting solutions. Particularly, it is important to realize that a simulation capable to describing materials or geometries that are not feasible or realistic representations of the samples begin produced. As an example, models can be easily described to include idealistic structures such as perfectly right corners. These discontinuities in curvature can represent potential problems in solver the finite domain boundary problems of the simulations, leading to discontinuities or other ‘computational artifacts’ in the results. Figure 67 below shows the transmittances for two nearly identical models of a plasmonic structure with and without smoothed edges that would be characteristic of an actual fabricated sample. Note the smoothing of corners in the model is able to eliminate a discontinuity in the transmittance at 1000 nm.

Simulation artifacts can also be introduced through an insufficiently small mesh size. Mesh is the distribution of finite domains that the solver finds solutions for. Setting to small of a domain can limit the results of a simulation by causing abrupt changes and discontinuities in solutions. Smaller features sizes and physical phenomena require a smaller (finer) mesh. A common test that this criterion has been met is by decreasing the mesh size until the solutions stop changing, such as the distribution of electric fields. It is common to use different mesh sizes or shapes for different region in a simulation. Exceedingly small mesh can unnecessarily increase the computational time of a model.

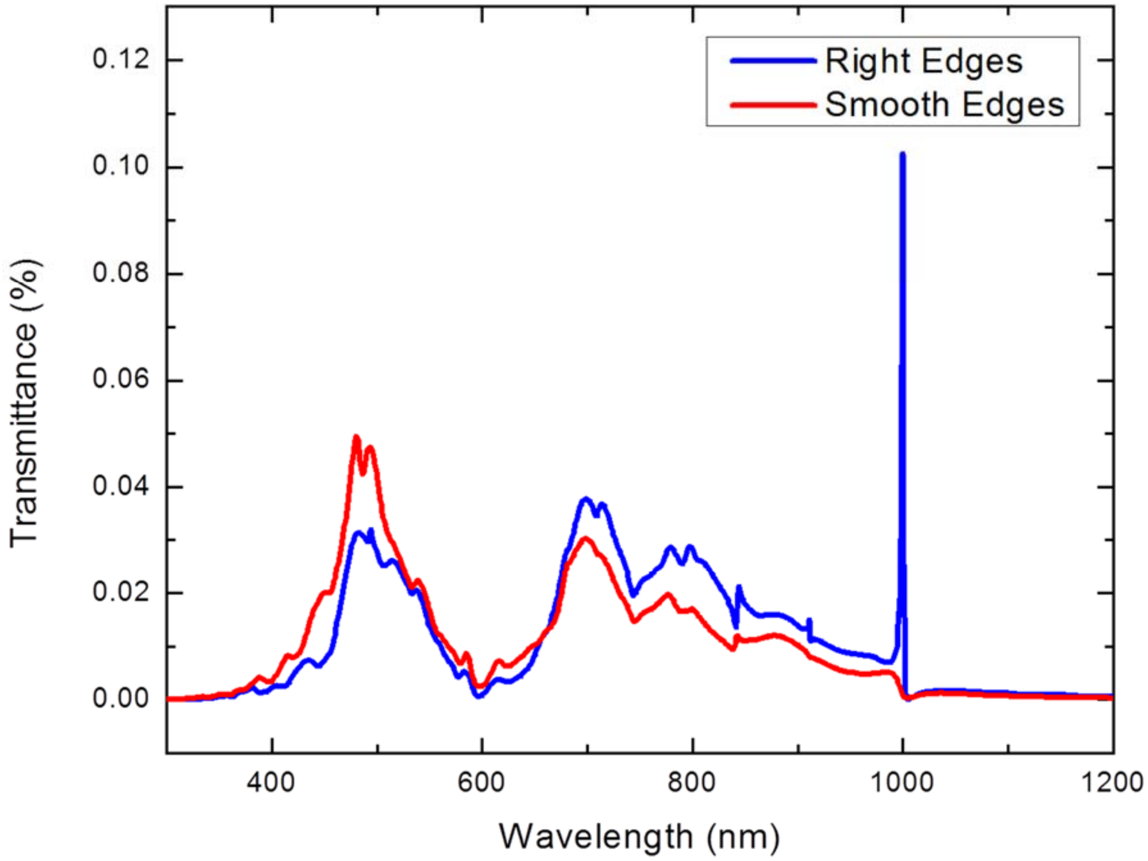

Figure 67. Simulated transmittances for different edges. Simulations for concentric ring nanostructure with and without smoothing of sharp corners in the geometry.

As another example, COMSOL was used to look at the relative effect of changes in metal thickness in vertically oriented regions of a structure. Different deposition tools and techniques will result in different aspect ratios of the vertically and horizontal thicknesses. This aspect ratio is also an important feature of structures towards increases transmitted light while necessitating that the light transmitted is mediated through surface plasmons, rather than just by reduced absorption. Figure 68 below plots the simulated transmittances for the same concentric ring nanostructure for different aspect ratios of sidewall thickness to planar region thickness, with 20% and 50% shown.

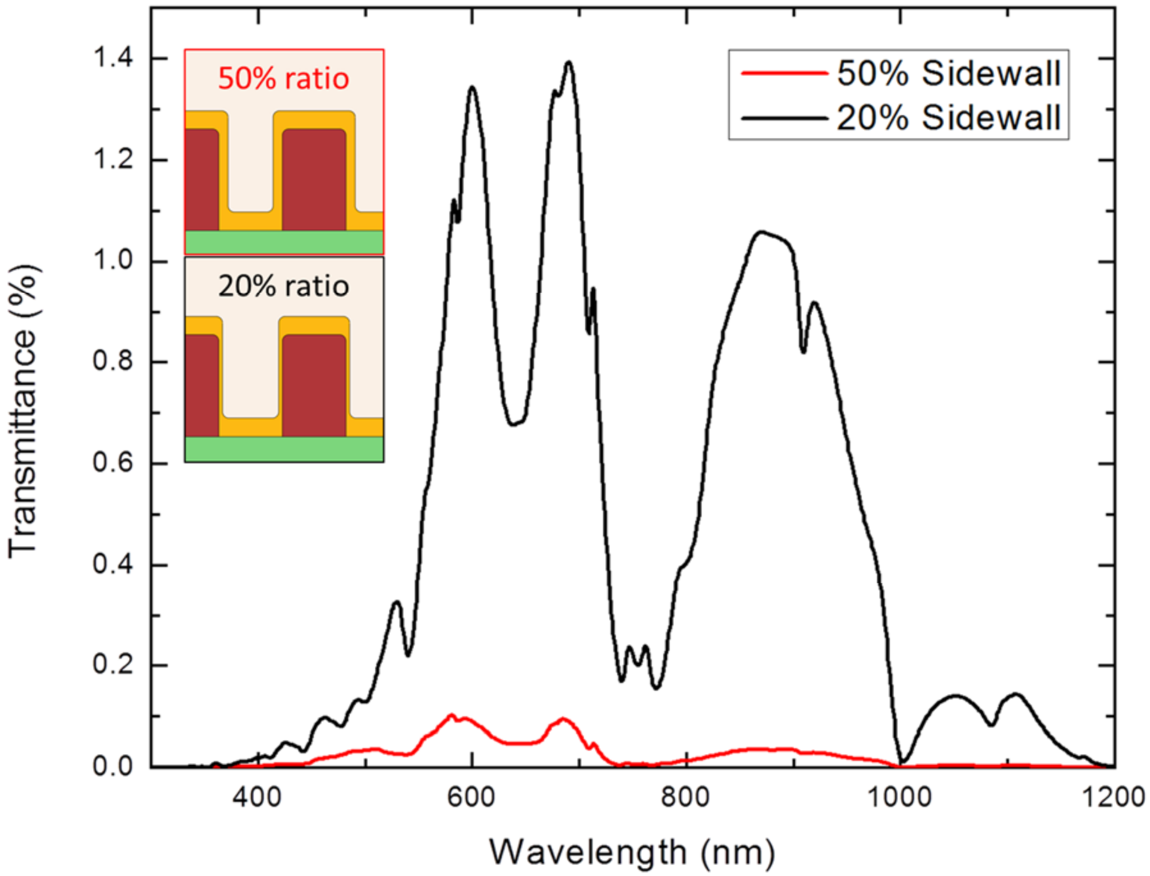

Figure 68. Simulated transmittances for different sidewall. Simulations for a concentric ring nanostructure for two different sidewall thickness aspect ratios.

These models hope to motivate combinations of materials and structural parameters for the incorporation in a sensing device. As such, we were interested in setting up simulations that would represent the types of changes that one might expect in a biosensing experiment. Using a metric for sensitivity defined in literation, discussed in section 3.5.2, we investigate how different models' transmittances change when the index of refraction of the dielectric material changes, shown in Figure 69 below. There a simulation of a nanostructure is solved for a small change in the index of refraction, Δn=0.01, and we look to see the wavelengths of minima and maxima in intensities, where larger changes in these wavelengths are defined to have higher sensitivities.

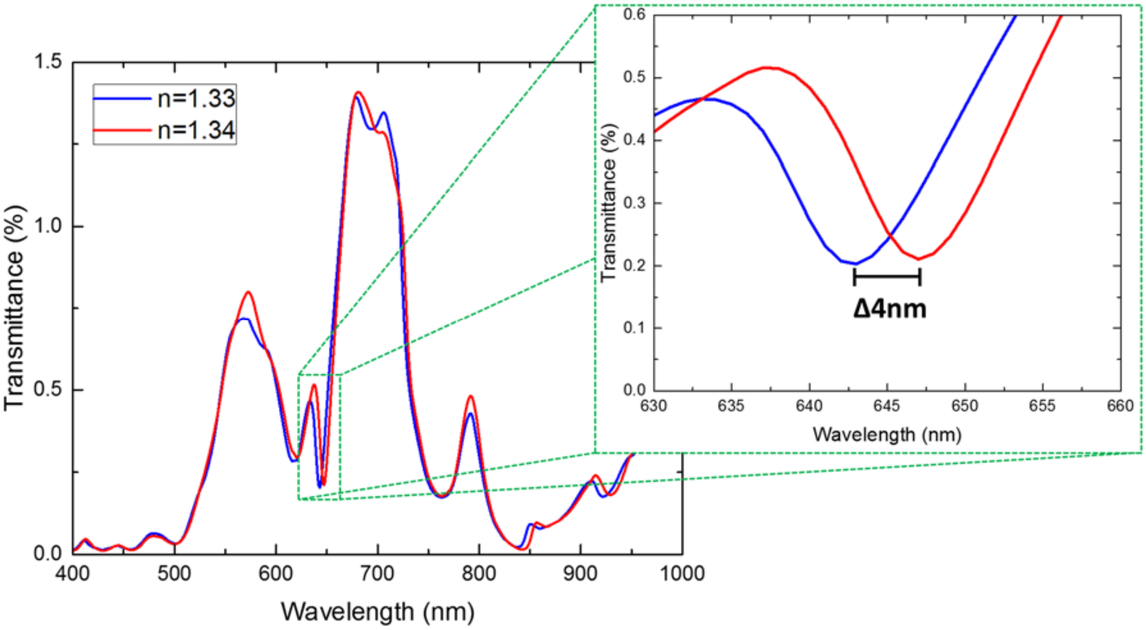

Figure 69. Simulated transmittances for change of *n*. Simulations for concentric ring nanostructure for index of refraction at structure interface of *n*=1.33 and *n*=1.34. Inset zoom showing change in wavelength minimum.

COMSOL is capable of calculating and plotting a wide variety of useful physical properties from the model's solutions. The 2D and 3D plotted results can be useful visualization for interpreting the simulated results, such as locations of maxima and minima in transmitted light. One can observed distribution of fields and other properties as a way of identifying locations of plasmonic activity, and to motivate parameters for pursuing optimal design parameters. Figure 70 below is a 3D, cross-sectional, titled view of one such simulation where the electromagnetic power-loss density is plotted for the metal region and the material domains are displayed for PMMA, ITO and glass incorporated in fabricated samples.

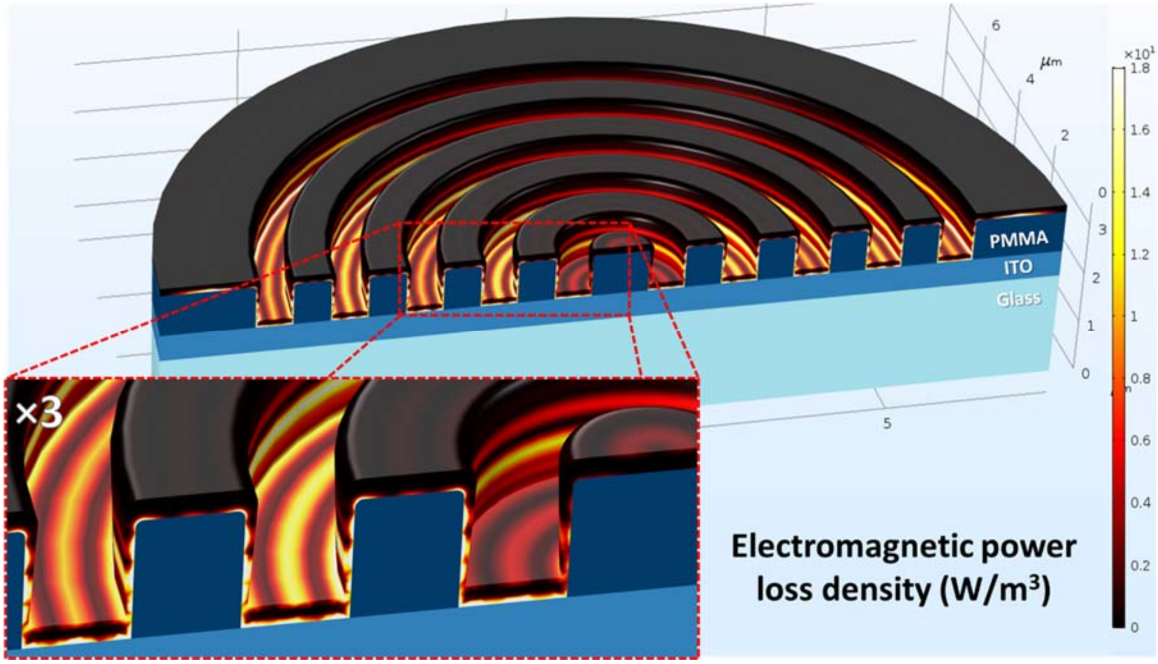

Figure 70. Simulated electromagnetic power loss density. Image showing a 3D, cross-sectional, titled view of concentric rings nanostructures with electromagnetic power-loss density plotted for the metal region and material domains. The grid is in µm, the scale is from 0 W/m^3 to 18 W/m^3, and the inset is a 3× zoom.

3.3.3 NPGS

The Nano Pattern Generation System (NPGS) is used to perform electron beam lithography (EBL) in order to produce nanostructures used in this project, excepting those few produced by photolithography as is discussed in section 3.4.3. Use of the NPGS software consists of the following three steps: 1) Design the pattern, 2) Configure the

Run File, and 3) Process the Run File. For 1), NPGS integrates the software DesignCAD into the program with writing commands and features specific to the NPGS system. Since designing patterns can take a while to make and does not require the use of the SEM, one can download the NPGS software to an external computer and write the files at an external location, thereby avoiding the cost of the cleanroom's hourly fee. One can use other CAD software to design the pattern and then translate it into DesignCAD, but there are several important details of patterns that need to be met in order to ensure that the file is processed in the same way as those written in NPGS's version of DesignCAD. See additional files for instructions on translating patterns produced in L-Edit to NPGS useable patterns.

In step 2) Configure the Run File, you specify the pattern(s) to be written and the writing parameters to use. Since detailed description of the NPGS software are provided with the NPGS user manual, I shall only point out a selection of important parameters to consider and change for producing the structures contained in this thesis. For all run files the Non-Stop Writing Mode option was changed to 'Yes'. The patterns to written were then added as entity to the run file, including appropriate positioning of each pattern if there were multiple patterns in the run file. For all patterns the dose was changed to 'area' selection such that the dose provided was in units of $\mu C/cm^2$. The dose value was then selected, with typical values ranging from 200 to 300 $\mu C/cm^2$. It is common to start a fabrication process by first performing a dose test with desired sample and pattern. This allows one to varying the dose over several steps in order to determine optimal dose for the given sample and pattern. The dose corresponds to a dwell time that is listed and the measured beam current, which is measured with the ammeter connected to the SEM and enter into the run file. When NPGS writes a pattern, it fills in the area to be written by snaking the beam location over the region to be exposed. The appropriate dose is delivered by using a beam blanker to pass the beam to the sample for a given amount of time at specific points along the snaked path and to blank the beam in between those points. The distance between those points is called the ‘Center-to-Center Distance’ in the NPGS software and needs to be specified. The distance between multiple snaked paths for a given region is called ‘Line Spacing’ in the NPGS software and also needs to be specified. Typically, the smaller these to values the more precisely a pattern can be written and so they are usually set to small distances under 10 nm. In a test to explore the effect of some of the NPGS parameters on the estimated write-time, the following was observed:

- Increasing the **Area Dose** will linearly increase the estimated write time.

- Increasing the **Measured Beam Current** will linearly decrease the estimated write time.

- Increasing the **Center-to-Center Distance** will negligibly affect the estimated write time.

- Increasing the **Line Spacing** will negligibly affect the estimated write time.

3.4 Device Process Engineering

3.4.1 Fresnel and Bullseye Structure

Concentric ring plasmonic nanostructures mentioned in section 3.1.2 gained our interest for their significant increase in plasmon-mediated transmitted light compared to that observed in traditional halo structure. Despite the traditional halo structure’s ability to modulate optical transmission through controllable structural parameters, this relatively low transmittance was problematic for obtaining good signal-to-noise measurements necessary for discerning the small changes in transmitted light that are commonly characteristic of SPR-based detection of antigen capture. The 6% maximum transmittance in the first report of the plasmonic halo without fill factor (Ye et al., 2012 Supplementary information), accounts for a 0.03% maximum transmittance without appropriate normalization to account for opaque regions within the measurement. While this normalization is the most objective way of presenting the data, as it removes arbitrary features such as the halo pitch, it introduces artificial amplification of noise by the fill factor. While transmittance varies significantly within an individual array's spectrum and between samples with different processing, the maximum transmittances of concentric ring structures investigated are approximately one to two orders of magnitude higher than the transmittances of similarly processed halo structures.

It is important to emphasize that the reason that higher transmittance is desired is *not* just for facilitating a measurement with good signal-to-noise, but rather to use a structure that is more like to be able to be used in a biosensing device. While good signal-to-noise measurements are a key to obtaining and analyzing the data for such a biosensing device, it does not mean that the sample is capable of biosensing simply because it has relatively high transmittance. As a simple example, one can note that a large transmittance can be simply achieved by making an array of large holes that simply pass the light without the necessity for any plasmonic materials or behavior whatsoever.

What we *do* want is to have a structure that has a high concentration of surface plasmon activity, and its related enhanced electric fields near the surface, such that targeted species adhering to the surface through biological capturing mechanisms will have the largest influence on the interface properties that dictate the way that the surface plasmons form resonant conditions. Furthermore, in order to be able to detect that influence of captured antigens, and therefore their presence or possibly concentration, there must be a discernable modulation to a measurable quantity of the system, in this case transmittance.

Using these aims, we can motivate structural characteristics by looking to see what features influence modulations in transmitted light, particularly those in the original halo structure. Figure 71 below (Figure S4 of supplemental material of Ye et al., 2012) shows how transmission suppression corresponds to SPP standing wave formation at the side wall of the halo structure, for resonant wavelengths 400 nm and 267 nm. Unlike the metal elsewhere in these samples, the thickness of the metal in this retrograde profile sidewall region is not opaque and is also sufficiently thin to allow the evanescent electric fields of SPP to penetrate through this sidewall. Light incident on this region can scatter into SPP at resonant conditions, thereby reducing the far-field transmission.

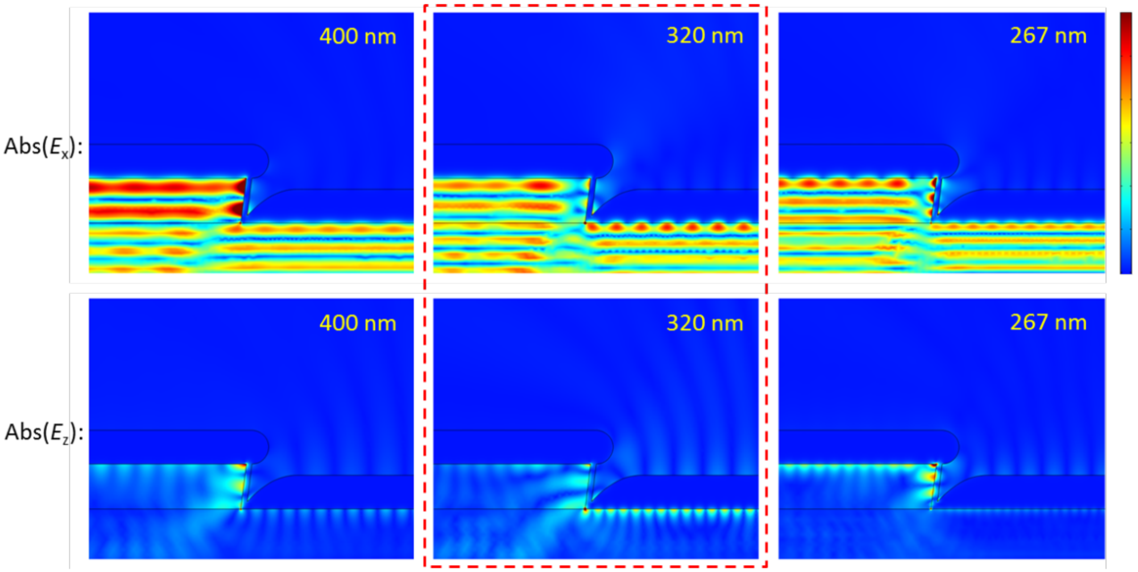

Figure 71. Simulated field profiles of halo. Plotted are the absolute values of E_z and E_x at a Ag/PMMA interface for SPP wavelengths on (267 and 400 nm) and off (320 nm) resonance. On resonance, SPP standing waves form at the side wall, leading to transmission suppression. On the contrary, no standing wave forms off resonance, yielding higher transmission (brighter vertical white lines). The linear color scale ranges from 0 to 3 V/m. Trench size corresponds to circular structure with radius of 1.6 µm. (Figure S4 of supplemental material of Ye et al., 2012)

Similar to the thickness of the planar samples used in the BioNavis system, the thickness of the metal in this sidewall region of the halo structure is large enough to contribute a sufficient amount of electrons to the SPP, though small enough such that the penetration depth of the surface plasmon encompasses the entire film thickness, ideally around 50nm. The central influence of this sidewall region is not a surprise when one remembers that the SPP modulated far-field light emanates from the eponymous halo-shaped region where this sidewall is located on the plasmonic halo. Plainly, if we want more SPP modulated far-field light then we need more sidewall.

The initial investigation of concentric ring structures was motivated by this same idea of improving upon the effect observed in the halo structure by creating a similar structure that invoked the aspects of halo that matter the most. The combination of regions with relatively thin sidewall and structural characteristics that impose boundary conditions on SPP formation exists at multiple regions in the concentric ring structure compared with the one perimeter region of the halo. The concentric ring structure first investigate was a Fresnel pattern, later followed a bullseye pattern, as shown in Figure 72. below for two patterns with similar diameter. There, the regions containing the blue would be the regions that would be exposed to the electron beam and therefore, the regions that the electron beam resist PMMA was removed from during subsequent development.

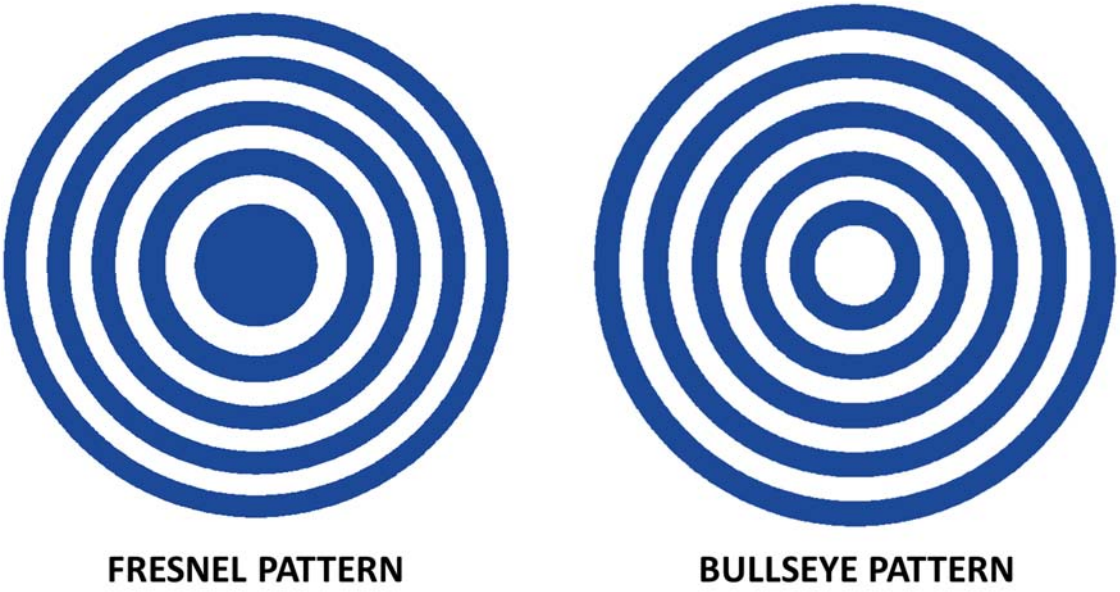

Figure 72. Schematic of concentric ring structures. Shown are two investigated for incorporation in plasmonic biosensing device; both patterns written in NPGS link of DesignCAD using the *Circle Array* option. The Fresnel pattern was written with wavelength of 500 nm, focal length of 1 µm, and 5 zones. The bullseye pattern was written with linewidth of 300nm, inner diameter of 1.3 µm, pitch of 600 nm, and 5 circles.

The bullseye structure ended up being the concentric ring pattern that we primarily investigated for a few reasons; the values of the patterns’ sizing could be specified directly rather than determining them through measurement or calculation using the focal distance, the gap size and pitch could be separately specified, the gap size is constant for different radii rings, and the central region could be patterned without a trench as it was found that the transmitted colors of this region would be different from the outer rings. Figure 73 below shows a schematic of the steps of the fabrication process for the bullseye structure, outlined further in section 3.4.3.

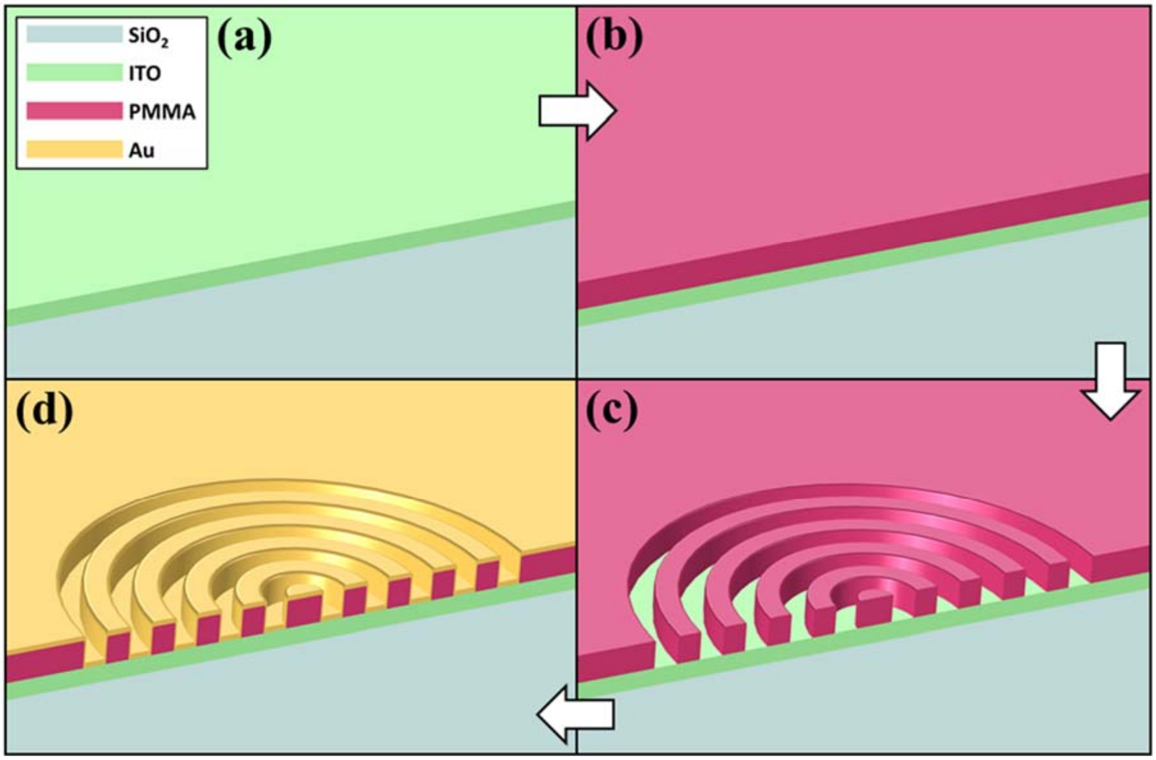

Figure 73. Schematic of bullseye structure. Tilted, cross-sectional view of fabrication steps. (a) ITO glass substrate, (b) spin coated PMMA, (c) EBL pattern post-development and (d) post-PVD of Au. See section 3.4.3 for details of fabrication.

An example bullseye sample produced is shown in Figure 74 below as a tilted, cross-sectional SEM. This cross-section was made using a focused ion beam (FIB) on the JEOL JIB-4500. It was observed that making FIB cuts on the highest beam current setting gave the cleanest cross-section and minimized gallium deposition from the ion beam.

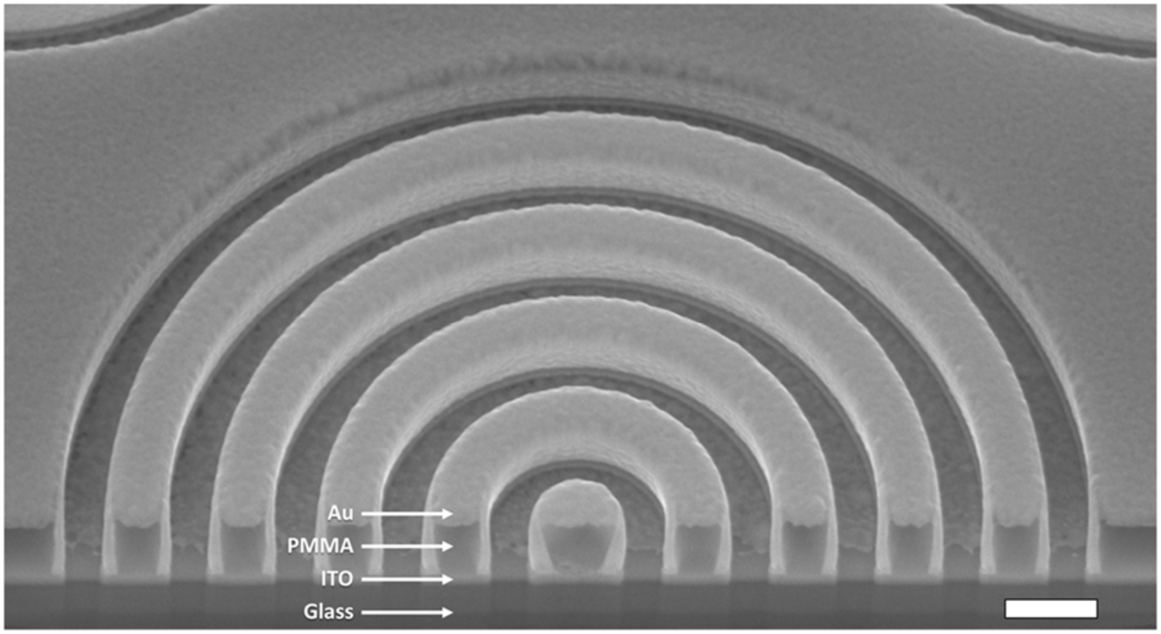

Figure 74. Cross-sectional SEM of bullseye. 30° tilted view of concentric ring trenches of the bullseye structure with cross-section made by FIB. Scale bar is 1 μm.

As discussed in section 3.2.2, measurements of transmitted light were then made through an array of bullseyes. Again, the path of transmittance being from the bottom, through the glass-ITO substrate, then through the PMMA, then through the metal, then to the camera or spectrometer. Modulation of transmitted light similar to that observed in the halo is observed for concentric ring structures and the modulation is also dependent on structural parameters as is discussed further in section 3.4.4 and shown in Figure 75 below. There an image of bullseye structures with a range of gap sizes are shown with white light incident from the bottom side of the sample. The bullseyes range from 300 nm gap size on the leftmost to 1 μm for the rightmost, increasing at 25 nm intervals. Each member of a given column have the same gap size, also showing the resilience of the apparent transmitted color to fluctuations in nanoscopic structural features, such as metal film roughness.

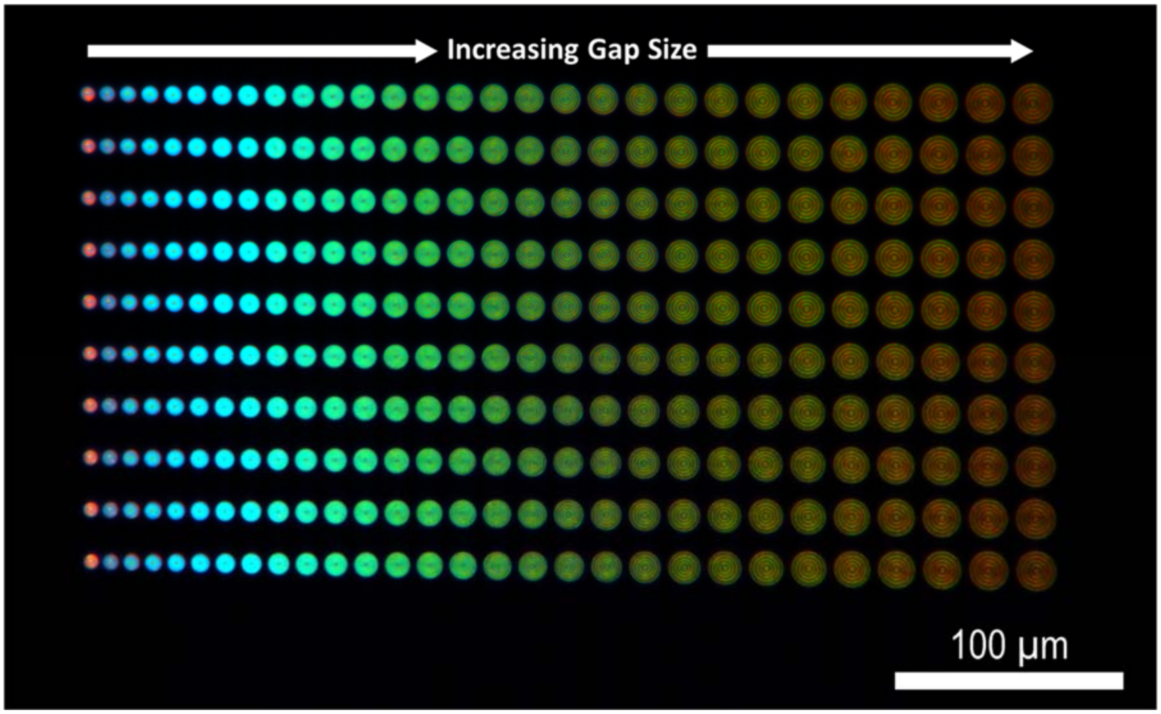

Figure 75. Transmitted light through bullseye sweep. Shown is bottom side incident white light through an array of Ag bullseye structures with varying gap sizes, ranging from 300 nm to 1 μm from left to right. The image was taken with an 8.61 ms integration time with 50× zoom, 0.85NA objective lens and 0.90NA condenser lens on the Leica DM6000M microscope.

3.4.2 Materials Problems and Solutions

The way that light will scatter into surface plasmons is dependent on the intertwined properties of both the structure and the materials. Furthermore, even if the combination light, material and structural conditions facilitate the coupling light into the surface plasmons, high absorption for certain wavelengths within the material may appreciably diminish the usefulness of the transmittance at those wavelengths. In addition to solid state material considerations, the desire to extend plasmonic nanostructures in our research to applications in biosensing means that biological and chemical considerations of the materials being used are often necessary. In particularly, since the metal in ours and most structures is the topmost material, its properties are the often the most important for consideration. As a brief list, a metal to be used in plasmonic-based biosensing device should have the following properties:

i) Have low absorption for the wavelengths being investigated.
ii) Be chemically robust to the physiological solutions involved.
iii) Be capable of biofunctionalization schemes needed to capture target species.

There are a few material-specific scattering mechanisms that dictate how a given metal will absorb light. Figure 76 below shows a schematic of a simplified energy band diagram for a noble metal, commonly used in this research and many other plasmonic devices (Khurgin et al., 2012). For our research, we are most concerned about interband transitions and how they will affect our choice of material. Particularly, when the energy of incident light becomes higher than energy difference between top of the d band and the fermi level, $\hbar\omega_B$ in the diagram, then transitions from the d-band to the hybridized-sp band become can occur. The spontaneous emission of the transitioned electrons leaves a large signature in the transmittance spectra at the wavelength corresponding to this difference in energy level.

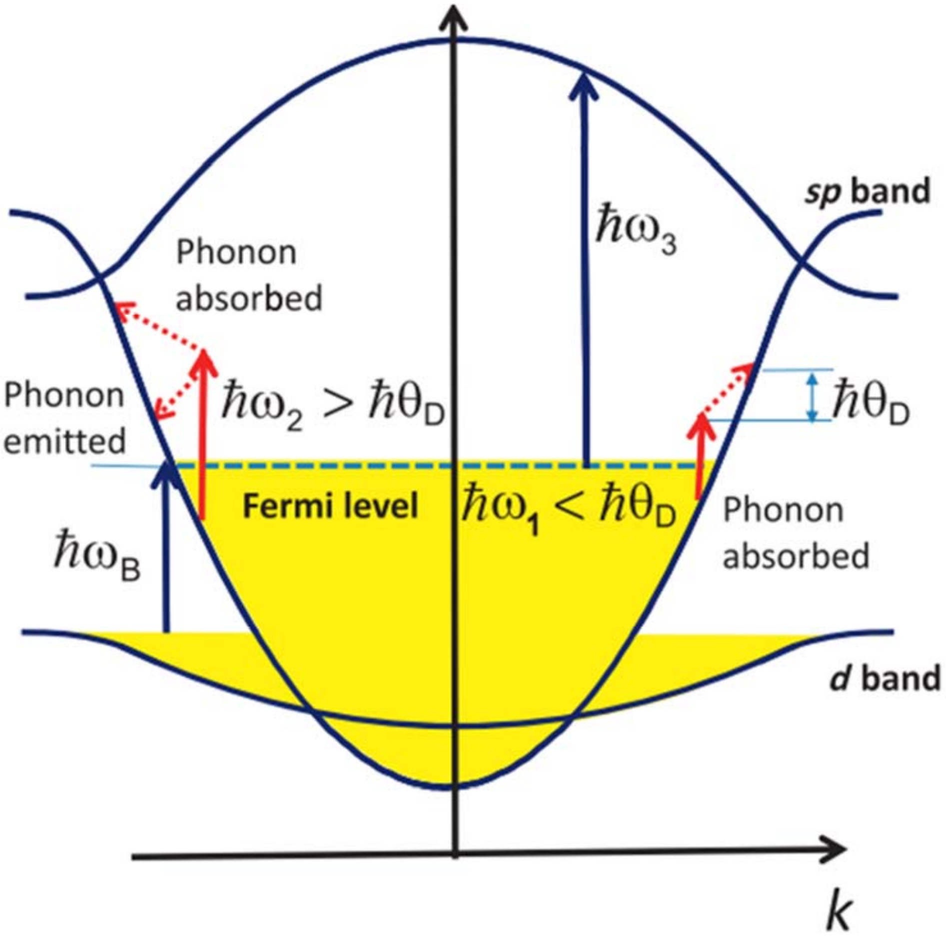

Figure 76. Simplified energy band diagram of a noble metal. Filled energy states are shown in yellow, with intraband free carrier absorption (red arrows) and interband absorption (blue arrows). On the right side, absorption of a low energy photon requires simultaneous absorption of a phonon. On the left side, absorption of higher energy photon can be accompanied by either absorption or emission of a phonon. k, wavevector; ħ, reduced Planck's constant; ω, frequency; ω_B, frequency at the interband absorption edge; ω_1, ω_2, ω_3, increasing values of the frequency; and θ_D, Debye frequency. Adapted from Khurgin et al., 2012.

For gold, the difference in energies for d-band transitions are they are near 2.3eV, 539nm, or 556THz (Saeger et al., 1977). Gold is commonly used is biosensing devices for it's high chemical stability and well-established biofunctionalization protocols. Many gold-based plasmonic biosensing devices have demonstrated success in the longer wavelengths of visible and infrared regions of the spectrum, without encountering the problem of the d-band transitions that occur at smaller wavelengths (Akter et al., 2019; Toma et al., 2014). Since an appreciable amount d-band transitions do not occur in silver until UV wavelengths, it is a commonly used metal for plasmonic applications covering the entire visible spectrum, including in the original halo works. The main problem with using Ag in a biosensing device is that common physiological solutions used in biofunctionalization and bioassays chemically react with the Ag film. This chemical deterioration causes changes in the physical properties, such as its transmittance such as is shown in Figure 77 below.

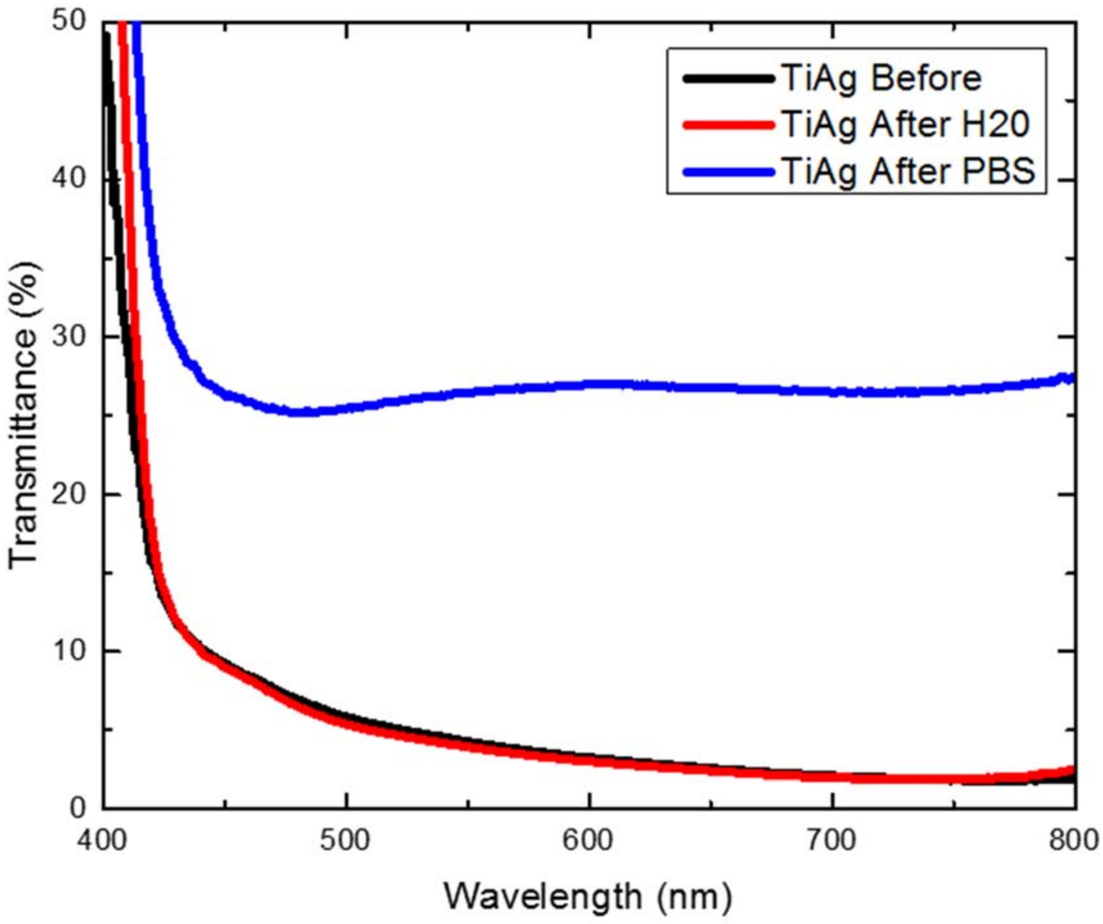

Figure 77. Ag thin film transmittances change. Measured for thin film of TiAg with constituent thicknesses of 3 nm and 47 nm, respectively. Plotted are the changes in transmittances after 4 h in DI-H_2O and PBS

Plotted there are the measured transmittances for thin films (~ 47 nm) of Ag with a small (~3 nm) Ti adhesion layer before and after immersion in deionized-H_2O and phosphate-buffered saline for 4 h. Note the nearly overlapping transmittance spectra of the before and after DI-H_2O case while there is a significant change due to immersion in the PBS. Unsurprisingly, the PBS causes visual and measurable change in the transmitted light through Ag-based nanostructures, as do similar solutions needed for implementing biological capturing assays. Figure 78 below shows images and spectra of an example concentric ring structure explored in the project before and after immersion in PBS for 50 minutes.

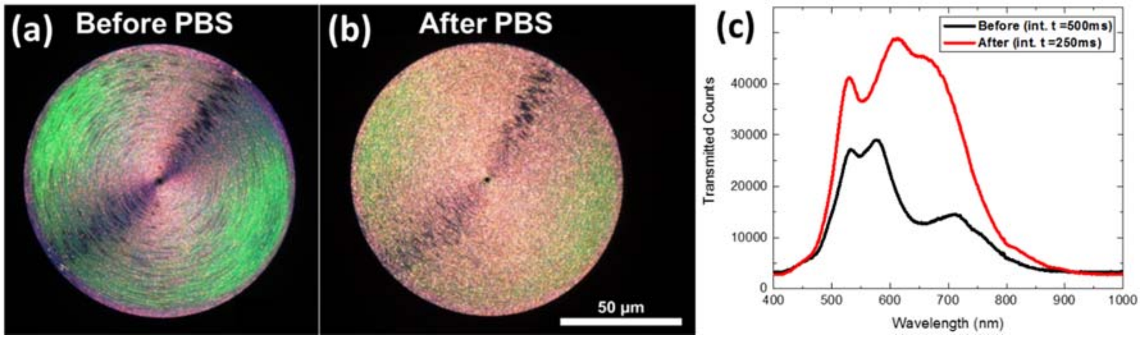

Figure 78. Ag nanostructure transmittances change. Ag-coated concentric ring nanostructure (early iteration with 100 rings) change due to immersion in PBS for 50 min. Transmitted light from incident white light (a) before PBS immersion with camera integration time 216 ms and (b) after PBS immersion with camera integration time 126ms. (c) Transmitted counts before and after PBS applications, note the difference in the spectrometer integration times used.

It is important to note that the integration times used for the spectra measurements for the sample before and after were different, at 500 ms and 250 ms, respectively. Even so, the transmitted counts of the post-PBS spectrum are larger despite the shorter integration time. Also, the peaks from the spectrum afterward are noticeably broader than the spectra before exposure to PBS (the source was the same for both measurements.) This can be qualitatively observed in the optical images having less pronounced colors after the exposure compared with before. This broadening of the peaks in addition to the increase in transmittance (including the factor of 2 from integration time) is indicative of the increased leaking of light through the sample as opposed to enhanced plasmonic activity. This is a confirmation that the PBS is destructive to the surface features and the plasmonic activity critical to the functioning of the device. While the metal should entirely cover the PMMA film, damage to this underlying resist was considered as a possible source of structural deterioration. To investigate this PMMA films prepared in the same way as samples were immersed in PBS and HCl solutions for 24 h. Before and after imaging and transmittance measurements through the PMMA films confirmed that there was no noticeable effect on this material due to immersion.

To address issues specific to either Ag or Au, previous works have investigated alloys or bimetallic layers of Ag and Au to overcome these noble metal limitations for plasmonic applications (Gong et al., 2016; Chen et al., 2011; Zynio at al., 2002). We investigated the ability of a thin (~8 nm) layer of Au deposited on top of thicker (~50 nm) to protect the surface for chemical deterioration from PBS immersion. Figure 79 shows four images of different combinations of material and solutions they were immersed in for a period of 4 h. It is qualitatively apparent that there is deterioration of the TiAg film in PBS, as discussed above and seen in Figure 79b. The deposition of a thin 8 nm film of Au above the Ag is able to prevent noticeable deterioration of the Ag film, maintaining the sample's mirror-like appearance.

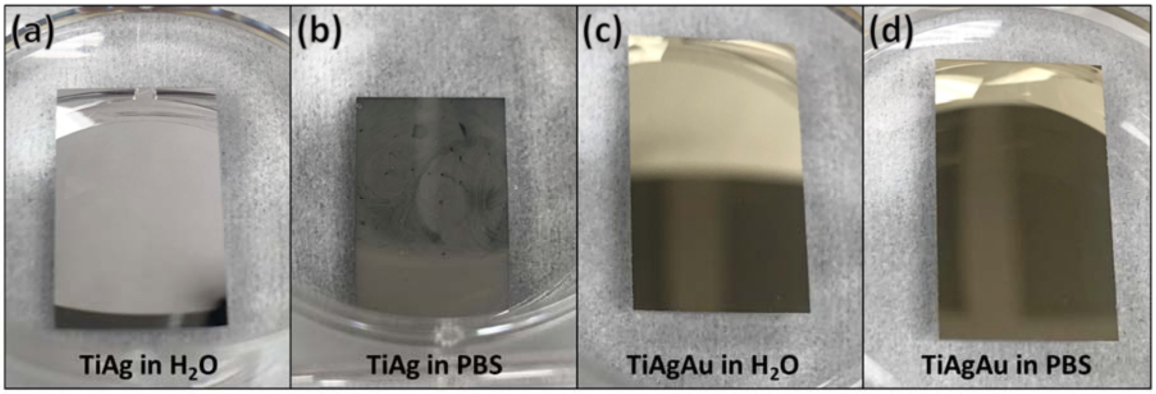

Figure 79. Metal thin films in PBS. Images of (a) TiAg after 4 h in DI-H_2O, (b) TiAg after 4 h in PBS, (c) TiAgAu after 4 h in DI-H_2O, and (d) TiAgAu after 4 h in PBS. Tarnishing only observable in sample (b). The corresponding thickness of Ti, Ag, and Au are 3 nm, 47 nm, and 8 nm, respectively.

Similar to Figure 77 above, Figure 80 below shows the measured transmittance of these bimetallic TiAgAu films for the three different cases i) after metal deposition, ii) after 4 h immersion in DI-H_2O and iii) after 4 h immersion in PBS.

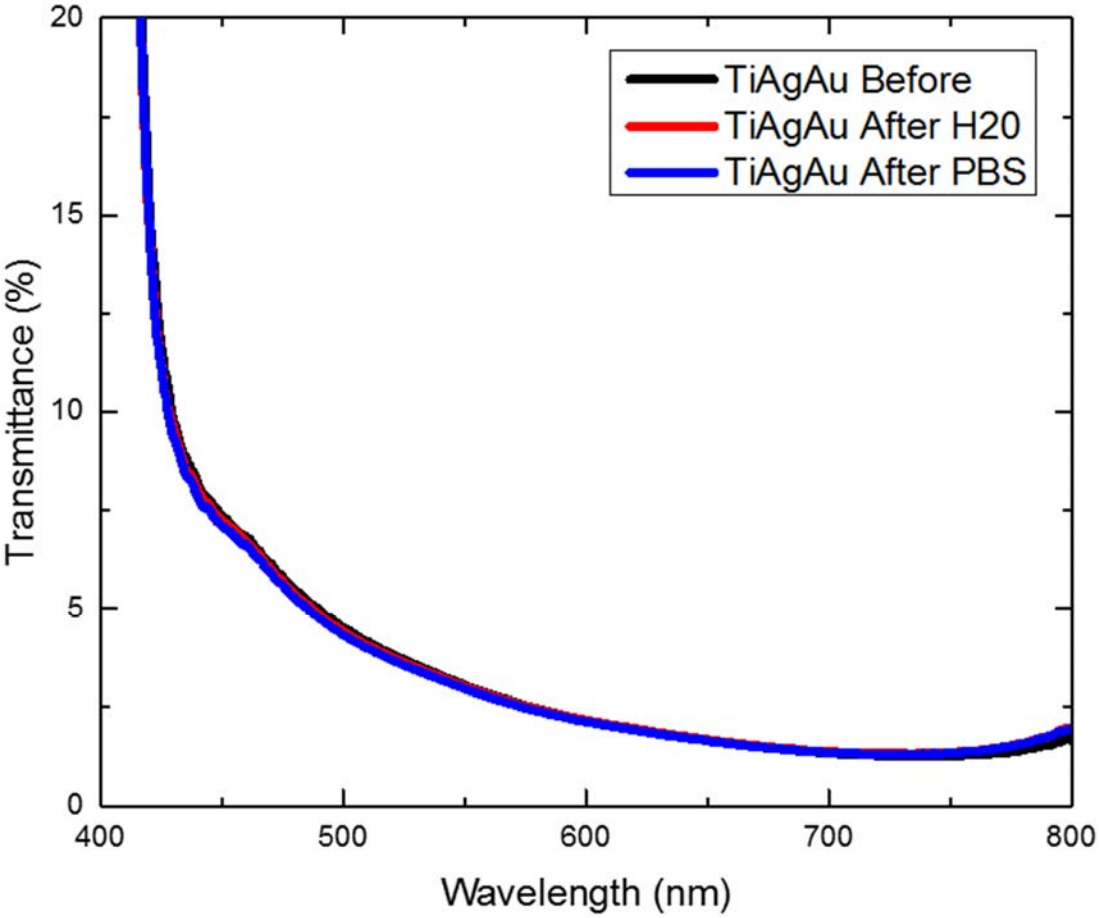

Figure 80. AgAu thin film transmittances change. Measured transmittances through a thin film of TiAgAu with constituent thicknesses of 3 nm, 47 nm, and 8 nm respectively. Plotted are the changes in transmittances after 4 h in DI-H_2O and PBS. The closely overlapping transmittances indicates a very small change between samples.

The thin Au layer was successful at chemically protecting the Ag films and represents an attractive option for many potential applications in plasmonic-based biosensing devices. This protective property was also tested for thin Pt layers deposited on top of Ag and the results show that Pt performs equally well at protecting the Ag metal.

Despite the fact that TiAgAu samples only have a proportionally small layer of Au at the surface, the samples still show significant visual and spectral presence of d-band transitions in the Au regions. While such a thin layer of Au is not an optimal thickness for supporting surface plasmon resonances, as explain in section 3.2.1, being adjacent to the thicker Ag layer underneath yields a sample that has substantial scattering of incident white light into plasmons that are dominated by the Ag material but have electric fields that are still the largest at the Au/dielectric interface. At least for this set of parameters, the problem of high d-band transitions persists and may possibly be comparably larger than that observed in pure Au films. Figure 81 below shows transmitted light from bottom side incident white light through arrays of TiAgAu bullseye structures with varying gap sizes between separate arrays. Qualitatively, the image is dominated by the green light characteristic of d-band transitions in gold, compared with a broad color range shown in the all Ag bullseye structures from Figure 75 and again, which even appears to be less pronounced in the all Au structures in Figure 71 later discussed in section 3.4.5.

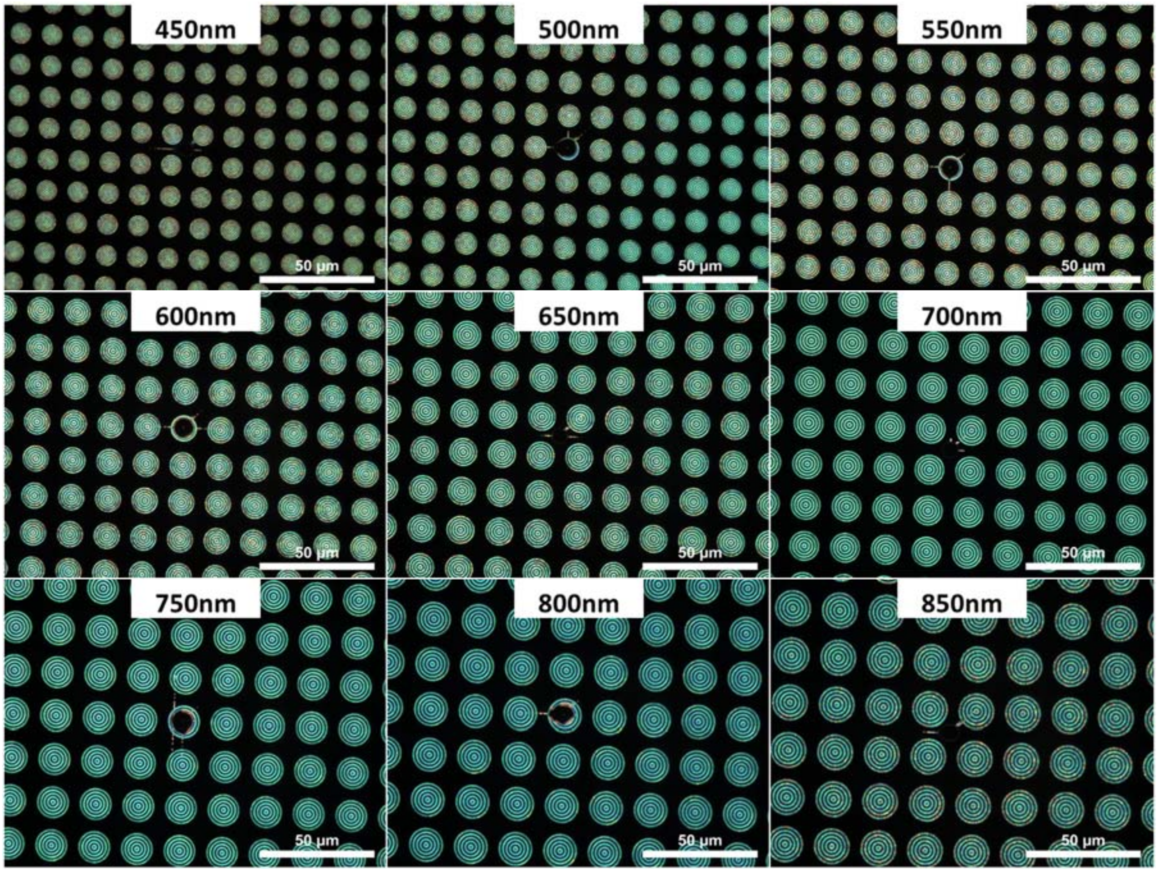

Figure 81. AgAu transmitted light images. Transmitted light from bottom side incident white light for arrays of bullseye structure of varying gap sizes and TiAgAu metallic layer.

The measured transmittances of these nine regions are shown in Figure 82 below. The dominant peak near 550 nm of the d-band transitions in Au are several times larger than others features in transmittance above 700 nm. This is one of the driving reasons why this spectral signature of the d-band transitions limits the applicability of the Au-based samples. Specifically, this dominant peak causes the following 2 problems: 1) the peak dominates transmittance for wavelengths spanning from 450 nm to 650 nm, thereby greatly diminishing the ability to resolves spectral feature in the region and 2) the integration time of the spectrometer is relatively reduced to prevent saturation of measured counts at these wavelengths, thereby lower the signal-to-noise for other regions, as can been seen by the relatively noisy transmittance data above 800 nm.

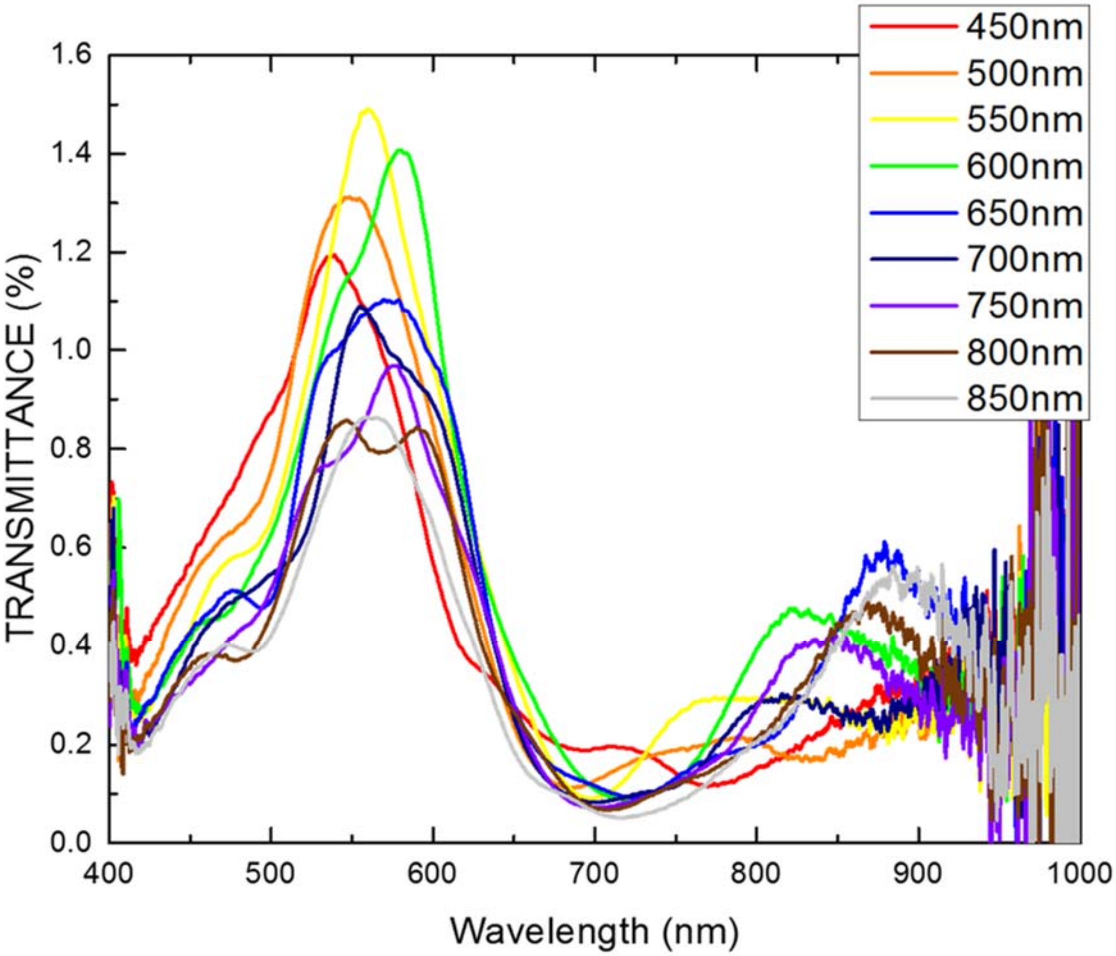

Figure 82. AgAu bullseyes transmittance spectra. Measured transmittances corresponding to the images in Figure 81. The gap size in constant within each array of bullseyes and varies between the different arrays, from 450 nm to 850 nm.

It is plausible that the problem discussed above could be greatly mitigated through a suitable combination of parameterizing the metal thicknesses, optical filtering, data processing and different equipment selection. Further investigation of these details is necessary to test the viability of bimetallic layers of Ag-Au and Ag-Pt.

In addition to protecting Ag plasmonic layers with chemically inert noble metals, there have been previous investigations of protecting Ag with nonmetallic layers, *e.g.* with a self-assembled monolayer (SAM), Si-C alloys, and other dielectrics (Wang et al., 2017; Touahir et al., 2010; Manesse et al., 2009; Szunerits et al., 2008). We found that deposition of a thin (~5 nm) layer of Al_2O_3 chemically protects the Ag film over several days of immersion in PBS. The foremost limitation of investigation of Al_2O_3 or other thin oxide layers on top of silver is that these materials require a different biofunctionalization protocol than Au or Ag and the adaption of reported protocols, commonly involving silane, has yet to be realized in this research. Also, surface modification by a SAM warrants investigation. Furthermore, any applied dielectric material on the topmost surface of the Ag needs to be thin (<10 nm) to ensure that captured biological species are still brought in close proximity to the evanescent electric fields of surface plasmons in order to have a measurable effect of the plasmon-mediated changes in transmittance.

Fortuitously, the first step in biofunctionalization needed for antigen capture, as described in section 3.5.3, can be used to significantly reduce degradation of the Ag surface. For Ag this first species is thiol-conjugated streptavidin (SA-thiol), which forms a bond to the Ag surface that is later used to attach antibodies that are specific to detecting targeted antigens. We used the BioNavis SPR system (Figure 40) to measure the change of SPR-mediate reflected intensity, see Figure 83. Recall that the minimum intensity corresponds to the angle where the in-plane component of the incident lights wavevector matches the SP wavevector at that frequency.

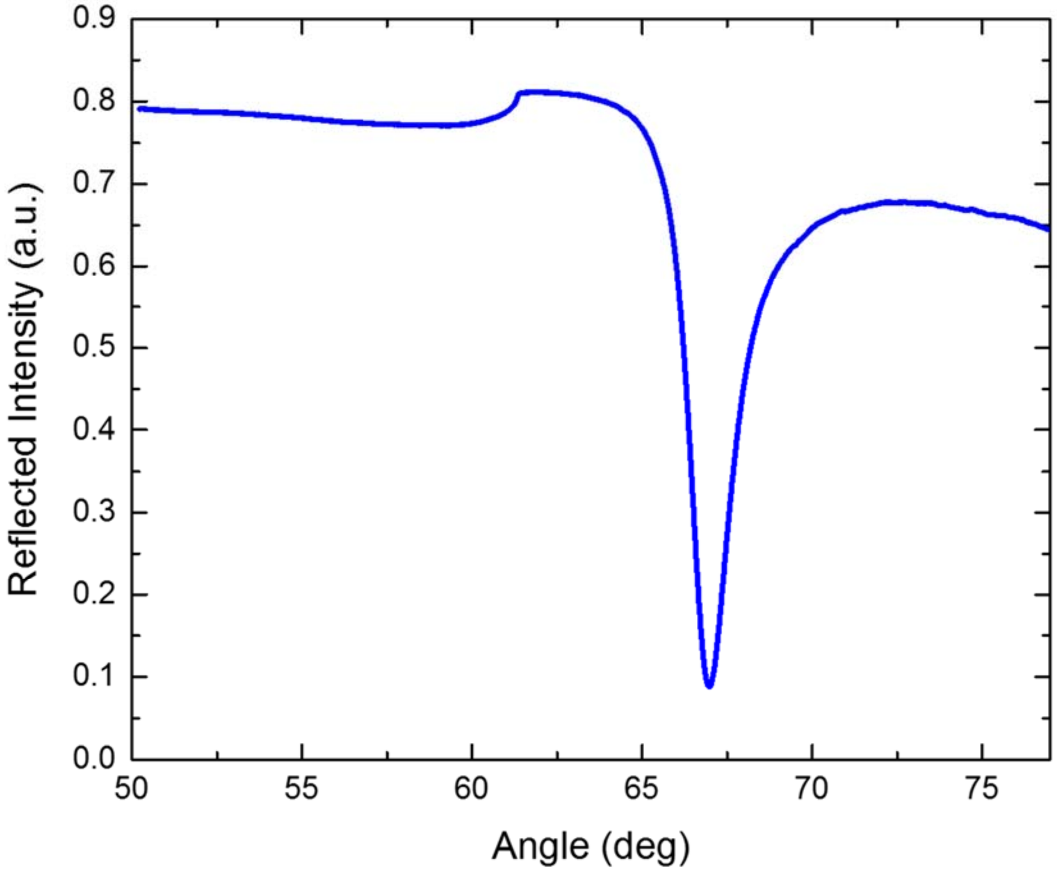

Figure 83. Reflected intensity vs. angle. Plot for Ag-coated glass in BioNavis SPR system.

Uniform planar films will have nice narrow-width dips as shown because the *Δk* will come mostly from the light and not from roughness or structures in the material, similar to that found in plasmonic gratings. As the film deteriorates the roughness of the film will increase and the width of the dip will broaden. In Figure 84 below, the change in the width of dip vs. time is plotted for a bare Ag sample and a sample functionalized with SA-thiol. While both samples experience peak broadening, the sample with SA-thiol bound to its surface experiences less broaden as a result of the partially protected Ag. This Ag protection is visually prominent in planar samples for time scale larger than 1 h.

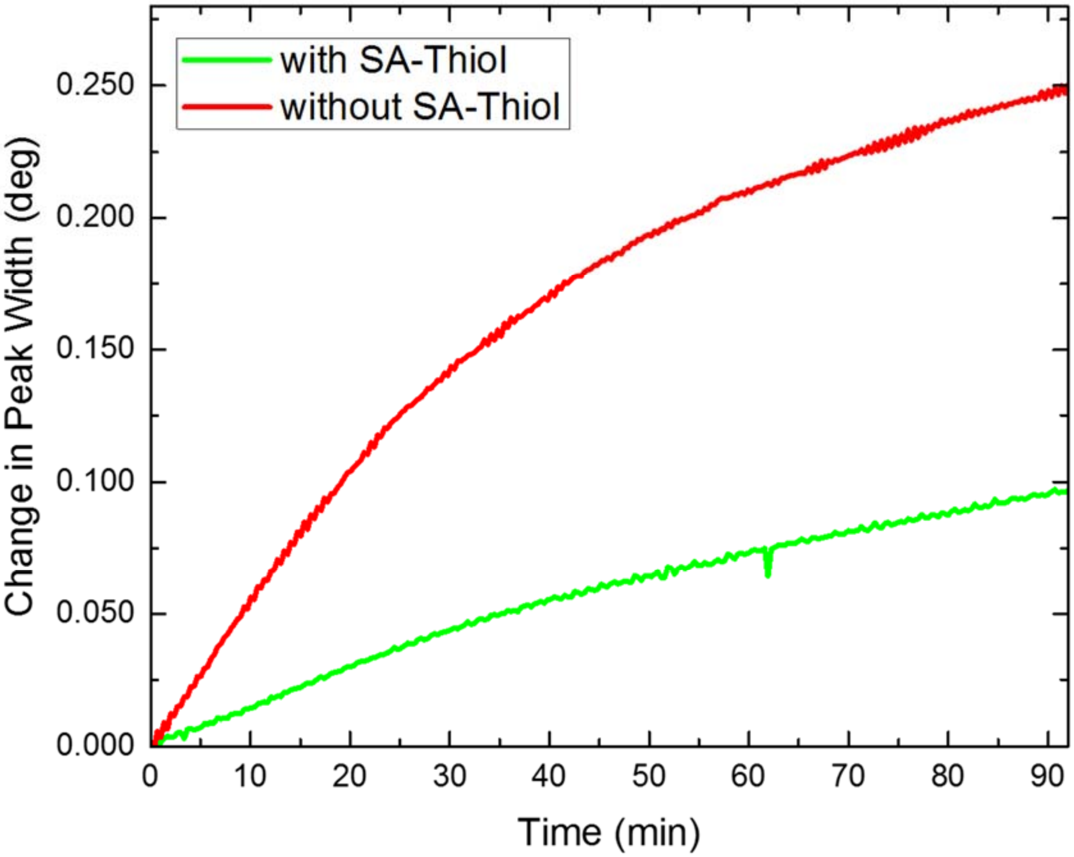

Figure 84. SA-thiol blocked Ag change. Change in SPR peak width at half max vs. time due to prolonged exposure to PBS for a sample with (green) and without (red) prior functionalization with SA-thiol.

Reduction and prevention of Ag degradation is also possible through protein adsorption during application of solutions. This has been previously observed in protein-mediated stabilization of nanostructured Ag films (Drachev et al., 2005). In that work they used x-ray diffraction to confirm that the Ag metal reacts with chlorine ions in buffer solution form AgCl crystals on the substrate surface. They also showed that the stabilization of the silver films was linearly dependent on the protein concentration. It is well known that the presence of proteins is characteristic of the physiological solutions, *e.g.* blood or urine, that are the final targeted sample used for many biosensing applications. The ability to prevent Ag deterioration through protecting with inherently present proteins was tested by immersing Ag coated glass samples in human urine for 24 h. There was no noticeable difference in the mirror-like reflectivity of the Ag films by visual inspection. The molarity of salts in urine and other real physiological solutions can vary considerable depending on outside factors such as hydration, though they are comparable to the PBS molarity on average. Further investigation, including before and after SEM inspection of Ag nanostructure, is needed to evaluate the viability of protein presence as a Ag stabilizing protocol and ultimately answer whether our bioassays and proxy physiological solutions appropriately represent our target sample and application.

Aluminum metallic layers were also briefly investigated and represent an attractive option with the potential for chemically stable use over optical wavelengths. Previous works have demonstrated aluminum attractive plasmonic properties (Gérard et al., 2015; Martin et al., 2014) and use in biosensing (Lee et al., 2017). Figure 85 below shows images and corresponding bullseye arrays with Al as the metallic layer.

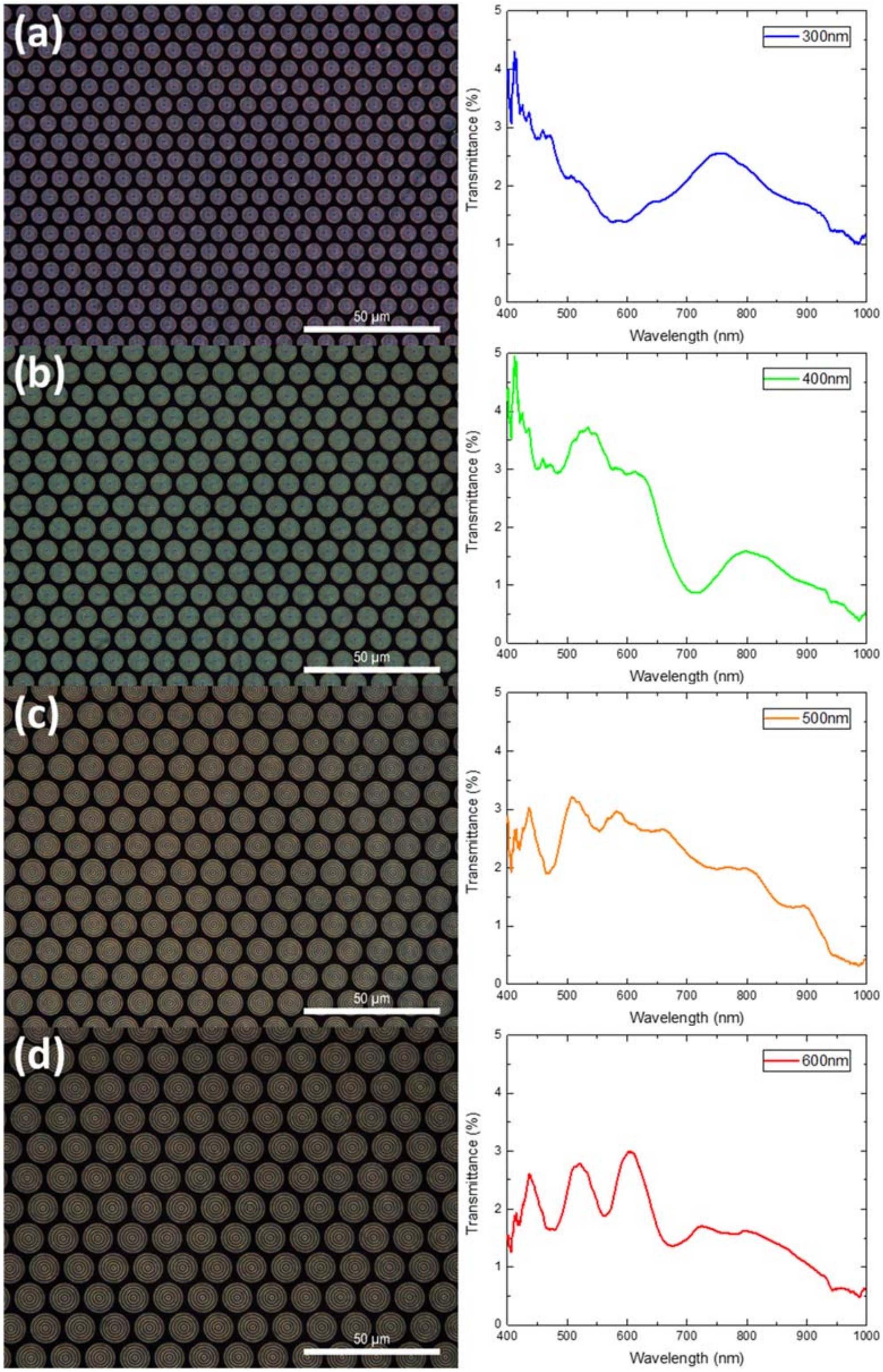

Figure 85. Al transmittance images and spectra. Images of transmitted light from bottom side incident white light through bullseye arrays (left) and their spectra (right) for gap sizes (a) 300 nm, (b) 400 nm, (c) 500 nm, and (d) 600 nm.

In particular, Al has attractive potential for is ability to support surface plasmons in the UV, thereby facilitating good overlap with excitation spectra of quantum dots, discussed in section 3.6.2. There remains the need to adapt a functionalization protocol of the aluminum surface in order to facilitate biofunctionalization. This presents and extra difficultly because the BioNavis system is not set up to couple to surface plasmons in aluminum, while both Au and Ag work in the system due to their similar plasma frequencies. Since aluminum with have a native oxide of Al_2O_3, an attractive option for adapting biofunctionalization protocol would be to use Au samples with a thin (~5 nm) layer of Al_2O_3 on top. Scattering to d-band transitions also need be considered for aluminum, which occur in the optical range around 850 nm. If there problems can be addressed for alumina, it's incorporation may enable biosensing capability and warrants further investigation.

3.4.3 Fabrication

A schematic of a bullseye fabrication process is shown in Figure 73 from section 3.4.1. Further modification and parameterization of the current fabrication processes can plausibly enable properties within samples that will be advantageous for pursuit of a bullseye-based plasmonic biosensing device. For this reason, rather than presenting a detailed procedure like section 2.2.1, I will instead use this section to discuss some of the current processes and some main changes that have been considered. When appropriate, I will discuss the motivations and options for different steps.

To start, I will describe the fabrication of samples by electron beam lithography in the Boston College Integrated Sciences Cleanroom and Nanofabrication Facility. Substrates used were ITO coated boroaluminosilicate glass (Delta Technologies, Loveland, CO). Samples currently used are item CB-40IN-0107 with sheet resistance 4-10 Ω/sq, nominal transmittance >82%, nominal ITO thickness 150–200 nm, 25 mm -square and thickness 0.7 mm. Thicker samples are available at 1.1 mm and were previously used though currently do not facilitate the focal plane of the condenser lens the to reach to top surface of the sample. Thinner ITO layers are available, down to 15–30 nm, having slightly larger nominal transmittance at 88%, though appreciable larger sheet resistance at 70–100 Ω/sq. The larger transmittance, depending are its spectral features, may be beneficial for coupling light into the sample. The higher resistance could allow chare accumulation during electron beam writing, thereby reducing writing resolution. Since plasmonic properties have been reported for ITO materials and structures (Wang et al., 2017; Franzen et al., 2009), investigation of other substrates or charge mitigation techniques may be desirable. Once a substrate is chosen the samples are cleaned, typically by sonication in acetone followed immediately subsequent rinsing in isopropanol, then DI water and thoroughly dried with N_2 gas. The samples are heating at 180° C to desiccate any surface moisture. The samples are then exposed to an oxygen plasma in a PVA TePla PS210 Plasma Barrel Etcher (Figure 12) for 1 min at power of 550W, pressure of 270 mTorr, and O_2 flowrate of 10 sccm. This plasma exposure is used to eliminate remaining organic contaminants and to promote adhesion of the following electron beam resist. Next a small amount (~ 1 ml) of PMMA is applied to the surface of the sample and is spin-coated to achieve the desired thickness and then soft-baked at 180° C for 5min. The thickness of the spin-coated PMMA film is primarily determined by the top spin speed and the type of PMMA applied. The explored PMMAs 495-A8 and 950-A9 have approximately thicknesses of 500 nm and 1 μm, respectively, when spun at 4,000 RPM. Since the PMMA remains as part of the final structure, this thickness is of crucial importance. A list of the most important consideration for PMMA relative thickness are as follows:

i) Thicker PMMA will require larger exposure doses during EBL.
ii) Thicker PMMA typically cannot achieve as small size in-plane resolution.
iii) Thicker PMMA can achieve higher aspect ratio structures.
iv) Thicker films will have a more pronounced retrograde profile.
v) Thicker PMMA cannot achieve as small of pitches, depending on beam voltage.

Regarding i), larger exposure dose will typically not considerably affect the writing process or capabilities. When Developing a new process, it is always ideal to start with an exposure dose test, where the same pattern is exposure on a given sample for a range of dosage. Subsequent imaging by SEM can show which dosage is best for that structure. Ideal dosages are not linearly proportional to the PMMA thickness, with 500 nm and 1 μm thick layer having ideal dosages of approximately 250 $\mu C/cm^2$ and 300 $\mu C/cm^2$, respectively. Regarding ii), it is my experience that thinner resists films are typically capable of achieving similar though slightly smaller sizes, though again not proportional to the ratio thicknesses. Regarding iii), since the achievable resolution for different thickness is somewhat similar and the thickness vary substantially, the aspect-ratios achievable for thicker films will be larger. The aspect ratio is important for creating structures that have more volume closer to the surfaces and within gap regions where electric field modes and enhancement can occur. Regarding iv), the retrograde profile that occurs in PMMA is due to scattering of electrons as they penetrate the film. Figure 86 below shows simulated scattering of electrons through PMMA on a Si substrate (Kyser et al., 1975) for two different acceleration voltages. While not explored in this work, it is worth noting that discontinuously retrograde profiles can be achieve by bi-layer processes using multiple PMMA layers with different molecular weights.

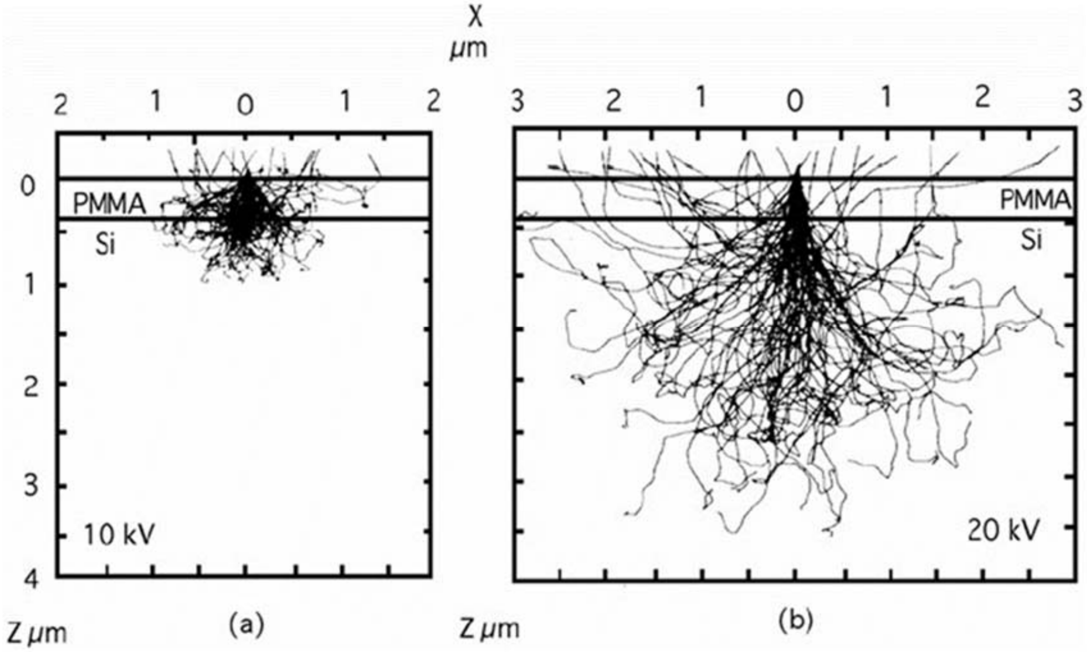

Figure 86. Electron scattering in PMMA. Monte Carlo simulation of electron scattering in PMMA on a silicon substrate at a) 10 kV and b) 20 kV (Kyser and Viswanathan, 1975

As the beam passes through the PMMA this scattering broadens the beam and therefore the volume exposed closer to the surface. A schematic cross-section of the resulting retrograde profile for two nearby trenches is shown in Figure 87 below. Notice that the retrograde profile will cause adjacent patterning to become undercut completely for certain combinations of parameters and will reduce the achievable pitch as is v). Geometrically, for a film thickness *th*, gap size *gs*, retrograde angle θ, the smallest pitch *p* possible before undercutting is experienced is $2 \cdot \tan(\theta) + gs$, though in practice the pitch needs to be somewhat larger as very small finite resists width will still break away from the substrate.

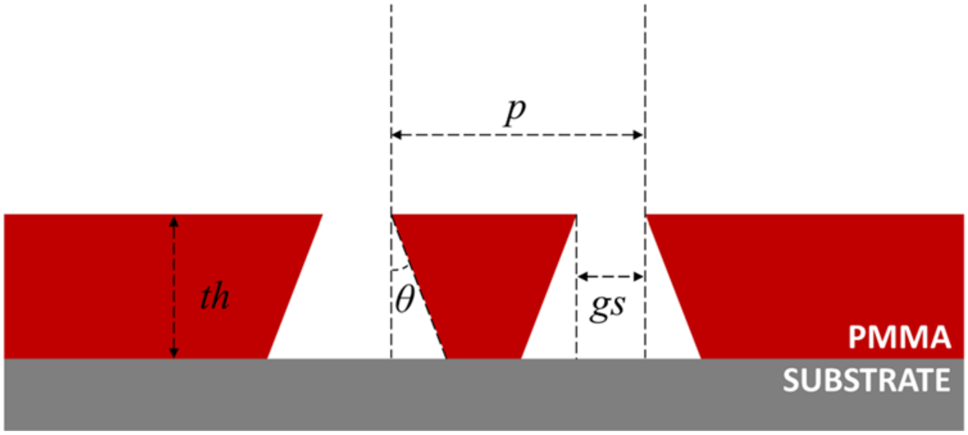

Figure 87. Schematic retrograde resist. Cross-section of two nearby trenches with retrograde profiles in PMMA. The substrate is in gray and PMMA is in red. *p*: pitch, *gs*: gap size, *th*: thickness of PMMA, θ: angle of retrograde profile.

The retrograde angle will increase for decreasing acceleration voltage and can be attractive parameter to considering for influencing future deposition characteristics, as will be discussed with the deposition step. The angle reported for the PMMA in the original halo work was 8°. The undercutting discussed above can be seen in Figure 88 SEM. Shown is an example bullseye structure from a parametric sweep test and with a relatively lower accelerating voltage of 20kV, compared with the typical 30kV used. During development most undercut structures wash away, either entering the developer solution or landing elsewhere on the surface. Coincidently, the four rings that were between the five lines written dislodged from the substrate, flipped over, and settled directly next to their place of origin, remaining there for subsequent metal deposition. Looking at the bottom side of these rings give a unique view of the retrograde profile that occurs between these circular trenches.

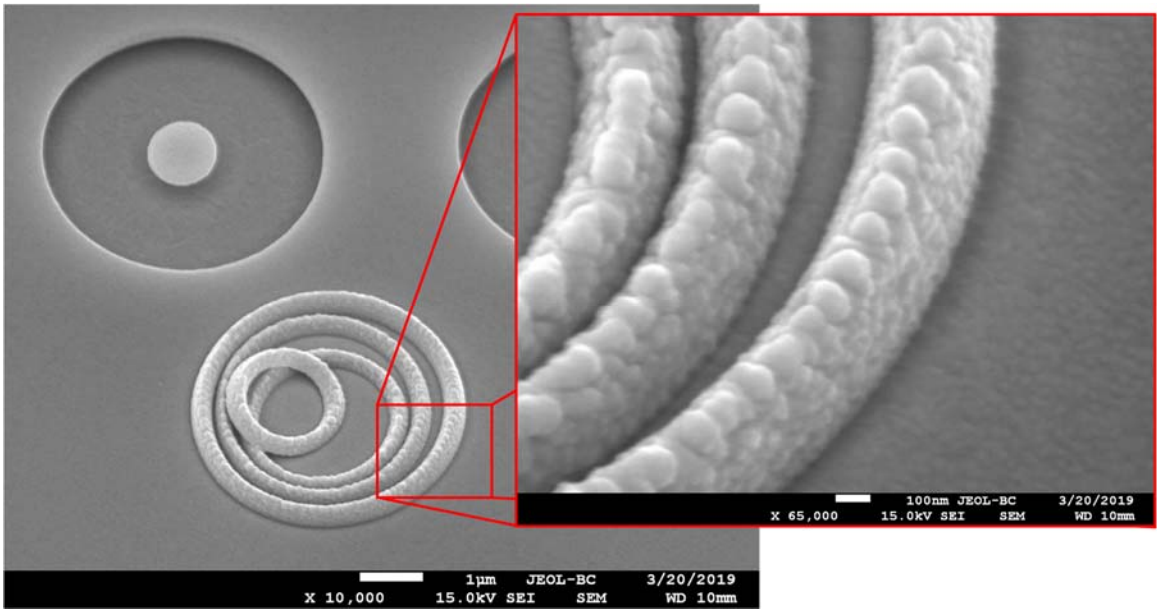

Figure 88. Disconnected concentric rings. SEM image of PMMA rings that became dislodge and flipped after undercut during exposure and development, after sputter deposition of 100 nm TiAu.

After the electron beam writing, discussed in section 3.3.3, the sample is developed in a 3:1 solution of isopropanol:methylisobutylketone (IPA:MIBK) for 1.5 min, followed by 10 s rinse in pure IPA, and then in DI H_2O for 30s, followed by drying with N_2 gas. Microscope images after development of regions of bullseyes for four different gap sizes are shown in Figure 89 below. Each region contains a hexagonal close pack array of bullseyes with five rings of the same gap size and pitch, with spacings of 300 nm, 400 nm, 500 nm, and 600 nm shown below. The arrays cover a total square region 500 µm ×

500 μm, intended to cover the entire collection region of the 50x objective on the Leica microscope. The four arrays of gap sizes listed above are shown in Figure 90 picture (taken with iPhone 8 camera) of a sample from right to left, respectively.

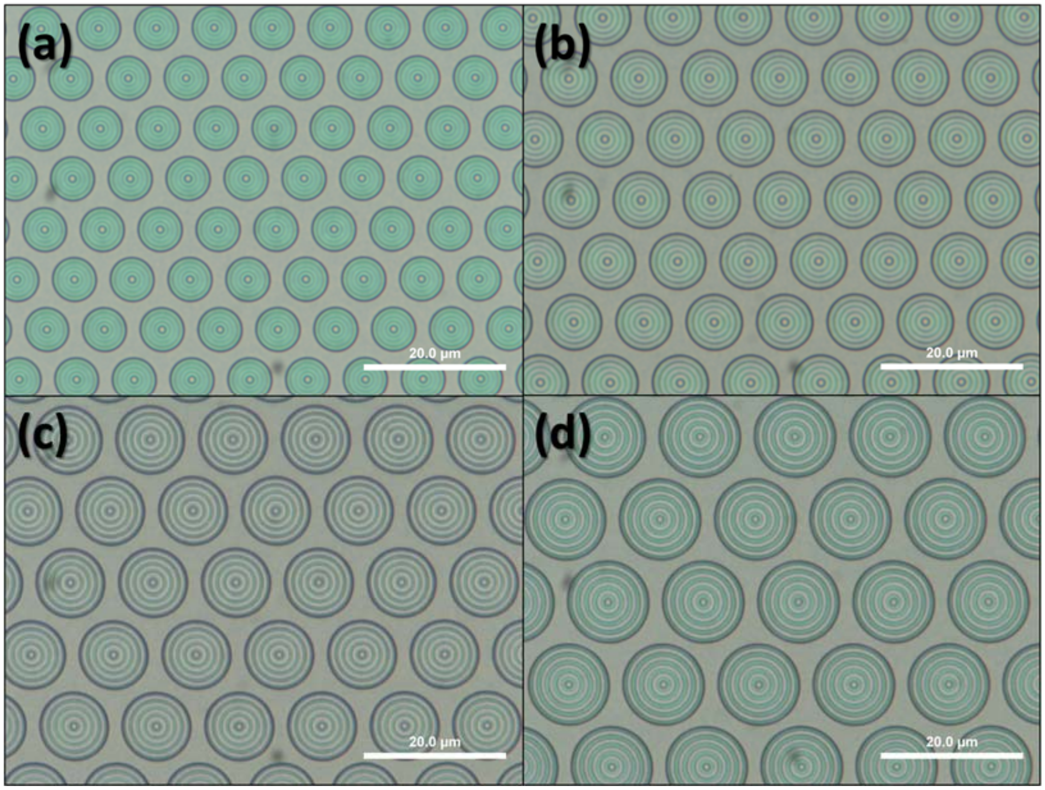

Figure 89. Microscope image of bullseye arrays. Images of bullseye array with gap size (a) 300nm, (b) 400nm, (c) 500nm, and (d) 600nm.

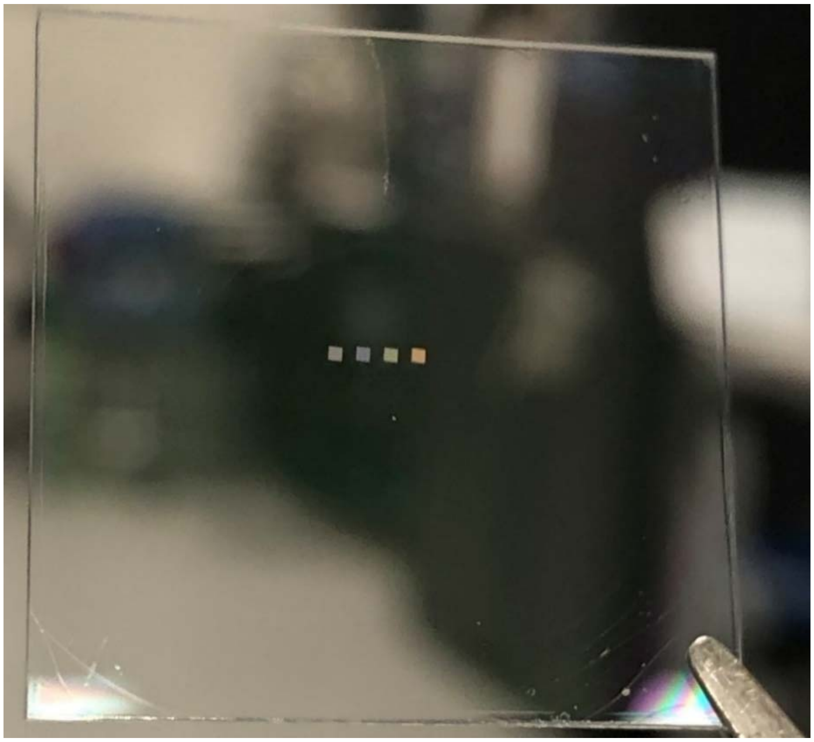

Figure 90. Arrays of bullseyes. Left to right, gap sizes 600nm, 500nm, 400nm, and 300nm.

The final step in fabrication is depositing a metal that will support the desired surface plasmons and meet the other material requirements discussed in section 3.4.2. When depositing the metal, the main considerations can be summarized in the following list:

i) The metal thickness must form a sufficiently opaque layer in the planar regions.
ii) The materials most be chosen to meet structural and device needs.
iii) The deposition tool's capabilities.
iv) The deposition's anisotropicity and its influence on the sidewall thickness ratio.

Regarding i), it is important to have opaque layer in the planar region in order to minimize the amount of white light that passes through the sample, which is not modulated by plasmonic activity in the structure. One can mitigate the contribution to the transmitted counts by subtracting the spectrum through an unstructured planar region under the same collection conditions, as discussed in section 3.3.1. This process can introduce artificial noise and it is best to avoid this by ensure the deposition thickness yield opaque layers, approximately for thickness 150 nm and above. Regarding ii), there are additional material and structural considerations beyond those discussed in section 3.4.2. Depositing a thin (~ 5 nm) layer of Ti or Cr before noble metals is typically done in order to improve surface adhesion. There can be appreciable loss in even thin adhesion layers, and one should process accordingly. Sequential deposition of certain materials will cause adverse interfacial reactions, *e.g.* such as that between aluminum and gold, referred to as the purple plague for its purplish appearance. Also, if deposited metal thickness exceeds a certain value then smaller gap sizes of bullseye will close completely. Regarding iii), the metals deposited on samples described herein were done on either the AJA sputter deposition system or the Sharon e-beam evaporator system. While there are many differences in the way these two tools deposit materials, the most relevant explored for samples described herein is the directionality of material, as listed in iv). Generally, the deposition performed in the AJA sputter system are more anisotropic, meaning that they will cover surface at angles not normal to the line of sight. This means that the sidewall thickness will be a larger fraction of the planar region thickness. The main reasons for lower deposition isotropy compared with that of the Sharon system are that 1) the AJA has a smaller distance between the target and the revolving sample, 2) the material targets are larger in the AJA, and 3) the gas used to produce plasma inherent to sputter deposition in the AJA collide with sputtered material introducing a somewhat stochastic deposition angle. Modifying the gas pressure and sample-target separation, currently at 3 mTorr and 37 cm, may be able to influence this anisotropy, though it may also affect the deposition rate and surface stresses. The reason that the anisotropy of deposition, in concert with the retrograde resist profile, is so important is that it will change the amount of light that will transmit through the sidewall region in the bullseye structure and specifically, whether the light will pass through a sufficiently thick metal region to be modulate through scattering into surface plasmons. In summary, if the metal thickness in the sidewall region is too large then the transmitted light will be so small that the transmitted counts will not have good signal-to-noise ratio. If the metal thickness in the sidewall region is too small then the white light directly transmitted will be large compared with the plasmon-modulated light, therefore necessitating smaller integration times of the spectrometer and smaller fractional change to the transmitted light and again, lower signal-to-noise ratio.

3.4.4 Photolithography

Arrays of halo and ring structures were made by photolithography and physical vapor deposition, as shown in Figure 91 below. The wafer-scale, high-throughput processing inherent to photolithographic fabrication remains an attractive alternative to producing nanostructures through serial direct write processing, *e.g.* through EBL. While the sample preparation times are similar for the two processes, the exposure time for photolithgraphy is constant at around 10 s whereas the exposure time for EBL approximately scales quadratically with area and would take several hours for filled of 1 mm^2. The equipment for EBL, an SEM with NPGS configuration, commonly have a higher in cost than mask aligners for photolithography, as are the rates charged at user facilities.

While the economic motivation is considerable for developing or adapting a fabrication processes for photolithography, diffraction limited resolution limits many common photolithogaphy systems. Such commonly available photolithography tools, including those available to this work, use near UV light sources between 436 nm and 365 nm wavelengths, called g-line and i-line spectral lines, respectively. Systems that use significantly smaller wavelenths in the extreme ultraviolet (EUV) down to 10 nm exist and are used for commercial production of micro- and nanoelectronics. Other photolithography tools and techniques are able to achieve sub-diffraction limited patterning, though their description is beyond the scoop of this work.

While the in-plane dimensions of a photolithographic pattern are diffraction limited, the vertical dimensions are not. Nanoscale features that may be important to desired structure can be achieve through all photolithogaphic pattern, *e.g.* the ECC described in chapter 2.

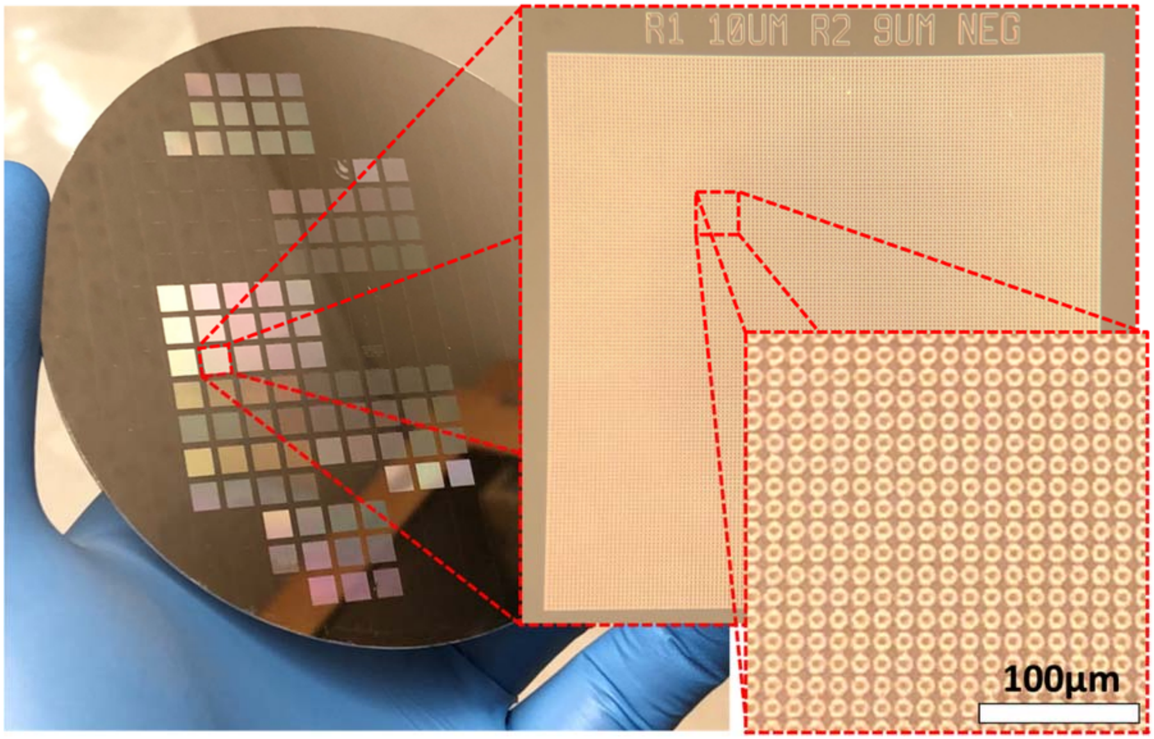

Figure 91. Photolithography sample. Optical images of sample made by photolithography with subsequent zooms into a region with an array of singular circular trenches with inner diameter 9 µm and outer diameter of 10 µm.

Standard ways of achieve nano-scale features through photolithogaphy is by the formation of retrograde resist profiles and throughout bilayer undercutting. These techniques are commonly used for perfomring lift-off deposition such that the edge of a pattern region are discontinous from the substrate to the later removed resist. These teechniques are important to this work because of the importance of the retrograde profile, as discussed in section 3.4.3. Listed in Figure 92 below are three common materials and techniques that can achieve undercut and retrograde profiles.

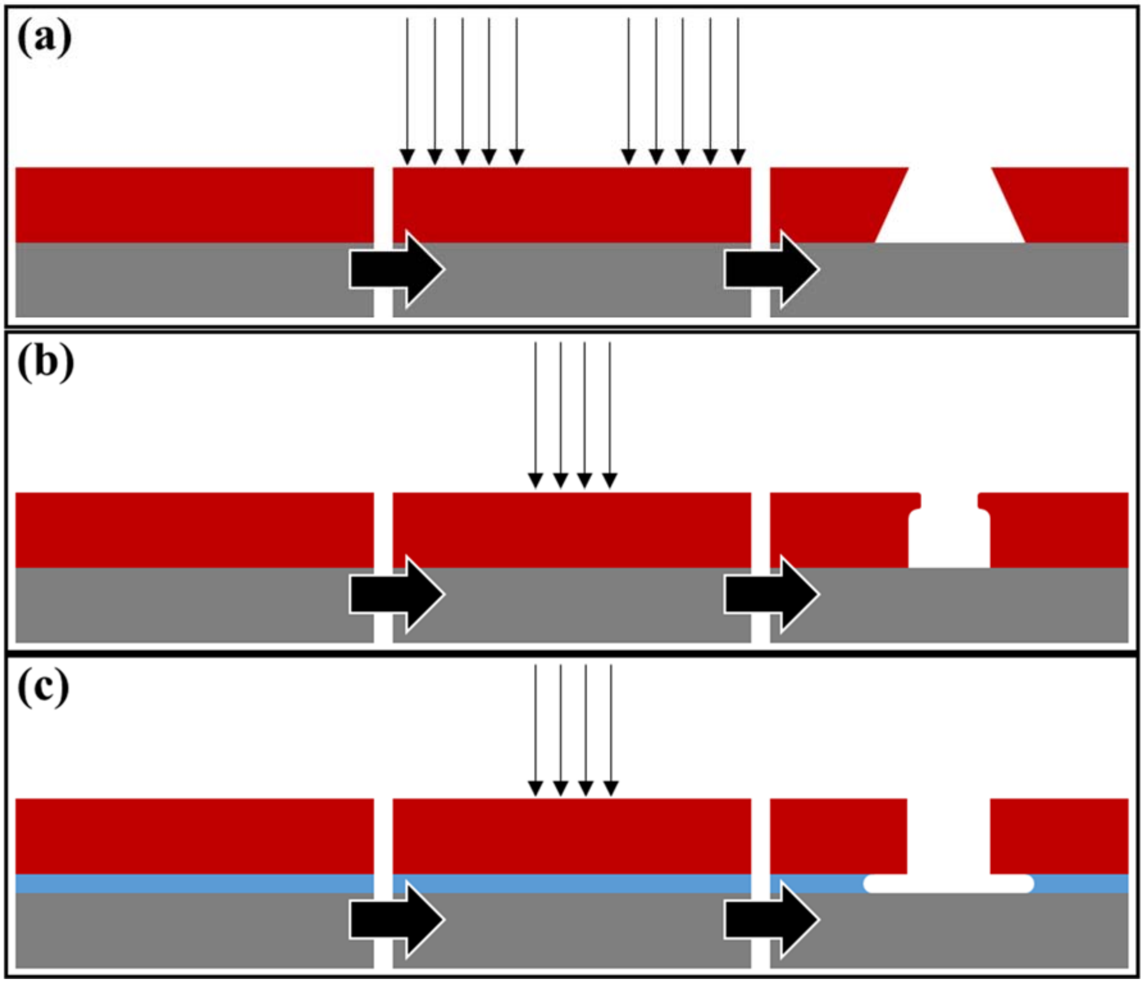

Figure 92. Retrograde photolthography processes. Schematic steps of three common photolithographic processes to achieve an undercut or retrograde resist profile. Processes use (a) negative tone resist or image reversal resist with a retrograde profile, (b) swelling of top-most region of resist by soaking with toluene after exposure and before development, and (c) lift-off resist (LOR) that is chemically undercut by developer.

3.4.5 Characterization

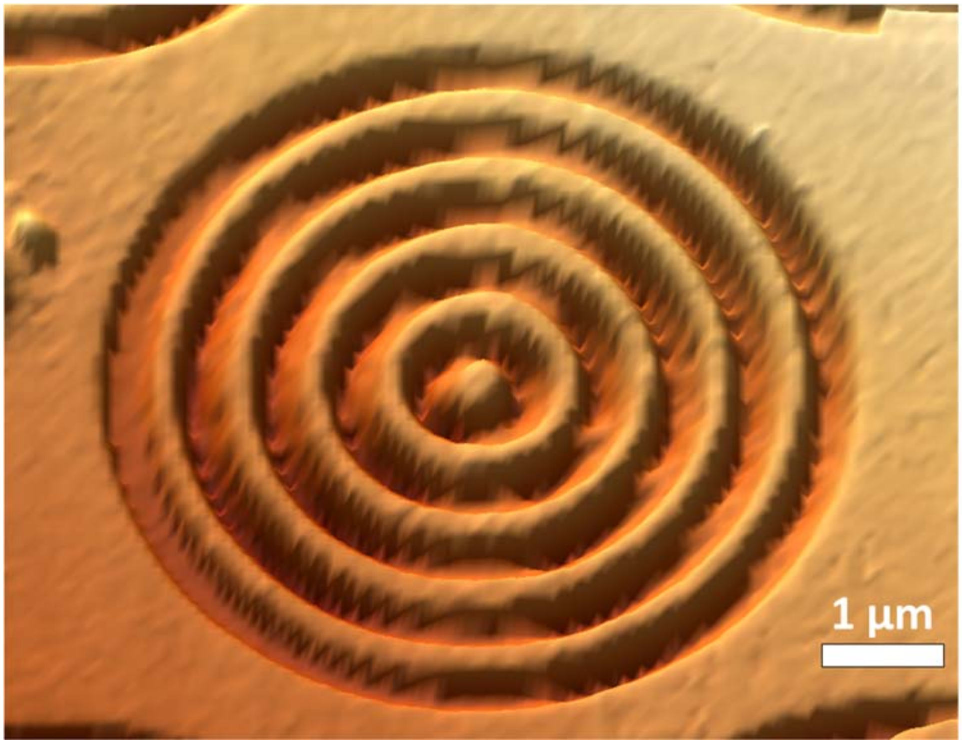

Figure 93. Bullseye AFM. 30°-tilted 3D image of bullseye topography measured by an atomic force microscope.

Figure 93 above shows topographical data from a Veeco Dimension 3100 AFM scan of a bullseye structure, for a 3D rendering tilted at 30° corresponding to SEM show in Figure 74. Structural characterization through the topographic information can be obtain through AFM and SEM imaging. Inspection by SEM will typically give a better image and is capable of discerning some things that AFM images cannot, such as retrograde profiles and material boundary in cross-sectional images. AFM imaging can be useful for optical diffraction limited inspection of bullseye before the metal is deposited onto the PMMA structure, both to prevent swelling in PMMA and forego the problem of charge accumulation.

As introduced in section 3.2.2, the most common avenue of investigation for samples in the chapter was through an optical microscope. While optical images provide only relative or qualitative information, they are very useful in obtaining an initial evaluation of a structure or process. Images of bullseye arrays from different samples are shown in Figure 94 and Figure 95 below, containing Ag and Au metallic layers, respectively.

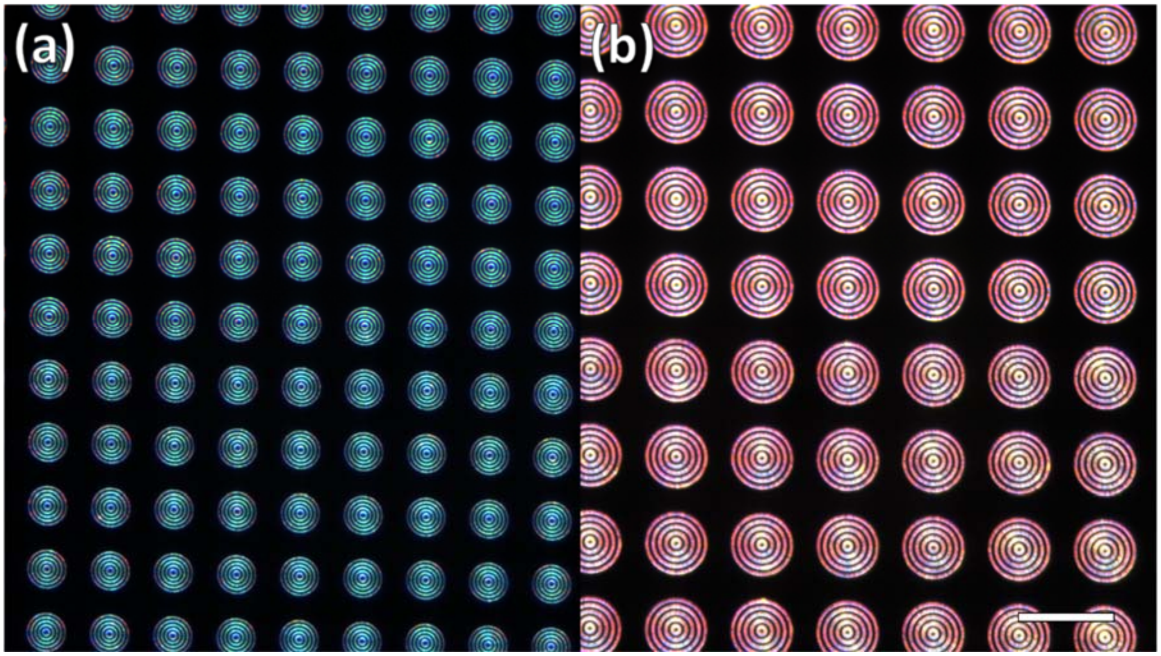

Figure 94. Images of Ag bullseye arrays. Transmitted light from bottom side incident white light through Ag bullseye arrays with gap sizes (a) 400 nm and (b) 675 nm. Inset scalebar is 20 μm.

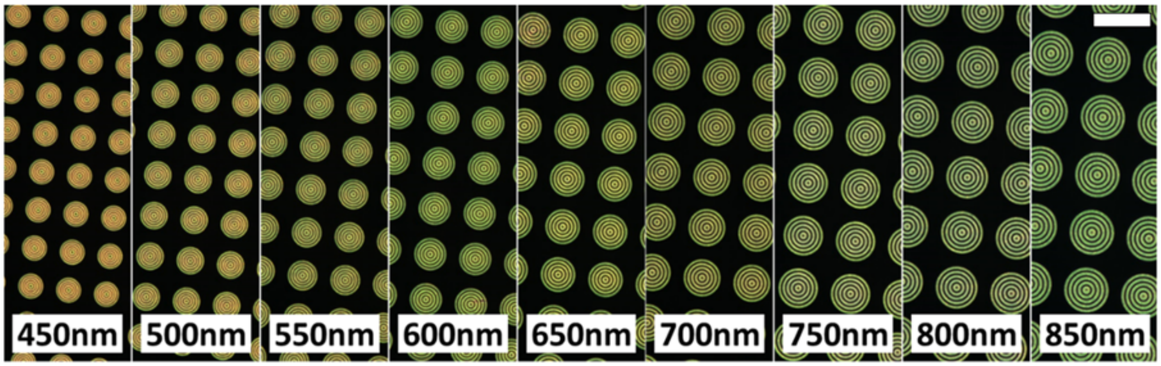

Figure 95. Images of Au bullseye arrays. Transmitted light from bottom side incident white light through Au bullseye arrays with gap sizes from 400 nm and to 850 nm from left to right. Inset scalebar is 20 µm.

This type of qualitative inspection is particularly valuable when motivating parameter selection with a parametric sweep, such as the one shown in Figure 75 of section 3.4.1. In fact, it was this type of visual inspection of an EBL parametric sweep of circular patterns that motivated the first inspection behind the original halo. In order facilitate an optimized and effective quantitative characterization of the transmittance spectra, large arrays of bullseyes need to be produced. Given that EBL is a serial and expensive process, this makes simultaneous quantitative analysis of many parameters unpractical. This is also the reason that higher-throughput processes like photolithography or nano-imprint lithography represent an attractive avenue for investigation, though faithfully reproducing similar feature shapes and sizes poses several difficulties.

We can characterize features in the transmittance spectra for different structural parameters. Figure 96 below shows how the wavelength of minima in the transmittance correspond to gap size for bullseye arrays image in Figure 95. In Figure 96c the minima wavelengths are plotted vs the nominal gap size of the bullseye structure Since the sample contains Au there is still a prominent peak near 550 nm wavelength, though peaks beyond this region can be discerned. Since we believe that the modulations in transmittance data are through surface plasmons in the metal, we can study how the wavelength of these features are influenced by molecular and biological material. The wavelength changes in minima and maxima in response to introduced material is widely used metric for detection and will be adopted for our studies, as discussed in section 3.5

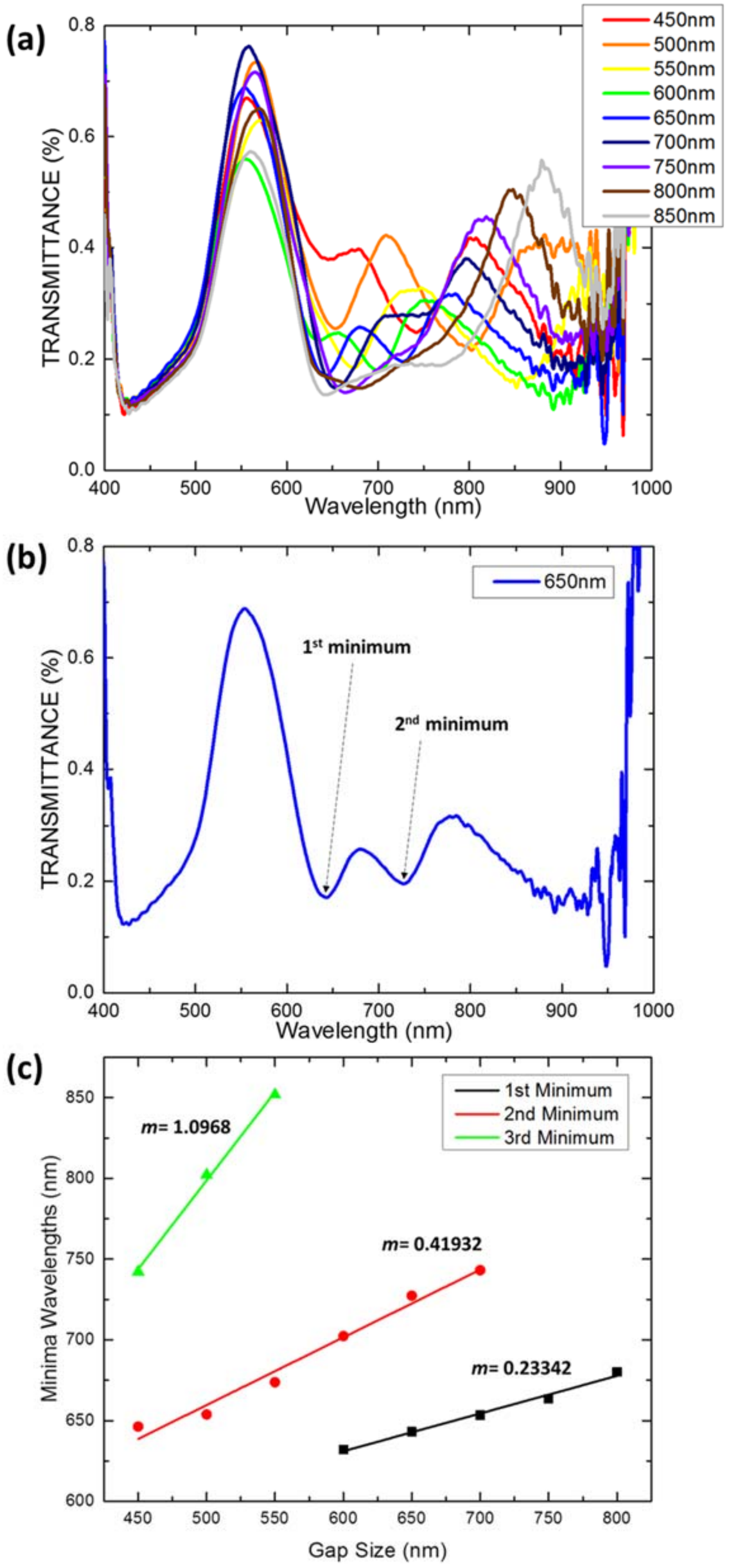

Figure 96. Transmittance minima. Spectra through bullseye arrays for (a) several gap sizes, (b) just 650 nm gap size, and (c) plot of minima wavelengths for different gap sizes with linear fits.

3.4.6 Plasmonic vs. photonic modulations

The nature of the features observed in Figure 96 are discussed in this section. Specifically, four points are made in favor of the modes being the result of coupling to surface plasmons in the structure as well as how these modulations in transmitted light cannot be fully described by photonic modes and diffraction patterns.

Point 1: *The simulated electric field distributions are consistent with surface plasmons.*

Figure 97 below shows the z-component of the electric field for a periodic trench structure upon bottom-side incident monochromatic light for the wavelengths 400 nm and 700 nm. The vertically facing metal thickness is 150 nm and the horizontal facing metal thickness, comprising the sidewall region, is 30 nm. The trench gap and pitch are both 650 nm. This structure is modeled with a gap region at the bottom of the side wall in order to allow a direct comparison of transmittances with a perfect electric conductor and a lossy metal (see point 4 below). Focusing on the bottom of the trenches, one can observe the exponentially decaying periodic electric fields that are characteristic of surface plasmon resonances. For 400 nm illumination, there is higher confinement of these modes while for 700 nm illumination, there is relatively lower confinement of modes. This analysis shows that the resonant modes are plasmon polaritons, *i.e.* have a mixed plasmon-photon character. These polaritons have a strong plasmonic character at wavelength of 400 nm, which approaches the plasmonic saturation of the dispersion, away from the light line. In contrast, at 700 nm, a strong coupled nature of the plasmon-polariton is apparent, with a much less pronounced surface localization of the fields. The remaining points reinforce the interpretation. Therefore, the detection system proposed can be convincingly described as a based on plasmon-polaritons, with the corresponding fields begin surface localized, enabling enhancement of the sensitivity.

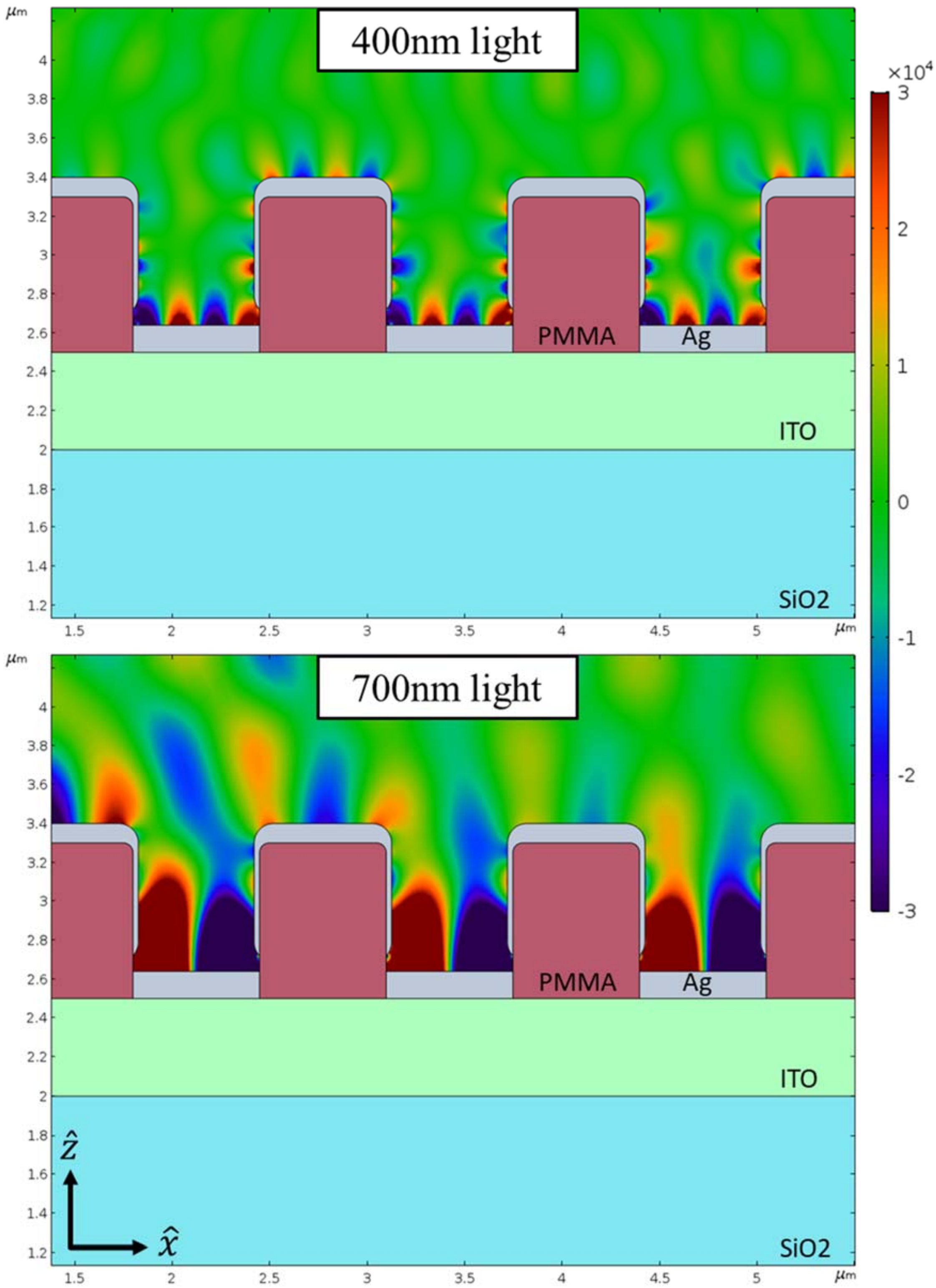

Figure 97. Simulated modes in periodic trenches. COMSOL simulated z-component of electric field for bottom-side incident monochromatic light for the wavelengths 400 nm and 700 nm showing confinement of plasmonic modes at the bottom of the trench gaps.

<u>Point 2</u>: *Changing gap sizes are perpendicular to the transmitted light axis and resulting changes to the transmitted light are lost during transmission in the optical fiber.*

It is known that changing film thickness of dielectric material, not capable of supporting plasmons, can create thin film interferes that pass different wavelength of light differently. This changing thickness represents an interference phenomenon that pertains to changes that are parallel to the propagation of light.

Conversely, the spectra of the changing gap size plotted in Figure 96 are structural changes that are perpendicular to the transmission axis for that measurement. Optical diffraction from periodic grating structures results in an interference pattern of maxima and minima in intensity in the far field. If these bullseye structures cause such interference patterns, then the far field light could have different distributions for different gap sizes or wavelengths. However, even if this is the case, when this light passes through the optical fiber any spatial distribution of intensities will be mixed during transmission through the fiber. Therefore, that diffraction-based information would be lost in the far-field collection and cannot explain the observed trends in transmittance plotted in Figure 96c.

<u>Point 3</u>: *If the numerical aperture (*NA*) of the objective lens is such that the number of collected orders of diffracted light is different for different wavelengths, then this would result in transmittance patterns that would be different from those observed in* Figure 96.

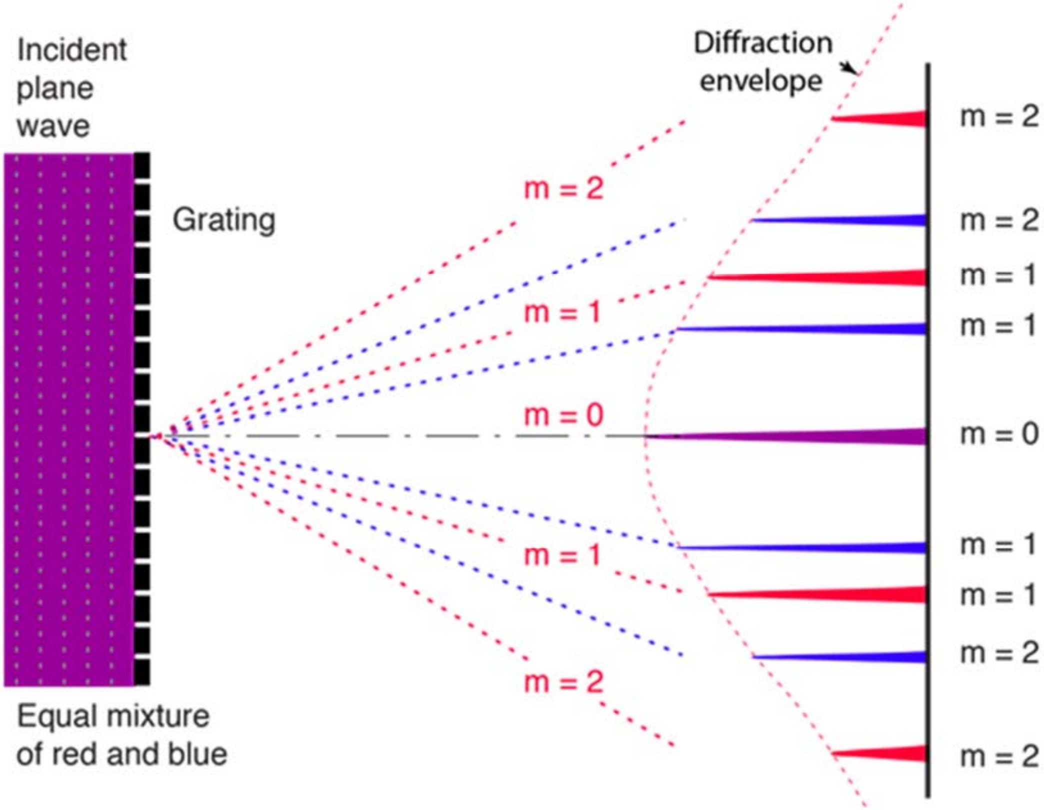

Figure 98. Diffracted orders of periodic grating. Schematic of grating structure and resulting diffractions pattern for different incident wavelengths showing different order maxima. Credit HyperPhysics, *C.R. Nave.*

The angular separation, θ, of the of maxima is dependent on dimensions of the diffraction structure, *e.g.* $p\ sin(\theta) = m\lambda$ for a linear diffraction grating, where p is the grating pitch, m is the maxima order, and λ is the wavelength of incident light. Light in the far field could be collected in with an objective lens with numerical aperture $NA = n\sin(\theta')$. In air n=1 and when focused on the surface $\theta = \theta'$. As is displayed in Figure 98 above, the angular position of maxima is also wavelength dependent. Specifically, the larger wavelengths will be diffracted to relatively higher angular positions. There are combinations of objective lens and grating pitch (equivalent to gap size in the bullseye structure plotted in Figure 96) such that different wavelengths will have a different number of maxima orders fall within the numerical aperture being collected from. This would be observed as the transmitted intensity dropping as the wavelength increased when an interference maximum moves outside of the *NA*. However, as the incident wavelength increases further the collected intensity should not go back up, resulting in local minima *i.e.*, those in the collected transmittance of Figure 96. Rather, the transmittance spectra would show a drop in transmittance each time the incident wavelength is large enough such that the next diffraction maxima would move outside of the *NA*. Figure 99 below shows an example sketch of what the transmittance would look like for orders m=2 and m=1 moving outside of the *NA* of the objective lens, without local minima.

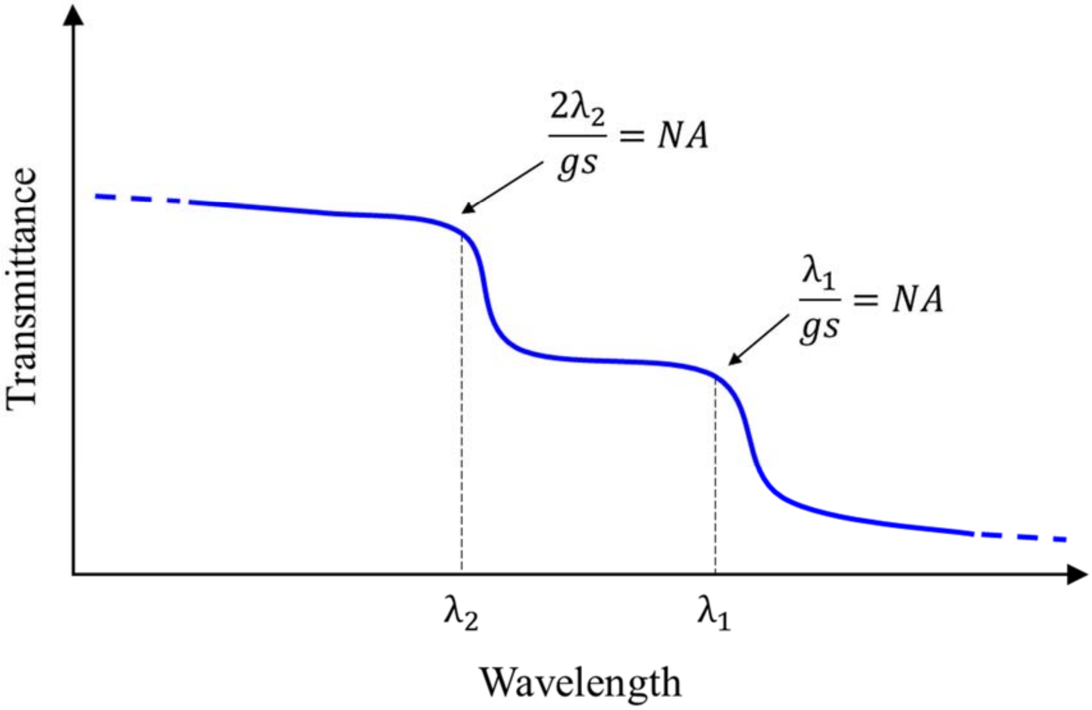

Figure 99. Sketch of collected diffraction orders. Example sketch of the changes in transmittance that would be observed for diffraction maxima moving outside of objective lens collection angle as a function of wavelength.

<u>Point 4</u>: *The simulated transmittance through periodic trench structures bearing a perfect electric conductor (PEC) is different from that of the same structure with a real metal.*

Figure 100 below shows transmittances through a periodic trench structure for a real metal and a metal with a PEC. The structure is the same as depicted in Figure 97. The notable differences in the two spectra are a confirmation that losses in the real metal result in appreciable changes to the transmitted spectra, possibly through plasmonic modulation. Therefore, since there is a considerable difference, photonic modulation of transmitted light cannot sufficiently account for modulations observed in real transmittances measurements.

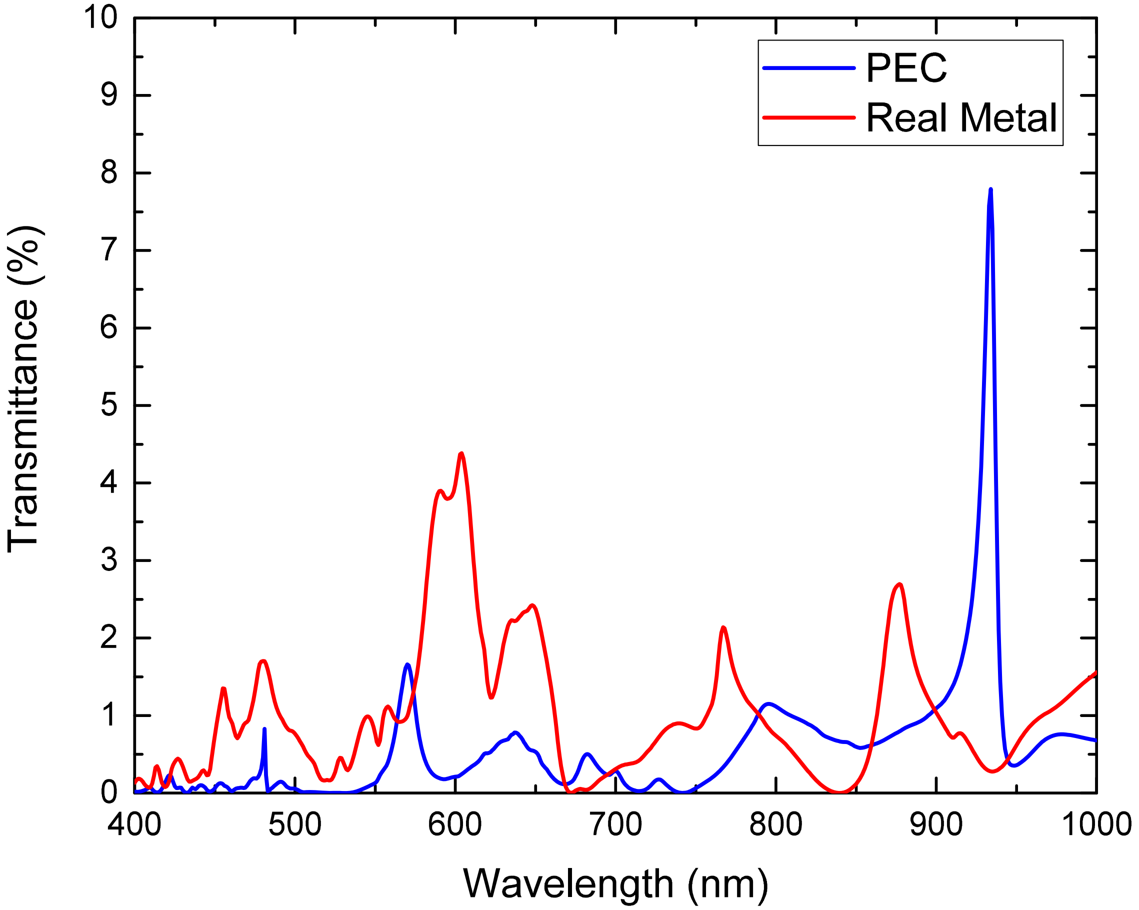

Figure 100. Simulated transmittances of PEC *vs.* real metal. COMSOL simulated transmittances through periodic trench structures with a real meal and a PEC, showing observably transmittance different spectra.

3.5 Initial Testing

3.5.1 Sensitivity Motives and Metrics

In order to develop a device whose sensitivity in dependent on potentially small changes in the data measured in the experiment, the device must have a stable measurement background throughout the experimental process. Otherwise, the presence of statistical or systematic errors will prevent any present signal from being observed, rendering the device ineffectual. As a way of testing this robustness, a sample twice underwent a sequence of measurement, PBS application, drying, measurement, rinsing, and drying, where transmittance measurements were made at the pre- and post-PBS states for both cycles. Figure 101 below shows the transmittances at these 4 different points, chronologically *DRY 1, PBS 1, DRY 2, and PBS 2.* The uniformity in the transmittances for each like state is observed and indicates small deviations caused by experimental procedure for this sample, one with Au metal on concentric ring nanostructure. Specifically, the variation in spectral features is very small as a function of wavelength, while the is some small offset in the intensities. This is likely due to the slight differences in the amount of light that scatters into the NA as a consequence of slightly similar positioning of the cover slides.

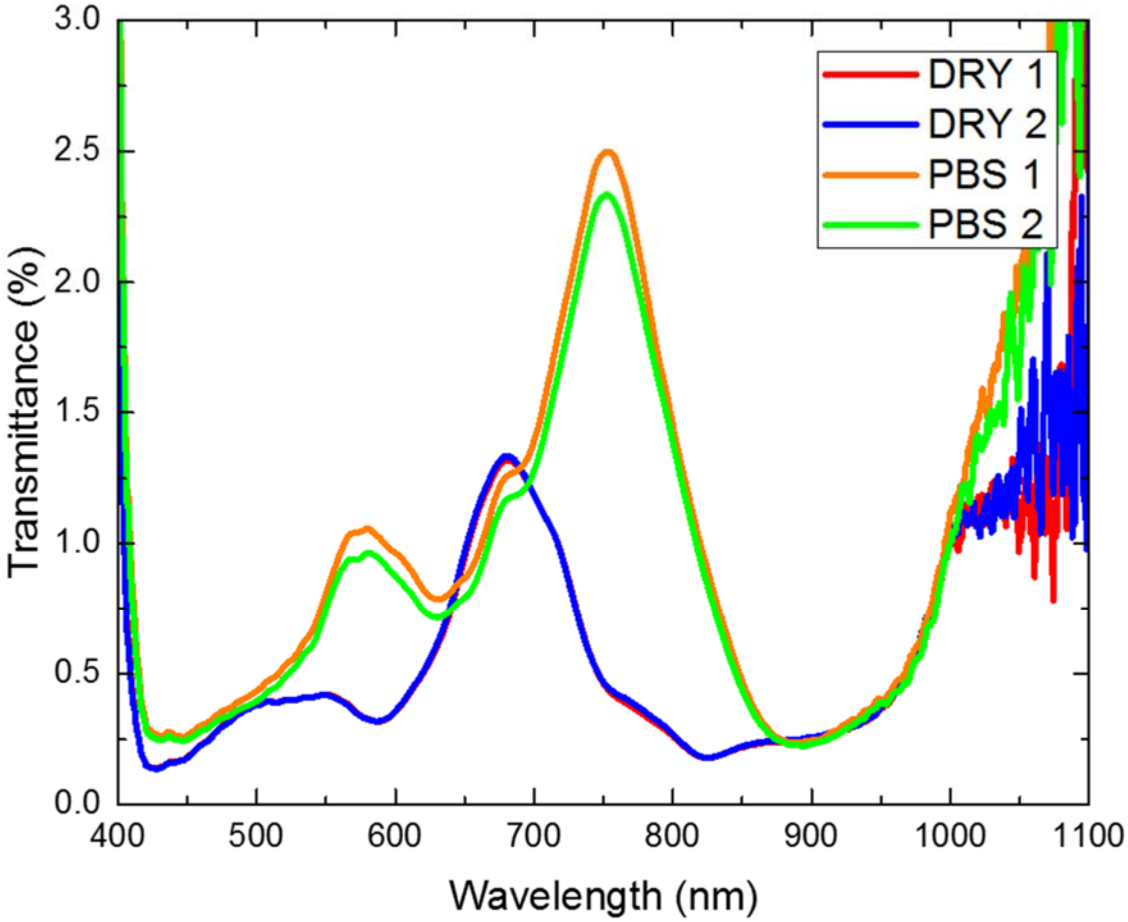

Figure 101. PBS before and after spectra. Measured transmittance through a Au nanostructure sample before and after the application, removal and drying of PBS, repeated twice.

As can been in Figure 101, a local maximum in wavelength of transmittance for the dry measurement is shifted from 680 nm to 753 nm for the PBS. As previously discussed, this shift is due to the plasmon-modulated transmittance's dependence on material properties at the metal dielectric interface, particularly the materials relative permittivity. More commonly discussed is the materials index of refraction, proportional to the square root of the relative permittivity given the non-magnetic properties of such materials for optical wavelengths. The relatively large shift from 680 nm to 753 nm is the result of a relatively large shift in the index of refraction from $n_{air} = 1$ to $n_{PBS} = 1.33$. The most commonly defined metric for sensitivity, S, used in literature is the ratio of relative change in a wavelength feature to the change in index of refraction for those separate measurements, as in $S \equiv \Delta\lambda \,/\, \Delta n$ with units of nm/RIU (refractive index units). For this definition the above sensitivity would be 73 nm / 0.33 RIU or 221 nm/RIU.

Another common figure of merit is defined as the above-defined sensitivity divided by the full width at half maximum (FWHM) of the peak being interrogated. This has the benefit of eliminate the units of the sensitivity, which is a sign of the wavelength's dependence on the sensitivity. For example, infrared-based biosensing devices are commonly found to have higher sensitivities the those in the visible regime, at least partially due to the fact that similar % changes in the wavelengths will correspond to larger $\Delta\lambda$ for infrared. Figure 102 below shows a table of different plasmonic-based nanostructures and their sensing characteristics (adapted from Chung et al., 2011).

Wavelength	Nanostructure	Sensitivity	RI Range	Reference
800-2800 nm	Nanocrescents	879 nm/RIU	Streptavidin	Bukasov et al., 2010
750-1000 nm	Nanopillar arrays	675 nm/RIU	1.33-1.45	Cetin et al., 2011
200-1000 nm	Aluminum nanotriangles	0.405 eV/RIU	1-1.5	Chan et al., 2008
3000-8000 nm	MIM nanodisk	1500 nm/RIU	1.3-1.39	Chang et al., 2018
550-750 nm	Nanostars	218 nm/RIU	1-1.38	Dondapati et al., 2010
350-650 nm	Nanocubes	165 nm/RIU	Neutravidin	Galush et al., 2009
400-900 nm	Chiral nanoparticles	1091 nm/RIU	1.333-1.357	Jeong et al., 2016
400-1000 nm	Nanorod metamaterial	30000 nm/RIU	1-1.36	Kabashin et al., 2009
1361 nm	Double nanopillar with nanogap	642 nm/RIU	1.34-1.44	Kubo et al., 2011
1512 nm	Double nanopillar with nanogap	1056 nm/RIU	1.34-1.44	Kubo et al., 2011
900-1500 nm	Gold Nanorings	880 nm/RIU	1.33-1.42	Larsson et al., 2007
800-1000 nm	Gold nano rods	650 nm/RIU	1.34-1.7	Lee et al., 2006
500-1000 nm	Arrays of gold nanodisk	167 nm/RIU	1.32-1.42	Lee et al., 2011
500-1000 nm	Arrays of gold nanodisk	327 nm/RIU	1.32-1.42	Lee et al., 2011
400-800 nm	Capped aluminum nanoslits	473 nm/RIU	1-1.35	Lee et al., 2017
500-1700 nm	Gold nanoring trimers	345 nm/RIU	1-1.5	Lin et al., 2010
950-2500 nm	Planar metamaterial	725 nm/RIU	1.332-1.372	Liu et al., 2010
450-900 nm	Gold nanohole arrays	300 nm/RIU	1.333-1.381	Martinez-Perdiguero et al., 2012
400-850 nm	Gold nanohole arrays	126 nm/RIU	1.33-1.39	Martinez-Perdiguero et al., 2013
450-700 nm	Silver triangular nanoparticles	197 nm/RIU	1-1.6	McFarland et al., 2003
450-700 nm	Silver rodlike nanoparticles	235 nm/RIU	1-1.6	McFarland et al., 2003
450-700 nm	Silver spherical nanoparticles	161 nm/RIU	1-1.6	McFarland, 2003
550-900 nm	Arrays of nanotubes	250 nm/RIU	1.333-1.368	McPhillips et al., 2010

Figure 102. Table of reported plasmonic biosensors. Listed are the used nanostructures and their sensing characteristics, including device sensitivity. Adapted from Chung et al., 2011 with additional works added.

Wavelength	Nanostructure	Sensitivity	RI Range	Reference
400-1000 nm	Nanohole array	420 nm/RIU	1.33-1.7	Nakamoto et al., 2011
450-600 nm	Gold colloidal nanoparticles	71 nm/RIU	1.32-1.5	Sun et al., 2002
400-800 nm	Hollow gold nanoshell	408 nm/RIU	1.32-1.5	Sun et al., 2002
900-2500 nm	Gold nanoring arrays	805 nm/RIU	1-1.35	Toma et al., 2013
600-750 nm	Small gold nanodisk trimers	170 nm/RIU	1-1.5	Lin et al., 2010
1100-1400 nm	Large gold nanodisk trimers	374 nm/RIU	1-1.5	Lin et al., 2010
500-900 nm	Fabry-Perot nanoholes	593 nm/RIU	1.333-1.378	Tu et al., 2018
1200-1900 nm	Nanocross	710 nm/RIU	1.333-1.38	Verellen et al., 2011
1200-1900 nm	Nanobar	1000 nm/RIU	1.333-1.38	Verellen et al., 2011
633 nm	Silver thin film with SAM	127 nm/RIU	1.3304-1.3311	Wang et al., 2017
650 nm, 850 nm	Gold nanohole arrays	9000 nm/RIU	1-1.33	Yesilkoy et al., 2018

Figure 102 continued. Table of reported plasmonic biosensors. Listed are the used nanostructures and their sensing characteristics, including device sensitivity. Adapted from Chung et al., 2011 with additional works added.

3.5.2 Sensitivity Testing

The most common way to measure the sensitivity of a device is by applying liquids with different refractive indices and measuring the change in a spectral feature, *e.g.* a minimum or maximum in transmittance. We used this method to on a sample with an array of bullseye structure. To do so we applied Cargille certified refractive index liquids for indices ranging from 1.4 to 1.49 and recorded the corresponding transmittance spectra in each case. Plotted in Figure 103 below are transmittance maxima located near 670 nm wavelength for different index oils and how those maxima change as a function on index.

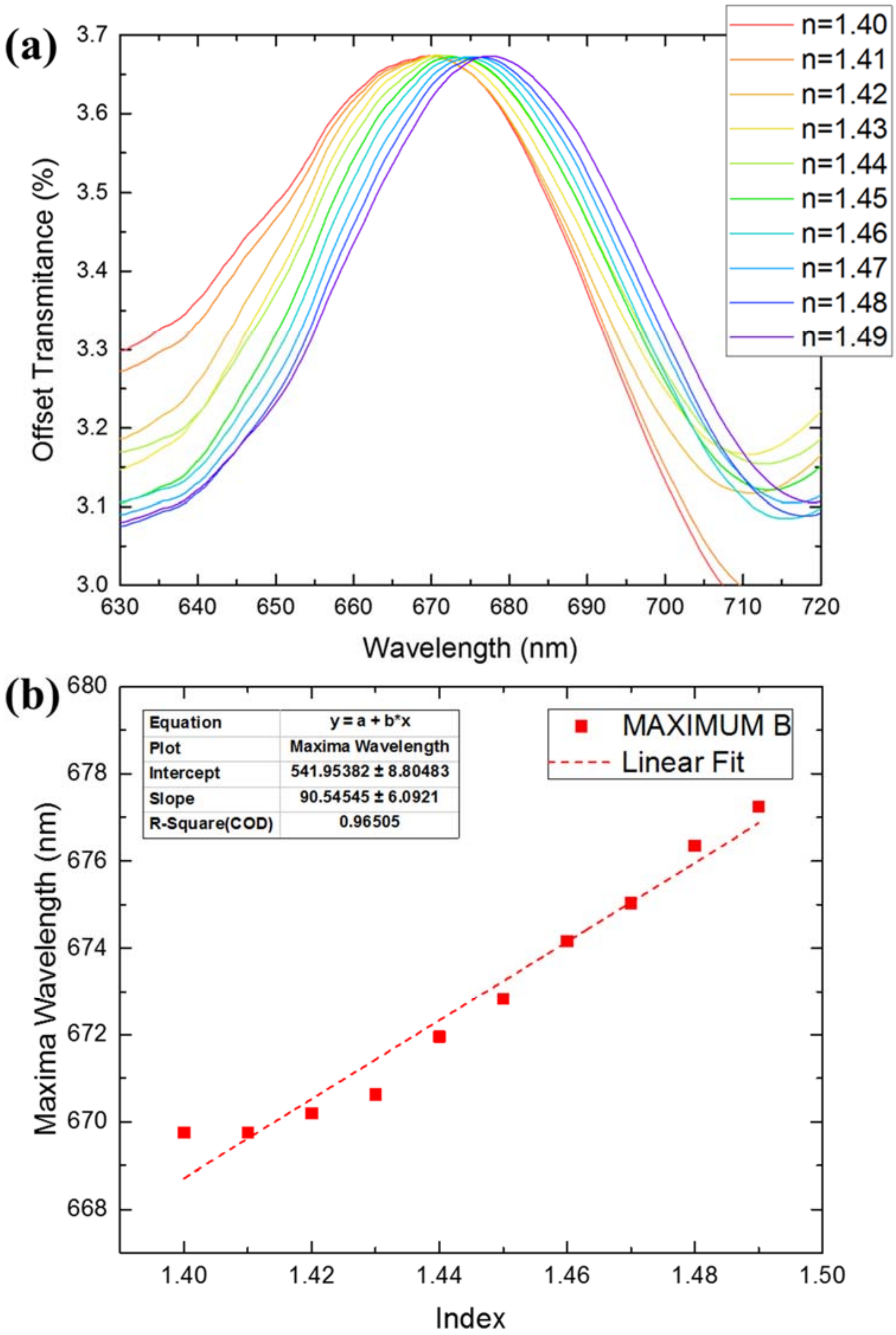

Figure 103. Immersion oil wavelength change. (a) A selected wavelength maximum for different index of refractions. (b) Plot of wavelength maxima *vs.* index, where slope determines sensitivity.

The slope of the wavelength maxima *vs.* the index of refraction is the sensitivity. In Figure 103 this value is 91 nm/RIU. This value and the 221 nm/RIU from Figure 101 are somewhat lower than commonly reporter values in literature. This technique is a valuable way of testing a process changes ability to improve the desired outcome for a sample.

Shown in Figure 104 are images and measured spectra of transmitted light through photolithographically patterned rings of Figure 91 for a sample in air (~green) and a sample immersed in DI-H_2O (~orange), with the same bottom side incident white light in both cases. Using the minimum at 648 nm for the *in air* case the *in H_2O* minimum moves to 749 nm. For a corresponding index change of 0.33 the sensitivity is 306 nm/RIU.

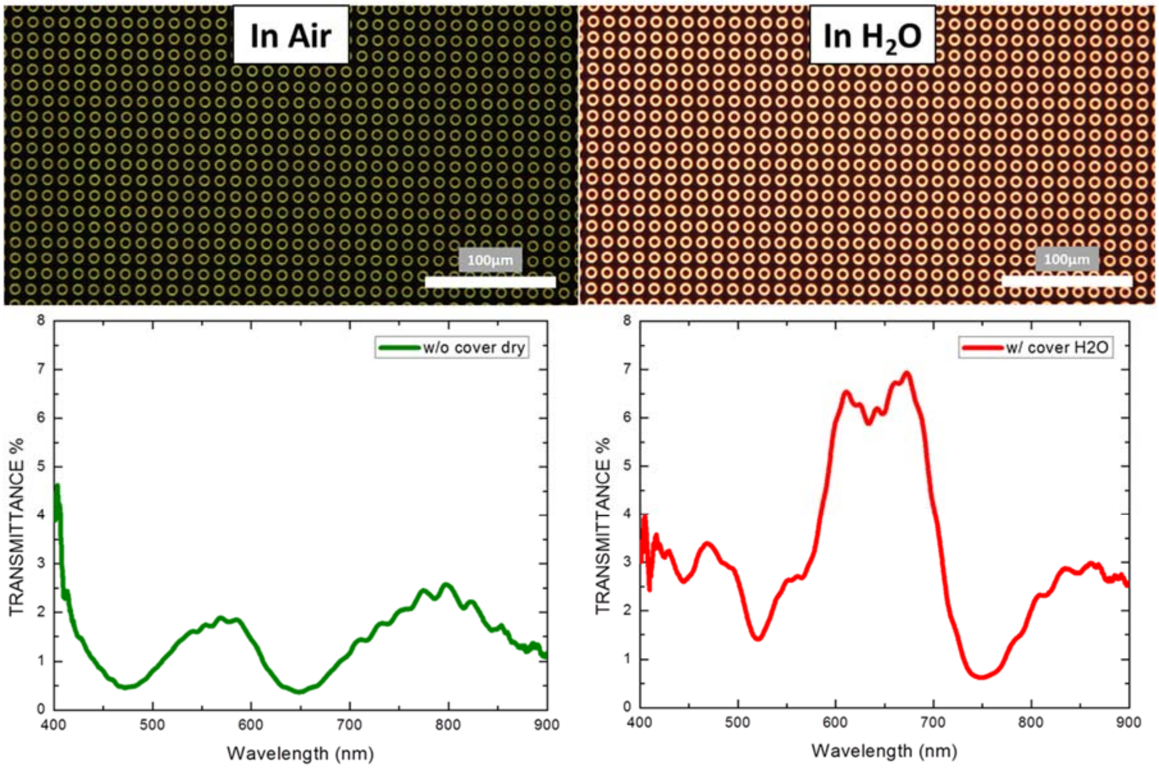

Figure 104. Photolithographic rings in air and H_2O. Shown are images of the transmitted light from bottom side incident white light for a sample in air and the same sample, light source and camera settings after the application of DI-H_2O.

3.5.3 Initial Results and Failures

The standard next step in demonstrating biosensing capability of a device is to measure the specific capture of a targeted antigen. This is done by showing a repeatable change in a measurable property of the device due to the introduction of the targeted species when compared to the absence of that change in an appropriate control test. Once proof-of-concept detection has been demonstrated the further testing and device improvement can be down to show and improve the device's limit of detection. The ability to model, make, and measure in such a way requires the precise coordination of tools, techniques, and materials across interdisciplinary fields of physics, chemistry and biology. In this section we discuss our attempts to develop biological protocols for use with previously described concentric ring bullseye nanostructures.

The initially pursued protocol is shown in Figure 105 below. Shown there are the steps for biofunctionalizing and capturing a targeted antigen. In step (a) the sample is immersed in a physiological solution of similar composition to the solution used in subsequent steps, *e.g.* PBS. In step (b) thiol-conjugated streptavidin (SA-thiol) is added to the sample. The thiol conjugate forms a strong bond to the Au surface and while the binding mechanism remains fully agreed upon (Pensa et al., 2012), the binding strength has been quantified (Xue et al., 2014). In step (c) biotin-conjugated immunoglobin G (biotin-IgG) is added to the sample, facilitating the immobilization of IgG antibodies through the streptavidin-biotin binding. The biotin is conjugated to the Fc region of IgG thereby facilitating the steric availability of the Fab region, which is specific to the targeted antigen. In step (d) the targeted antigen is added and is captured by the IgG. In step (e) the final configuration is measured for both wet and dry cases.

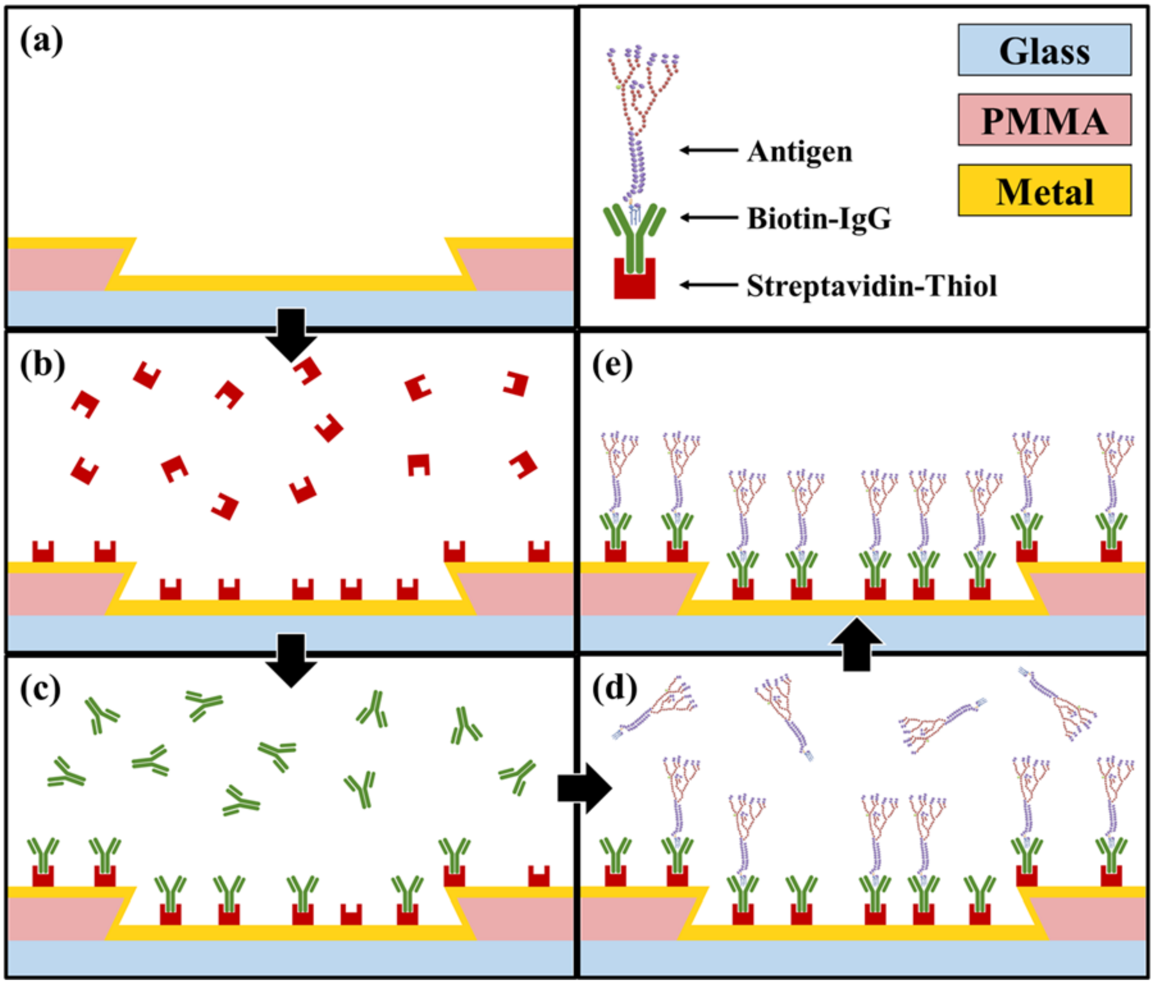

Figure 105. Antigen capture schematic. (a) Start by measuring the sample baseline with physiological liquid, (b) add SA-thiol, (c) add biotinylated-IgG specific to targeted antigen, (d) add antigen, and (e) record final configuration both wet and dry.

A blocking step is commonly incorporated after step (b) or (c) as a way of preventing non-specific binging, especially if the antigen-containing solution also contains other proteins, as real physiological samples do. The transmittance was recorded at each step, a total of 6 times in order to view any potential changes particular to each step. The anticipated detection mechanism, described in section 3.5.2, was a redshift in wavelength of minima and maxima in the transmittance spectra due to the material immobilizing at the structure surface, given that hydrated proteins have a typical index of refraction of *n*=1.45 (Vörös, 2004).

An experiment was conducted to show the immobilization of biotinylated-IgG for a sample with SA-thiol compared with a control sample with SA-thiol. Figure 106 below transmittance spectra for incident white light through arrays of bullseye with corresponding gap size 400 nm, 500 nm, 600 nm, and 700 nm. These samples have Au metallic layer and were measured with an Ocean optics USB2000 spectrometer.

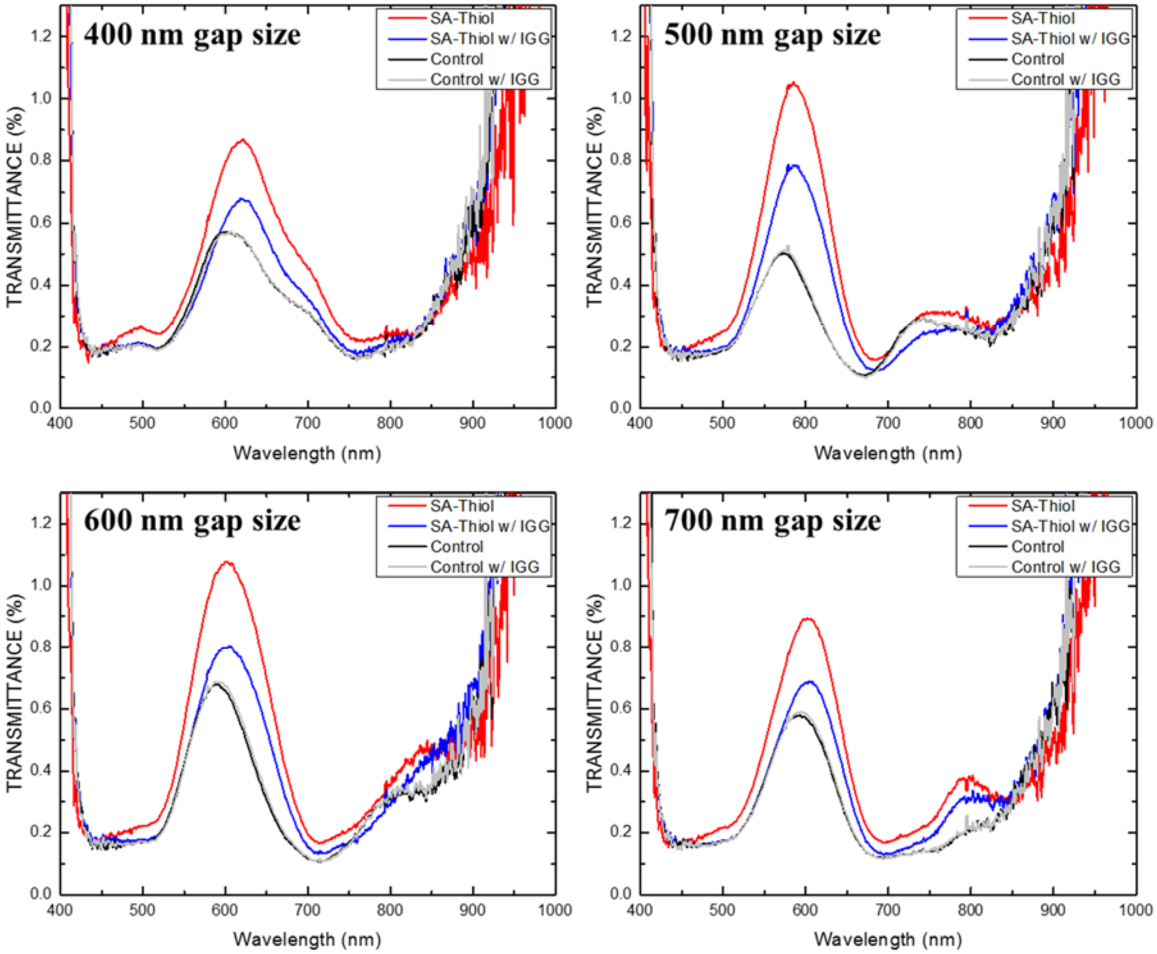

Figure 106. Transmittance before and after IgG. Plotted are the transmittances of four bullseye arrays of different gap sizes for 2 separate chips (8 regions in total). For each sizing, spectra were measured before and after the addition of biotin-IgG to a sample with previously added SA-thiol and a control sample without previously added SA-thiol.

There was an observable difference in the transmittance for the sample with SA-thiol compared to relatively no change for the control sample. The change in the SA-thiol bearing sample predominately preserved the wavelengths of the spectral features and therefore is not consistent with the redshift anticipated for a surface plasmon mediated changed. It is worth restating that the USB2000 spectrometer used has relatively lower intensity sensitivity and, along with lower transmitted sample intensities, resulted in relatively high noise data for wavelengths above 800 nm, where there may exist important spectral features. Additionally, since the samples were made with Au, there is a falsely inflated peak in transmittance between 500 nm and 700 nm, indicating a possible source of surface plasmon dissipation. There is a consistent observable difference in the samples with and without SA-thiol before the addition of IgG, as is expected do the immobilization of the SA-thiol.

Similar tests were performed for different samples and equipment, primarily to investigate the potential impact of a more sensitive spectrometer. An experiment was run adding PBS to a sample, then adding SA-thiol, and finally adding biotin-IgG. Figure 107 shows the transmittances (a) before and after adding SA-thiol and (b) before and after adding the biotin-IgG. While there is a discernable shift from the binding of SA-thiol, the shift from the IgG is in the opposite direction than SPR interaction would indicate, likely due to the dissociation of unbound SA-thiol on the sample surface.

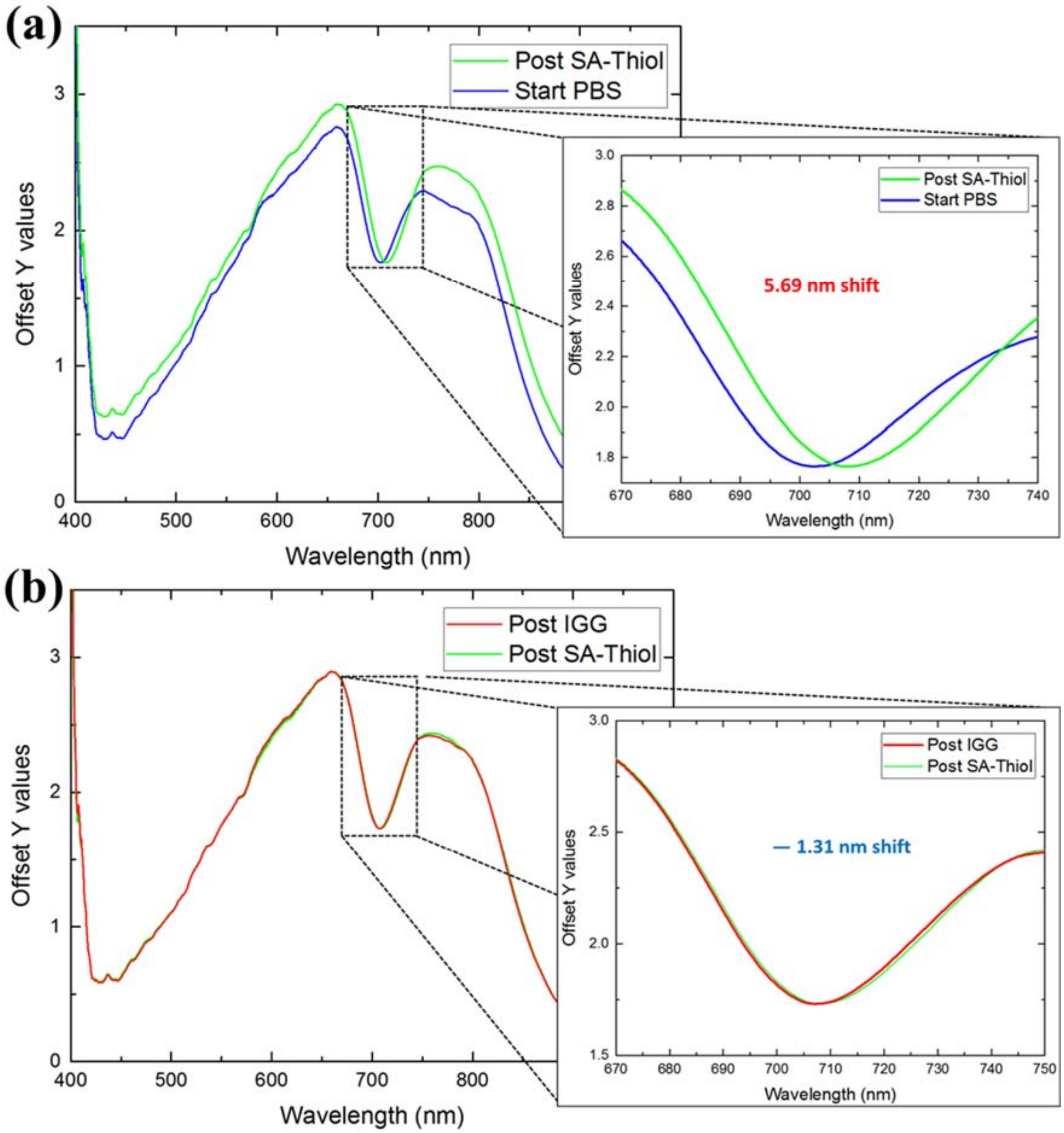

Figure 107. Transmittances post- SA-thiol and IgG. (a) before and after addition of SA-thiol and (b) before and after the addition of biotin-IgG.

Since the detection of biotin-IgG binding was not evident, this combination of structure, biological assay and detection method were incapable of biofunctionalized biosensing. The next section describes some attempted signal enhancement schemes investigate in effort to realize biosensing capability. The remains a vast parameter space to be explored for biosensing experimentation without such enhancement schemes, some of which are highlighted in section 3.7

3.6 Signal Enhancement Schemes

3.6.1 Metal Nanoparticles

Nanoparticles have been the subject of much interest and application for their ability to enhance chemical and biological detection (Belushkin et al., 2018; Farka et al., 2017). This enhancement is due of electric fields of localized surface plasmon resonances of the nanoparticles interacting with nearby materials. Since many techniques are available to conjugate nanoparticles to antibodies or ligands, the localized field enhancement of nanoparticles can be brought in the vicinity of and immobilized to regions were the effects can be measured. An example of protocol for nanoparticle enhanced detection is shown in Figure 108 below.

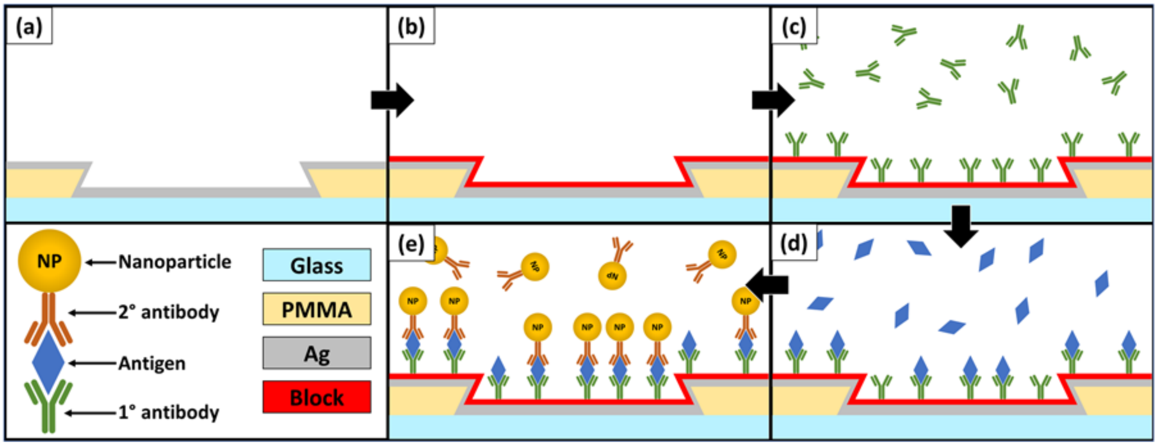

Figure 108. Nanoparticle biosensing schematic. Steps to immobilize a nanoparticle to a surface contingent upon the presence of the targeted antigen.

This protocol can be implemented as a way detecting antigen presence when the antigen itself does not lead to a detectable change for the given measurement. From Figure 108 the steps are: (a) prepare the structure, (b) block the surface (if material degradation is a concern), (c) functionalize a primary antibody to the surface or to the blocking layer, (d) add in the solution containing the antigen, and (e) add a nanoparticle conjugated with a secondary antibody against a different region of the antigen from the primary antibody. As a first test, we directly bound thiol conjugated gold nanoparticles (AuNPs) to the Au surface of a bullseye array. An SEM image of a bullseye with immobilized Au nanoparticle is shown in Figure 109 below.

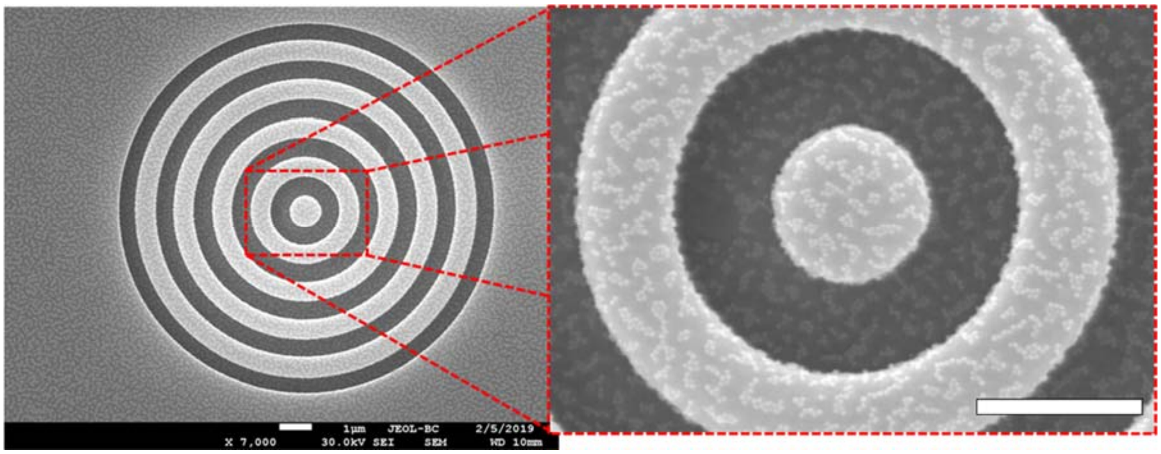

Figure 109. Au nanoparticles on a bullseye. AuNPs were conjugated with thiol and bound to the surface. Inset image is 5× zoom and both images have an inset scalebar of 1 µm.

The transmittance through the sample was measured before and after the AuNP functionalization in order to investigate potential changes in spectral features. A relatively large redshift of 18.73 nm was observed for a minimum shown in Figure 110.

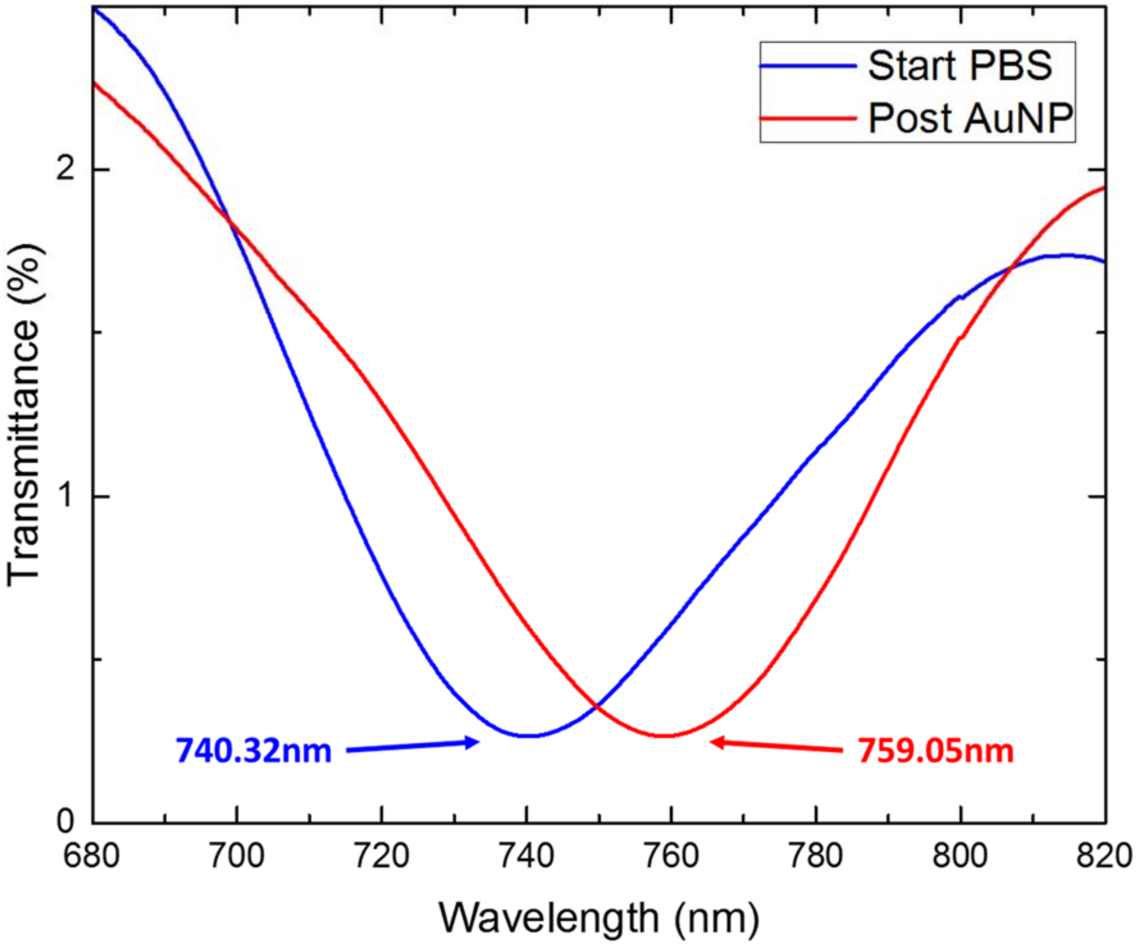

Figure 110. Au nanoparticle redshift. Plotted are minimum transmittance values for a sample before (blue) and after (red) biofunctionalization of bullseye array with thiol conjugated AuNP.

Next we elaborated the AuNP capture protocol to included SA-thiol and biotinylated-IgG biofunctionalization steps to capture a AuNP conjugated 2° antibody. A 1° antibody was selected directly against the 2° antibody in order to test just the positive antigen case, while forgoing the antigen inclusion for sake of simplicity. There was a relatively small, though non-negligible, redshift for transmittance features observed, as shown in Figure 111 below. The plotted transmittance ranges and wavelength ranges were chosen to both span 0.8% and 125 nm, respectively.

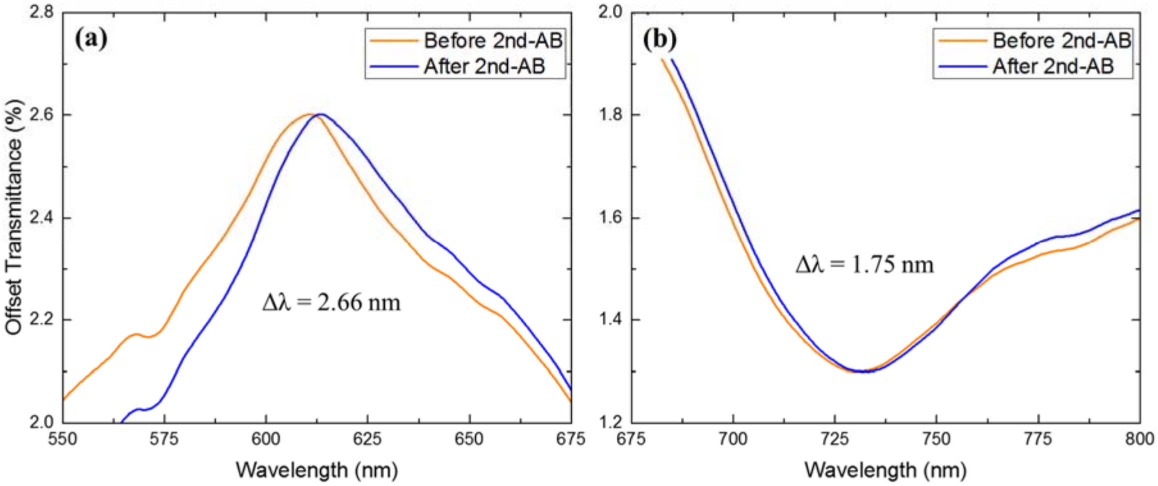

Figure 111. 2° antibody conjugated AuNP capture. Measured transmittances (offset) through a biofunctionalized bullseye array before and after the addition and capture of a secondary antibody for (a) a maximum and (b) a minimum with changes of 2.66 nm and 1.75 nm, respectively.

The use of nanoparticle conjugated antibodies remains an attractive option for enhancing a detection mechanism. With improvement on the plasmon-modulated optical filtering of the bullseye structure, enhancement of redshifts through nanoparticles should be investigated further. Once such transmittance changes would be observed, it will be necessary to compare the observed change to a suitable reference, such as a planar gold film, in order to determine if and what added benefit the bullseye structure has.

3.6.2 Quantum Dots

Quantum dots have become a widely employed means for imaging and biosensing devices (Ma et al., 2018; Park et al., 2017; Singh et a., 2018; Hong et al., 2018). Since the emission intensity of quantum dots scales monotonically with the excitation intensity, the large electric near-fields of surface plasmons of nearby metals have been used to enhance quantum dot emission (Gryczynski et al., 2005; Sadeghi et al., 2014; Zhang et al., 2018; Wu et al., 2011; Park et al, 2017). Quantum dots are an attractive option for use in our efforts to develop a plasmonic-based biosensing device, in a similar protocol to that shown for nanoparticles in Figure 108. The primary difference in the use of quantum dots is that the enhancement effect would theoretically be that experienced within the quantum dots. Furthermore, this would potentially enable us to demonstrate biosensing phenomena with a binary determination of whether the quantum dot emission signature is measured. This could be achieved with our structure in two ways: 1) by observing a peak in recorded spectra at the quantum dot's characteristic emission wavelength or 2) by imaging a sample functionalized with quantum dots and by using image analysis to locate quantum dot emitters. In either case, the spectra or images collected would need to be compared with an appropriate control sample in order to prove the benefit of the accompanying structure.

It is common for fluorescent microscopes to use optical filters and narrowband light sources to selectively illuminate fluorescent species with certain wavelengths that align with their excitation spectrum. Filters are similarly used in fluorescence microscopy to differentiate the emission wavelength from surrounding light or background. We implemented such filtering and light sources in our experiments.

For the experiments described herein we used CdSSe/ZnS core-shell semiconductor quantum dots with peak emission at 625 nm and FWHM of 23 nm (DiagNano, Creative Diagnostics). For illumination, we used a nominally 405 nm collimated LED with FWHM of 12 nm and max beam power of 450mW (Thorlabs). Two additional filters were used for these experiments; a 495 nm long-pass filter and a 410 nm bandpass filter.

While the quantum dots have high fluorescent efficiency, the intensity of quantum dot emission is still much smaller than the illuminating intensity, even for large concentrations of quantum dots. Therefore, the long-pass filter was used to block the higher intensity 405 nm LED in order to allow investigation of the of spectral features above the 495 nm cutoff wavelength. At the larger integration times used (≥100 ms), higher order wavelength peaks become prominent as can be seen in the orange curve of Figure 112 below. There the principle 405 nm peak (violet) is shown with a normalized scale of the same light-source after the 495 nm long-pass filter (orange) for a much larger integration time.

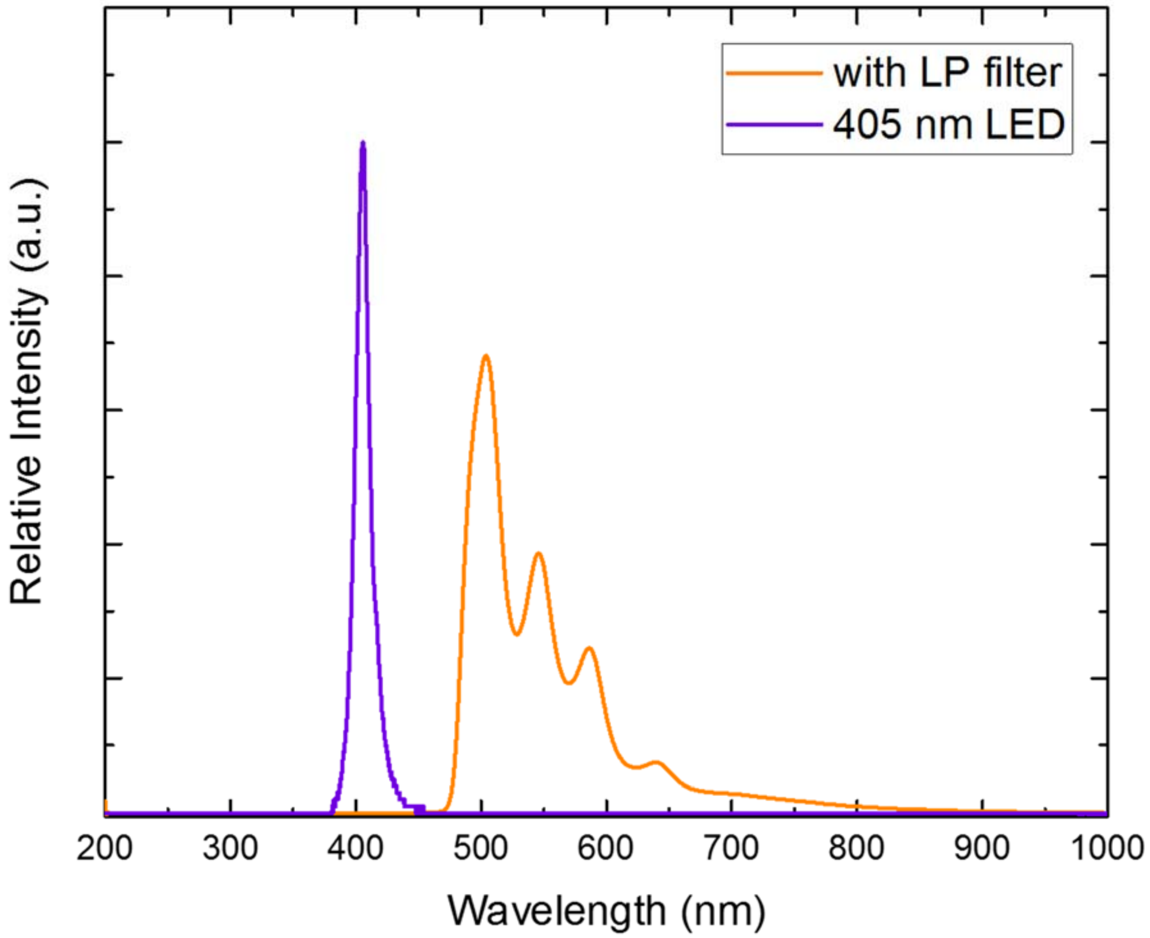

Figure 112. 405nm LED and long-pass filter. Relative transmitted counts for integration times 10 ms and lower power (violet) and maximum power, 1 s, and with the 495 nm long-pass filter (orange).

In order to eliminate these higher wavelength peaks from the light source, a band-pass filter with a 410 nm center-wavelength and 10 nm FWHM was used. As mentioned above, both spectra and images were collected for a series of experiments with the quantum dots. As a reference Figure 113 below shows a schematic of the TL setup and images for different filter configurations for dispersed quantum dots on glass. The integration times and filter configurations are labeled for each imaged.

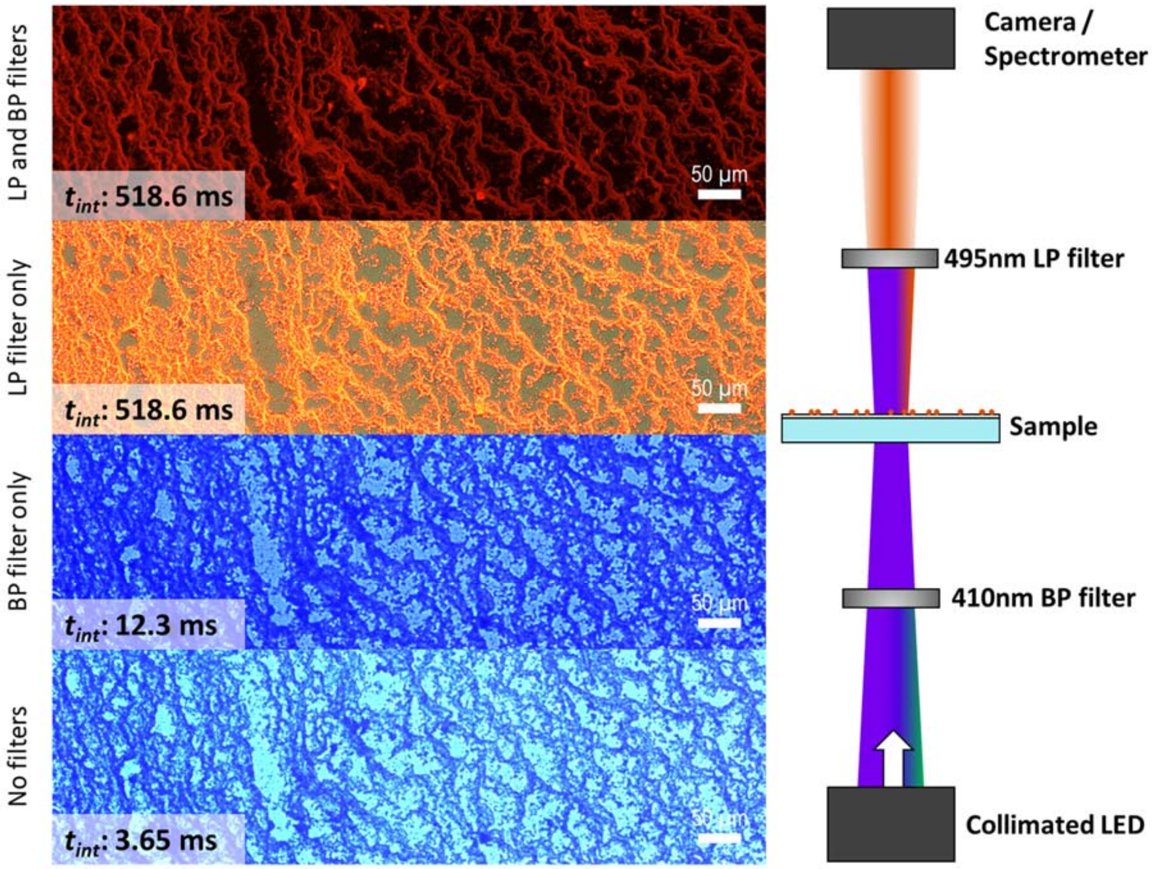

Figure 113. Quantum dots on glass with filters.

In Figure 113 the relative integration times used of for the images with and without the long-pass filter emphasize the relative intensities of the light source and quantum dot emitted intensities. If quantum dots were used in an experiment where the was a measurable difference in the emitted intensity from plasmon-coupled enhancement, then the different integration times for similarly saturated images would also be required. By using the saturation setting on the Leica microscope (to show when the camera pixels saturate), images of dispersed quantum dots with and without adjacent bullseye structures can be taken at similar saturation levels for their respective intensities. Then the relative integration times for the images could be used for a quantitative comparison of quantum dot emission, to demonstrate the occurrence of surface plasmon-mediated enhancement. The relative emission intensity could be similarly, and more accurately, quantified by comparison of transmitted counts measured with a spectrometer.

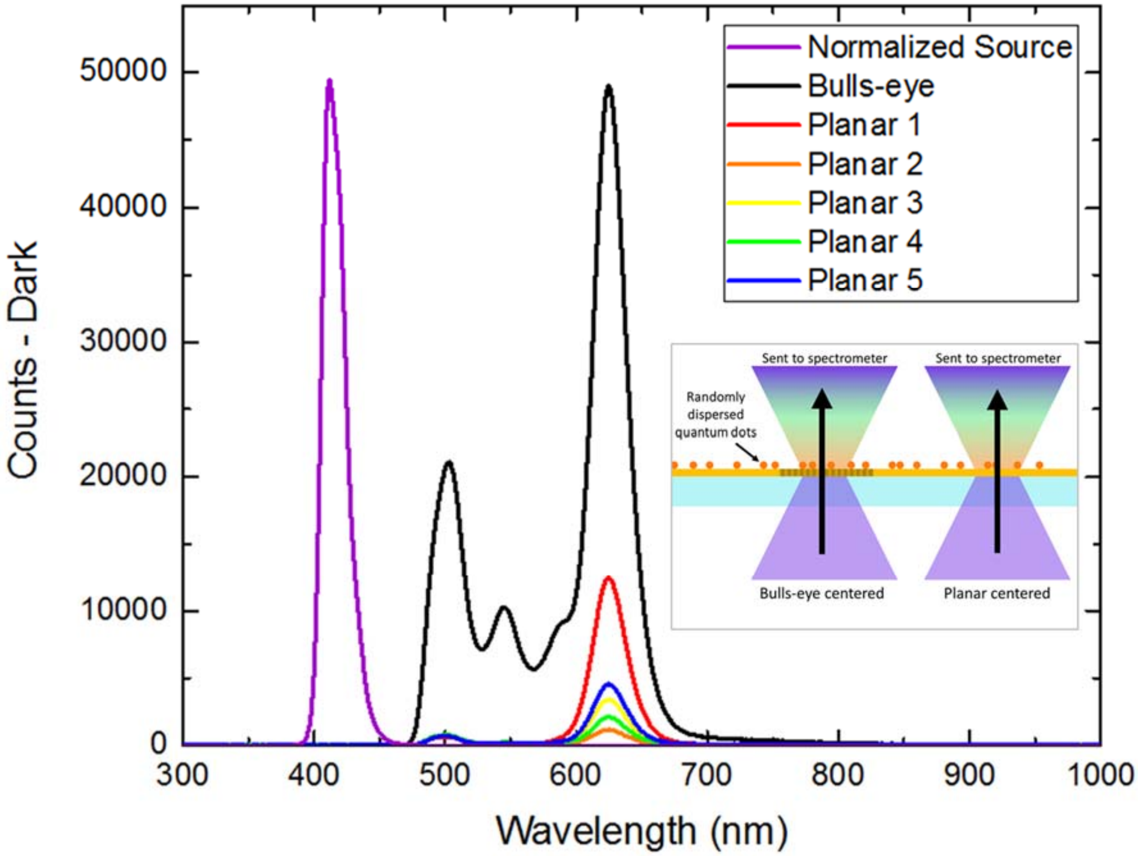

Figure 114. Quantum dots transmitted light. Shown are spectra for the normalized LED (violet), and quantum dots above a bullseye array (black) and planar regions (red, orange, yellow, green, blue).

An example of comparing the transmitted counts is shown in Figure 114 above, alongside the normalized illumination source spectra. This plot shows the transmitted light for regions centered on an array of bullseye structures (black) and for five different regions above planar metal film. All spectra show a dominant peak at the 625 nm quantum dot emission peak and also the tail peaks of the LED light source. While the bulls-eye centered 625 nm peak is larger than the planar values, it is likely predominantly due to the fact that more light is able to pass through the bullseye's thinner metal sidewall regions, rather than an enhancement effect. Again, if there is to be any enhancement demonstrated then there needs to be an appropriate control for comparison.

We also investigated the relative intensities of bullseye-centered and planar-centered for reflected light, this time with both long-pass and short-pass filters, shown in Figure 115.

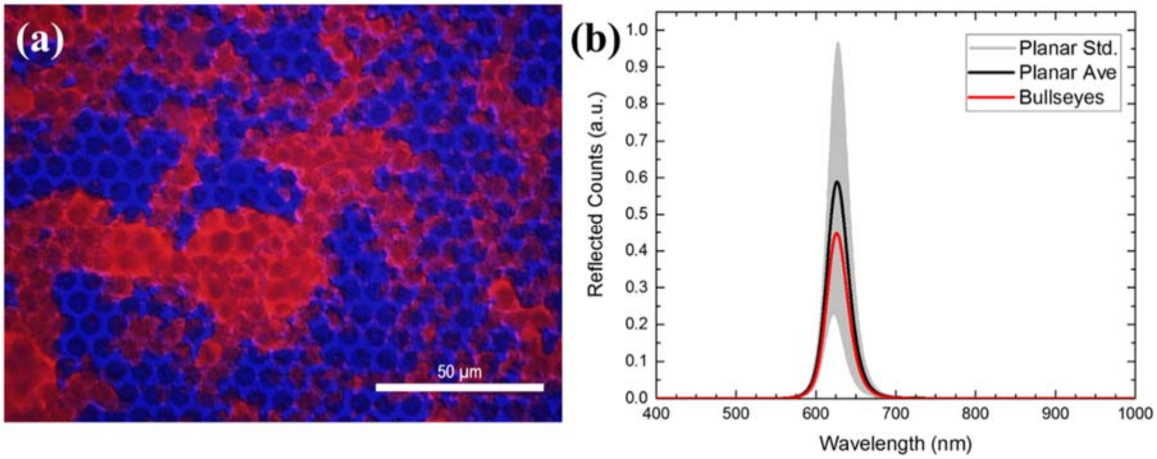

Figure 115. Quantum dot reflected light. (a) Compiled image of 625 nm emitting quantum dots and 405 nm LED through bullseyes. (b) Reflected counts spectra above

The image in Figure 115a was compiled for the quantum dots image with the long-pass filter overlaid on the LED dominated image without the long-pass filter. The reflected counts were lower than the average of eight different planar region, though the variation is large due non-uniform aggregation of this older quantum dots supply. Similar to the transmitted light, this may not be an appropriate reference for determining enhancement phenomena due to the increased scattering of illuminating light for the bullseye array.

In order to justify the use of a quantum dot enhancement scheme, the resulting spectra counts for bullseye samples must be higher than that of a simple planar sample. I feel that the easiest example of this by comparing quantum dot emission counts from the same substrate with a sufficiently thick metal layer to allow the same biofunctionalization used for the nanostructured sample. Otherwise, the presence of the emission peak for them quantum dots, while an attractive detection strategy on its own, would not be demonstrably benefited from the plasmonic nanostructure. For a complete study, one also needs to account for additional spectral variations sometimes observed in quantum dots (Van Sark et al., 2002).

Additional changes worth considering for pursuing quantum dot enhancement schemes are: i) using a different metal, ii) using a different light source, and iii) using different quantum dots. Since enhancement has been observed to be due to coupling to surface plasmons, there needs to be significant surface-plasmon formation at the excitation wavelengths of the quantum dots. That means that it necessary to choose a quantum dot with appropriate excitation wavelengths, the appropriate selection of light source capable of exciting plasmons at those wavelengths, the appropriate selection of metal capable of supporting plasmons with low losses at those wavelengths and appropriate structure that supports plasmon resonances at those wavelengths. One such change would be the use of Al for the nanostructure's metallic layer, due to know UV plasmonic behavior and enhancement of quantum dots (Kannegulla et al., 2017).

3.7 Discussion and Future Works

3.7.1 Additional Features

During optical investigation of bullseye structures, localized bright spots were observed for focal planes above and below the sample surface. This focusing of light has been previously reported and described in concentric ring plasmonic nanostructures (Cao et al., 2016; Liu et al., 2011; Aouani et al., 2011).

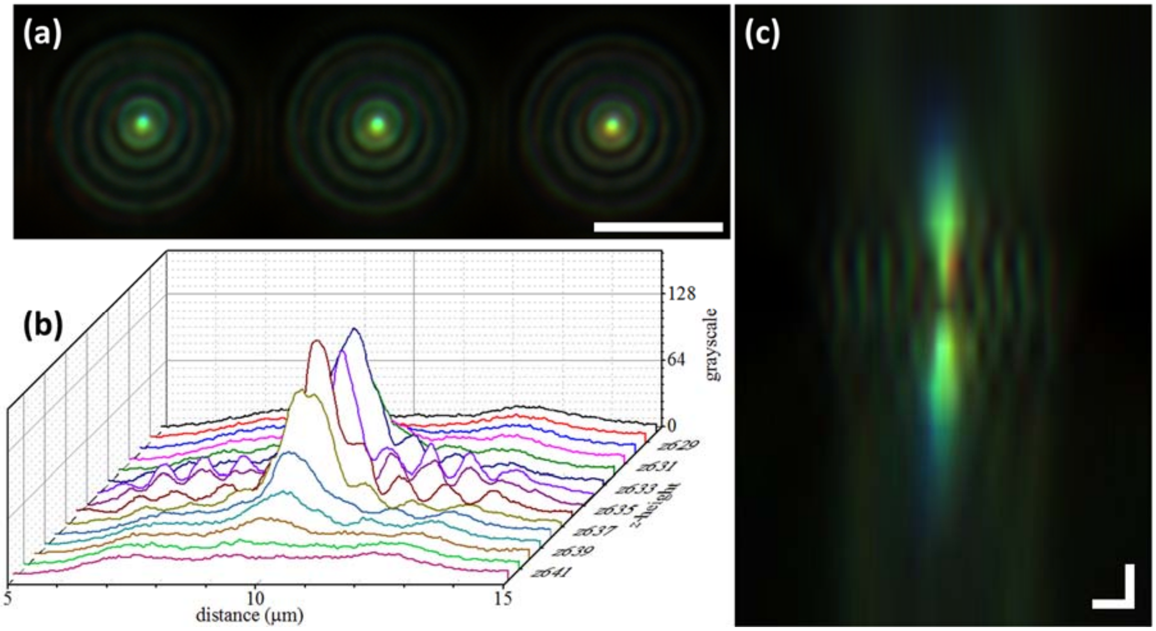

Figure 116. Bullseye light focusing. (a) optical image of three adjacent bullseyes at a focal plane slight above the sample surface with 5um scalebar. (b) Waterfall plot of greyscale pixel values for a centered line cut through bullseye images for focal distances above and below the sample surface. (c) Compiled line cut RBG pixel values of different focal distances, centered on sample surface with 1 µm x & y scale bar. Credit Yitzi Calm.

Figure 116 above show images this light focusing phenomenon. Image (c) is as if looking at a cross-sectional image of the light at different focal distances. This focusing property has been previously studied for its potential applications in superresolution optical microscopy and even enhancing the fluorescent intensity and directionality of molecular detection in fluorescent microscopy. This remains an attractive feature for further investigation in developing the bullseye plasmonic biosensor.

Another feature observed and worth mentioning was the observation of quantum dots emission localized to between the concentric ring trenches, as opposed to within the trenches. This was observed for Al metallic structures and is shown in Figure 117 below.

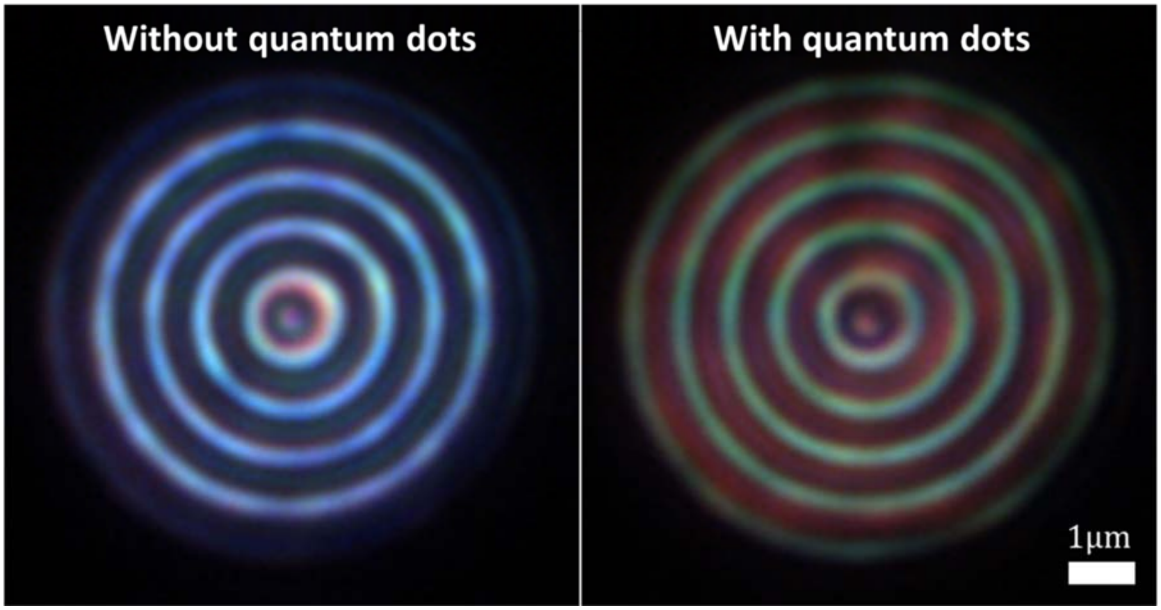

Figure 117. Al bullseye with & without quantum dots. Images of transmitted light from bottom side incident white light though Al bullseye structure without (left) and with (right) addition of 625 nm emission peak quantum dots.

The image before the addition of the quantum dots appears blue by eye, while the image with the quantum dots shows the approximately red color of the quantum dots and an apparently green color where the blue was emanating from, which may be indicative of the increased quantum dot absorbance at smaller wavelengths. Since simulations show increased electric fields within the concentric ring trenches the apparent quantum dot emission specific the between the trenches suggest further analysis, including the investigation of possible liquid loading issues.

3.7.2 The Future of the Project

In this project there has been much progress towards the understanding and development of a plasmonic-based biosensing structure. The experimentation and results discussed herein have demonstrated a number of important methods and material properties that are valuable towards achieving a biosensing device, incorporating the promising plasmonic-based structures described.

As an end to this chapter, I will provide a list of specific recommendations to most succinctly motivate future progress and as a summary observation. They are as follows:

a) When exploring new materials or structural parameters, first test a samples sensitivity by measuring the change in spectral features *vs.* varying index of refraction materials.
b) Use the angled deposition tool shown in Figure 55 to have higher control of the ratio of planar to side-wall metal thicknesses. Good planar and side-wall thickness are near 150 nm and 50 nm, respectively. This will be more useful for thicker PMMAs.
c) Further test Ag's degradation in physiological solutions, with and without the application of the first biofunctionalization. This should include a longer inspection run by BioNavis (~4 h) and before and after imaging by AFM and/or SEM.
d) Perform photolithography for different process parameters and sensitivity testing of those samples. Use the photomask used to produce the sample shown in Figure 91.

e) Replicate previously reported functionalization protocols for oxides, particularly with the inclusion of a silane functional group. This may be important for Al-based samples and Ag-based sample with a thin (~5 nm) protective Al_2O_2 or SiO_2 layer.

f) Shorten the functionalization times down from 1 h to 5 min. As can be seen in Figure 43, the time from injection to stabilization is approximately 1 min. Make sure that this value remains constant for different experiments.

g) Test spectral changes for objective with different NAs and similar magnifications.

h) Test influence of metal nanoparticles for metals different than that in the sample.

i) Use Al-based structures with quantum dots that excite in the UV range.

4. Summary

In Chapter 1 we have motivated the importance of biosensing devices, referenced their growing interest, and the benefit that has occurred through the incorporation nanostructures and other nanoscale properties. Chapter 2 describes our research involving a nanogap coaxial electrode architecture. Chapter 3 describes our research involving a concentric ring plasmonic architecture.

We have discussed the development, characterization and experimentation of these two nanoscale structures towards use in a biosensing device. We describe the tools and techniques used in fabrication of nanoscale features and show how precise manipulation of these features can translate to significant changes to transduced signal. We discuss the importance and methods in which the transduced signals are processed and presented.

Included is a thorough inclusion and review of relevant literature as it pertains to process engineering considerations and device capabilities discussed throughout this thesis. The results and progresses contained within this thesis are able to advance the understanding of biosensing-inspired nanostructures.

5. Bibliography

Akter, Sanjida, and S. M. Abdur Razzak. 2019. “Highly Sensitive Open-Channels Based Plasmonic Biosensor in Visible to near-Infrared Wavelength.” *Results in Physics* 13 (May): 102328. https://doi.org/10.1016/j.rinp.2019.102328.

Anker, Jeffrey N, W Paige Hall, Olga Lyandres, Nilam C Shah, Jing Zhao, and Richard P Van Duyne. 2008. “<Anker2008.Pdf>.” *Nature Materials* 7 (June): 8–10. https://doi.org/10.1038/nmat2162.

Aouani, Heykel, Oussama Mahboub, Nicolas Bonod, Eloïse Devaux, Evgeny Popov, Hervé Rigneault, Thomas W. Ebbesen, and Jérôme Wenger. 2011. “Bright Unidirectional Fluorescence Emission of Molecules in a Nanoaperture with Plasmonic Corrugations.” *Nano Letters* 11 (2): 637–44. https://doi.org/10.1021/nl103738d.

Archibald, Michelle M., Binod Rizal, Timothy Connolly, Michael J. Burns, Michael J. Naughton, and Thomas C. Chiles. 2015. “A Nanocoaxial-Based Electrochemical Sensor for the Detection of Cholera Toxin.” *Biosensors and Bioelectronics* 74 (December): 406–10. https://doi.org/10.1016/J.BIOS.2015.06.069.

Arlett, J. L., E. B. Myers, and M. L. Roukes. 2011. “Comparative Advantages of Mechanical Biosensors.” *Nature Nanotechnology* 6 (4): 203–15. https://doi.org/10.1038/nnano.2011.44.

Arroyo-Currás, Netzahualcóyotl, Karen Scida, Kyle L. Ploense, Tod E. Kippin, and Kevin W. Plaxco. 2017. “High Surface Area Electrodes Generated via Electrochemical Roughening Improve the Signaling of Electrochemical Aptamer-Based Biosensors.” *Analytical Chemistry* 89 (22): 12185–91. https://doi.org/10.1021/acs.analchem.7b02830.

Baragiola, R. A., S. M. Ritzau, R. C. Monreal, C. A. Dukes, and P. Riccardi. 1999. “Mechanisms for Ion-Induced Plasmon Excitation in Metals.” *Nuclear Instruments and Methods in Physics Research, Section B: Beam Interactions with Materials and Atoms* 157 (1–4): 110–15. https://doi.org/10.1016/S0168-583X(99)00430-9.

Bauch, Martin, Koji Toma, Mana Toma, Qingwen Zhang, and Jakub Dostalek. 2014. “Plasmon-Enhanced Fluorescence Biosensors: A Review.” *Plasmonics* 9 (4): 781–99. https://doi.org/10.1007/s11468-013-9660-5.

Belushkin, Alexander, Filiz Yesilkoy, and Hatice Altug. 2018. “Nanoparticle-Enhanced Plasmonic Biosensor for Digital Biomarker Detection in a Microarray.” Research-article. *ACS Nano* 12 (5): 4453–61. https://doi.org/10.1021/acsnano.8b00519.

Bergveld, P. 2003. “Thirty Years of ISFETOLOGY.” *Sensors and Actuators B: Chemical* 88 (1): 1–20. https://doi.org/10.1016/s0925-4005(02)00301-5.

Björck, L, and G Kronvall. 1984. “Purification and Some Properties of Streptococcal Protein G, a Novel IgG-Binding Reagent.” *Journal of Immunology (Baltimore, Md. : 1950)* 133 (2): 969–74. https://doi.org/10.1385/1-59259-076-4:281.

Brazaca, L.C., L. Ribovski, B.C. Janegitz, and V. Zucolotto. 2017. “Nanostructured Materials and Nanoparticles for Point of Care (POC) Medical Biosensors.” *Medical Biosensors for Point of Care (POC) Applications*, January, 229–54. https://doi.org/10.1016/B978-0-08-100072-4.00010-1.

Bukasov, Rostislav, Tamer A. Ali, Peter Nordlander, and Jennifer S. Shumaker-Parry. 2010. “Probing the Plasmonic Near-Field of Gold Nanocrescent Antennas.” *ACS Nano* 4 (11): 6639–50. https://doi.org/10.1021/nn101994t.

Cao, Pengfei, Lin Cheng, Xiaoping Zhang, Xuelin Huang, and Hongmei Jiang. 2016. “Near-Infrared Plasmonic Far-Field Nanofocusing Effects with Elongated Depth of Focus Based on Hybrid Au–Dielectric–Ag Subwavelength Structures.” *Plasmonics* 11 (5): 1219–31. https://doi.org/10.1007/s11468-015-0165-2.

Chan, George H., Jing Zhao, George C. Schatz, and Richard P.Van Duyne. 2008. “Localized Surface Plasmon Resonance Spectroscopy of Triangular Aluminum Nanoparticles.” *Journal of Physical Chemistry C* 112 (36): 13958–63. https://doi.org/10.1021/jp804088z.

Chang, Chiao Yun, Hsiang Ting Lin, Ming Sheng Lai, Teng Yi Shieh, Chien Chung Peng, Min Hsiung Shih, and Yi Chung Tung. 2018. “Flexible Localized Surface Plasmon Resonance Sensor with Metal–Insulator–Metal Nanodisks on PDMS Substrate.” *Scientific Reports* 8 (1): 1–8. https://doi.org/10.1038/s41598-018-30180-8.

Chen, Tianhong, Yan Hong, and Björn M. Reinhard. 2015. “Probing DNA Stiffness through Optical Fluctuation Analysis of Plasmon Rulers.” *Nano Letters* 15 (8): 5349–57. https://doi.org/10.1021/acs.nanolett.5b01725.

Chen, Xing, Zheng Guo, Gui Mei Yang, Jie Li, Min Qiang Li, Jin Huai Liu, and Xing Jiu Huang. 2010. “Electrical Nanogap Devices for Biosensing.” *Materials Today* 13 (11): 28–41. https://doi.org/10.1016/S1369-7021(10)70201-7.

Chen, Y., R. S. Zheng, D. G. Zhang, Y. H. Lu, P. Wang, H. Ming, Z. F. Luo, and Q. Kan. 2011. “Bimetallic Chips for a Surface Plasmon Resonance Instrument.” *Applied Optics* 50 (3): 387–91. https://doi.org/10.1364/AO.50.000387.

Chung, Taerin, Seung Yeol Lee, Eui Young Song, Honggu Chun, and Byoungho Lee. 2011. “Plasmonic Nanostructures for Nano-Scale Bio-Sensing.” *Sensors* 11 (11): 10907–29. https://doi.org/10.3390/s111110907.

Cooper, M., and Eric Westhof. 2007. “Recognition Highlights and Commentaries A Tale in Molecular Recognition : The Hammerhead Ribozyme.” *Journal of Molecular Recognition*, no. November 2006: 1–3. https://doi.org/10.1002/jmr.

D'Imperio, L.A., A.E. Valera, J.R. Naughton, M.M. Archibald, J.M. Merlo, T.J. Connolly, M.J. Burns, T.C. Chiles, and M.J. Naughton. 2019. "An Extended Core Nanocoax Pillar Architecture for Enhanced Molecular Detection." *Biosensors and Bioelectronics* 134. https://doi.org/10.1016/j.bios.2019.03.045.

Digital Science & Research Solutions, Inc. 2019. "Dimensions." 2019. https://app.dimensions.ai/discover/publication.

Dong, Jiangli, Yaxin Zhang, Yajun Wang, Fan Yang, Shiqi Hu, Yaofei Chen, Wenguo Zhu, et al. 2019. "Side-Polished Few-Mode Fiber Based Surface Plasmon Resonance Biosensor." *Optics Express* 27 (8): 11348. https://doi.org/10.1364/oe.27.011348.

Drachev, Vladimir P., Vishal C. Nashine, Mark D. Thoreson, Dor Ben-Amotz, V. Jo Davisson, and Vladimir M. Shalaev. 2005. "Adaptive Silver Films for Detection of Antibody-Antigen Binding." *Langmuir* 21 (18): 8368–73. https://doi.org/10.1021/la0502490.

Dubois, Valentin, Simon J. Bleiker, Göran Stemme, and Frank Niklaus. 2018. "Scalable Manufacturing of Nanogaps." *Advanced Materials* 30 (46): 1–18. https://doi.org/10.1002/adma.201801124.

Erickson, Harold P. 2009. "Size and Shape of Protein Molecules at the Nanometer Level Determined by Sedimentation, Gel Filtration, and Electron Microscopy." *Biological Procedures Online* 11 (1): 32–51. https://doi.org/10.1007/s12575-009-9008-x.

Etin, A. E., Ahmet Ali Yanik, Cihan Yilmaz, Sivasubramanian Somu, Ahmed Busnaina, and Hatice Altug. 2011. "Monopole Antenna Arrays for Optical Trapping, Spectroscopy, and Sensing." *Applied Physics Letters* 98 (11): 2–4. https://doi.org/10.1063/1.3559620.

European Observatory on Health Systems and Policies, and World Health Organization. 2016. "Ensuring Innovation in Diagnostics for Bacterial Infection," 1–317.

Fan, Xudong, Ian M. White, Siyka I. Shopova, Hongying Zhu, Jonathan D. Suter, and Yuze Sun. 2008. "Sensitive Optical Biosensors for Unlabeled Targets: A Review." *Analytica Chimica Acta* 620 (1–2): 8–26. https://doi.org/10.1016/j.aca.2008.05.022.

Farka, Zdeněk, Tomáš Juřík, David Kovář, Libuše Trnková, and Petr Skládal. 2017. "Nanoparticle-Based Immunochemical Biosensors and Assays: Recent Advances and Challenges." *Chemical Reviews* 117 (15): 9973–10042. https://doi.org/10.1021/acs.chemrev.7b00037.

Fedyanin, Dmitry Yu, and Yury V. Stebunov. 2015. "All-Nanophotonic NEMS Biosensor on a Chip." *Scientific Reports* 5: 1–12. https://doi.org/10.1038/srep10968.

Feng, Yanxiao, Yuechuan Zhang, Cuifeng Ying, Deqiang Wang, and Chunlei Du. 2015. "Nanopore-Based Fourth-Generation DNA Sequencing Technology." *Genomics, Proteomics and Bioinformatics* 13 (1): 4–16. https://doi.org/10.1016/j.gpb.2015.01.009.

Ferhan, Abdul Rahim, Joshua A. Jackman, Jae Hyeon Park, and Nam Joon Cho. 2018. "Nanoplasmonic Sensors for Detecting Circulating Cancer Biomarkers." *Advanced Drug Delivery Reviews* 125: 48–77. https://doi.org/10.1016/j.addr.2017.12.004.

Franzen, Stefan, Crissy Rhodes, Marta Cerruti, Ralph W. Gerber, Mark Losego, Jon-Paul Maria, and D. E. Aspnes. 2009. "Plasmonic Phenomena in Indium Tin Oxide and ITO-Au Hybrid Films." *Optics Letters* 34 (18): 2867. https://doi.org/10.1364/ol.34.002867.

Galush, William J., Sarah A. Shelby, Martin J. Mulvihill, Andrea Tao, Peidong Yang, and Jay T. Groves. 2009. "A Nanocube Plasmonic Sensor for Molecular Binding on Membrane Surfaces." *Nano Letters* 9 (5): 2077–82. https://doi.org/10.1021/nl900513k.

Gerard, Davy, and Stephen K. Gray. 2015. "Aluminium Plasmonics." *Journal of Physics D: Applied Physics* 48 (18). https://doi.org/10.1088/0022-3727/48/18/184001.

Gong, Chen, and Marina S. Leite. 2016. "Noble Metal Alloys for Plasmonics." *ACS Photonics* 3 (4): 507–13. https://doi.org/10.1021/acsphotonics.5b00586.

Gong, Sen, Min Hu, Renbin Zhong, Xiaoxing Chen, Ping Zhang, Tao Zhao, and Shenggang Liu. 2014. "Electron Beam Excitation of Surface Plasmon Polaritons." *Optics Express* 22 (16): 19252. https://doi.org/10.1364/oe.22.019252.

Goode, J. A., J. V.H. Rushworth, and P. A. Millner. 2015. "Biosensor Regeneration: A Review of Common Techniques and Outcomes." *Langmuir* 31 (23): 6267–76. https://doi.org/10.1021/la503533g.

Grieshaber, Dorothee, Robert MacKenzie, Janos Vörös, and Erik Reimhult. 2008. "Electrochemical Biosensors - Sensor Principles and Architectures." *Sensors*. https://doi.org/10.3390/s8031400.

Gryczynski, Ignacy, Joanna Malicka, Wen Jiang, Hans Fischer, Warren C W Chan, Zygmunt Gryczynski, Wojciech Grudzinski, and Joseph R. Lakowicz. 2005. "Surface-Plasmon-Coupled Emission of Quantum Dots." *Journal of Physical Chemistry B* 109 (3): 1088–93. https://doi.org/10.1021/jp046173i.

Hastings, J. T., J. Guo, P. D. Keathley, P. B. Kumaresh, Y. Wei, S. Law, and L. G. Bachas. 2007. "Optimal Self-Referenced Sensing Using Long- and Short- Range Surface Plasmons." *Optics Express* 15 (26): 17661. https://doi.org/10.1364/oe.15.017661.

Henzie, Joel, Min Hyung Lee, and Teri W. Odom. 2007. "Multiscale Patterning of Plasmonic Metamaterials." *Nature Nanotechnology* 2 (9): 549–54. https://doi.org/10.1038/nnano.2007.252.

Heo, Chaejeong, Hyejin Park, Yong Tae Kim, Eunha Baeg, Yong Ho Kim, Seong Gi Kim, and Minah Suh. 2016. "A Soft, Transparent, Freely Accessible Cranial Window for Chronic Imaging and Electrophysiology." *Scientific Reports* 6 (February): 1–11. https://doi.org/10.1038/srep27818.

Higson, S. 2012. *Biosensors for Medical Applications*. Woodhead Publishing.

Hill, Ryan T. 2015. “Plasmonic Biosensors.” *Wiley Interdisciplinary Reviews: Nanomedicine and Nanobiotechnology* 7 (2): 152–68. https://doi.org/10.1002/wnan.1314.

Homola, Jiří. 2003. “Present and Future of Surface Plasmon Resonance Biosensors.” *Analytical and Bioanalytical Chemistry* 377 (3): 528–39. https://doi.org/10.1007/s00216-003-2101-0.

Hong, Sungyeap, and Cheolho Lee. 2018. “The Current Status and Future Outlook of Quantum Dot-Based Biosensors for Plant Virus Detection.” *Plant Pathology Journal* 34 (2): 85–92. https://doi.org/10.5423/PPJ.RW.08.2017.0184.

Hsu, Che Wei, and Gou Jen Wang. 2014. “Highly Sensitive Glucose Biosensor Based on Au-Ni Coaxial Nanorod Array Having High Aspect Ratio.” *Biosensors and Bioelectronics* 56: 204–9. https://doi.org/10.1016/j.bios.2014.01.023.

Hsueh, Hsiao Ting, and Chih Ting Lin. 2016. “An Incremental Double-Layer Capacitance of a Planar Nano Gap and Its Application in Cardiac-Troponin T Detection.” *Biosensors and Bioelectronics* 79: 636–43. https://doi.org/10.1016/j.bios.2015.12.105.

Hurst, Sarah J. 2011. *Biomedical Nanotechnology*. Humana Press. https://doi.org/https://doi.org/10.1007/978-1-61779-052-2.

Ilyas, Azhar, Waseem Asghar, Peter B. Allen, Holli Duhon, Andrew D. Ellington, and Samir M. Iqbal. 2012. “Electrical Detection of Cancer Biomarker Using Aptamers with Nanogap Break-Junctions.” *Nanotechnology* 23 (27). https://doi.org/10.1088/0957-4484/23/27/275502.

Carlo, Din Di, Hokwan Kang, Xianghui Zeng, Ki-hun Jeong, and Luke P Lee. 2003. “Immunosensing, Nanogap-based Dielectric " (5 10) 642-5855, 1180–83.

Ives, Megan, Travis M. Autry, Steven T. Cundiff, and Gaël Nardin. 2016. “Direct Imaging of Surface Plasmon Polariton Dispersion in Gold and Silver Thin Films.” *Journal of the Optical Society of America B* 33 (7): C17. https://doi.org/10.1364/josab.33.000c17.

Jeong, Hyeon Ho, Andrew G. Mark, Mariana Alarcón-Correa, Insook Kim, Peter Oswald, Tung Chun Lee, and Peer Fischer. 2016. “Dispersion and Shape Engineered Plasmonic Nanosensors.” *Nature Communications* 7. https://doi.org/10.1038/ncomms11331.

Justino, Celine I.L., Ana R. Gomes, Ana C. Freitas, Armando C. Duarte, and Teresa A.P. Rocha-Santos. 2017. “Graphene Based Sensors and Biosensors.” *TrAC - Trends in Analytical Chemistry* 91: 53–66. https://doi.org/10.1016/j.trac.2017.04.003.

Kabashin, A. V., P. Evans, S. Pastkovsky, W. Hendren, G. A. Wurtz, R. Atkinson, R. Pollard, V. A. Podolskiy, and A. V. Zayats. 2009. "Plasmonic Nanorod Metamaterials for Biosensing." *Nature Materials* 8 (11): 867–71. https://doi.org/10.1038/nmat2546.

Kannegulla, A., Y. Liu, B. Wu, and L. J. Cheng. 2017. "Aluminum Ultraviolet-Visible Plasmonic Arrays for Broadband and Wavelength-Selective Enhancements of Quantum Dot Emission." *Applied Physics Letters* 111 (8): 1–5. https://doi.org/10.1063/1.4986970.

Kasemo, Bengt. 1998. "Biological Surface Science." *Current Opinion in Solid State and Materials Science* 3 (5): 451–59. https://doi.org/10.1016/S1359-0286(98)80006-5.

Khurgin, Jacob B., and Alexandra Boltasseva. 2012. "Reflecting upon the Losses in Plasmonics and Metamaterials." *MRS Bulletin* 37 (8): 768–79. https://doi.org/10.1557/mrs.2012.173.

Klantsataya, Elizaveta, Alexandre François, Agnieszka Zuber, Valeria Torok, Roman Kostecki, and Tanya M. Monro. 2014. "Exposed Core Microstructured Optical Fiber Surface Plasmon Resonance Biosensor." *Optical Fibers and Sensors for Medical Diagnostics and Treatment Applications XIV* 8938 (February): 89380X. https://doi.org/10.1117/12.2039336.

Kottaram Amrithanath, Abhishek, Heming Wei, and Sridhar Krishnaswamy. 2019. "Direct Laser Writing of Optical Biosensor Based on Photonic Floquet Topological Insulator for Protein-Detection," no. March: 33. https://doi.org/10.1117/12.2511158.

Kubo, Wakana, and Shigenori Fujikawa. 2011. "Au Double Nanopillars with Nanogap for Plasmonic Sensor." *Nano Letters* 11 (1): 8–15. https://doi.org/10.1021/nl100787b.

Kyser, D. F., and N. S. Viswanathan. 1975. "Monte Carlo Simulation of Spatially Distributed Beams in Electron-Beam Lithography." *J Vac Sci Technol* 12 (6): 1305–8. https://doi.org/10.1116/1.568524.

Kyu Kim, Sang, Hyunmin Cho, Hye Jung Park, Dohyoung Kwon, Jeong Min Lee, and Bong Hyun Chung. 2009. "Nanogap Biosensors for Electrical and Label-Free Detection of Biomolecular Interactions." *Nanotechnology* 20 (45). https://doi.org/10.1088/0957-4484/20/45/455502.

Larsson, Elin M., Joan Alegret, Mikael Kăll, and Duncan S. Sutherland. 2007. "Sensing Characteristics of NIR Localized Surface Plasmon Resonances in Gold Nanorings for Application as Ultrasensitive Biosensors." *Nano Letters* 7 (5): 1256–63. https://doi.org/10.1021/nl0701612.

Lee, Chang Soo, Sang Kyu Kim, and Moonil Kim. 2009. "Ion-Sensitive Field-Effect Transistor for Biological Sensing." *Sensors* 9 (9): 7111–31. https://doi.org/10.3390/s90907111.

Lee, Kuang Li, Hsuan Yeh Hsu, Meng Lin You, Chia Chun Chang, Ming Yang Pan, Xu Shi, Kosei Ueno, Hiroaki Misawa, and Pei Kuen Wei. 2017. "Highly Sensitive Aluminum-Based Biosensors Using Tailorable Fano Resonances in Capped Nanostructures." *Scientific Reports* 7 (March): 1–14. https://doi.org/10.1038/srep44104.

Lee, Kyeong Seok, and Mostafa A. El-Sayed. 2006. "Gold and Silver Nanoparticles in Sensing and Imaging: Sensitivity of Plasmon Response to Size, Shape, and Metal Composition." *Journal of Physical Chemistry B* 110 (39): 19220–25. https://doi.org/10.1021/jp062536y.

Lee, Seung Woo, and Shelley I. Fried. 2013. "Magnetic Stimulation of Subthalamic Nucleus Neurons Using Micro-Coils for Deep Brain Stimulation." *2013 6th International IEEE/EMBS Conference on Neural Engineering (NER)*, 133–35. https://doi.org/10.1109/NER.2013.6695889.

Lee, Seung Woo, Kyeong Seok Lee, Junhyoung Ahn, Jae Jong Lee, Min Gon Kim, and Yong Beom Shin. 2011. "Highly Sensitive Biosensing Using Arrays of Plasmonic Au Nanodisks Realized by Nanoimprint Lithography." *ACS Nano* 5 (2): 897–904. https://doi.org/10.1021/nn102041m.

Lee, Wonryung, Dongmin Kim, Naoji Matsuhisa, Masae Nagase, Masaki Sekino, George G Malliaras, Tomoyuki Yokota, and Takao Someya. 2017. "Transparent, Conformable, Active Multielectrode Array Using Organic Electrochemical Transistors." *Proceedings of the National Academy of Sciences of the United States of America* 114 (40): 10554–59. https://doi.org/10.1073/pnas.1703886114.

Li, Heng, Shi ren Sun, John Q. Yap, Jiang hua Chen, and Qi Qian. 2016. "0.9% Saline Is Neither Normal Nor Physiological." *Journal of Zhejiang University: Science B* 17 (3): 181–87. https://doi.org/10.1631/jzus.B1500201.

Li, Tao, Wenping Hu, and Daoben Zhu. 2010. "Nanogap Electrodes." *Advanced Materials* 22 (2): 286–300. https://doi.org/10.1002/adma.200900864.

Li, Wanbo, Li Zhang, Jianhua Zhou, and Hongkai Wu. 2015. "Well-Designed Metal Nanostructured Arrays for Label-Free Plasmonic Biosensing." *Journal of Materials Chemistry C* 3 (25): 6479–92. https://doi.org/10.1039/c5tc00553a.

Lin, Vivian Kaixin, Siew Lang Teo, Renaud Marty, Arnaud Arbouet, Christian Girard, Esther Alarcon-Llado, Shu Hua Liu, Ming Yong Han, Sudhiranjan Tripathy, and Adnen Mlayah. 2010. "Dual Wavelength Sensing Based on Interacting Gold Nanodisk Trimers." *Nanotechnology* 21 (30). https://doi.org/10.1088/0957-4484/21/30/305501.

Liu, Na, Thomas Weiss, Martin Mesch, Lutz Langguth, Ulrike Eigenthaler, Michael Hirscher, Carsten Sönnichsen, and Harald Giessen. 2010. "Planar Metamaterial Analogue of Electromagnetically Induced Transparency for Plasmonic Sensing." *Nano Letters* 10 (4): 1103–7. https://doi.org/10.1021/nl902621d.

Liu, Sen, Ziying Wang, Fengjiao Wang, Bo Yu, and Tong Zhang. 2014. "High Surface Area Mesoporous CuO: A High-Performance Electrocatalyst for Non-Enzymatic Glucose Biosensing." *RSC Advances* 4 (63): 33327–31. https://doi.org/10.1039/c4ra04700a.

Liu, Yuxiang, Hua Xu, Felix Stief, Nikolai Zhitenev, and Miao Yu. 2011. "Far-Field Superfocusing with an Optical Fiber Based Surface Plasmonic Lens Made of Nanoscale Concentric Annular Slits." *Optics Express* 19 (21): 20233. https://doi.org/10.1364/oe.19.020233.

Lowe, Christopher R. 1984. "Biosensors." *Trends in Biotechnology* 2 (3): 59–65. https://doi.org/10.1016/0167-7799(84)90011-8.

Luther, Joseph M., Prashant K. Jain, Trevor Ewers, and A. Paul Alivisatos. 2011. "Localized Surface Plasmon Resonances Arising from Free Carriers in Doped Quantum Dots." *Nature Materials* 10 (5): 361–66. https://doi.org/10.1038/nmat3004.

Ma, Fei, Chen chen Li, and Chun yang Zhang. 2018. "Development of Quantum Dot-Based Biosensors: Principles and Applications." *Journal of Materials Chemistry B* 6 (39): 6173–90. https://doi.org/10.1039/c8tb01869c.

MacKay, Scott, Peter Hermansen, David Wishart, and Jie Chen. 2015. "Simulations of Interdigitated Electrode Interactions with Gold Nanoparticles for Impedance-Based Biosensing Applications." *Sensors (Switzerland)* 15 (9): 22192–208. https://doi.org/10.3390/s150922192.

Maldonado, Stephen, Edgardo García-Berríos, Marc D. Woodka, Bruce S. Brunschwig, and Nathan S. Lewis. 2008. "Detection of Organic Vapors and NH3(g) Using Thin-Film Carbon Black-Metallophthalocyanine Composite Chemiresistors." *Sensors and Actuators, B: Chemical* 134 (2): 521–31. https://doi.org/10.1016/j.snb.2008.05.047.

Manesse, Maël, Rosendo Sanjines, Valerie Stambouli, Corentin Jorel, Bernard Pelissier, Marcin Pisarek, Rabah Boukherroub, and Sabine Szunerits. 2009. "Preparation and Characterization of Silver Substrates Coated with Antimony-Boped Sno2 Thin Films for Surface Plasmon Resonance Studies." *Langmuir* 25 (14): 8036–41. https://doi.org/10.1021/la900502y.

Martin, Jerome, and Jerome Plain. 2015. "Fabrication of Aluminium Nanostructures for Plasmonics." *Journal of Physics D: Applied Physics* 48 (18). https://doi.org/10.1088/0022-3727/48/18/184002.

Martinez-Perdiguero, J., A. Retolaza, A. Juarros, D. Otaduy, and S. Merino. 2012. "Enhanced Transmission through Gold Nanohole Arrays Fabricated by Thermal Nanoimprint Lithography for Surface Plasmon Based Biosensors." *Procedia Engineering* 47: 805–8. https://doi.org/10.1016/j.proeng.2012.09.269.

Martinez-Perdiguero, Josu, Aritz Retolaza, Deitze Otaduy, Aritz Juarros, and Santos Merino. 2013. "Real-Time Label-Free Surface Plasmon Resonance Biosensing with Gold Nanohole Arrays Fabricated by Nanoimprint Lithography." *Sensors (Switzerland)* 13 (10): 13960–68. https://doi.org/10.3390/s131013960.

Mauriz, E., M. C. García-Fernández, and L. M. Lechuga. 2016. "Towards the Design of Universal Immunosurfaces for SPR-Based Assays: A Review." *TrAC - Trends in Analytical Chemistry* 79: 191–98. https://doi.org/10.1016/j.trac.2016.02.006.

McFarland, Adam D., and Richard P. Van Duyne. 2003. "Single Silver Nanoparticles as Real-Time Optical Sensors with Zeptomole Sensitivity." *Nano Letters* 3 (8): 1057–62. https://doi.org/10.1021/nl034372s.

McPeak, Kevin M., Sriharsha V. Jayanti, Stephan J.P. Kress, Stefan Meyer, Stelio Iotti, Aurelio Rossinelli, and David J. Norris. 2015. "Plasmonic Films Can Easily Be Better: Rules and Recipes." *ACS Photonics* 2 (3): 326–33. https://doi.org/10.1021/ph5004237.

McPhillips, John, Antony Murphy, Magnus P. Jonsson, William R. Hendren, Ronald Atkinson, Fredrik Höök, Anatoly V. Zayats, and Robert J. Pollard. 2010. "High-Performance Biosensing Using Arrays of Plasmonic Nanotubes." *ACS Nano* 4 (4): 2210–16. https://doi.org/10.1021/nn9015828.

Mehrotra, Parikha, Baibhab Chatterjee, and Shreyas Sen. 2019. "EM-Wave Biosensors: A Review of RF, Microwave, Mm-Wave and Optical Sensing." *Sensors (Switzerland)* 19 (5). https://doi.org/10.3390/s19051013.

Mejía-Salazar, J. R., and Osvaldo N. Oliveira. 2018. "Plasmonic Biosensing." *Chemical Reviews* 118 (20): 10617–25. https://doi.org/10.1021/acs.chemrev.8b00359.

Merlo, Juan M., Fan Ye, Binod Rizal, Michael J. Burns, and Michael J. Naughton. 2014. "Near-Field Observation of Light Propagation in Nanocoax Waveguides." *Optics Express* 22 (12): 14148. https://doi.org/10.1364/OE.22.014148.

Mohammadniaei, Mohsen, Jinho Yoon, Taek Lee, Bapurao G. Bharate, Jinhee Jo, Donghyun Lee, and Jeong Woo Choi. 2018. "Electrochemical Biosensor Composed of Silver Ion-Mediated DsDNA on Au-Encapsulated Bi2Se3 Nanoparticles for the Detection of H2O2 Released from Breast Cancer Cells." *Small* 14 (16): 1–13. https://doi.org/10.1002/smll.201703970.

Morgan, Donald M., and Stephen G. Weber. 1984. "Noise and Signal-to-Noise Ratio in Electrochemical Detectors." *Analytical Chemistry* 56 (13): 2560–67. https://doi.org/10.1021/ac00277a065.

Nakamoto, Kohei, Ryoji Kurita, Osamu Niwa, Toshiyuki Fujii, and Munehiro Nishida. 2011. "Development of a Mass-Producible on-Chip Plasmonic Nanohole Array Biosensor." *Nanoscale* 3 (12): 5067–75. https://doi.org/10.1039/c1nr10883b.

Nanostars, Gold, Srujan K Dondapati, Tapan K Sau, Calin Hrelescu, Thomas a Klar, Fernando D Stefani, and Jochen Feldmann. 2010. "Label-Free Biosensing Based on Single." *ACS Nano* 4 (11): 6318–22.

Naughton, Jeffrey R., Timothy Connolly, Juan A. Varela, Jaclyn Lundberg, Michael J. Burns, Thomas C. Chiles, John P. Christianson, and Michael J. Naughton. 2016. "Shielded Coaxial Optrode Arrays for Neurophysiology." *Frontiers in Neuroscience* 10 (JUN): 1–10. https://doi.org/10.3389/fnins.2016.00252.

Naughton, M. J., K. Kempa, Z. F. Ren, Y. Gao, J. Rybczynski, N. Argenti, W. Gao, et al. 2010. “Efficient Nanocoax-Based Solar Cells.” *Physica Status Solidi - Rapid Research Letters* 4 (7): 181–83. https://doi.org/10.1002/pssr.201004154.

Nehra, Anuj, Sweeti Ahlawat, and Krishna Pal Singh. 2019. “A Biosensing Expedition of Nanopore: A Review.” *Sensors and Actuators, B: Chemical* 284 (December 2018): 595–622. https://doi.org/10.1016/j.snb.2018.12.143.

Otero, Toribio F., Jose G. Martinez, and Kinji Asaka. 2016. “Faradaic and Capacitive Components of the CNT Electrochemical Responses.” *Frontiers in Materials* 3 (February): 1–11. https://doi.org/10.3389/fmats.2016.00003.

Park, Hyun Chul, Isnaeni, Suhyun Gong, and Yong Hoon Cho. 2017. “How Effective Is Plasmonic Enhancement of Colloidal Quantum Dots for Color-Conversion Light-Emitting Devices?” *Small* 13 (48): 1–9. https://doi.org/10.1002/smll.201701805.

Park, Youngrong, Sanghwa Jeong, and Sungjee Kim. 2017. “Medically Translatable Quantum Dots for Biosensing and Imaging.” *Journal of Photochemistry and Photobiology C: Photochemistry Reviews* 30: 51–70. https://doi.org/10.1016/j.jphotochemrev.2017.01.002.

Peale, Robert E., Evan Smith, Christian W. Smith, Farnood Khalilzadeh-Rezaie, Masa Ishigami, Nima Nader, Shiva Vangala, and Justin W. Cleary. 2016. “Electronic Detection of Surface Plasmon Polaritons by Metal-Oxide-Silicon Capacitor.” *APL Photonics* 1 (6). https://doi.org/10.1063/1.4962428.

Peña-Bahamonde, Janire, Hang N. Nguyen, Sofia K. Fanourakis, and Debora F. Rodrigues. 2018. “Recent Advances in Graphene-Based Biosensor Technology with Applications in Life Sciences.” *Journal of Nanobiotechnology* 16 (1): 1–17. https://doi.org/10.1186/s12951-018-0400-z.

Pensa, Evangelina, Emiliano Cortés, Gastón Corthey, Pilar Carro, Carolina Vericat, Mariano H. Fonticelli, Guillermo Benítez, Aldo A. Rubert, and Roberto C. Salvarezza. 2012a. “The Chemistry of the Sulfur-Gold Interface: In Search of a Unified Model.” *Accounts of Chemical Research* 45 (8): 1183–92. https://doi.org/10.1021/ar200260p.

Pines, David, and David Bohm. 1952. “A Collective Description of Electron Interactions - II. Collective vs Individual Particle Aspects of the Interactions.” *Physical Review* 85 (2): 338–53. https://doi.org/https://doi.org/10.1103/PhysRev.85.338.

Pohanka, Miroslav. 2017. “The Piezoelectric Biosensors: Principles and Applications, a Review.” *International Journal of Electrochemical Science* 12 (1): 496–506. https://doi.org/10.20964/2017.01.44.

Politano, Antonio . 2017. “On the Prospect of Bioelectronics and Biosensors with the Novel Topological Phases of Matter.” *International Journal of Biosensors & Bioelectronics* 2 (4): 104–5. https://doi.org/10.15406/ijbsbe.2017.02.00028.

Purohit, Prashant K., Mandar M. Inamdar, Paul D. Grayson, Todd M. Squires, Jané Kondev, and Rob Phillips. 2005. “Forces during Bacteriophage DNA Packaging and Ejection.” *Biophysical Journal* 88 (2): 851–66. https://doi.org/10.1529/BIOPHYSJ.104.047134.

Riedel, Tomáš, František Surman, Simone Hageneder, Ognen Pop-Georgievski, Christa Noehammer, Manuela Hofner, Eduard Brynda, Cesar Rodriguez-Emmenegger, and Jakub Dostálek. 2016. “Hepatitis B Plasmonic Biosensor for the Analysis of Clinical Serum Samples.” *Biosensors and Bioelectronics* 85: 272–79. https://doi.org/10.1016/j.bios.2016.05.014.

Rizal, Binod, Michelle M. Archibald, Timothy Connolly, Stephen Shepard, Michael J. Burns, Thomas C. Chiles, and Michael J. Naughton. 2013. “Nanocoax-Based Electrochemical Sensor.” *Analytical Chemistry* 85 (21): 10040–44. https://doi.org/10.1021/ac402441x.

Rizal, Binod, Juan Merlo, Michael Burns, Thomas Chiles, and Michael J Naughton. 2015. “Nanocoaxes for Optical and Electronic Devices.” *Analyst* 140 (1): 39–58. https://doi.org/10.1039/C4AN01447B.

Roy, Somenath, and Zhiqiang Gao. 2009a. “Nanostructure-Based Electrical Biosensors.” *Nano Today* 4 (4): 318–34. https://doi.org/10.1016/j.nantod.2009.06.003.

Rybczynski, J., K. Kempa, A. Herczynski, Y. Wang, M. J. Naughton, Z. F. Ren, Z. P. Huang, D. Cai, and M. Giersig. 2007. “Subwavelength Waveguide for Visible Light.” *Applied Physics Letters* 90 (2). https://doi.org/10.1063/1.2430400.

Sadeghi, S. M., B. Hood, A. Nejat, R. G. West, and A. Hatef. 2014. “Excitation Intensity Dependence of Plasmonic Enhancement of Energy Transfer between Quantum Dots.” *Journal of Physics D: Applied Physics* 47 (16). https://doi.org/10.1088/0022-3727/47/16/165302.

Saeger, K. E., and J. Rodies. 1977. “The Colour of Gold and Its Alloys - The Mechanism of Variation in Optical Properties.” *Gold Bulletin* 10 (1): 10–14. https://doi.org/10.1007/BF03216519.

Sangeetha, P, and A Vimala Juliet. 2013. “Biosensor for Tuberculosis Detection Using MEMS Device.” *3rd International Conference on Electronics, Biomedical Engineering and Its Applications (ICEBEA). Hong Kong, China*, 26–27.

Sark, Wilfried G.J.H.M. van, Patrick L.T.M. Frederix, Ageeth A. Bol, Hans C. Gerritsen, and Andries Meijerink. 2002. “Blueing, Bleaching, and Blinking of Single CdSe/ZnS Quantum Dots.” *ChemPhysChem* 3 (10): 871–79. https://doi.org/10.1002/1439-7641(20021018)3:10<871::AID-CPHC871>3.0.CO;2-T.

Shim, Joon S., Michael J. Rust, and Chong H. Ahn. 2013. “A Large Area Nano-Gap Interdigitated Electrode Array on a Polymer Substrate as a Disposable Nano-Biosensor.” *Journal of Micromechanics and Microengineering* 23 (3). https://doi.org/10.1088/0960-1317/23/3/035002.

Singh, Kanwar Vikas, Allison M. Whited, Yaswanth Ragineni, Thomas W. Barrett, Jeff King, and Raj Solanki. 2010. "3D Nanogap Interdigitated Electrode Array Biosensors." *Analytical and Bioanalytical Chemistry* 397 (4): 1493–1502. https://doi.org/10.1007/s00216-010-3682-z.

Singh, Radha D., Ruchita Shandilya, Arpit Bhargava, Rajat Kumar, Rajnarayan Tiwari, Koel Chaudhury, Rupesh K. Srivastava, Irina Y. Goryacheva, and Pradyumna K. Mishra. 2018. "Quantum Dot Based Nano-Biosensors for Detection of Circulating Cell Free MiRNAs in Lung Carcinogenesis: From Biology to Clinical Translation." *Frontiers in Genetics* 9 (December): 1–23. https://doi.org/10.3389/fgene.2018.00616.

Sivaraj, Lalitha, Nurul Amziah Md Yunus, Mohd Nazim Mohtar, Samsuzana Abd Aziz, Zurina Zainal Abidin, M. Iqbal Saripan, and Fakhrul Zaman Rokhani. 2016. "Portable Biosensor for Chronic Malaria Detection." *Proceedings - International Symposium on Quality Electronic Design, ISQED* 2016-May: 248–51. https://doi.org/10.1109/ISQED.2016.7479208.

Sjöbring, U, L Björck, and W Kastern. 1991. "Streptococcal Protein G." *The Journal of Biological Chemistry* 266 (1): 399–405. https://doi.org/10.1099/mic.0.039578-0.

Spitzberg, Joshua D., Adam Zrehen, Xander F. van Kooten, and Amit Meller. 2019. "Plasmonic-Nanopore Biosensors for Superior Single-Molecule Detection." *Advanced Materials* 31 (23): 1–18. https://doi.org/10.1002/adma.201900422.

Stepnika, Petr. 2008. *Ferrocenes: Ligands, Materials and Biomolecules*. Edited by Petr Stepnika. Wiley.

Stockman, Mark I., Katrin Kneipp, Sergey I. Bozhevolnyi, Soham Saha, Aveek Dutta, Justus Ndukaife, Nathaniel Kinsey, et al. 2018. "Roadmap on Plasmonics." *Journal of Optics (United Kingdom)* 20 (4). https://doi.org/10.1088/2040-8986/aaa114.

Sun, Yugang, and Younan Xia. 2002. "Increased Sensitivity of Surface Plasmon Resonance of Gold Nanoshells Compared to That of Gold Solid Colloids in Response to Environmental Changes." *Analytical Chemistry* 74 (20): 5297–5305. https://doi.org/10.1021/ac0258352.

Szunerits, Sabine, Xavier Castel, and Rabah Boukherroub. 2008. "Preparation of Electrochemical and Surface Plasmon Resonance Active Interfaces: Deposition of Indium Tin Oxide on Silver Thin Films." *Journal of Physical Chemistry C* 112 (29): 10883–88. https://doi.org/10.1021/jp8025682.

Takahashi, Kazuhiro, Hiroki Oyama, Nobuo Misawa, Koichi Okumura, Makoto Ishida, and Kazuaki Sawada. 2013. "Surface Stress Sensor Using MEMS-Based Fabry-Perot Interferometer for Label-Free Biosensing." *Sensors and Actuators, B: Chemical* 188: 393–99. https://doi.org/10.1016/j.snb.2013.06.106.

Tehrani, Z., G. Burwell, M. A. Mohd Azmi, A. Castaing, R. Rickman, J. Almarashi, P. Dunstan, A. Miran Beigi, S. H. Doak, and O. J. Guy. 2014. "Generic Epitaxial Graphene Biosensors for Ultrasensitive Detection of Cancer Risk Biomarker." *2D Materials* 1 (2). https://doi.org/10.1088/2053-1583/1/2/025004.

Teo, Siew Lang, Vivian Kaixin Lin, Renaud Marty, Nicolas Large, Esther Alarcon Llado, Arnaud Arbouet, Christian Girard, Javier Aizpurua, Sudhiranjan Tripathy, and Adnen Mlayah. 2010. "Gold Nanoring Trimers: A Versatile Structure for Infrared Sensing." *Optics Express* 18 (21): 22271. https://doi.org/10.1364/oe.18.022271.

Toma, Mana, Kyunghee Cho, Jennifer B. Wood, and Robert M. Corn. 2014. "Gold Nanoring Arrays for Near Infrared Plasmonic Biosensing." *Plasmonics* 9 (4): 765–72. https://doi.org/10.1007/s11468-013-9657-0.

Tu, Long, Liang Huang, and Wenhui Wang. 2019. "A Novel Micromachined Fabry-Perot Interferometer Integrating Nano-Holes and Dielectrophoresis for Enhanced Biochemical Sensing." *Biosensors and Bioelectronics* 127 (December 2018): 19–24. https://doi.org/10.1016/j.bios.2018.12.013.

Verellen, Niels, Pol Van Dorpe, Chengjun Huang, Kristof Lodewijks, Guy A.E. Vandenbosch, Liesbet Lagae, and Victor V. Moshchalkov. 2011. "Plasmon Line Shaping Using Nanocrosses for High Sensitivity Localized Surface Plasmon Resonance Sensing." *Nano Letters* 11 (2): 391–97. https://doi.org/10.1021/nl102991v.

Vörös, Janos. 2004. "The Density and Refractive Index of Adsorbing Protein Layers." *Biophysical Journal* 87 (1): 553–61. https://doi.org/10.1529/biophysj.103.030072.

Wang, Guiqiang, Chunnan Wang, Rui Yang, Wenlan Liu, and Shuqing Sun. 2017. "A Sensitive and Stable Surface Plasmon Resonance Sensor Based on Monolayer Protected Silver Film." *Sensors (Switzerland)* 17 (12). https://doi.org/10.3390/s17122777.

Wang, Yu, Adam C. Overvig, Sajan Shrestha, Ran Zhang, Ren Wang, Nanfang Yu, and Luca Dal Negro. 2017. "Tunability of Indium Tin Oxide Materials for Mid-Infrared Plasmonics Applications." *Optical Materials Express* 7 (8): 2727. https://doi.org/10.1364/ome.7.002727.

White, Henry S., and Kim McKelvey. 2018. "Redox Cycling in Nanogap Electrochemical Cells." *Current Opinion in Electrochemistry* 7 (January): 48–53. https://doi.org/10.1016/J.COELEC.2017.10.021.

Whited, Allison M., Kanwar Vikas Singh, David Evans, and Raj Solanki. 2012. "An Electronic Sensor for Detection of Early-Stage Biomarker/s for Ovarian Cancer." *BioNanoScience* 2 (4): 161–70. https://doi.org/10.1007/s12668-012-0049-2.

Williams, Kirt R., K. Gupta, and M. Wasilik. 2003. "Etch Rates for Micromachining Processing - Part II." *Journal of Microelectromechanical Systems* 12 (6): 1689–99. https://doi.org/10.1017/CBO9781107415324.004.

Wolfrum, Bernhard, Enno Kätelhön, Alexey Yakushenko, Kay J. Krause, Nouran Adly, Martin Hüske, and Philipp Rinklin. 2016. "Nanoscale Electrochemical Sensor Arrays: Redox Cycling Amplification in Dual-Electrode Systems." *Accounts of Chemical Research* 49 (9): 2031–40. https://doi.org/10.1021/acs.accounts.6b00333.

Wongkaew, Nongnoot, Marcel Simsek, Christian Griesche, and Antje J. Baeumner. 2018. "Functional Nanomaterials and Nanostructures Enhancing Electrochemical Biosensors and Lab-on-a-Chip Performances: Recent Progress, Applications, and Future Perspective." Review-article. *Chemical Reviews*. https://doi.org/10.1021/acs.chemrev.8b00172.

Wood, Aaron, Syed Barizuddin, Charles M. Darr, Cherian J. Mathai, Alexey Ball, Kyle Minch, Akos Somoskovi, et al. 2019. "Ultrasensitive Detection of Lipoarabinomannan with Plasmonic Grating Biosensors in Clinical Samples of HIV Negative Patients with Tuberculosis." *PLoS ONE* 14 (3): 1–12. https://doi.org/10.1371/journal.pone.0214161.

World Health Organization. 2016. *Ensuring Innovation in Diagnostics for Bacterial Infection*. Edited by Chantal Morel. Europen Observatory on Health Systems and Policies.

Wu, Jiang, Seungyong Lee, V. R. Reddy, M. O. Manasreh, B. D. Weaver, M. K. Yakes, C. S. Furrow, Va S.P. Kunets, M. Benamara, and G. J. Salamo. 2011. "Photoluminescence Plasmonic Enhancement in InAs Quantum Dots Coupled to Gold Nanoparticles." *Materials Letters* 65 (23–24): 3605–8. https://doi.org/10.1016/j.matlet.2011.08.019.

Xue, Yurui, Xun Li, Hongbin Li, and Wenke Zhang. 2014. "Quantifying Thiol-Gold Interactions towards the Efficient Strength Control." *Nature Communications* 5: 1–9. https://doi.org/10.1038/ncomms5348.

Ye, Fan, Michael J. Burns, and Michael J. Naughton. 2013. "Plasmonic Halos - Optical Surface Plasmon Drumhead Modes." *Nano Letters* 13 (2): 519–23. https://doi.org/10.1021/nl303955x.

Yesilkoy, Filiz, Roland A Terborg, Josselin Pello, Alexander A Belushkin, Yasaman Jahani, Valerio Pruneri, and Hatice Altug. 2018. "Phase-Sensitive Plasmonic Biosensor Using a Portable and Large Field-of-View Interferometric Microarray Imager." *Light: Science & Applications* 7 (2): 17152–17152. https://doi.org/10.1038/lsa.2017.152.

Zeng, Shuwen. 2019. "Sensitivity Improved Surface Plasmon Resonance Biosensor for Cancer Biomarker Detection Based on 2D Perovskite-Based Metasurfaces." In *Proceedings Volume 10894, Plasmonics in Biology and Medicine XVI; 108940Q (2019)*. San Francisco. https://doi.org/https://doi.org/10.1117/12.2504472.

Zhang, Shuaidi, Ren Geryak, Jeffrey Geldmeier, Sunghan Kim, and Vladimir V. Tsukruk. 2017. "Synthesis, Assembly, and Applications of Hybrid Nanostructures for Biosensing." *Chemical Reviews* 117 (20): 12942–38. https://doi.org/10.1021/acs.chemrev.7b00088.

Zhang, Weichun, Martín Caldarola, Xuxing Lu, and Michel Orrit. 2018. "Plasmonic Enhancement of Two-Photon-Excited Luminescence of Single Quantum Dots by Individual Gold Nanorods." *ACS Photonics* 5 (7): 2960–68. https://doi.org/10.1021/acsphotonics.8b00306.

Zhao, Huaizhou, Binod Rizal, Gregory McMahon, Hengzhi Wang, Pashupati Dhakal, Timothy Kirkpatrick, Zhifeng Ren, Thomas C. Chiles, Michael J. Naughton, and Dong Cai. 2012. "Ultrasensitive Chemical Detection Using a Nanocoax Sensor." *ACS Nano* 6 (4): 3171–78. https://doi.org/10.1021/nn205036e.

Zhu, Chengzhou, Guohai Yang, He Li, Dan Du, and Yuehe Lin. 2015. "Electrochemical Sensors and Biosensors Based on Nanomaterials and Nanostructures." *Analytical Chemistry* 87 (1): 230–49. https://doi.org/10.1021/ac5039863.

Zijlstra, Peter, Pedro M.R. Paulo, and Michel Orrit. 2012. "Optical Detection of Single Non-Absorbing Molecules Using the Surface Plasmon Resonance of a Gold Nanorod." *Nature Nanotechnology* 7 (6): 379–82. https://doi.org/10.1038/nnano.2012.51.

Zynio, Stepan A., Anton V. Samoylov, Elena R. Surovtseva, Vladimir M. Mirsky, and Yuri M. Shirshov. 2002. "Bimetallic Layers Increase Sensitivity of Affinity Sensors Based on Surface Plasmon Resonance." *Sensors* 2 (2): 62–70.

6. List of Publications

- **L.A. D'Imperio**†, A.E. Valera†, J.R. Naughton, M.M. Archibald, J.M. Merlo, T.C. Connolly, M.J. Burns, T.C. Chiles, and M.J. Naughton (†contributed equally), *Biosensors and Bioelectronics*. DOI: 10.1016/j.bios.2019.03.045

- C. Yang, J.M. Merlo, **L.A. D'Imperio**, A.H. Rose, Y.M. Calm, B. Han, J. Gao, G. Zhou, M.J. Burns, K. Kempa, and M.J. Naughton, *Physica Status Solidi - Rapid Research Letter*. DOI: 10.1002/pssr.201900010

- **L.A. D'Imperio**, A.F. McCrossan, J.R. Naughton, J.M. Merlo, Y.M. Calm, M.J. Burns, and M.J. Naughton, *Flexible Printed Electronics*. DOI: 10.1088/2058-8585/aac8fc

- J.M. Merlo, N.T. Nesbitt, Y.M. Calm, A.H. Rose, **L. D'Imperio**, C. Yang, J.R. Naughton, M.J. Burns, K. Kempa, and M.J. Naughton, *Scientific Reports*. DOI:10.1038/srep31710

Submitted/In preparation

- Y.M. Calm, **L.A. D'Imperio**, M.J. Naughton *et al.*, "Optical confinement in the nanocoax: coupling to the fundamental TEM-like mode"............*submitted*

- J.M. Merlo, **L.A. D'Imperio**, and M.J. Naughton, "Electromechanical color filter for visible range manipulation"..................................*in preparation*

- **L.A. D'Imperio**, T.J. Connolly, M.J. Naughton *et al.*, "A Plasmonic Halo Biosensor"..*in preparation*

- A.H. Rose†, **L.A. D'Imperio**†, J. Park, M.J. Naughton *et al.*, (†contributed equally) "Intraoral pressure measurements in preterm infants"...*in preparation*